Molecular Beam Epitaxy of GaAs Nanowires and their Suitability for Optoelectronic Applications

Comparing Au- and Self-Assisted Growth Methods

DISSERTATION

zur Erlangung des akademischen Grades

doctor rerum naturalium
(Dr. rer. nat.)
im Fach Physik

eingereicht an der
Mathematisch-Naturwissenschaftlichen Fakultät I
Humboldt-Universität zu Berlin

von
Dipl.-Phys. Steffen Breuer B.Sc.

Präsident der Humboldt-Universität zu Berlin:
Prof. Dr. Jan-Hendrik Olbertz

Dekan der Mathematisch-Naturwissenschaftlichen Fakultät I:
Prof. Dr. Andreas Herrmann

Gutachter:
1. Prof. Dr. Henning Riechert
2. Prof. Dr. W. Ted Masselink
3. Prof. Dr. Erik P. A. M. Bakkers

eingereicht am: 20. Juni 2011
Tag der mündlichen Prüfung: 28. September 2011

„Genialität ist ein Prozent Inspiration
und 99 Prozent Transpiration.“
Thomas Alva Edison (1847-1931)

Für meine Mädels und Jungs.

Abstract

In this work we investigate the synthesis of GaAs nanowires by molecular beam epitaxy (MBE) and compare the Au- and the self-assisted variants of the vapour-liquid-solid (VLS) mechanism. We focus on the growth on Si(111) and give additional results for the growth on GaAs(111)B. We study the morphological and structural properties of the nanowires after long growth times as well as during the nucleation. In addition, we examine the suitability of GaAs/(Al,Ga)As core-shell nanowires for optoelectronic applications using photoluminescence (PL) spectroscopy.

A brief introduction to the fundamental concepts used for the growth of GaAs nanowires is given. The Au-assisted VLS mechanism is known as a versatile tool for nanowire growth, while the recent self-assisted variation results in the exchange of Au by Ga droplets and eliminates the possible incorporation of Au impurities.

We investigate the growth in order to obtain GaAs nanowires with high aspect ratio, which are epitaxially aligned to the substrates. We achieve [111]-oriented nanowires with epitaxial alignment, typical diameters between 20 and 100 nm and lengths exceeding several micrometres by both methods. While a parasitic planar layer grows between the nanowires by the Au-assisted method, we can avoid layer formation by the self-assisted method and reduce the parasitic growth of islands to 1/4 of the total volume. We find that when using the Au-assisted method the nanowires grow predominantly in the metastable wurtzite (WZ) crystal structure, while their self-assisted counterparts have the zincblende (ZB) structure and contain twin defects. All GaAs nanowires are fully relaxed and the strain arising from the lattice mismatch between GaAs and Si of 4.1% is accommodated by misfit dislocations at the interface.

We find that the nucleation stage on Si(111) strongly depends on the growth method. The Au-assisted nucleation is dominated by an early stage during which no vertical nanowires grow. We explain this by an analysis of interface energies that make the Au droplets stick to the Si substrate surface. So vertical nanowires grow only after the Si substrate surface is covered by GaAs. This understanding is corroborated by a comparative study of the Au-assisted nucleation on GaAs(111)B, which does not show the formation of any GaAs traces. We demonstrate that the self-assisted method leads to immediate vertical nanowire growth also on Si(111) and we explain this by the preferred wetting of GaAs by the Ga droplets.

The nanowires exhibit different side facets, which depend on the growth method. Self-assisted GaAs nanowires are generally found to have non-polar $\{1\bar{1}0\}$ side facets, while different (112)-type polar facets were described for Au-assisted GaAs nanowires with the ZB structure. We employ the current understanding of VLS growth theory to predict the effect of the droplet material on the stability of the lateral facet. We predict that $\{1\bar{1}0\}$ facets must result for Ga droplets, while different (112)-type composed facets can result for Au droplets. This behaviour is understood to be caused by the larger surface energy of the liquid Au droplets.

Finally, we investigate the suitability of our nanowires for optoelectronic applications, which in general require a large internal quantum efficiency and thus long minority carrier lifetimes. We fabricate GaAs/(Al,Ga)As core-shell nanowires and determine their minority carrier lifetimes at room temperature by transient PL spectroscopy. The results are (2.5 ± 0.1) ns for the self-assisted nanowires as well as (9 ± 1) ps for the Au-assisted nanowires. From this large difference we conclude that an additional non-radiative recombination channel is present in the Au-assisted nanowires. By temperature-dependent PL measurements we find a characteristic activation energy of 77 meV that is present only in the Au-assisted nanowires. We conclude that most likely Au is incorporated during Au-assisted VLS growth into the GaAs nanowires and acts as a deep, non-radiative recombination centre.

Keywords: Gallium Arsenide, Nanowires, Silicon Substrates, Molecular Beam Epitaxy, Crystal Growth, Nucleation, Facets, Minority Carrier Lifetime

Zusammenfassung

Thema dieser Arbeit ist die Synthese von GaAs Nanodrähten mittels Molekularstrahlepitaxie. Dabei wird das Wachstum mittels Au- und jenes mittels selbst-induziertem VLS-Mechanismus verglichen. Das Wachstum auf Si(111) Substraten steht im Mittelpunkt, ergänzt durch zusätzliche Resultate auf GaAs(111)B. Die morphologischen und strukturellen Eigenschaften der Nanodrähte werden sowohl nach langem Wachstum als auch während der Keimbildungsphase analysiert. Ferner wird mittels Photolumineszenzspektroskopie (PL) die Eignung von GaAs Nanodrähten mit (Al,Ga)As Hüllen für optoelektronische Anwendungen untersucht.

Die Arbeit beginnt mit einer kurzen Einführung in die grundlegenden Konzepte, welche für das Wachstum von GaAs Nanodrähten ausgearbeitet wurden. Der Au-induzierte VLS-Mechanismus ist weithin als vielseitiger Ansatz für die Herstellung von Nanodrähten bekannt. Darüberhinaus wird seit Neuerem der selbst-induzierte Mechanismus untersucht, bei dem Galliumtropfen die Rolle des Goldes übernehmen, da so eine etwaige ungewollte Verunreinigung mit Au von vornherein ausgeschlossen werden kann.

Ziel der Wachstumsstudien sind GaAs Nanodrähte mit großem Aspektverhältnis und epitaktischer Beziehung zum Substrat. Dieses wurde mit beiden Wachstumsmethoden erreicht. Die Drähte wachsen in die [111] Kristallrichtung, haben typische Durchmesser zwischen 20 und 100 nm und erreichen leicht Längen von mehreren Mikrometern. Während des Au-induzierten Wachstums entsteht parallel eine parasitäre Schicht zwischen den Drähten. Mittels des selbst-induzierten Mechanismus kann dies vermieden und parasitäres Inselwachstum auf 1/4 des Gesamtvolumens verringert werden. Die Au-induzierten GaAs Drähte haben hauptsächlich die Wurtzit (WZ) Kristallstruktur, während die selbst-induzierten Drähte in der Zinkblende (ZB) Kristallstruktur wachsen und Zwillingsbildung zeigen. Alle GaAs Drähte sind vollständig relaxiert. Die durch die Gitterfehlanpassung (4,1% zwischen GaAs und Si) verursachte Verspannung wird durch Versetzungen an der Grenzfläche abgebaut.

An Nanodrähten mit ZB Kristallstruktur werde abhängig von der Wachstumsmethode unterschiedliche Seitenfacetten beobachtet. Bei den selbst-induzierten Drähten sind dies ausschließlich unpolare $\{1\bar{1}0\}$ Facetten, während verschiedene (112)-artige, polare Facetten für Au-induzierte Nanodrähte beschrieben werden. Wir benutzen die aktuelle VLS-Wachstumstheorie, um den Einfluss des Tropfenmaterials auf die Stabilität der verschiedenen Seitenfacetten zu bestimmen. Im Ergebnis werden $\{1\bar{1}0\}$ Facetten für Ga Tropfen und (112)-artige Facetten für Au Tropfen unter bestimmten Bedingungen vorhergesagt. Das unterschiedliche Verhalten resultiert wesentlich aus der größeren Oberflächenenergie der flüssigen Au Tropfen.

Zum Abschluss wird die Eignung der Nanodrähte für die Optoelektronik untersucht, wozu eine hohe interne Quanteneffizienz und damit lange Lebensdauern von Minoritätsladungsträgern vorteilhaft sind. Dazu werden Au- und selbst-induziert gewachsene GaAs Nanodrähte für eine geringere Grenzflächenrekombination mit (Al,Ga)As Hüllen ummantelt und die Lebensdauer der Minoritätsladungsträger mittels zeitaufgelöster PL bei Raumtemperatur bestimmt. Das Ergebnis von (2.5 ± 0.1) ns für die selbst-induzierten und (9 ± 1) ps für die Au-induzierten Nanodrähte zeigt, dass ein zusätzlicher Rekombinationskanal in den Au-induzierten Drähten vorhanden ist. Durch temperaturabhängige PL Messungen kann eine charakteristische Aktivierungsenergie von 77 meV nachgewiesen werden, die nur in den Au-induzierten Nanodrähten vorliegt. Daraus wird gefolgert, dass sich Au während des Au-induzierten Wachstums in die GaAs Nanodrähte einbaut und dort als tiefes, nichtstrahlendes Rekombinationszentrum fungiert.

Stichworte: Galliumarsenid, Nanodrähte, Siliziumsubstrate, Molekularstrahlepitaxie, Kristallwachstum, Keimbildung, Lebensdauer von Minoritätsladungsträgern

Publications

M. Hilse, Y. Takagaki, J. Herford, M. Ramsteiner, C. Herrmann, S. Breuer, L. Geelhaar, H. Riechert, *Ferromagnet-semiconductor nanowire coaxial heterostructures grown by molecular-beam epitaxy*, Appl. Phys. Lett. **95**, 133126 (2009)

M. Hilse, M. Ramsteiner, S. Breuer, L. Geelhaar, H. Riechert, *Incorporation of the dopants Si and Be into GaAs nanowires*, Appl. Phys. Lett. **96**, 193104 (2010)

S. Breuer, M. Hilse, A. Trampert, L. Geelhaar, H. Riechert, *Vapor-liquid-solid nucleation of GaAs on Si(111): Growth evolution from traces to nanowires*, Phys. Rev. B **82**, 075406 (2010)

S. Breuer, M. Hilse, L. Geelhaar, H. Riechert, *Nucleation and growth of Au-assisted GaAs nanowires on GaAs(111)B and Si(111) in comparison*, J. Crystal Growth **323**, 311 (2011)

S. Breuer, C. Pfüller, T. Flissikowski, O. Brandt, H. T. Grahn, L. Geelhaar, H. Riechert, *Suitability of Au- and Self-assisted GaAs Nanowires for Optoelectronic Applications*, Nano Lett. **11**, 1276 (2011)

A. Biermanns, S. Breuer, A. Davydok, L. Geelhaar, U. Pietsch, *Structural evolution of self-assisted GaAs nanowires grown on Si(111)*, Phys. Stat. Sol. RRL **5**, 156 (2011)

Conference presentations

S. Breuer, A. Trampert, L. Geelhaar, H. Riechert, *MBE-grown GaAs nanowires using Au on GaAs(111)B and Si(111)* (poster), Summer School on Semiconductor Nanowires, Roscoff, France, 16-20 June 2008

S. Breuer, L. Geelhaar, A. Trampert, H. Riechert, *Nucleation of GaAs nanowires on Si(111) and GaAs(111)B substrates* (oral), Deutscher MBE Workshop (DMBE), Zürich, Switzerland, 1-2 September 2008

S. Breuer, A. Trampert, L. Geelhaar, H. Riechert, *MBE-grown GaAs nanowires using Au on GaAs(111)B and Si(111)* (poster), Summerschool "Functional Nanostructures" of the Deutsche Physikalische Gesellschaft (DPG), Bad Honnef, Germany, 14-19 September 2008

S. Breuer, L. Geelhaar, C. Pfüller, M. Wagler, O. Brandt, A. Trampert, H. Riechert, *Nucleation of Au-assisted GaAs nanowires on Si(111) and GaAs(111)B* (poster), European Molecular Beam Epitaxy Workshop, Zakopane, Poland, 8-11 March 2009

S. Breuer, M. Wagler, C. Pfüller, O. Brandt, A. Trampert, L. Geelhaar, H. Riechert, *Nucleation and Growth of Au-assisted GaAs nanowires on Si(111) and GaAs(111)B* (oral), Spring Meeting of the Deutsche Physikalische Gesellschaft (DPG), Dresden, Germany, 25 March 2009

S. Breuer, M. Wagler, A. Trampert, L. Geelhaar, H. Riechert, *Competitive growth of GaAs nanowires, islands and traces on Si in MBE* (poster), SemiconNano 2009, Anan, Japan, 9-14 August 2009

S. Breuer, M. Wagler, A. Trampert, L. Geelhaar, H. Riechert, *Au-assisted nucleation of GaAs on Si – Growth evolution from traces to nanowires* (oral), International Conference on Molecular Beam Epitaxy (ICMBE), Berlin, 24 August 2010

S. Breuer, C. Pfüller, T. Flissikowski, O. Brandt, H. T. Grahn, L. Geelhaar, H. Riechert, *Enhanced Room Temperature Carrier Lifetime in Self-assisted GaAs/(Al,Ga)As Core-Shell Nanowires* (poster), Fall Conference of the Materials Research Society (MRS), Boston, USA, 1 December 2010

Abbreviations

AFM	Atomic force microscopy
APB	Anti phase boundary
BEP	Beam equivalent pressure
BSE	Backscattered electrons
CBE	Chemical beam epitaxy
CL	Cathodoluminescence
CMOS	Complementary metal oxide semiconductor
cwPL	Continuous-wave photoluminescence
DFT	Density functional theory
DH	Double heterostructure
DLTS	Deep level transient spectroscopy
EBSD	Electron back-scattering diffraction
EDX	Energy dispersive X-ray spectroscopy
FWHM	Full width at half maximum
HR-TEM	High resolution transmission electron microscopy
LED	Light-emitting diode
LN	Liquid nitrogen
MBE	Molecular beam epitaxy
MEE	Migration enhanced epitaxy
MOVPE	Metal-organic vapour phase epitaxy
MPL	Conventional photoluminescence
μPL	Micro-photoluminescence
PL	Photoluminescence
RHEED	Reflection high-energy electron diffraction
SEM	Scanning electron microscopy
SF	Stacking fault
SIMS	Secondary ion mass spectroscopy
STEM	Scanning transmission electron microscopy
TD	Threading dislocation
TEM	Transmission electron microscopy
TP	Twin plane
TPL	Triple phase line
TRPL	Time-resolved photoluminescence
UHV	Ultra high vacuum
VLS	Vapour-liquid-solid
VS	Vapour-solid
WZ	Wurtzite
XRD	X-ray diffractometry
ZB	Zincblende

Contents

1. Introduction

The fundamental properties of semiconductors are caused by the mutual dynamic effects of electrons in the periodic potential of crystalline lattices. As a result, the propagation of electrons in a semiconductor has to be described by an intricate electronic band structure with a characteristic energy gap.

In the dominating semiconductor device, the transistor[1], charge transport can be well controlled by external potentials. This development has led to integrated circuits for the control and amplification of electronic signals and even further to modern digital microprocessors. In this field of modern electronics, silicon is the most important material for several reasons, which include that Si crystals can be produced with extremely high purity, in very large diameter boules and at low cost.

One of the few disadvantages of Si arises from its indirect bandgap, which causes electronic de-excitations to couple only very weakly to light emission. Most compound semiconductors, of which GaAs is the prototype, have a direct bandgap and therefore provide very efficient electron-light coupling. This property is central to optoelectronic devices such as light-emitting and laser diodes[2] and high-efficiency solar cells[3]. Furthermore, extremely high performance electronic devices such as the high electron mobility transistor (HEMT)[4] employ the low effective electron mass in GaAs and the high-quality GaAs/(Al,Ga)As interface.

In order to combine their respective advantages, the integration of GaAs and Si devices is highly desirable. However, the two materials have mismatching structural parameters, most importantly their lattice constants differ by 4.1%. As a result, their monolithic integration by heteroepitaxy (the well-oriented growth of one single crystal on another) leads to extended structural defects that originate at their common interface, which significantly compromise the final device performance.

A new approach to increasing the crystal quality of structurally dissimilar materials in general is to drastically reduce the continuous common interface area by the formation of vertical arrays of nanowires.[5,6] The small footprint of the nanowires and their high surface-to-volume ratio are expected to allow efficient accommodation of the strain that arises from the substrate interface or likewise within axial heterostructures.[7,8] Extended defects that are introduced into a nanowire are regularly found to bend to its lateral surface, except when exactly positioned along the nanowire main axis.[9] As a result, the structural quality of nanowires are believed to be completely independent from their substrate. Other advantages of nanowires include that their large surface-to-volume ratio makes them ideal materials for molecular sensors,[10] that their geometry may ease the coupling of light into and out of them,[11] and that they may facilitate new electronic device concepts based on the crossbar motif.[12]

Nanowires can be produced in the traditional top-down approach by resist deposition, its lithographic structuring, and selective etching of originally bulky structures. However, this process needs increasingly expensive lithographic tools the more the feature size is reduced below the wavelength of light. Alternatively, nanowire crystals can be grown by bottom-up techniques, which function independently of the nanowire diameter. Unidirectional crystals with radial dimensions ranging from the nanometre to the millimetre regime are regularly and reliably fabricated using the vapour-liquid-solid (VLS) growth mechanism.[13] The VLS mechanism explains unidirectional crystal growth by the presence of a liquid metal droplet, which i) serves as the preferred site for deposition of the crystal constituents supplied in the vapour phase, ii) alloys and supersaturates with these components, and iii) is lifted upwards by the precipitating solid.

Presently, gold is the technologically most important VLS-assisting metal, because it is versatile to form nanowires from a wide range of materials and in a broad range of conditions.[14] However, the presence of Au in the growth process is also of great concern, since Au may produce deep-level, carrier recombination centres, which drastically reduce the minority carrier lifetime.[15] Indeed, the incorporation of Au into Si nanowires during VLS growth has recently been verified using secondary-ion mass spectroscopy (SIMS).[16]

For VLS growth of compound semiconductor nanowires, a conceivable alternative to Au consists in the use of the intrinsic metal, which makes contamination impossible. GaAs nanowires can be fabricated using Ga droplets, which form in molecular beam epitaxy (MBE) without special treatment during the first seconds of growth on substrates covered by thin silicon oxide.[17] This mechanism is called ′self-assisted′ VLS, in order to underline that the droplet material is intrinsic to the compound.

It is the aim of this thesis to establish the fabrication of GaAs nanowires on Si substrates by MBE. This was realized first by the Au-assisted and soon afterwards by the self-assisted VLS growth mechanism. A detailed comparison of the two methods is the constant theme of this work.

In Chapter 2, fundamental aspects of epitaxial crystal growth in the planar as well as the nanowire shape are presented, including nanowire growth techniques and focussing on the integration of GaAs on Si.

Our own growth experiments of GaAs nanowires on Si substrates by the Au- as well as the self-assisted VLS mechanism are described in Chapter 3, which also comprises the results of morphological and structural characterisation of the resulting nanowires and of the nanowire-substrate interfaces. In addition, growth studies for the optimization of nanowire growth under morphological aspects are presented.

Chapter 4 is dedicated to a study of the nucleation, the early stage of growth, which was found to differ significantly between the Au- and the self-assisted method. Since the nucleation of Au-assisted GaAs nanowires on Si was found to follow an indirect route, an extra study of the homoepitaxial case on GaAs substrates is presented for comparison.

In Chapter 5, the orientation of the nanowire side facets is studied and the finding of a mutual difference between the two growth methods is analysed. Building on the current theoretical understanding of VLS nanowire growth, a model which describes the energy required for the formation of various side facets is presented. An analytical expression is employed to understand why and to predict how the probable side facets depend on the droplet material.

Optical measurements of photoluminescence spectra and transients are presented in Chapter 6, and the minority carrier lifetimes for nanowires grown by each method are extracted. This is a very important aspect of the comparison between the Au- and the self-assisted growth method, since the minority carrier lifetime is a central quantity which determines the material suitability for applications in optoelectronic devices.

In order to round up this work, a concluding summary of the different aspects of the comparison is presented in Chapter 7.

2. Fundamental Aspects

2.1. Epitaxial Crystal Growth

Epitaxy may be defined as the formation of monocrystalline material on a monocrystalline substrate. The term derives from the greek words $\epsilon\pi\iota$ = above and $\tau\alpha\xi\iota\varsigma$ = in an ordered manner. Epitaxial crystal growth can take place from the vapour or the liquid phase. Traditionally, the growth of thin epitaxial films is considered. In homoepitaxy, the growing film and the substrate consist of the same material. This technology can be used to produce epitaxial films of semiconductors with lower defect densities than the substrate. In heteroepitaxy, the growing film and the substrate consist of different materials. Heteroepitaxy can be used to achieve different aims: first, monocrystalline growth of a material for which no homoepitaxial substrates exist, and second, the creation of an interface region (called heterostructure) with new physical properties.[18] Arguably, the most advanced techniques for creating multi-layered epitaxial heterostructures is molecular beam epitaxy (MBE).

2.1.1. Molecular Beam Epitaxy

MBE is a modern epitaxial growth technique dedicated to the growth of semiconductor crystals with the highest achievable purity and the largest degree of external control. While this makes MBE the ideal tool for epitaxy research and extremely high performance applications, other techniques such as metal-organic vapour phase epitaxy (MOVPE) prevail in industry mainly for their faster growth rates.

In the MBE growth chamber, very high purity source elements are evaporated or sublimated from special effusion cells and then redeposited on an appropriate substrate. High vacuum conditions in the chamber ensure that the mean free path of the vaporized particles is larger than the chamber diameter, such that there is no interaction between them before they reach the substrate surface (*free molecular flow*). In fact, ultra high vacuum (UHV) conditions (p between 10^{-7} and 10^{-12} mbar) are employed to minimize the incorporation of impurities into the growing crystal. The substrate is usually heated and rotated during growth in order to increase the crystalline quality and the surface homogeneity. Typical growth rates lie between 1 and 4 Å/s. An additional advantage of MBE is that the epitaxial growth process can be monitored in situ via reflection high-energy electron diffraction (RHEED). The technology and thermodynamics of MBE growth have been thoroughly developed.[19–21]

Crystalline growth, whether by MBE or other methods, is governed by thermodynamics.[22,23] Growth occurs when there exists a *chemical potential difference* between the supplied species in the vapour phase and the solid material to be grown. A steady-state non-equilibrium situation is established by the continuous consumption of the supplied species. This leads to a constant chemical potential difference, which represents the driving force for crystalline growth.

$$\Delta\mu = \mu_V - \mu_S = kT\ln(p/p_0), \tag{2.1}$$

where the ratio p/p_0 is called the *supersaturation*, p is the actual, and p_0 the equilibrium vapour pressure. If growth takes place under p_0, the vapour is in equilibrium with the solid and $\mu_V = \mu_S$.

2.1.2. Epitaxial Growth Modes

There exist three modes of epitaxial growth on surfaces, irrespective of the supply phase being liquid or solid.[24] These are described in the following.

Islanding (Volmer-Weber) In the islanding mode, small clusters are nucleated directly on the substrate and then grow into islands of the condensed phase. This results from a stronger binding of the growing constituents to each other than to the substrate.

Layer by Layer (Frank-van der Merve) The layer by layer mode shows opposite characteristics. Since the atoms are more strongly bound to the substrate than to each other, a complete monolayer (ML) is formed first, before growth of the next ML begins, which is somewhat less strongly bound. Layer growth is obtained provided that the decrease in binding energy is monotonic and reaches the value of the supplied material in bulk phase.

Layer+Island (Stranski-Krastanov) This intermediate case can arise if after growth of the first (few) ML, which are strongly bound to the substrate, a strong decrease in the binding energy makes subsequent layer growth unfavourable. Islands are formed on top of this *wetting layer*. There may be many different origins for this growth mode. Anything that disturbs the monotonic decrease in binding energy may be the origin. A popular application of the Stranski-Krastanov growth mode, where the accumulation of strain leads to island formation is the self-organized growth of quantum dots.

A distinction between islanding and layer growth can be made using the surface energies of film γ_F and substrate γ_S, as well as their interface energy γ_{SF}. Epitaxial growth starts in the islanding mode, if the criterion

$$\gamma_S < \gamma_F + \gamma_{SF} \tag{2.2}$$

holds, and otherwise in the layer mode. Because high quality heterostructures require smooth interfaces, a smooth surface during growth via the layer mode is favourable. If the completion of started ML is faster than the nucleation of a new layer, layer growth happens via step-flow.

2.1.3. Challenges in Planar Heteroepitaxy of GaAs on Si

In addition to its own technological importance, the heteroepitaxy of GaAs on Si can be considered a role model for the monolithic integration of polar on non-polar semiconductors.[25,26] First, the challenges are introduced in general, followed by a detailed discussion of the case of GaAs on Si.

There are several factors that control the structural quality of heteroepitaxial layers.

Lattice Mismatch The most immediate issue for planar heteroepitaxy is *lattice matching*. When two materials with significantly different lattice parameters are grown on top of each other, a huge amount of strain develops quickly with increasing layer thickness. The following situations can result. Thin enough epitaxial films can adopt the lattice constant of the substrate (*pseudomorphic or coherent growth*) and stay strained. Beyond a *critical thickness*, the strain energy suffices to create defects at the interface between substrate and layer (*plastic relaxation*). Line defects, which are confined to the interface, are called *misfit dislocations*. Since the lattice mismatch between layer and substrate occurs in two directions, a 2-D network of misfit dislocations is created. Misfit dislocations remain located at the heterointerface but they can create *threading dislocation*, which can extend through the whole crystal bulk. Both kinds of line defects terminate only at a free surface or else cancel with another extended defect.

Thermal Mismatch Differences in *thermal expansion coefficients* of the two materials lead to tensile or compressive strains when the heterostructure is cooled from growth temperature to ambient conditions. Substrate bowing and bending can result. The epilayer *cracks* form when the layer thickness exceeds a critical cracking thickness.

Anti-Phase Boundaries The structural problem of *anti-phase-boundaries* (APBs) arises in the case of compound semiconductor growth on a column-IV elemental semiconductor. In elemental (non-polar) semiconductors, both sublattices of the diamond structure are occupied by the same atoms, while in compound (polar) semiconductors, each atom resides in a particular sublattice. Anti-phase boundaries arise if the constituent atoms occupy incorrect sublattices. These structural planar defects typically form at single atomic steps at the elemental semiconductor surface, when the neighbouring terraces are decorated by the identical compound.

These structural problems may appear sobering at first, and indeed the heterointerface with the lowest defect density to date remains the GaAs/(Al,Ga)As system, which is essentially lattice matched and does not permit APBs. Nevertheless, the goal of combining the polar compound semiconductors with the well-engineered non-polar silicon substrates is sufficiently attractive that several strategies were found which address the above challenges. One of the most important material combinations, that of GaAs on Si, is presented in the following.

The 4.1% lattice mismatch and between Si and GaAs leads to a very small critical thickness for coherent growth, i.e. $\sim$ 4 ML on Si(001).[27] Another challenge results from the fact that GaAs on Si grows in the Volmer-Weber islanding mode. Misfit dislocations nucleate in higher-stress regions near island edges by way of which the islands partially relax. After island coalescence, the defects become trapped and difficult to remove by subsequent operations. Furthermore, the mismatch in the thermal expansion coefficients α (5.6×10^{-6} for GaAs and 2.6×10^{-6} for Si) is large. The critical thickness for the onset of crack formation in GaAs epilayers on Si has been experimentally determined to be approximately 7 µm for $\Delta T = -575°\mathrm{C}$.[28] As an effect, threading dislocation densities as high as $10^9 - 10^{10}$ cm^{-2} are typical for direct growth of GaAs on Si.[26]

Several techniques have been developed to reduce the dislocation density in GaAs on Si. The formation of APBs can completely be avoided by slight *substrat misorientation* and high-temperature surface anneal, which leads to a pairing of all Si surface steps.[29,25] *Two-step growth* uses the effect that the number of dislocations is strongly reduced when the islands coalesce before plastic relaxation takes place. This can be achieved by a low temperature nucleation step (around 400°C instead of the typical growth temperature of

550-600°C) or instead by migration enhanced epitaxy (MEE).[30] *Cyclic thermal annealing* uses the large thermal mismatch, such that the strain in the grown layer changes between compressive and tensile. This reverses the motion of threading dislocations and facilitates their annihilation.[31] *Strained layer superlattices* employ the force that is exerted on threading dislocation lines by interaction with stress fields from strained interlayers. InGaAs/GaAs or GaAsP/GaAs interlayers introduce compressive strain which repulses the dislocation lines arising from the equally compressively strained GaAs/Si interface.[25]

Using these techniques, dislocation densities as low as 10^5 cm^{-2} have been achieved.[32] Such low dislocation densities correspond to an X-ray diffraction (XRD) full-width at half maximum (FWHM) of approximately 0.03°.[30] This represents a remarkable achievement, yet state-of-the-art Si, Ge and GaAs substrates show significantly smaller XRD FWHM nevertheless.

2.2. Nanowires - Quasi 1-D Nanostructures

A different and relatively new solution to the problems of heteroepitaxy is offered by free standing nanowires. Nanowires are quasi 1-D needle-like crystallites with lateral extensions in the nanometre regime. Such filamentary crystals were originally called whiskers, but inspired by the popularity of nanotechnology, the term nanowires has taken over in scientific use since around the year 2000.[33]

2.2.1. Mechanical Properties

Heterostructures in free-standing nanowires differ from their planar counterparts in their freedom from lateral boundary conditions. While planar layers are laterally constrained, since their surface to volume ratio is small, strain originating from the interface can be relieved in free-standing nanowires via elastic relaxation.

Strain relaxation in nanowires is described by the classical mechanical *Principle of St. Venant*, formulated in 1855, which applies to the strain in a long rod introduced by a clamp at one end.[34,35] It can be can be paraphrased as follows:

> The strain introduced into an elastic rod that is clamped at one end is completely released within a distance from the clamp equal to the diameter d of the rod.

The Principle of St. Venant applies to a nanowire whose one end is connected to the substrate and which is otherwise free. Further away from the interface, the nanowire is thus strain-free and extended defects are not necessary. Therefore, strain and defect-free crystals should be much easier to achieve in the nanowire geometry than in planar layers.[36]

The interface (and interface region within $\approx \pm d$) between nanowire and substrate can still be defective. But is was shown experimentally, that even threading dislocations which are initially co-aligned with the major nanowire axis bend off to the nearest lateral sidewall.[9] The concept of critical thickness for pseudomorphic growth in planar heteroepitaxy translates to a critical diameter d_c for nanowires. Obviously, d_c is expected to be larger for axial heterostructures *within* one nanowire than for heterointerfaces between nanowires and a semi-infinite substrate.

For the GaAs on Si heterointerface within a nanowire, different values were calculated by theoretical methods. Ertekin et al. arrived at $d_c = 40\,\text{nm}$,[8] while a $d_c = 80\,\text{nm}$ was calculated by a Glas et al. a little later.[7] Cirlin et al. determined the critical diameter by analysing SEM images of straight vertical as well as kinked GaAs nanowires grown on Si(111) substrates.[37] They argued that above the critical diameter "nanowires do not grow at all or bend out of shape by dislocations" and obtained 110 nm. A more reliable experimental determination of the critical diameter basing on HRTEM analysis of the GaAs nanowires of different diameters on Si(111) substrates was presented very recently and resulted in $d_c = 40\,\mathrm{nm}$.[38]

A superior crystalline quality of nanowires, which is largely independent from the substrate, is a major impulse for research in nanowires.

2.2.2. Bottom Up Nanowire Fabrication

A large variety of mechanisms exist for the epitaxial growth of semiconductor nanowires.[33,39,40] Common to all nanowire growth methods is the need for

1. a strong anisotropy of the growth rate in order to achieve a much faster growth in the axial than the radial direction, and
2. the nucleation of numerous isolated nanowires instead of one continuous structure.

Both, anisotropic growth rate and isolated nucleation can quite generally be achieved by the symmetry-breaking action of particles that collect arriving atoms and locally concentrate them. A variety of such *particle-assisted* mechanisms has been developed and they were successfully applied to the growth of nanowires from a very large range of materials.[40,41] Amongst them, the most widely used method is the VLS mechanism, which will be discussed in detail below. Several similar particle-assisted nanowire growth mechanisms exist, that are closely related to VLS growth, but either the supply or the collecting phase is different. Examples are the *Vapour-Solid-Solid* (VSS) mechanism,[42] and the *Solution-Liquid-Solid* mechanism.[43–45]

Focussing on GaAs nanowires, the VSS mechanism was discussed controversially: In contrast to the conclusion by Hiruma that GaAs nanowires grow by the VLS mechanism in MOVPE,[46] Persson et al. concluded that the Au alloy is in fact solid,[42] basing on the observation of diffraction spots during post-growth heating experiments at 540°C *within* a Transmission Electron Microscope (TEM). This conclusion was refuted by Harmand et al., who studied the RHEED patterns that formed during MBE growth of GaAs nanowires and found diffraction spots originating from solid Au-Ga alloys only at temperature below 400°C.[47,48]

For another class of growth mechanisms no particle is found at the tip of the nanowires. These can be summarized as *particle-free* mechanisms. Of current importance for the fabrication of GaAs nanowires is the *Selective Area Growth*: Material can grow only in the windows of a lithographically structured mask, while nucleation on the mask is inhibited. Growth on partly masked substrates is carried out under conditions that promote highly anisotropic growth rates.[49] Selective area growth has been applied successfully to form arrays of free-standing GaAs nanowires by MOVPE.[50–52]

2.2.3. Au-assisted Vapour-Liquid-Solid Mechanism

The most common of the particle-assisted mechanisms, and also the oldest, is the *Vapor-Liquid-Solid* (VLS) growth mechanism, which dates back to 1964.[13] Au droplets have regularly been employed since the very beginning, but the VLS mechanism itself is independent of the specific liquid material. The versatility of the general VLS mechanism is underlined by the fact that it does work not only in advanced growth techniques like molecular beam epitaxy (MBE), but has also been found in nature[53] and even on the moon.[54]

In most simple terms, growth species that are supplied in the vapour phase are concentrated by a liquid metal droplet acting as a preferred sink for the growth species, which supersaturates, forms Si by precipitation, and lifts up the droplet in the process. The material arrives at the droplet by direct impingement as well as by surface diffusion from nearby surfaces.

In the case of growth from precursor molecules (e.g. MOVPE), the underlying reason for the concentration in the droplet might be its catalytic action in the chemical reaction of the precursor decomposition.[55] In MBE growth, for which no decomposition of the elemental growth species is necessary, another process leads to the increased local concentration of the growth species in the droplet, which Wagner ascribed to a large accommodation coefficient of the droplet surface.[56]

In the following, we subscribe to the terminology that the liquid material X *assists* in the VLS growth of nanowires, and will commonly use the term ″nanowires grown by the X-assisted VLS mechanism“ or simply “X-assisted nanowires”, as shorthand. The standard Au-assisted VLS mechanism is described in more detail in the following.

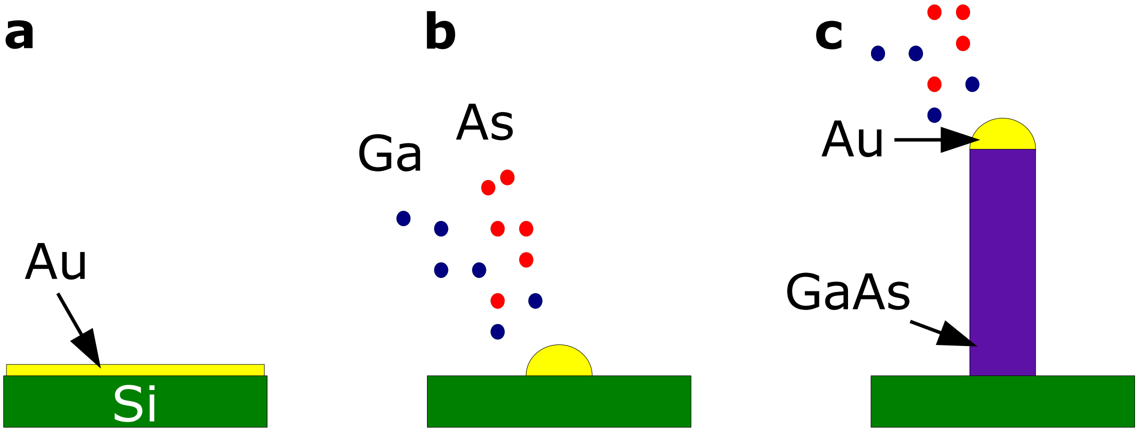

Figure 2.1.: **Au-assisted Vapour-Liquid-Solid Growth of GaAs Nanowires.** (a) Creation of Au droplets by deposition of a thin film and subsequent annealing. (b) Supplied Ga and As in the vapour phase are collected by the liquid Au droplet. (c) Supersaturation of the Au droplets leads to crystallization of the supplied species at the liquid -solid interface.

The original article of Wagner and Ellis[13] sparked intensive research in 1-D crystalline wires, in the course of which it was found that compounds including GaAs could also be grown in the same form using liquid Au droplets.[56,57] Figure 2.1 presents an illustration of GaAs nanowire growth by the Au-assisted VLS mechanism.

Conceptually, the growth of compound semiconductors by the VLS mechanism is more complex, since it requires the formation of a ternary alloy. For the Au-Ga subsystem, several stable binaries exist, which are all liquid above 491°C,[58] and of which AuGa as well as β'Au$_7$Ga$_2$ could be detected by TEM after nanowire growth.[47] However, the As solubility in Au-Ga alloys is very small, and there is no binary Au-As solid compound under 636°C.[59,58]

The understanding of the As incorporation was recently advanced by Glas et al. in a detailed analysis of the nucleation statistics during $InP_{1-x}As_x$ nanowire growth by the Au-assisted VLS mechanism.[60] An intentional modulation of the As content x created markers similar to tree rings, whose distances were measured to extract changes in the growth rate. Statistical analysis led to the finding of sub-Poissonian statistics and the understanding that the growth takes place by uncorrelated nucleation events. This was interpreted as being caused by the significant depletion of the droplet from both group-V elements after one monolayer has nucleated and grown. This effect reduces the supersaturation, such that the nucleation of the next monolayer is delayed until the group-V elements have refilled.

The Au-assisted VLS mechanism is very versatile and Nanowires have been grown from a large variety of other materials (including virtually any elemental and compound semiconductor).[14] Nevertheless, any incorporation of Au can severely affects the electronic properties of semiconductors, which makes Au incompatible with CMOS technology.[15]

2.2.4. Self-assisted Vapour-Liquid-Solid Mechanism

For compound materials such as III-V semiconductors, an obvious alternative to Au is to use the metal compound as the assisting particle. Extrinsic defects from the droplet can completely be avoided when GaAs nanowires are fabricated by Ga-assisted VLS growth. Fontcuberta et al. have presented GaAs nanowires with Ga droplets at their top, grown on GaAs substrates covered by a thin layer of silicon (sub-)oxide SiO_x. They proposed the following mechanism and called it Ga-assisted VLS growth.[17] In order to underline the fact that the Ga droplets form by themselves in the beginning of growth, the related term self-assisted is used in the following.

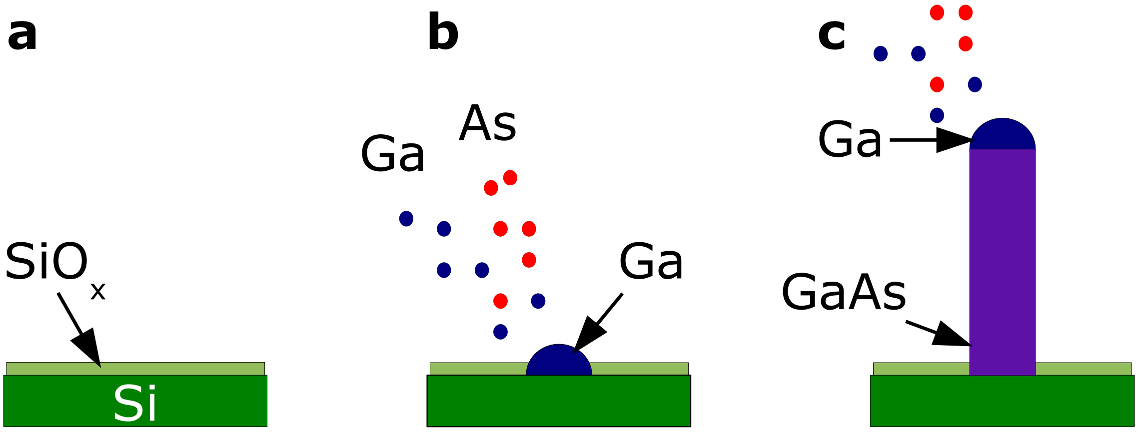

Figure 2.2.: **Self-assisted Vapour-Liquid-Solid Growth of GaAs Nanowires.** (a) A thin film of SiO_x is prepared on the substrate. (b) While the supplied arsenic initially desorbs, the diffusing Ga atoms form liquid droplets, which are immobilized by either pre-existing or Ga-etched pinholes in the SiO_x. (c) Once the droplets have formed, supersaturation of the Ga droplet with As leads to the crystallization of GaAs at the liquid-solid interface.

A schematic of the self-assisted growth of GaAs nanowires on Si substrates is presented in Figure 2.2. The Si substrate is covered by a thin film of its native oxide (SiO_x) or other silicon oxide prepared dedicatedly.

- Upon supply of the growth species, the arsenic initially desorbs, while the supplied Ga forms liquid droplets. This may be assisted by the enhanced Ga diffusion length on the SiO_x. The Ga droplets are immobilized by pinholes in the oxide, whose origin is not clear. They may either be pre-existing or have been 'etched' into the SiO_x by a reaction with Ga. In this way, epitaxial contact to the Si substrate can be created, provided the oxide is not too thick (< 30 nm for sputter coated SiO_x).[17]

- Once the droplets have formed, enrichment and supersaturation of the Ga droplet with As leads to the crystallization of GaAs at the liquid-solid interface.

The understanding that the surface oxide helps in the formation of Ga droplets clarified earlier reports on "oxide-assisted" nanowire growth.[61] Later on, Mandl et al. could demonstrate that a thin oxide layer on the substrate is beneficial for the formation of sufficiently small metal droplets and their immobilisation during the initiation of nanowire growth.[62] Recently, Plissard et al. have shown that self-assisted GaAs nanowire growth is possible directly on clean Si, but the formation of unwanted islands between the nanowires had strongly increased.[63]

2.3. Zincblende-Wurtzite Polytypism

At ambient conditions, many III-V and II-VI semiconductors, including the III-As, adopt the zincblende (ZB) crystal structure. However, the segments of the closely related hexagonal Wurtzite structure (WZ) are also regularly found in III-V nanowires.[64–66] *Polytypism* is the co-existence of related crystal structures, which differ in their stacking sequence.

The two crystal structures are presented in Figure 2.3 in order to highlight their similar structural qualities. Both structures are 4-fold coordinated, but the WZ has an ABABAB... stacking sequence along its hexagonal [111] axis, rather than the ABCABC... stacking of the ZB along its cubic [111] axis. Thus, they differ only in the geometry of bonding of their third nearest neighbours, which explains their close similarity. As a result, they have only small differences in their internal energies. In the hexagonal WZ structure, the bond lengths can be (slightly) unequal, while the ZB structure has ideal tetrahedral coordination. Therefore, two basis vectors a and c are necessary to determine the WZ unit cell, while one suffices for the complete description of the ZB one.

While some compound semiconductors, e.g. AlN, GaN, and ZnO, are stable in the WZ structure, WZ GaAs does not naturally occur. However, nanowires can adopt the WZ structure for kinetic reasons.[67] In order to create WZ GaAs in the bulk, very high pressures are needed, which was achieved by McMahon et al.[68] After subjecting finely powdered ZB GaAs to a pressure of 14 GPa, moderate heat, and subsequent slow recovering to ambient pressure, they found that the GaAs had transformed to the WZ phase. They analysed the crystal structure of the WZ GaAs by Synchrotron XRD and could determine the lattice parameters to very high precision. The result is presented in Table 2.1 together with the well-known values for ZB GaAs, which can be found in databases.[69]

A comparison of the lattice parameters measured by McMahon et al. for WZ GaAs with those well-known for ZB GaAs demonstrates that a is slightly smaller and c is slightly larger than the equivalent ZB lattice spacings d_{110} and $2 \times d_{111}$. Therefore the c/a ratio is larger than its ideal value for perfect tetrahedral coordination ($\sqrt{8/3} \approx 1.633$, like in ZB). According to McMahon et al., this is clear evidence for metastability of the WZ

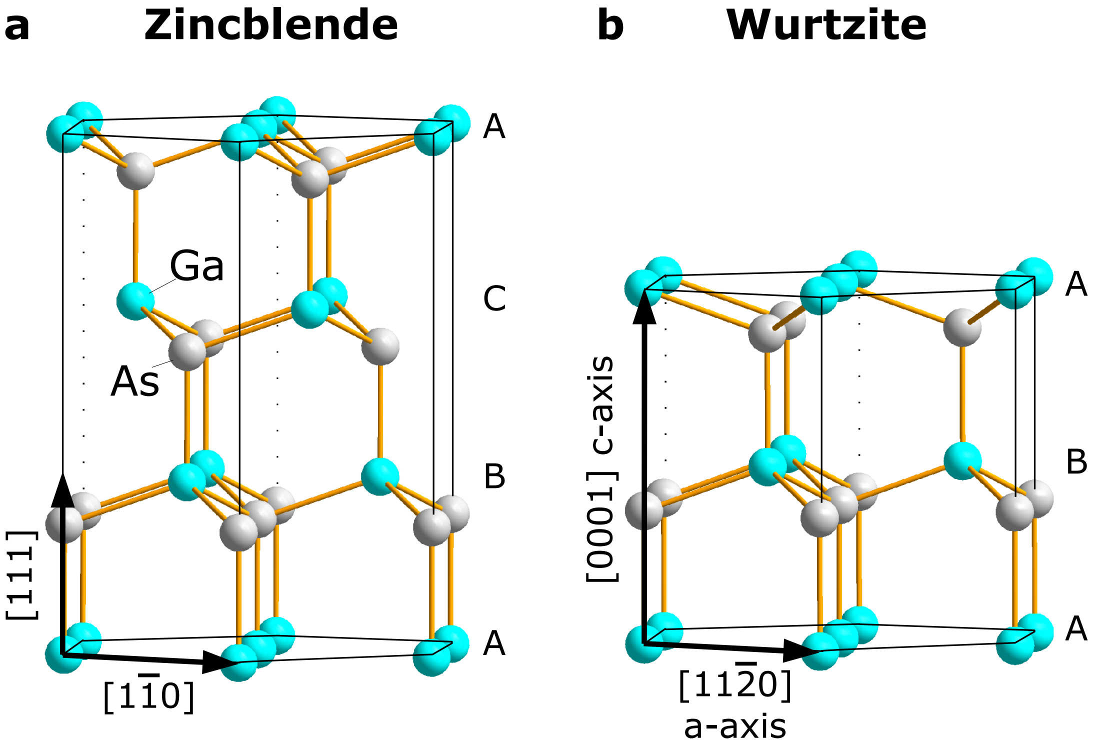

Figure 2.3.: **Zincblende (ZB, a) and Wurtzite (WZ, b) stacking sequences** Both structures are four-fold coordinated and differ only in the bonding geometry of their third nearest neighbour. The stacking sequence is ABCABC... for ZB along the cubic [111] direction and ABABAB... for WZ along the equivalent hexagonal [0001] direction (c-axis). Other equivalent directions are $\langle 1\bar{1}0 \rangle$ and $\langle 11\bar{2}0 \rangle$ (a-axis) as well as $\langle 11\bar{2} \rangle$ and $\langle 10\bar{1}0 \rangle$.

structure. Three slightly longer bond lengths for WZ GaAs in comparison to ZB GaAs indicate likewise.*

GaAs is stable in the ZB but only metastable in the WZ structure. Therefore, there is an additional energy associated with its formation, which has been calculated in computational studies and was reported to be $\sim$ 12 meV/atom.[68] Nevertheless, Hiruma et al. reported, that III-As nanowires grown by the Au-assisted VLS mechanism in MBE adopt the WZ crystal structure.[64,46] They also found *rotational twins* in their ZB InAs and GaAs nanowires and explained how the WZ structure could be built up by many of them. Rotational twins mean that in discrete sections of a nanowire the atomic positions are rotated by 180° around a twin axis, which in their case was co-aligned to the [111] growth axis. In these twin segments, the ABCABC... stacking sequence of zincblende is reverted to CBACBA... . Therefore, the sequence is ABC(AB | A)CBA... around the twin boundary denoted by a vertical line. The brackets indicate a 3 ML thin segment of the WZ crystal structure, for which the stacking sequence is ABAB... . Thus, when a rotational twin occurs after every ML, pure WZ is generated.

ZB-WZ Polytypism is so frequently found in GaAs nanowires, that it appears to be rather the rule than the exception.[42,47,70] Since electronic and optical defects can be as-

---

*In contrast, for compounds like GaN that naturally adopt the WZ structure, the c/a ratio is smaller than 1.633.

Structure	Zincblende (ZB)	Wurtzite (WZ)
Space group	F -4 3 m (216)	P 6 3 m c (186)
Lattice	2 face centred cubic sublattices	2 hexagonal sublattices
Basis	Ga $(0,0,0)$ and As $(\frac{1}{4},\frac{1}{4},\frac{1}{4})$	Ga $(\frac{1}{3},\frac{2}{3},0)$ and As $(\frac{1}{3},\frac{2}{3},u=0.373)$
Lattice Parameters	$a = 5.65359$ Å	
	$d_{110} = 3.99769$ Å	$a = (3.989 \pm 0.001)$ Å
	$2 \times d_{111} = 6.52820$ Å	$c = (6.564 \pm 0.001)$ Å
c/a ratio	$d_{110}/(2 \times d_{111}) = \sqrt{8/3} \approx 1.633$	$c/a = (1.645 \pm 0.005)$ Å
Bond lengths	2.448 Å (4 bonds)	2.448 Å (1 bond), 2.449 Å (3 bonds)

Table 2.1.: **Structure Parameters of Zincblende and Wurtzite GaAs** after 68,69.

sociated with the twin boundaries,[71] it is favourable to control their formation and to achieve either phase-pure nanowires[72,73] or a twinning superlattices.[74]

Therefore, the understanding of the origins of ZB-WZ polytypism is of high relevance for the nanowire community. It has been shown by Glas et al. in 2007 that the formation of WZ GaAs in nanowires can be explained by the kinetics of VLS growth and arises from the lower lateral energy of the WZ nanowire side facets.[67] The detailed argumentation is presented in Chapter 5.

3. GaAs Nanowire Growth Studies

All growth experiments for the presented work were performed in MBE VI machine (M6) at Paul-Drude-Institut, see Figure 3.1, which contains two growth chambers. One (the *Au chamber*) is equipped with a Au source for nanowire growth using this metal. It contains a very reliable arsenic cracker cell made by EPI, whose cracker zone temperature was set at 600°C to provide a molecular beam of As_4. The second growth chamber (*III-V chamber*) is dedicated to the growth of high-quality III-As semiconductors and equipped with Si and Be dopant sources. It contains both an arsenic cracker cell made by Addon and an additional arsenic evaporation cell from Createc, which were similarly set up to provide As_4. Although the self-assisted VLS growth of GaAs nanowires was established in both chambers, most of the presented experiments were performed in the Au-chamber in order to facilitate the highest comparability with the nanowires grown by the Au-assisted method.

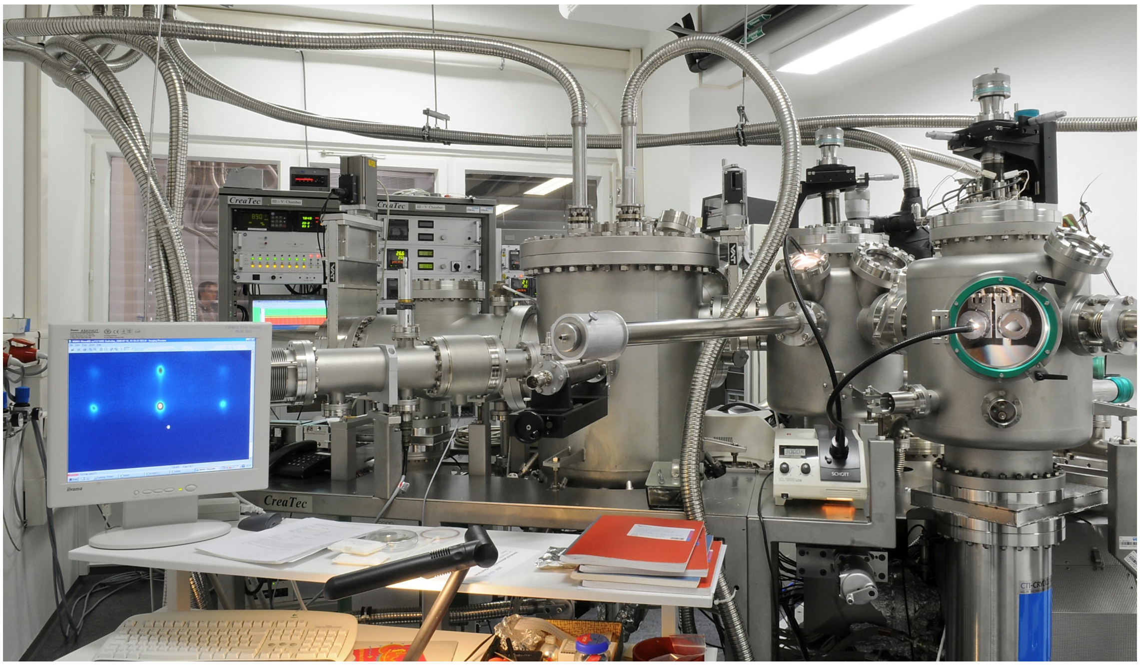

Figure 3.1.: **Photograph of MBE VI machine (M6) at Paul Drude Institute.** From left to right, the III-V chamber, middle chamber and loading chamber are shown. The Au chamber is hidden.

In this chapter, details of the growth processes and the resulting nanowire morphologies and microstructures are presented. Section 3.1 describes Au-assisted GaAs nanowire growth on GaAs(111)B as well as on Si(111) substrates. For the latter, the overall crystal structure and the interface morphology are reported. In Section 3.2, nanowire growth by the self-assisted VLS mechanism, using automatically formed Ga droplets and a thin SiO_x layer, is subsequently described and growth series for the optimization of the nanowire morphology and their yield are presented. Finally, the resultant morphology, microstructure and crystal structure of the obtained nanowires are shown.

3.1. Au-assisted VLS Nanowire Growth

The VLS mechanism originally described the growth of elongated Si crystals using Au droplets (Sect. 2.2.2). However, already in their original work of 1964, Wagner and Ellis formulated the expectation that the mechanism also works for "compound crystals, for example GaAs",[13] which was indeed soon demonstrated.[75,76]

These early reports on III-V whiskers were followed up in the early to mid 1990s by Hiruma et al. at Hitachi in an effort to employ 1-D crystals for optoelectronics applications.[46] They grew GaAs nanowires by the Au-assisted VLS mechanism and established that the preferred growth direction is [111]B, which allows ZB-WZ polytypism (see Sec. 2.3). Despite the success of the group in producing p-/n-junctions and even an LED, their work was discontinued.

However, towards the end of the 1990s, strong interest arose in the applications of very small structures, which was subsumed under the buzz-word *nanotechnology*. In this spirit, reports on Au-assisted VLS growth of Si, Ge and III-V nanowires with diameters as low as 3 nm by Lieber and co-workers have attracted a lot of attention.[77,78] Unfortunately, the originally employed growth method, laser-assisted growth in a quartz tube, had the effect that the wires formed far from the substrate without any epitaxial relation.

Soon afterwards, Samuelson and his group at Lund University followed up the work by Hiruma et al.: Ohlsson et al. reported on the Au-assisted VLS growth of GaAs nanowires on GaAs(111)B substrates by chemical beam epitaxy (CBE) and demonstrated size, position and shape control.[79] In 2004, as an important step towards an integration of III-V nanowires with Si, Martensson et al. demonstrated Au-assisted VLS growth of GaAs and other III-V nanowires on Si substrates.[6] They used Si(111) as well as Si(001) substrates and found vertical nanowires only on the former orientation. Wacaser et al. focused again on GaAs nanowires and showed that when they are grown on (111)A substrates with an additional organic layer, phase-pure ZB nanowires can be grown on GaAs(111)A, while on GaAs(111)B the nanowires contained many stacking faults.[72]

Among the first demonstrations of GaAs nanowire growth in MBE were Wu et al. who used a combination of Au-assisted VLS mechanism and selective area epitaxy through porous alumina templates.[80,81] By 2005 Dubrovskii et al. demonstrated that the Au-assisted VLS mechanism alone is sufficient for the MBE growth of GaAs nanowires, and that the length to diameter relation could be understood in terms of a sidewall diffusion model.[82] It was shown in the same year by Harmand et al. using RHEED, that the Au particle is indeed a liquid alloy during growth,[47] which contrasts to results of heating experiments of CBE-grown GaAs nanowires suggesting that it is solid.[42] Tchernycheva et al. reported that Au-assisted VLS growth produces GaAs nanowires on GaAs(111)B in the temperature range between 470 and 570°C at a V/III flux ratio of 2,[65] which is in good agreement with a temperature window between 500 and 600°C at V/III flux ratios of 1.5 and 2.3 in gas-source MBE, as reported by Plante et al.[83]

The first reports on MBE growth of GaAs nanowires on Si substrates appeared in 2007: Ihn et al. demonstrated that the nanowires grow again along [111], and that stacking faults lead to wurtzite-zincblende polytypism,[84] both well known features from growth on GaAs substrates. Similar results were published by Soshnikov et al., amended by a detailed RHEED study that also showed the polytypism.[85] PL spectra of Au-assisted

GaAs nanowires on Si were also demonstrated.[86,87] In the following year, a detailed study of the influence of the As flux on the nanowire morphology was published by Paek et al., which showed that radial growth can be avoided at high As fluxes.[88]

3.1.1. Au-assisted GaAs Nanowires on GaAs(111)B

When the work on this thesis was started in 2007, there was no previous experience with any particle-assisted nanowire growth at Paul Drude Institute. A detailed study of nanowire growth on Si substrates was our main goal from the beginning. The first successful growth of GaAs nanowires on Si by MBE had just been reported in that year, but the growth conditions were not described in sufficient detail for direct reproduction of the conditions.[84] Therefore, we started our GaAs nanowire growth experiments on GaAs substrates, following the conditions described by the Harmand group.[47,65] Substrates with the (111)B orientation were used, such that the usual ⟨111⟩B growth direction is vertical.[46]

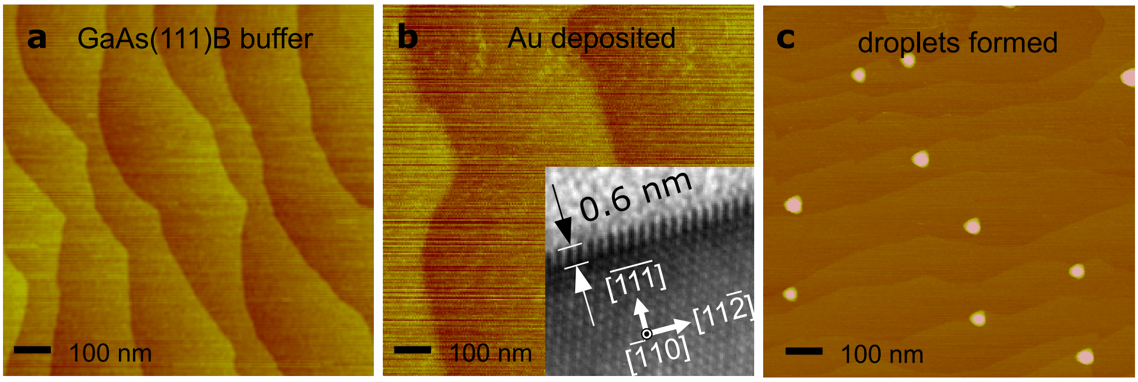

Figure 3.2.: **Au droplet preparation on GaAs(111)B** AFM micrographs of (a) terraced GaAs(111)B buffer layer, (b) after Au layer deposition, inset shows HR-TEM cross section for the determination of the layer thickness, (c) Au droplets formed after annealing.

The semi-insulating, on-axis GaAs(111)B substrates were degassed in the load lock at 300°C for 20 min and then transferred into the "Au" growth chamber of M6, of which one Knudsen cell had been filled with Au (5 g of 99.995% gold). A terraced GaAs(111)B buffer layer[89–91] was grown at 600°C, in order to cover surface impurities, to level the initially rough surface, and thus to reduce the possibility for the creation of crystallographic defects in the following structures. Formation of atomic terraces was checked by AFM as presented in Fig. 3.2a.

A film of Au was deposited from the effusion cell (source temperature $T_{Au} = 1000°\text{C}$) onto the buffer layer for 6 min at a substrate temperature of $T_S = 20°\text{C}$. This process led to a continuous film of Au on GaAs as presented in Fig. 3.2b, with a film thickness of 0.6 Å as determined by HR-TEM (inset). Subsequent annealing for 5 min at $T_S = 550°\text{C}$ under As atmosphere (Fig. 3.2.c) led to the de-wetting of the Au film and the creation of Au droplets, which may already form eutectic alloys with substrate Ga atoms at this temperature.[58] We will use the simple term "Au droplets" hereafter, notwithstanding that there may be a substantial amount of Ga in the alloy. At this point the Au droplets had average area densities of 10 droplets/μm^2 and diameters of 35 ± 8 nm as determined by AFM. The true diameters of the Au droplets are probably somewhat smaller, since small pyramidal bases of GaAs appear to have formed prior to growth by consumption of As from the background supply provided to prevent substrate disintegration.

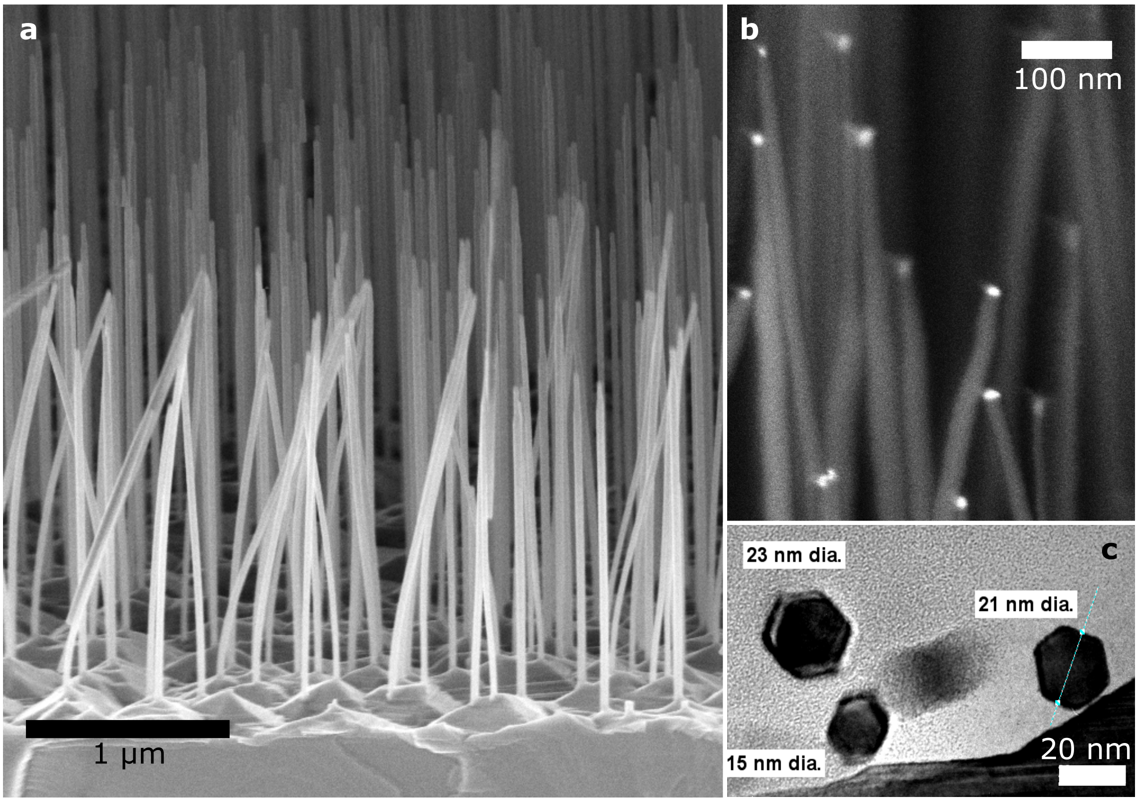

Figure 3.3.: **Au-assisted GaAs nanowires on GaAs(111)B** (a) SEM micrograph (80° inclined substrate) of as-grown nanowires, with nanowires bending due to SEM charging effects, (b) magnification with material contrast using the BSE detector indicating the presence of heavy atoms at the nanowire tips, (c) TEM micrograph of hexagonal nanowire cross sections (image taken by A. Trampert).

After the Au droplet preparation, nanowire growth could be initiated. A growth temperature of $T_S = 500°\text{C}$ and a V/III flux ratio of $J_{As}/J_{Ga} = 2$ had been shown to give GaAs nanowires with minimized tapering.[65,83] Thus, the substrate temperature was ramped down to $T_S = 500°\text{C}$ and the system was allowed to settle for 5 min under a high As supply flux of $J_{As} = 5\ \text{nm}^{-2}\text{s}^{-1}$ (the equivalent BEP was 1.2×10^{-5} torr). For an exemplary nanowire growth run, the Ga shutter was opened for 30 min with a Ga supply flux of $J_{Ga} = 2.5\ \text{nm}^{-2}\text{s}^{-1}$ such that $J_{As}/J_{Ga} = 2$ (the equivalent Ga-limited planar growth rate was $v_{Ga} = 400\ \text{nm/h}$). The sample was rotated continuously except for interruptions for obtaining RHEED patterns. After closing of the Ga shutter, the substrate temperature was ramped down to $T_S = 20°\text{C}$ with 10 K/min and the As supply flux was at first reduced to 1/2 and then completely closed below $T_S = 400°\text{C}$. The sample was then unloaded, cleaved into smaller pieces and analysed.

Figure 3.3 depicts micrographs of an exemplary sample of Au-assisted GaAs nanowires grown on GaAs(111)B in this way. An SEM image obtained with the electron beam incidence inclined 80° to substrate normal is presented in Fig. 3.3a. The wires are aligned vertically to the substrate, but bend in the SEM due to charging effects. At the top 100 nm, the nanowires are tapered. Using further SEM images, the average lengths ($1.7 \pm 0.2\mu\text{m}$), diameters at the bottom (40 nm) and top (20 nm), as well as the nanowire area density (10/µm^2) were determined. At the nanowire base, faceted pyramids are visible and additional 2-D growth of a closed basal layer appears likely, since only about one half of the provided GaAs volume is present in the nanowires. Fig. 3.3b depicts the nanowire top regions under enhanced material contrast using a detector for back-scattered electrons (BSE). Since the heavy Au atoms provide a high contrast, the Au droplets at the nanowire tips with diameters ≈20 nm can clearly be identified. Some tapering can be seen in addition, although the image is slightly distorted vertically. The nanowire cross sections are hexagonal, as can be seen in a TEM image (Fig. 3.3c) of detached nanowires. The nanowire diameters obtained here fit to those determined by SEM close to the tapered nanowire tips.

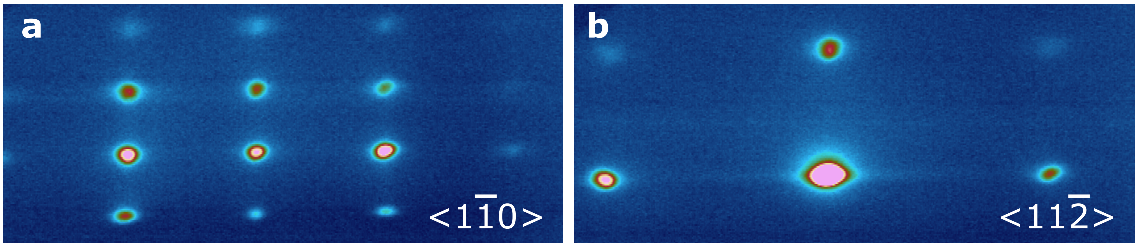

Figure 3.4.: **RHEED during growth of Au-assisted GaAs nanowires on GaAs(111)B** When the beam was incident in substrate azimuths (a) $\langle 1\bar{1}0\rangle$ and (b) $\langle 11\bar{2}\rangle$, the characteristic transmission patterns of Wurtzite GaAs are observed, indicating epitaxial alignment of nanowires and substrate.

Figure 3.4 presents RHEED patterns obtained during nanowire growth and show the characteristic transmission patterns of WZ GaAs, when the beam was incident along the high-symmetry substrate azimuths. They indicate a dominance of the WZ crystal structure and a [0001]-oriented growth axis. The epitaxial alignment of hexagonal [0001], $\langle 11\bar{2}0\rangle$, and $\langle 10\bar{1}0\rangle$ directions of the nanowires with their equivalent cubic directions [111], $\langle 1\bar{1}0\rangle$, and $\langle 11\bar{2}\rangle$, respectively, of the substrate can be deduced.

Successful growth of epitaxially aligned Au-assisted GaAs nanowires on GaAs(111)B substrates was thus established. The presence of Au droplets at the nanowire tips as well as the correspondence of droplet and nanowire diameter clearly demonstrate that growth followed the VLS mechanism.

3.1.2. Au-assisted GaAs Nanowires on Si(111)

Successful MBE growth of Au-assisted GaAs nanowires on Si substrates had just been reported by Ihn et al. when our own experiments begun in 2007.[84] However, their growth conditions were not reported in sufficient detail to allow straight-forward reproduction. Therefore, we transferred the conditions from our own growth experiments on GaAs(111)B to growth on Si. Si substrates with (111) orientation were used in order to obtain a majority of vertical nanowires.

Different batches of Si(111) substrates were used during this work, which were either full 2″ wafers, or quarters thereof, or 2 × 2 cm^2 square pieces. The substrates were either unintentionally doped or n-doped (by phosphorous) and had different degrees of miscut between 0.5° and 2°. These minor differences between the substrate batches were later found to have no effect on the nanowire morphology.

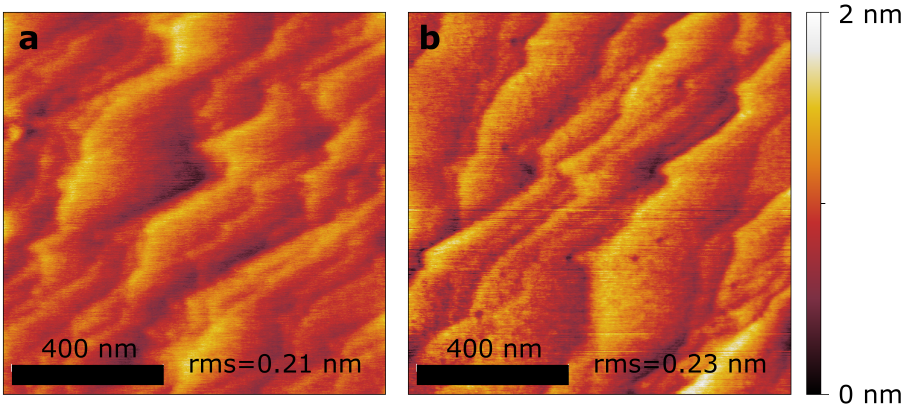

Figure 3.5.: **Si(111) before and after Au droplet preparation** AFM micrographs of Si(111) substrates cleaned by anisotropic chemical etching using NH_4F. (a) terraced Si(111) surface, (b) surface after deposition of 0.6 nm Au and annealing at 550°C for 5 min. Au droplets appear to have formed holes on the surface, probably related to the formation of a Au-Si eutectic alloy.

For a reproducible preparation of a planar surface in MBE, buffer layer growth is ideal. However, the Si source available in M6, a standard effusion cell dedicated to doping, does not provide sufficient fluxes for this purpose. An additional problem is the removal of the native silicon oxide. Thermal desorption would require heat treatments at substrate temperatures above 900°C, which cannot be reached by the MBE system used here.[92,93] Three different methods for Si(111) surface preparation were employed: The silicon oxide was removed either by "polishing" under an incident Ga-flux, or by wet chemical procedures before loading, which create an H-terminated (hydrophobic) Si surface. Details of Ga-polishing, and chemical HF- and NH_4F- procedures can be found in Section A.2.

An AFM image of a Si(111) substrate, chemically cleaned using NH_4F, is presented in Figure 3.5a and depicts (111) terraces produced by the anisotropic etching. The step heights correspond to mono-, bi-, tri-, and tetra-layers of Si(111). After chemical etching, the substrates were loaded into the MBE within 15 min, in order to avoid the formation of native oxide. The H-terminated substrates were then heated in the preparation chamber to 300°C for 30 min under UHV and transferred into the "Au" growth chamber. In the following, Au droplets were prepared by deposition of 0.6 nm of Au at $T_S = 400°C$ onto the Si(111) surface and annealing at $T_S = 550°C$ for 5 min. Figure 3.5b depicts an AFM image of a Ga-polished Si(111) substrate after Au deposition and anneal. Several holes with depths of approximately 0.4 nm, diameters between 10 and 20 nm and a density of $\sim 10\,\mu m^{-2}$ are visible, which appear to be the result of Au-Si eutectic alloy formation. Again, the term Au droplets will be used hereafter for this Au-Si alloy, which is expected to remain liquid above the eutectic temperature of 360°C.[58]

After Au droplets had been prepared on the Si(111) substrates, nanowire growth was initiated with identical parameters to the case on GaAs(111)B. In this way it was tested if the same growth parameters work for both substrates. At a substrate temperature of 500°C, the As valve was opened before growth to establish a stable As_4 supply equivalent to $J_{As} = 5\,nm^{-2}s^{-1}$ and a BEP of 1.2×10^{-5} torr. Opening of the Ga shutter initiated GaAs growth, the exemplary sample discussed below was grown for 30 min. The Ga supply flux was $J_{Ga} = 2.5\,nm^{-2}s^{-1}$, such that $J_{As}/J_{Ga} = 2$ and that the equivalent Ga-limited planar growth rate was $v_{Ga} = 400\,nm/h$. Again, the sample was rotated continuously

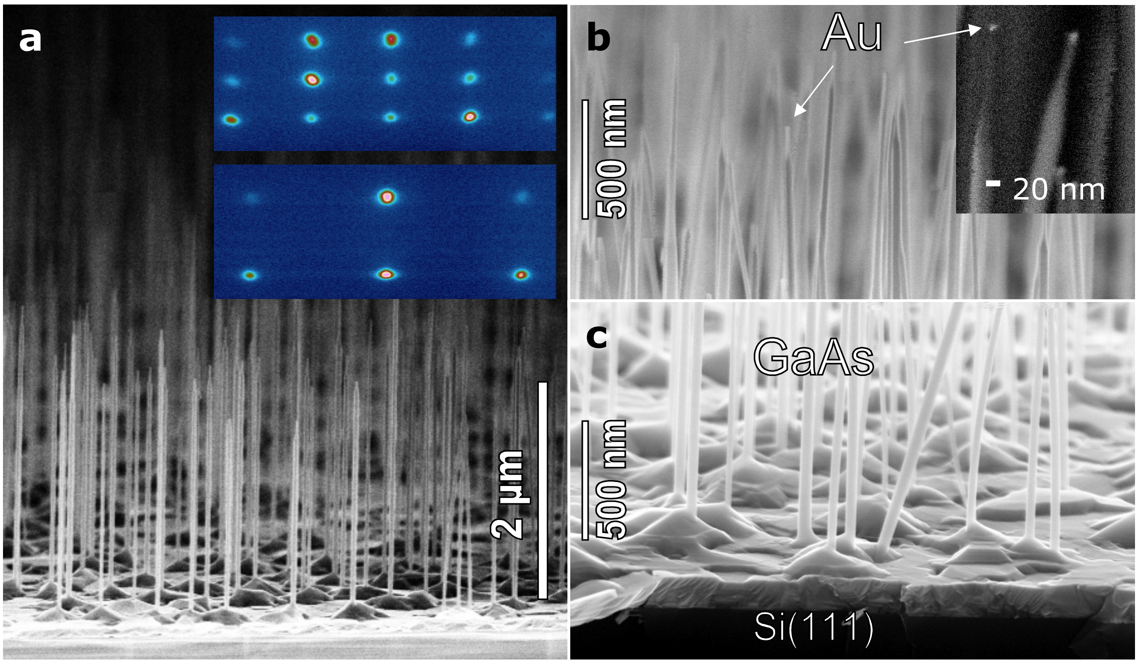

Figure 3.6.: **Au-assisted GaAs nanowires grown on Si(111)** (a) SEM micrograph (side view) detailing nearly perfect vertical alignment of the nanowires to the substrate; top and bottom insets show transmission RHEED patterns of the WZ crystal structure, as obtained in the $\langle 1\bar{1}0\rangle$ and $\langle 11\bar{2}\rangle$ substrate azimuths, respectively, which demonstrate the epitaxial alignment of nanowires and substrate. (b) magnification of the top region evidencing tapering of the nanowire tips; inset SEM micrograph with enhanced element contrast (by BSE detector) indicates the position and small size of Au droplets. (c) magnification of the bottom region revealing a closed GaAs layer and pyramids at the base of the nanowires.

except for interruptions for obtaining RHEED patterns. After closing of the Ga shutter, the substrate temperature was ramped down to $T_S = 20°\mathrm{C}$ with 10 K/min and the As supply flux was switched off immediately. Following unloading and cleaving, the sample was characterised.

Figure 3.6 presents SEM micrographs of an exemplary sample of Au-assisted GaAs nanowires grown for 30 min on Si(111), cleaned by Ga-polishing. In an overview SEM micrograph (3.6a), nanowires with very similar shapes as for the case on GaAs(111)B are apparent. Again, the nanowires are tapered in the top region, and there are pyramids and a closed layer at their feet. On average, the nanowires had main diameters of 50 nm and tip diameters between 10 and 20 nm, lengths of 2.1 ± 0.3 µm, and an area density of $6/\mu\mathrm{m}^2$. The total volume in the nanowires corresponds to a layer thickness of 70 nm.

Again, the appearance of distinct RHEED transmission reflections in the high-symmetry substrate azimuths verifies the epitaxial alignment of nanowires and substrate with hexagonal [0001], $\langle 11\bar{2}0\rangle$, and $\langle 10\bar{1}0\rangle$ aligned parallel to the cubic [111], $\langle 1\bar{1}0\rangle$, and $\langle 11\bar{2}\rangle$, respectively. The transmission RHEED patterns, obtained in the $\langle 1\bar{1}0\rangle$ (top inset) and $\langle 11\bar{2}\rangle$ substrate azimuth (bottom inset), evidence that the nanowire crystal structure is mainly WZ. A magnification of the nanowire tip region (3.6b) illustrates a pencil shape of the wires, caused by tapering of the top 100 nm. The inset presents an SEM micrograph, whose element contrast has been enhanced by use of the BSE detector. The positioning of Au at the very tip of the nanowires is confirmed and the diameter of the Au alloy droplets is estimated to be $\approx$ 10 nm. A magnified SEM micrograph of the nanowire base region (3.6.c) reveals that pyramids and a 130 $\pm$ 20 nm thick closed GaAs layer have formed at the nanowire base. Thus, the basal layer takes up approximately 2/3 of the incident amount of Ga.

3.1.3. Structural Properties of Au-assisted GaAs nanowires on Si(111)

The overall crystal structure of the exemplary sample of Au-assisted GaAs nanowires grown on Si(111) was analysed by XRD and the microstructure by HRTEM.

X-Ray Diffraction

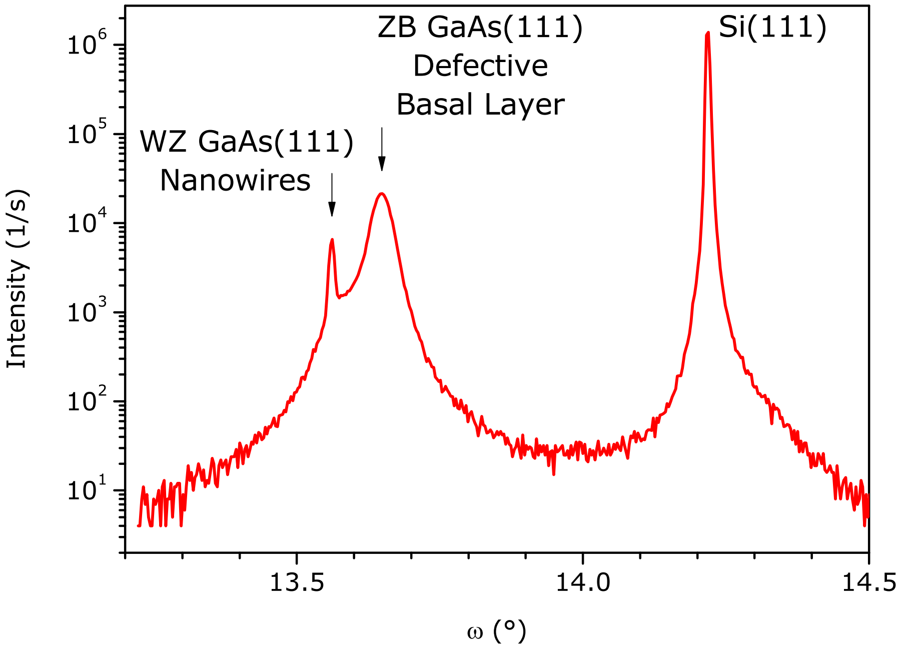

Figure 3.7.: **Symmetric XRD Scan of Au-assisted GaAs Nanowires on Si(111)** An $\omega 2\theta$ scan near the 111 substrate reflection is shown. (Measurement performed by B. Jenichen)

The structural quality of the GaAs, which had formed nanowires as intended but also had formed parasitic pyramids and a closed layer, was analysed by X-ray diffraction (XRD). Measurements were performed at the PANalytical X'Pert MRD diffractometer with a Cu Kα source, employing a triple crystal setup with analyser crystal at the detection side for increased angular resolution.

In figure 3.7, a symmetric $\omega 2\theta$-scan is presented as measured for the exemplary sample described before. From these data the out-of-plane lattice parameters can be obtained. Three peaks are visible. The strongest peak at 14.22° corresponds to the Si(111) substrate reflection with the lattice parameter $d_{Si(111)} = 0.313560$ nm.[69] Using this as a reference, the lattice spacing for the peak at 13.65° is determined to be 0.3264 nm, which corresponds to the 111 reflection in relaxed ZB GaAs. This structure is attributed to the basal layer, since the nanowires were found by RHEED to be WZ instead. Furthermore, the larger peak intensity agrees with the observation of more material volume in the basal layer than in the nanowires. In a similar fashion, the peak at 13.56° corresponds to a lattice spacing of 0.3284 nm, which is in good agreement with c/2 in relaxed WZ GaAs (0.3282 nm).[68] This peak and the WZ crystal structure are attributed to the nanowires, in accordance with the in-situ RHEED observations.

The full-width-at-half-maximum (FWHM) of the nanowire reflection of 0.01° is comparable to that of the Si substrate (0.007°). In contrast, the layer peak is considerable broader, i.e., 0.04° FWHM. Such broadening is typical for GaAs layers on Si substrates and is known to arise from structural defects and residual strain in the epitaxial GaAs layer, ultimately caused by lattice mismatch, thermal expansion mismatch and anti-phase boundaries between Si and GaAs.[26] Finally, the range of structural tilt has been determined by measurement of the FWHM of omega scans with fixed detector position. FWHM values of $0.2 \pm 0.1°$ for the ZB layer and $0.4 \pm 0.2°$ for the WZ nanowires are obtained. These are low values particularly in comparison with self-induced (non-VLS) GaN nanowires grown on Si(111), which typically show 3° of tilt and more.[94]

Although the basal GaAs layer on Si shows strong broadening due to extended defects, the GaAs nanowires themselves are nevertheless epitaxially well aligned to the substrate and they appear to have very few extended defects.

Microstructure of Nanowires and Parasitic Growth

Complementary to the integral structure analysis by XRD, the local microstructure has been analysed by TEM. Figure 3.8 depicts micrographs obtained for Au-assisted GaAs nanowires grown on Si(111) for 30 min. In Fig. 3.8a, a conventional high-resolution TEM image with the incident beam close to the $\langle 1\bar{1}0 \rangle$ zone axis is shown. The Au droplet at the nanowire tip is clearly visible and appears to be in a polycrystalline phase under ambient conditions, as indicated by lattice fringes in the top region of the Au droplet. The ABAB stacking in the growth direction indicates that the GaAs nanowire is in the WZ crystal structure. This agrees well with the observation of WZ pattern by RHEED during and after growth.

Figure 3.8b presents a HR-TEM lattice fringes image, which demonstrates almost perfect WZ crystal structure both at the bottom end of the nanowire and at the neighbouring top of the basal pyramid. The only defects are (probably two) planar stacking faults indicated by an arrow. Otherwise, the crystal structure appears to be perfect. However, the density of stacking faults increases drastically towards the bottom of the basal pyramid, see Figure 3.8c.

The microstructure of the parasitic planar GaAs layer and the GaAs-Si interface is presented in Figure 3.9. A micrograph of the region directly below a nanowire that was broken off during sample preparation (original position indicated by white arrow) is presented in Fig. 3.9a. At this position the maximum thickness of the basal layer (which includes the basal pyramid) is 280 nm, while the average nanowire length of this sample was 2100 nm (Sect. 3.1.2). Several extended defects are present in the layer: stacking faults and (micro-) twins along 111 planes both parallel and 70° inclined with respect to the interface, grain boundaries between regions with different stacking. Furthermore, the strain contrast indicates plastic relaxation by misfit dislocations at the interface, and probably also threading dislocations as well as anti-phase boundaries.

Fig. 3.9b presents a HR-TEM magnification of the region around the GaAs-Si interface. Again, stacking faults, twins and microtwins are apparent in the GaAs layer. At the in-

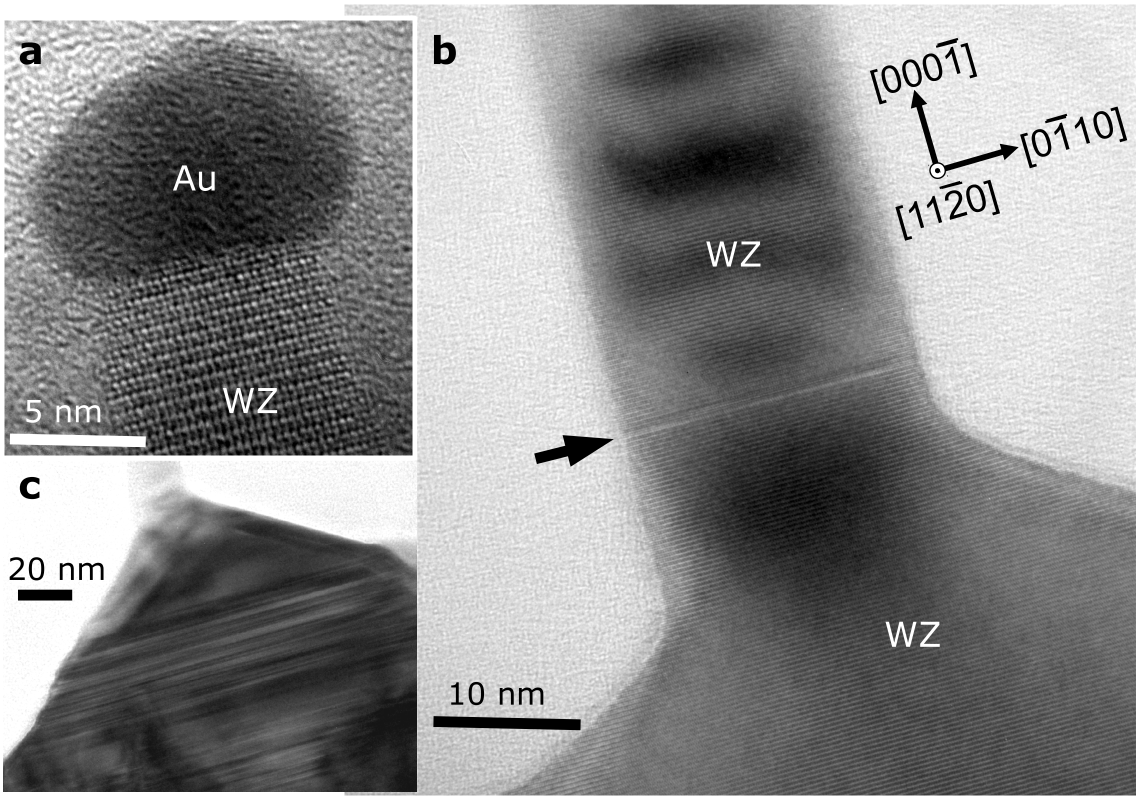

Figure 3.8.: **Microstructure of Au-assisted GaAs Nanowire and Basal Pyramid** HR-TEM images (a) of Au droplet and nanowire top end (in WZ crystal structure), (b) of nanowire bottom end with pyramidal base (both WZ, arrow indicates one pair of stacking faults), and (c) TEM image of pyramidal base, which has a high number of stacking faults. (Images taken by A. Trampert)

terface, steps on the Si surface and misfit dislocations are identified. In addition, clusters of a separate phase are found as indicated by arrows. While some clusters appear amorphous, others are crystalline and show a lattice spacing approximately 20% smaller than Si (0.543095 nm). Since the lattice constant of Au (0.40782 nm) is roughly 24% smaller than that of Si, the clusters are concluded to consist mainly of Au. These Au clusters, which remain at the GaAs-Si interface, cannot contribute to nanowire growth by the VLS mechanism for an unknown reason. Furthermore, Au clusters are expected to have deleterious effects on the electrical and optical properties of both Si substrate and GaAs layer.

3.1.4. Summary of Au-Assisted Growth Experiments

Au-assisted GaAs nanowire growth was achieved both on GaAs(111)B and on Si(111) substrates. The fact that identical growth conditions could be used for both substrates demonstrates the versatility of the employed Au-assisted VLS mechanism. Morphologically, the obtained Au-assisted GaAs nanowires show a very high aspect ratio and are epitaxially well aligned to the substrate. Typically, the nanowire diameters ranged between 20 to 50 nm, but tapered tips lead to a ”pencil-shape”. This corresponds to reports by Plante et al., who furthermore observed that the lateral facets differed between the top and the main part of the nanowires, and who explained this by non-VLS lateral growth.[95]

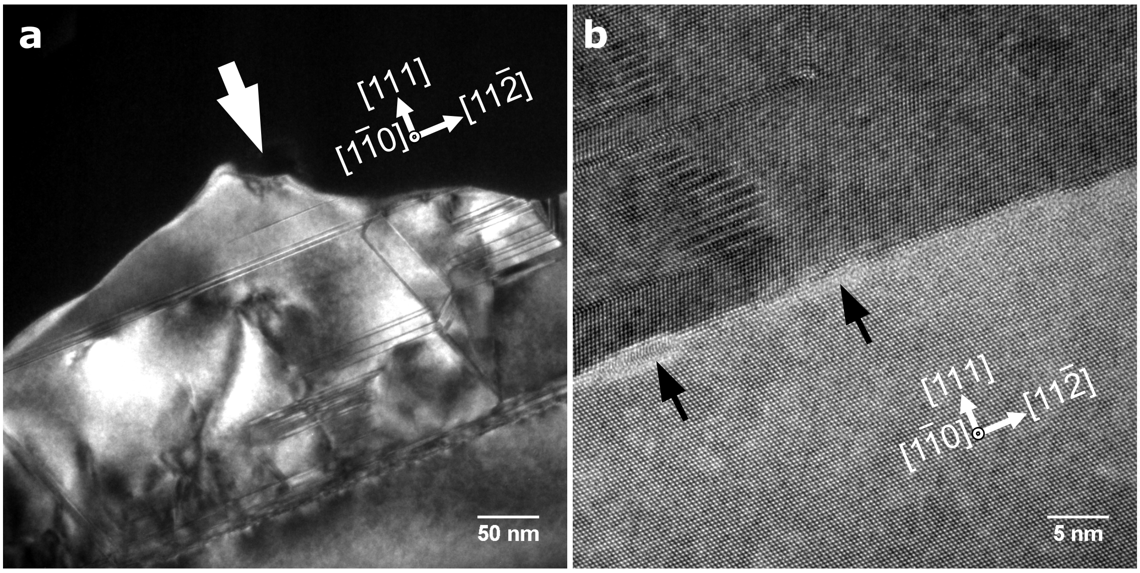

Figure 3.9.: **Microstructure of Basal GaAs Layer formed during Au-assisted GaAs nanowire growth on Si(111).** (a) TEM image of basal layer with stacking faults, micro-twins, misfit dislocations at the interface, and strain contrast due to residual strain. (b) HR-TEM image of interface region showing clusters at the interface. (Images taken by A. Trampert)

Independent of the substrate there is a substantial amount of parasitic, i.e. non-nanowire, growth of GaAs: at the base of each nanowires a pyramidal pedestal and between them a thick planar layer forms.

In the considered window of growth parameters, all Au-assisted nanowires were found to adopt the WZ crystal structure and show very few defects. For growth on Si(111), not surprisingly, the parasitic basal GaAs layer is of low structural quality. The formation of a closed GaAs layer at the nanowire base leads to plastic strain relaxation and the formation of extended defects in the layer. Nevertheless, XRD and HRTEM data demonstrate that even on Si(111), GaAs nanowires by Au-assisted VLS growth are fully relaxed and epitaxially well aligned, despite the fact that the basal layer is highly defective.

Furthermore, Au-related clusters were found at the interface. This is a matter of concern, since Au atoms may diffuse into the Si bulk and form deep trap states, which severely reduce carrier mobility in the substrate. This process caused the exclusion of Au from the standard CMOS process. Au cluster formation at the Si interface might be overcome by a different method of Au droplet preparation, such as deposition as coloidal solutions.[14] However, Au-diffusion into the GaAs nanowires themselves can also lead to defect states. This issue will be discussed further in Chapter 6.

3.2. Self-assisted VLS Nanowire Growth

Two articles in 2006 reported VLS growth by MOVPE of In(P)As nanowires that was remarkably *Au-free* and used a thin oxide layer: Mandl et al. observed no metal droplets at the nanowire tips and concluded that ″the catalyst (droplet) function is taken over by a thin film of SiO_x″, but they did not provide a more detailed nanowire growth mechanism.[61] In contrast, Mattila et al. demonstrated the presence of In droplets at the tips of their nanowire and concluded that the thin native oxide on the Si substrates had played a crucial role in the formation of these droplets.[96] Two years later, Fontcuberta i Morral and her group demonstrated by MBE that GaAs nanowires grow in a similar fashion on GaAs substrates covered with a thin film of SiO_x.[97] They showed furthermore, that the nanowires nucleate in holes of the oxide and that epitaxial relation between nanowire and substrate results provided the oxide thickness is below 30 nm.[17] Self-assisted GaAs nanowire growth on Si substrates was at first demonstrated by Jabeen et al.[98] It was established by Mandl et al. that the main role of the SiO_x film is to immobilize the droplets in well-defined areas on the surface and to change the size and density distribution from few very large to many small droplets.[62]

3.2.1. Self-assisted GaAs Nanowires on Si(111)

During our initial studies of nanowire growth in 2008, several articles improved the understanding of the self-assisted VLS mechanism for III-V nanowires.[97,17,99] Motivated by the prospect to remove Au from the growth process, we set out to grow GaAs nanowires by the self-assisted VLS mechanism. Since the necessary thin film of SiO_x must be deposited onto GaAs substrates by additional processing but forms natively in air on Si, growth experiments were directly started on Si substrates.

Different batches of Si(111) substrates were used during this work, which were either full 2″ wafers, or quarters thereof, or 2×2 cm^2 square pieces. The substrates had different degrees of miscut between 0.5° and 2°, were n-type (doped with As or P), and had usually had a high resistivity between 1 and 20 Ωcm, which corresponds to a dopant concentration of $n \sim 10^{15}$ cm^{-3}. These minor differences between the substrate batches were not found to have an effect on the nanowire morphology.

The formation of the necessary SiO_x layer turned out to be somewhat more critical. Initial experiments with as-delivered native oxide as well as chemically prepared oxide (using H_2SO_4:H_2O_2, see Sec. A.2) had not resulted in nanowire growth. Successful growth was achieved, when the Si substrates were first chemically cleaned by the HF or the NH_4F-procedure and then stored in flow-box air in order to form a native SiO_x thin film, which grows in a self-limited fashion up to a thickness of around 1.5 nm.[100] While the oxidation of H-terminated Si in air begins within minutes, the growth rate is very slow and the equilibrium thickness is reached only after several days under ambient conditions.[101] When the samples had been in air for two weeks or longer, we found our nanowire growth experiments to be most reproducible.

It was found later that the oxidation time can be drastically reduced to a few hours by the storage of the substrates in deionized water, stirring and mild heating to 80°C, since the rate-limiting step for the oxidation of H-terminated Si is the exchange of Si-H for Si-OH under the influence of (ambient) water.[102] In this alternative process, the complete coverage with native oxide can easily be checked by the hydrophilicity of the surface. The samples presented hereafter had their native oxide prepared in air.

Figure 3.10 presents an AFM micrograph of an NH_4F-cleaned Si(111) substrate after formation of the native oxide. While atomic terraces are still discernible, the step edges appear blurred due to the formation of amorphous native SiO_x. When the Si substrates had initially been cleaned using HF, no terraces were present but no effect on the growth was found. Several SiO_x covered Si(111) substrates were prepared in one run and then stored in the flow-box.

For the growth of self-assisted nanowires, a Si(111) substrate with the native SiO_x film

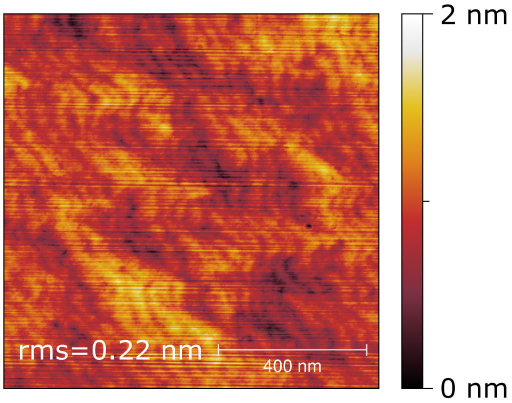

Figure 3.10.: **Si(111) with native oxide** AFM micrograph of Si(111) (cleaned by NH_4F procedure) after native oxide formed in air. The Si(111) terraces below the native oxide are still discernible.

was loaded and degassed as described above. Central experiments were performed in both growth chambers of M6, between which the BEP readings that correspond to a specific atomic flux differed. For an easy comparison with the Au-assisted mechanism, the values for the Au-chamber are given in the following.

Reports on MBE growth conditions for obtaining self-assisted GaAs nanowires differ from those used for the Au-assisted mechanism in the requirement of higher growth temperatures (T_S between 580 and 630°C) and comparably low As fluxes.[97,99] Here, an exemplary growth run with a substrate temperature of 580°C and As and Ga fluxes identical to those used for the Au-assisted experiments ($J_{As}/J_{Ga} = 2$) is described. Initially, the 'Au' chamber of M6 was used for the self-assisted nanowire growth experiments. Variation of the growth conditions will be presented later. The As valve was opened before growth to establish a stable As_4 supply equivalent to $J_{As} = 5\,\mathrm{nm}^{-2}\mathrm{s}^{-1}$ and a BEP of 1.2×10^{-5} torr. Opening of the Ga shutter initiated GaAs growth, the exemplary sample discussed below was grown for 30 min. The Ga supply flux was $J_{Ga} = 2.5\,\mathrm{nm}^{-2}\mathrm{s}^{-1}$, such that $J_{As}/J_{Ga} = 2$ and that the equivalent Ga-limited planar growth rate was $v_{Ga} = 400\,\mathrm{nm/h}$. The sample was rotated continuously except for interruptions for obtaining RHEED patterns. After closing of the Ga shutter, the substrate temperature was ramped down to $T_S = 20$°C with 10 K/min and the As supply flux was switched off immediately. Following unloading and cleaving, the sample was characterised.

Figure 3.11 presents micrographs of self-assisted GaAs nanowires grown on Si(111). An overview SEM micrograph of the exemplary sample (3.11a), which was grown under identical nominal fluxes as for the Au-assisted case, proves successful nanowire growth. Most GaAs nanowires are vertical and have length of 5.0 ± 0.3 µm. There is no tapering at the nanowire top, and the average nanowire diameter is 60 nm, although some nanowires are slightly wider at their base. Few nanowires show no droplet at their tip and are considerably shorter than the average. Between the bottom ends of the nanowires, parasitic islands and tilted structures are found.

A magnification of the nanowire tip region is depicted in Figure 3.6b. The liquid Ga droplets with spherical segment shape are clearly visible. The droplet diameter (80 nm on average) is larger than that of the nanowires, resulting in a droplet-nanowire contact angle $\beta \simeq 120°$. In order to establish the chemical nature of the droplet, figure 3.6c presents energy dispersive X-ray (EDX) maps of the top region of self-assisted nanowires. The

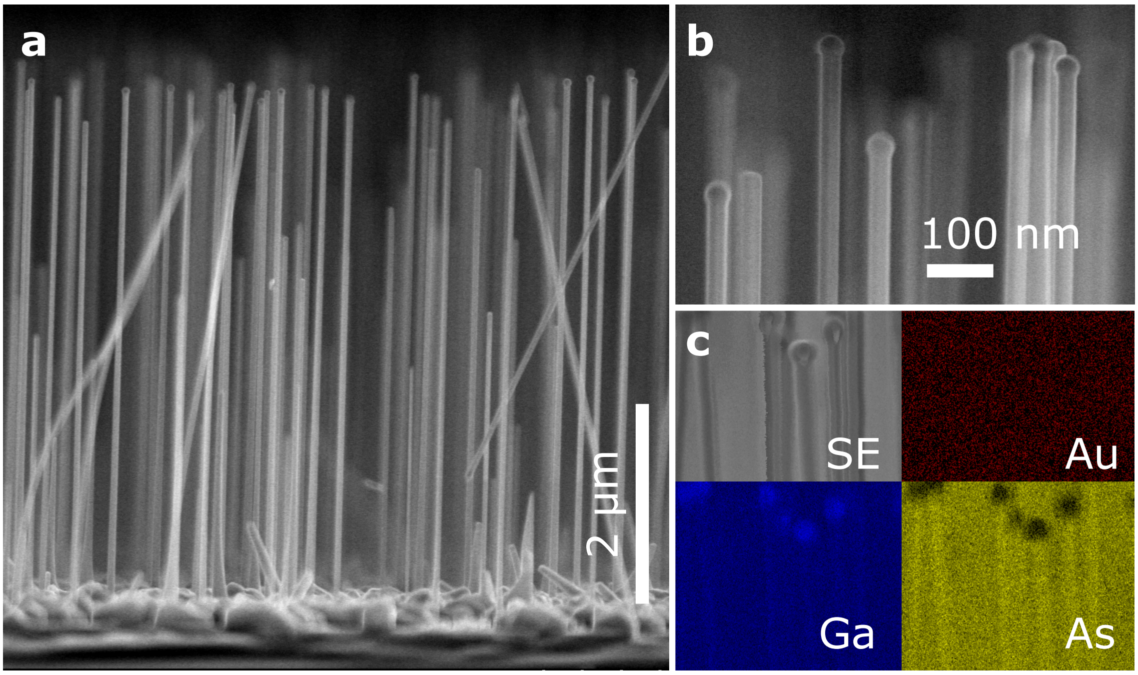

Figure 3.11.: **Micrographs of self-assisted GaAs nanowires grown on Si(111)** The SEM micrographs present side views of the nanowires and show (a) nanowires with large aspect ratio and vertical alignment, (b) a magnification of the droplets at the nanowire tips, and (c) EDX maps (measured by J. Lähnemann), which indicate the high Ga and low As content in the droplets.

secondary electron (SE) image depicts the imaged morphology. The Ga signal dominates at the droplet positions, while there appears to be very little or no As content. The Au signal was below detection level (1%) as expected. These measurements prove that the droplets consist mainly of Ga.

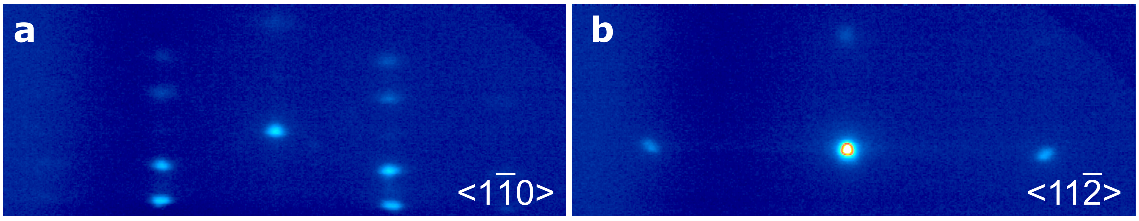

Figure 3.12.: **RHEED patterns obtained during self-assisted growth of GaAs nanowire on Si(111)** When the beam was incident in substrate azimuths (a) $\langle 1\bar{1}0\rangle$ and (b) $\langle 11\bar{2}\rangle$, the characteristic transmission patterns of Zincblende GaAs with rotational twin defects are observed.

The nanowires are epitaxially aligned to the substrate - the hexagonal [0001], $\langle 11\bar{2}0\rangle$, and $\langle 10\bar{1}0\rangle$ directions are co-aligned with cubic [111], $\langle 1\bar{1}0\rangle$, and $\langle 11\bar{2}\rangle$ direction, respectively - as indicated by the appearance of distinct RHEED transmission reflections in the high-symmetry substrate azimuths (Fig. 3.12). The pattern obtained in the $\langle 1\bar{1}0\rangle$ substrate azimuth indicates that the nanowires predominantly adopted the ZB crystal structure and contain rotational twins with the twin axis along the [111] growth direction.

3.2.2. Optimised Conditions for Reduced Parasitic Growth

In order to study the influence of the growth parameters on the morphology of the nanowires and the parasitic islands, series of experiments were performed under variation of one growth parameter and the morphology of the samples was analysed by SEM.

Effect of the V/III Ratio

Studies of self-assisted GaAs nanowire diameters and lengths as well as their axial and radial growth rates as functions of either the As or the Ga flux have been reported in the literature,[97,99] and our own results are already contained in the master thesis (Diplomarbeit) of Maria Hilse.[103] All three studies demonstrate a linear increase in the axial nanowire growth rate with the As flux. This indicates that the self-assisted GaAs nanowire growth rate is limited by the As supply, which is the opposite to the case of planar GaAs layer growth. For GaAs layers, the formation of Ga droplets is strictly avoided, therefore conditions are always As-rich and the growth rate is limited by the Ga supply,[22] see also section A.1. The process of As-limitation during VLS nanowire growth was described in detail by Harmand and Glas, who demonstrated that the droplet is substantially depleted from group V material after nucleation and growth of each new monolayer.[60,104]

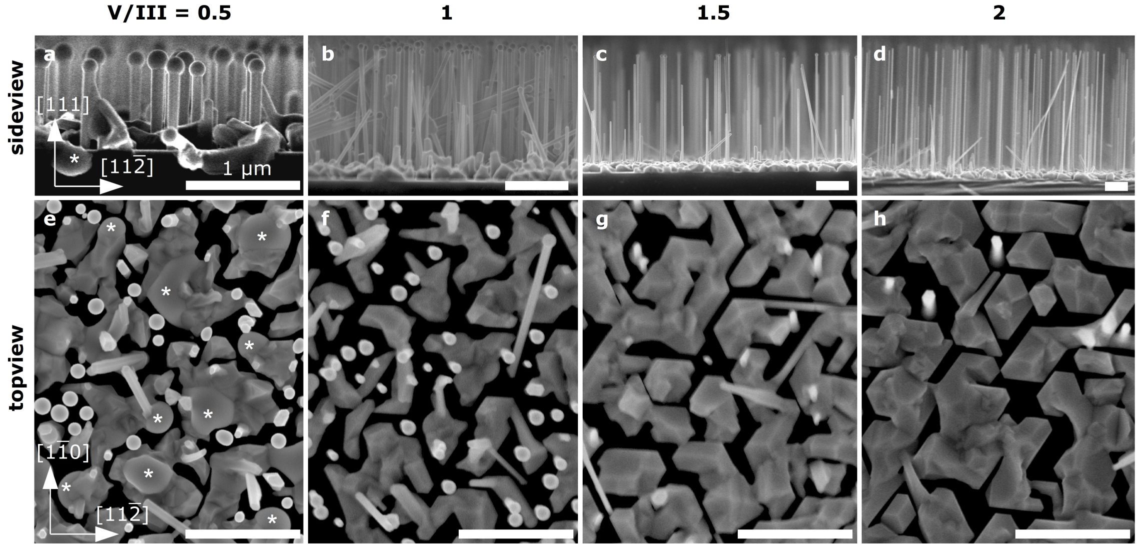

Figure 3.13.: **SEM images of nanowires grown under different V/III flux ratios.** Series of self-assisted GaAs growth experiments on SiO_x/Si(111) under identical Ga flux but different As fluxes, corresponding to V/III flux ratios of (a, e) 0.5, (b, f) 1, (c, g) 1.5, and (d, h) 2. The nanowires are imaged in sideview (a-d, electron beam incidence normal to nanowire axis) as well as in topview (e-h, incidence approximately along nanowire axis). All scale bars are 1 µm. Note the different scale for the sideview micrographs. Sessile Ga droplets are indicated by stars.

Thus, the influence which growth conditions have on the shape of the nanowires has already been studied in some detail. However, little information is available about the conditions for an optimal overall morphology, which means a reduction of parasitic growth. M. Hilse studied top-view SEM images of nanowires grown under constant As flux and different Ga fluxes.[103] She found that the fraction of surface area covered by nanowires over surface area covered by parasitic islands is maximal for J_{As}/J_{Ga} =0.5 but concluded that the nanowire morphology is best at J_{As}/J_{Ga} =1, where no tapering was observed. Here, we present the complementary growth study under constant Ga flux and different As fluxes. The focus is set on the parameters under which parasitic island growth is reduced and the material fraction growing as nanowires is maximized.

A series of samples was grown in the 'Au' chamber of M6 under variation of the As flux. While an identical J_{Ga} of 2.5 $\text{nm}^{-2}\text{s}^{-1}$ was used for each nanowire growth experiment, different values of 1.2, 2.5, 3.7, 5 $\text{nm}^{-2}\text{s}^{-1}$ were used for J_{As}, resulting in V/III flux ratios J_{As}/J_{Ga} of 0.5, 1, 1.5, and 2, respectively. Otherwise, the growth conditions were identical to those described in the last section. In particular, the planar growth rate equivalent to the Ga flux was $v_0 = 400$ nm/h, the growth duration was 30 min, and the substrate temperature was $T_S = 580°\text{C}$. Nanowires grew under all conditions. In some cases, the nanowire density was low in irregular regions around the centre and the very edge of the sample. This behaviour appears to be caused by an inhomogeneous SiO_x thickness. In the following all micrographs were prepared from areas 5 mm from the sample edge.

SEM micrographs of the As flux series samples are presented in Figure 3.13. From the micrographs, a decreasing number density and an increasing nanowire length with increasing As flux are apparent. The latter trend demonstrates that the self-assisted VLS mechanism is As-limited. The topview micrographs allow to distinguish between nanowires (white or light grey), parasitic growth of islands (middle grey, sharp edges) and sessile Ga droplets (middle grey, round edges), as well as uncovered $\text{SiO}_x/\text{Si(111)}$ substrate (black). Remarkably, under each condition studied, a substantial fraction b_S of the substrate remains uncovered and vertical nanowires without contact to any parasitic GaAs can be found. Both observations are in strong contrast to the case of Au-assisted nanowire growth, for which a thick continuous GaAs layer is generally found, compare with Fig. 3.6c.

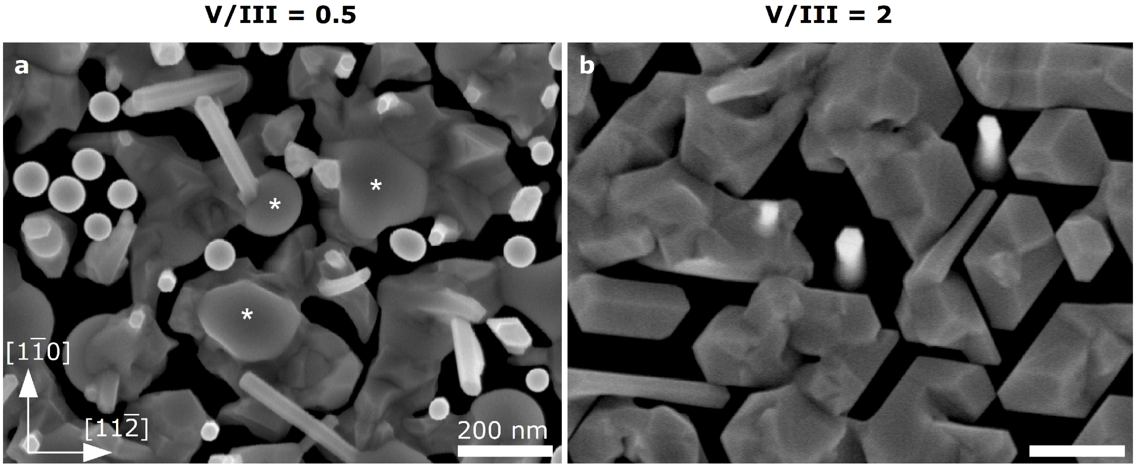

Figure 3.14.: **Magnified top view SEM images of samples grown under (a) Ga-rich and (b) As-rich conditions.** Identical Ga fluxes but different As fluxes were used, corresponding to V/III flux ratios of (a) 0.5, and (b) 2. Sessile Ga droplets are indicated by stars.

In order to visualize the morphology of parasitic growth, Figures 3.14a and b present magnifications of two top view micrographs (from Fig. 3.13e and h). In Figure 3.14a, islands with sharp edges and sessile Ga droplets with round edges can be distinguished between the nanowires, which are hidden under their top Ga droplets. Some oblique nanowires are also found, and generally do not show any droplet at their tip. The formation of sessile Ga droplets is expected for Ga-rich growth conditions, since desorption of excess Ga is very low. In Figure 3.14b, no sessile Ga droplets can be observed and the parasitic islands all have $\{1\bar{1}0\}$ oriented edges, which demonstrates their epitaxial alignment with the substrate. In addition, two free-standing nanowires are depicted, of which only the bottom part is in focus, due to their length of several µm, while their top part and droplet is blurred. The hexagonal cross section and $\{1\bar{1}0\}$ sidewalls of the nanowire are visible.

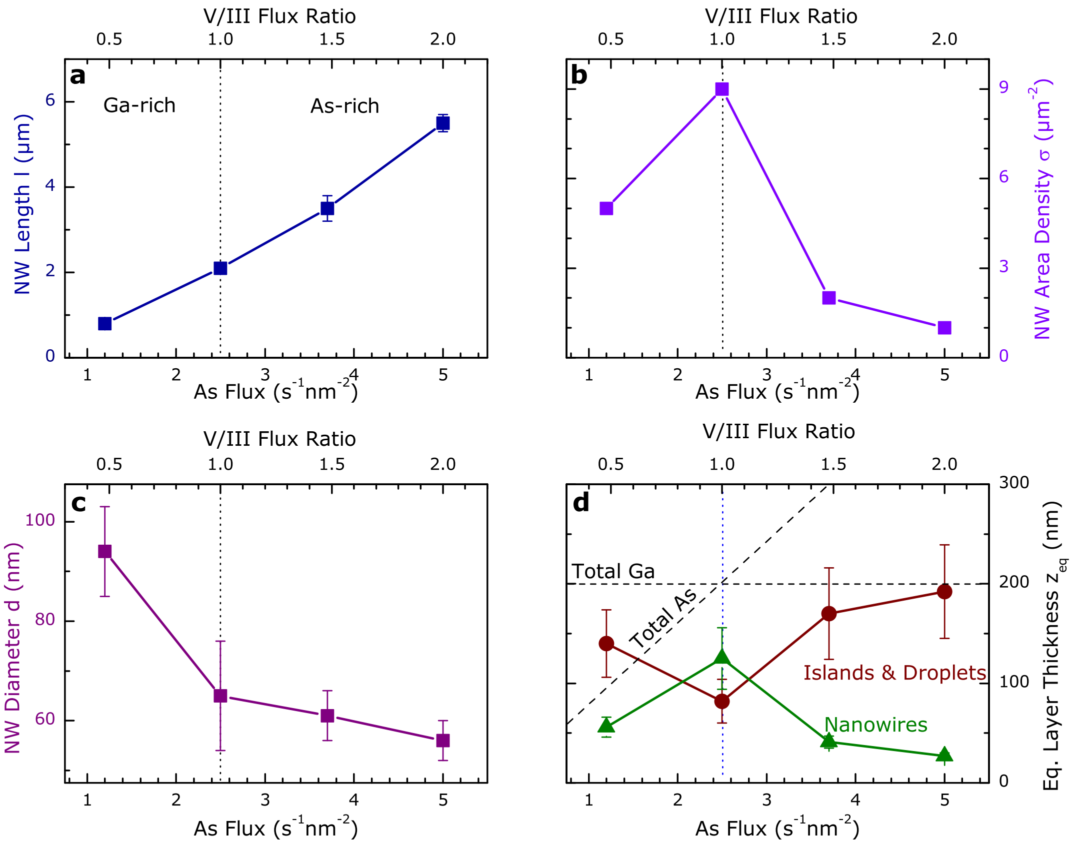

Figure 3.15.: **SEM Analysis of As-Flux Series.** Plots of average length l, area density σ, diameter d, and equivalent layer thickness z_{eq}^{NW} for nanowires as well as for parasitic GaAs z_{eq}^{P} as a function of the As Flux. The boundary between globally As-rich ($J_{As}/J_{Ga} > 1$) and globally Ga-rich ($J_{As}/J_{Ga} < 1$) conditions is indicated by a dotted line.

A detailed analysis of the dimensions of nanowires and parasitic islands was performed for the samples of the As flux series. The average nanowire length l, nanowire diameter d, and island height h were obtained from sideview SEM micrographs. Complementary topview micrographs were used to determine the nanowire area density σ as well as the surface fraction b_P covered by parasitic growth (islands and sessile Ga droplets). Error values for l and d show the standard deviation for an ensemble of at least 10 measured nanowires, while the values for h and b_P estimate systematic errors.

Figure 3.15a depicts the nanowire length l as a function of the As-Flux. The increasing trend clearly demonstrates that growth is As-limited, in accordance with earlier reports.[97,99] Even under globally As-rich conditions, Ga droplets can form and assist in VLS nanowire growth, which is locally Ga-rich. The nanowire area density σ is presented in Figure 3.15b. At stoichiometry (J_{As} =J_{Ga}), σ takes a maximum value of 9 μm ^{2}. For more As-rich conditions, σ drops and we conclude that the initial formation of Ga droplets is limited by a shortage in Ga supply. However, fewer nanowires are also found for more Ga-rich conditions, for which the excess Ga is taken up into sessile Ga droplets. As plotted in Figure 3.15c, the nanowire diameter d monotonically decreases with increasing As flux. This could be caused by the smaller amount of Ga available for droplet formation and possibly also by a reduced diffusion length of Ga.

In order to compare the total GaAs volume in the nanowires with that in the parasitic islands and sessile Ga droplets, the volume per sample area or equivalent layer thickness z_{eq} were quantified. From the values of l, d, and σ, the equivalent layer thickness for the nanowires, which were approximated as circular cylinders, was estimated using $z_{eq}^{NW} = \frac{\pi}{2} d^2 l \sigma$. The equivalent layer thickness of parasitic growth was estimated using $z_{eq}^{P} = h b_P$. Figure 3.15c shows plots of both quantities, and estimations of measurement errors, which are particularly significant for parasitic growth. The total incident amount of Ga, which corresponds to that present in a 200-nm-thick GaAs layer, is indicated by a horizontal dashed line. Under stoichiometric conditions, the volume in the GaAs nanowires is maximal while the volume in the parasitic structures is minimal: about 3/5 of the incident Ga (and As) form GaAs nanowires and only 2/5 remain for parasitic growth.

Why stoichiometric conditions are ideal for a maximum yield in self-assisted nanowires can be understood in the following way. For As-rich conditions ($J_{As}/J_{Ga} > 1$), only relatively few nanowires can grow by the VLS mechanism since the initial formation of Ga droplets is limited by a shortage in Ga supply. Instead, most of the incident Ga is taken up by the VS growth of parasitic islands. The parasitic volume z_{eq}^{P} therefore increases with increasing J_{As}. Excess As simply desorbs. Besides, although the growth conditions are overall As-rich, the axial nanowire growth rate (where a Ga droplet has formed) is limited by the As supply as indicated by the scaling of nanowire length with J_{As}. As-limitation was also found for Au-assisted VLS growth by Harmand et al.[104] It indicates that a significant barrier exists for the incorporation of As into the liquid droplet. For Ga-rich conditions ($J_{As}/J_{Ga} < 1$), many Ga droplets are initially created on the SiO_x surface, but they compete for As, which is in short supply. Those Ga droplets, which are fed with sufficient As start to form GaAs nanowires by the VLS mechanism. The remaining Ga droplets turn into sessile droplets: they rest at the substrate surface and grow larger by more Ga incorporation. With decreasing J_{As}, the Ga excess increases and the volume in parasitic sessile droplets increases. Therefore, the uncovered substrate area and the nanowire area density σ are maximal for stoichiometric conditions ($J_{As}/J_{Ga} = 1$). In this case, VLS growth is neither hampered by a supply shortage in As nor in Ga.

Effect of Reduced Growth Rates

Experiments with reduced supply rates typically reduce kinetic effects, since arriving atoms have longer diffusion lengths. Therefore it is studied, whether such a proportional reduction in both Ga and As can reduce parasitic growth further.

For all samples of this series, a $J_{As}/J_{Ga} = 1$ was employed, which in the last section was identified to yield minimal parasitic growth, and J_{Ga} and J_{As} were reduced in parallel. Samples were grown under reduced J_{As} and J_{Ga} but with proportionally increased growth times, such that identical amounts of material were supplied for each sample. A common Ga flux of $J_0 = J_{Ga} = 2.5\ \mathrm{s}^{-1}\mathrm{nm}^{-2}$ had been used for all experiments presented in this section up to here as well as in the previous sections (self-assisted as well as Au-assisted growth), which is equivalent to a (Ga-limited) planar layer growth rate $v_0 = 400$ nm/h. Additional self-assisted nanowire growth runs were performed with $J_{Ga} = J_{As}$ of $J_0/2$ and $J_0/2$, corresponding to planar growth rates of 200 nm/h and 100 nm/h, while the original growth duration t_0 of 30 min was increased to 1 h and 2 h, respectively.

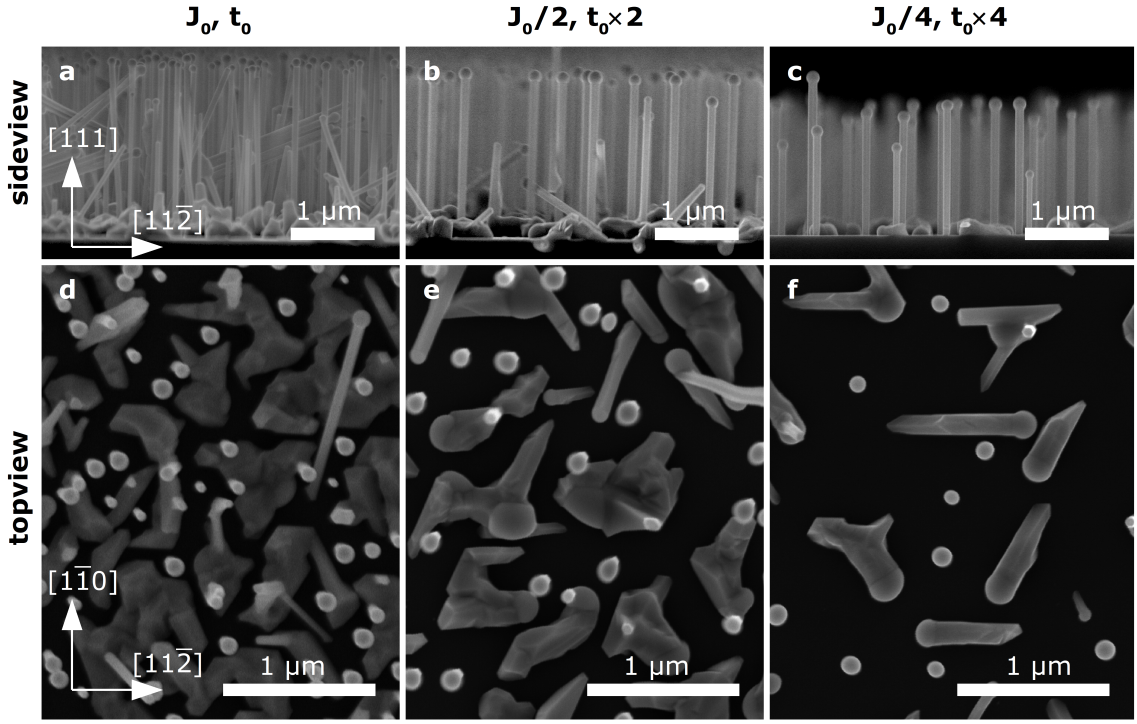

Figure 3.16.: **SEM images of nanowires grown under different growth rates** Series of self-assisted GaAs nanowire growth experiments on SiO_x/Si(111) under identical Ga and As fluxes ($J_{As}/J_{Ga} = 1$), grown (a, d) for $t_0 = 1/2$ hour with $J_{As} = J_{Ga} = J_0 = 2.5\ \mathrm{s}^{-1}\mathrm{nm}^{-2}$, (b, e) for 1 hour with $J_0/2$, and (c, f) for 2 hours with $J_0/4$. The nanowires are imaged in side view (a-c) as well as in top view (d-f).

SEM micrographs of the samples are presented in Figure 3.16. From a comparison of the top view micrographs, it immediately becomes clear that the amount of nanowire and parasitic growth is substantially reduced for lower supply rates (and longer growth times). As J_{Ga} and J_{As} decrease, so does the nanowire density, and the nanowire length is somewhat reduced. For the $J_0/4$ sample (Fig. 3.16f), it appears that only a fraction of the supplied material has remained on the surface, indicating substantial desorption of both Ga and As_2 at the growth temperature of 580°C. This, however is not surprising, considering that the sticking coefficient of Ga on SiO_2 has been shown to steadily decrease for temperatures $T \geq 565$°C, which can be used for selective area growth.[105] At the same time, the shape of the islands in Fig. 3.16f strongly suggests that each island was formed by in-plane VLS growth, i.e. under assistance of the Ga droplet, which remains in contact with the substrate and the island. This variety of the VLS growth mechanism is described in more detail in Section 4.2.

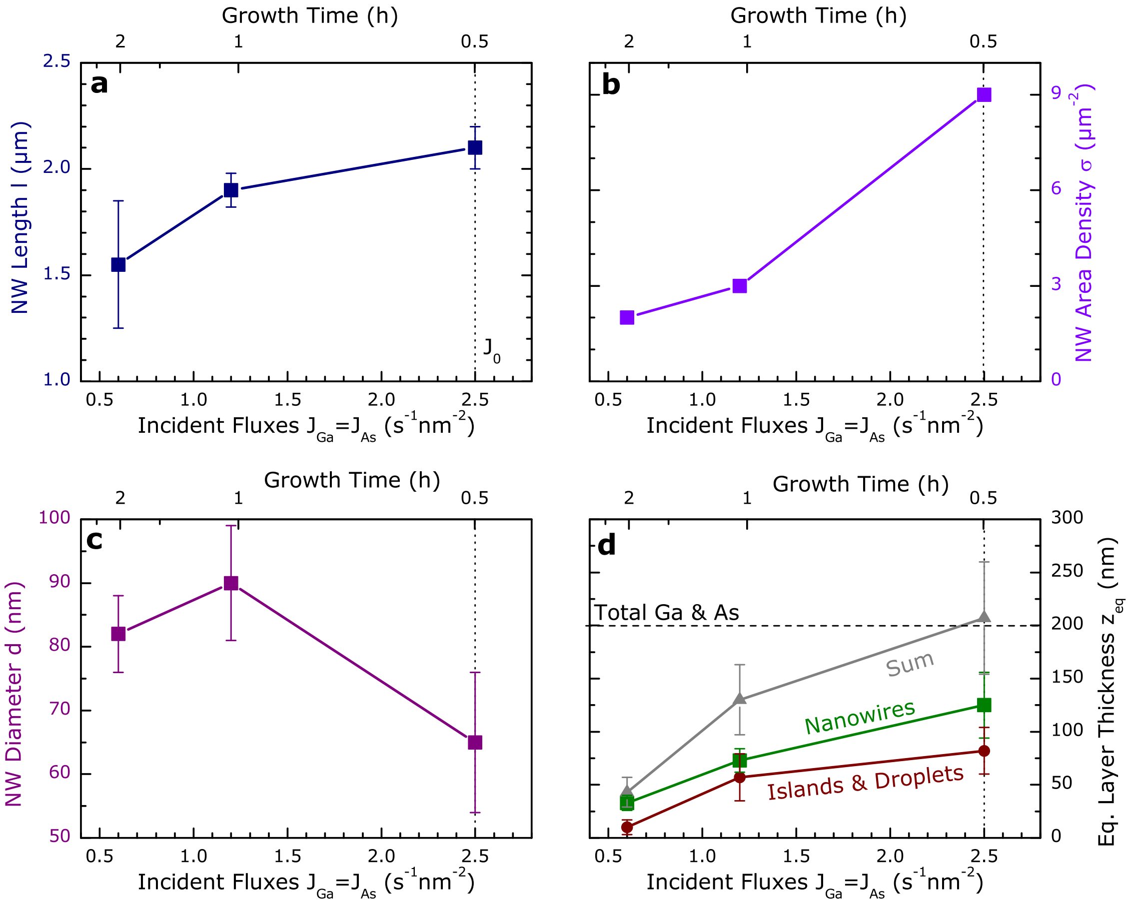

Figure 3.17.: **SEM Analysis of Growth Rate Series.** Plots of average length l, area density σ, diameter d, and equivalent layer thickness z_{eq}^{NW} for nanowires as well as for parasitic GaAs z_{eq}^{P} as a function of the incident supply fluxes. The growth time t was adjusted to arrive at identical incident total amount of material for all samples. The growth time t for each sample can be read off at two top axes. The reference values for flux J_0 and growth time t_0 are indicated by the vertical dotted lines.

The geometries of nanowires and islands were analysed and central parameters are plotted as a function of the two source fluxes $J_{As} = J_{Ga}$ in Figure 3.17, which demonstrates that l decreases somewhat with reduced supply fluxes (Plot 3.17a), in accordance with increased material desorption at longer mean free paths. A similar decreasing trend is found for the nanowire area density σ (Plot 3.17b). This also indicates that most pin-holes in the SiO_x are formed after the Ga shutter is opened, since otherwise their density should not depend on the Ga flux and σ should be constant. Apparently, pin holes form directly under a Ga droplet by a chemical reaction with the SiO_x (Sec. 2.2.2). The fact that not all SiO_x is reduced by Ga in this way can again be explained by the high mobility of single Ga atoms: only larger Ga droplets move slow enough (and may even be pinned) to allow sufficient interaction time for hole formation to start. Therefore hole-formation only happens at the beginning of growth, since soon an equilibrium number of larger Ga droplets has formed within reach of all incident Ga atoms. Then, the probability for adsorption of incident Ga atoms to preformed Ga droplets is much higher than that for the creation of a Ga droplet at a new position.

In Figure 3.17c the nanowire diameter d is plotted versus source flux and there is no clear trend. An increase in d might originate from a larger Ga diffusion length, while a decrease in d might be caused by a larger Ga desorption rate. The value of the equivalent layer thickness of nanowires and parasitic growth are plotted in Figure 3.17d. The sum of both contributions is added in order to show the effect of desorption. While at $J_0 = 2.5\ \mathrm{s}^{-1}\mathrm{nm}^{-2}$, the sum equals the incident total thickness with good accuracy, there is clearly less material grown than what was incident for the lower flux samples. At $0.6\ \mathrm{s}^{-1}\mathrm{nm}^{-2}$, about 3/4 of the supplied material desorbs. This has a positive effect, namely that the amount of parasitic growth has much diminished and makes up only 1/4 of the GaAs present on the surface. The nanowire yield is thus significantly increased when very slow growth rates are used.

3.2.3. Structural Properties of Self-assisted GaAs nanowires on Si(111)

The overall crystal structure of samples of self-assisted GaAs nanowires grown on Si(111) was analysed by XRD and the microstructure by HRTEM.

X-Ray Diffraction

Since the self-assisted GaAs nanowires were under all analysed conditions found to adopt the ZB crystal structure in RHEED, a simple distinction between nanowires and parasitic growth on the basis of different lattice spacings (as for the Au-assisted nanowires with WZ structure) is not possible. However, it was shown in the last section that under optimized growth conditions ($J_{As}/J_{Ga} = 1$, low v), the overall nanowire volume is larger than that of the parasitic islands. Therefore, the contribution of the nanowires is expected to dominate in the XRD intensity.

A sample of self-assisted GaAs nanowires grown under $J_{As}/J_{Ga} \approx 1$, $J_{Ga} = J_0/4 \Leftrightarrow v = 100$ nm/h for $t_G = 1$ h was analysed by XRD. Its morphology is presented in Figure 3.18a and shows nanowires and parasitic islands. Close to the substrate interface, the nanowires are tapered and show characteristic pedestals. This sample was grown in the 'III-V' chamber of M6, after the self-assisted growth process had been transferred to it from the 'Au' chamber, where all earlier presented growth experiments were performed.

The structural quality of this sample of self-assisted GaAs nanowires was analysed using the in-house XRD diffractometer equipped with an analyser crystal for increased angular resolution. Figure 3.18b presents a symmetric $\omega 2\theta$-scan for the determination of the out-of-plane lattice parameters. The most intense peak at 14.22° corresponds to the Si(111) substrate reflection ($d_{Si(111)} = 0.313560$ nm). The FWHM of the Si(111) peak equals 0.007° as determined before (Fig. 3.7). The shoulder on the lower angle side of the Si reflection indicates that a fraction of the material has a larger lattice constant. In conjunction with the HRTEM results presented in the next section, we can conclude that this is caused by an intermixing of Si with GaAs in the interface region.

The second peak at 13.66° indicates a lattice spacing of 0.3266 nm, which corresponds to relaxed GaAs(111) planes in the ZB structure ($d_{GaAs(111)} = 0.32641$ nm). The main contribution to this peak is attributed to the GaAs nanowires in accordance with their

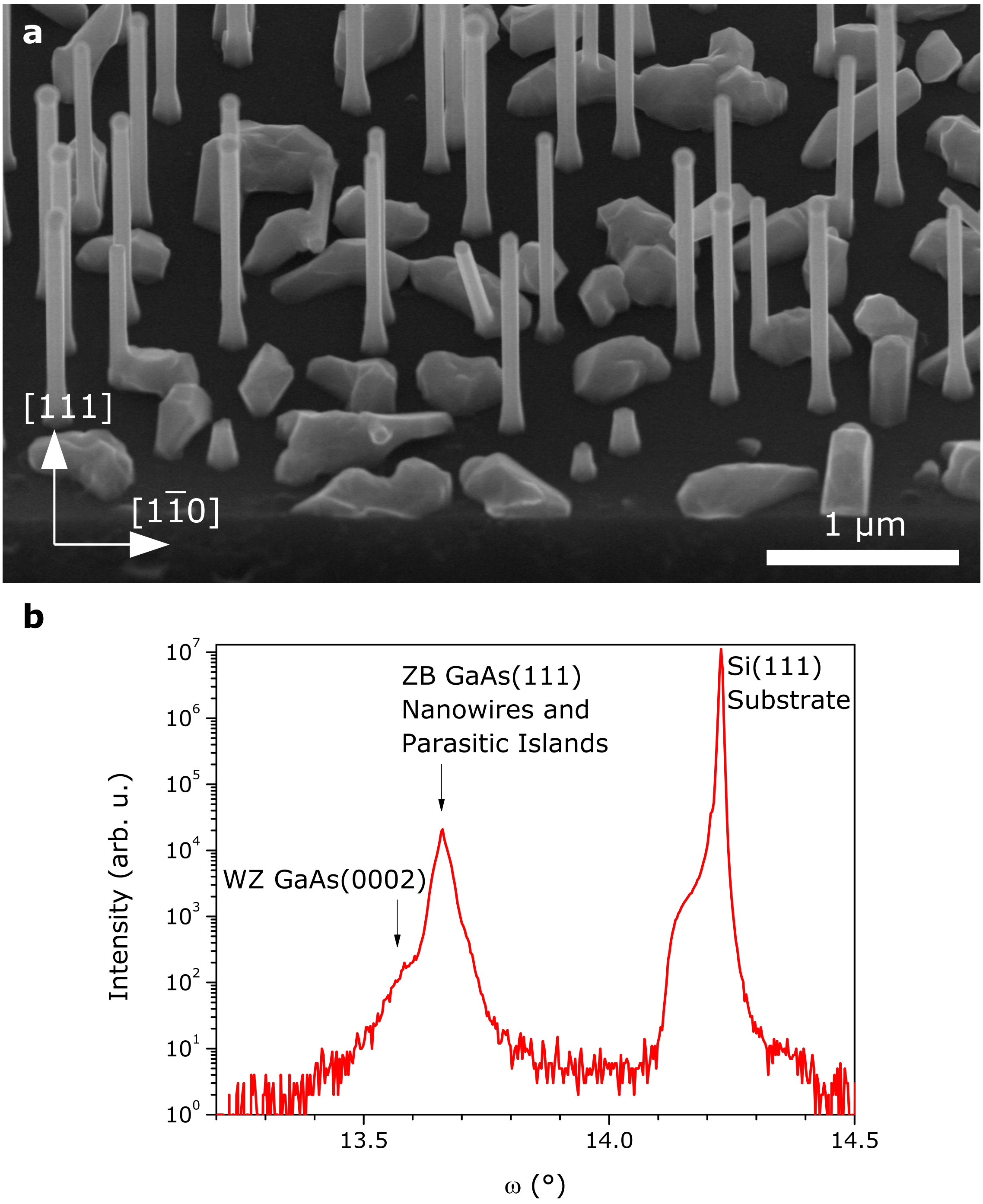

Figure 3.18.: **SEM and XRD of Self-assisted GaAs Nanowires on Si(111).** (a) SEM micrograph of analysed sample in 45° view. (b) Symmetric XRD $\omega 2\theta$ Scan, indicating that only a small fraction of the GaAs is present in the WZ crystal structure (measurement performed by B. Jenichen).

higher volume. Nevertheless, a minor contribution is expected to arise from unstrained parasitic GaAs islands. The FWHM of the GaAs(111) peak is 0.02°, which lies between the values obtained for nanowires and for parasitic planar growth using Au-assisted VLS (0.01° and 0.04° respectively, see Fig. 3.7). At the WZ position of 13.56°, only a shoulder is present, whose intensity is more than two orders of magnitude lower than that at the peak. This indicates that only a small GaAs volume fraction has adopted the WZ crystal structure.

Transmission Electron Miscroscopy

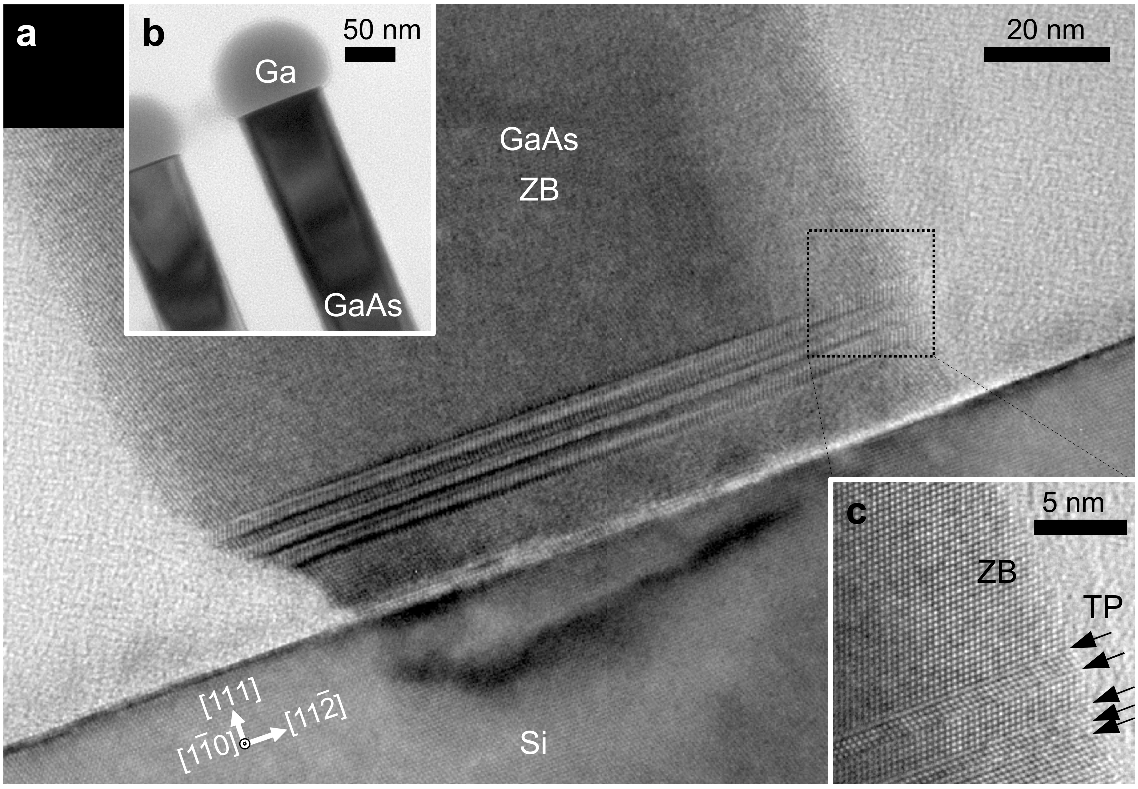

Figure 3.19.: **Microstructure of Self-assisted GaAs Nanowire on Si(111)** TEM micrographs show (a) HR-TEM micrograph of interface region, (b) TEM micrograph of nanowire top region and droplets, and (c) HR-TEM magnification of twin planes (TP), stacking faults and side facets. (Images taken by A. Trampert.)

Complementary to the integral determination of lattice parameters by XRD, the microstructure of self-assisted GaAs nanowires on Si(111) was analysed by TEM. Figure 3.19 presents TEM images of the sample grown under $J_{Ga} = J_0$ and $J_{As}/J_{Ga} = 0.5$, whose morphology was already presented in Figures 3.13a,e and 3.14a.

A composite bright-field HR-TEM micrograph (Figure 3.19a) depicts the nanowire base (diameter 125 nm) and the GaAs-Si interface region. The lattice contrast demonstrates that the GaAs nanowire base region entirely adopted the ZB structure, interrupted only by a few planar defects which were found at a distance of 10-25 nm from the interface. For all nanowires of this sample, the ZB crystal structure was found to extend up to their top end. A TEM micrograph of the top 300-400 nm of two nanowires (Figure 3.19b) demonstrates phase purity in that region by the absence of any planar defects, which would show as contrast lines perpendicular to the growth direction. The observed planar defects, i.e. stacking faults or twin planes, which are found close to the nanowire base (Figure 3.19a), appear in conjunction with faceted portions of the side wall to the right. Figure 3.19c presents a magnification of the planar defects and the side wall. The planar defects in this region consist of several rotational twin planes (TP, indicated by arrows) and additional stacking faults. In contrast to the Au-assisted nanowires, no extended defects are induced from neighbouring and coalescing GaAs structures, since the self-assisted nanowires grow isolated and have no crystalline interfaces other than to the substrate.

An additional sample of self-assisted nanowires, which was grown in the 'III-V' chamber of M6 under $J_{As}/J_{Ga} \approx 1$, $J_{Ga} = J_0/4 \Leftrightarrow v = 100$ nm/h, and a short growth time of $t_G = 300$ s, was analysed by TEM. The morphology of the sample shows very large Ga droplets (diameters up to 300 nm) and, as a result, very thick and also short nanowires (see Fig. 4.10).

Figure 3.20a depicts a high-resolution micrograph of the interface region between the GaAs nanowire and the Si substrate. The GaAs nanowire base contains a WZ section at a distance between 8 and 25 nm from the interface and some isolated planar stacking faults above. Since the WZ structure is equivalent to stacking ZB with the maximum number of twin planes, WZ stacking can be thought of as an extreme case of twin plane formation, as observed before in Fig. 3.19. At the interface, strain is accommodated by misfit dislocations.

The second micrograph recorded with 90° rotated electron incidence (Figure 3.20b) demonstrates that the interface is significantly rougher than the free Si surface and that the native oxide has been removed. The observed interface roughness appears to be associated with the intermixing of GaAs and Si found by XRD before (Fig. 3.18). These effects are most likely caused by meltback etching, i.e. the formation of a liquid Si-Ga alloy, which partially consumes part the substrate,[106] and subsequent GaAs growth. The removal of the native oxide is very probably caused by the same reaction with liquid Ga that is employed for Ga-polishing (see Sec. A.2).

Figure 3.21 presents two TEM micrographs recorded with the sample tilted by 20° around the $[1\bar{1}0]$ axis out of the $[11\bar{2}]$ zone axis. A bright-field TEM micrograph (a) shows an amorphous Ga droplet (with a crystalline inclusion), a very short GaAs nanowire and the Si substrate. At the interface between nanowire and substrate, a Moiré pattern can be seen, which arises from the overlapping Si and GaAs lattices as well as misfit dislocations. Figure 3.21b shows a corresponding weak-beam dark-field TEM micrograph using the 220 reflection. Under these imaging conditions, the interface contrast arises only from misfit dislocations. At the interface a network of misfit dislocations is visible, whose distance is approximately 5 nm. By way of these dislocations, misfit strain is relaxed almost completely, as was found by analysis of the corresponding TEM diffraction patterns (not shown). The crystal structure in this and similar samples with different growth times were further analysed by Synchrotron XRD performed by our cooperating group at the University of Siegen and published in a joint article:[107] In all samples, the overall structure is ZB but segments with the WZ structure were always found, most of them close to the interface. The lattice parameters were determined for the ZB and the WZ segments and are both in good agreement with the fully relaxed values (see Section 2.3).

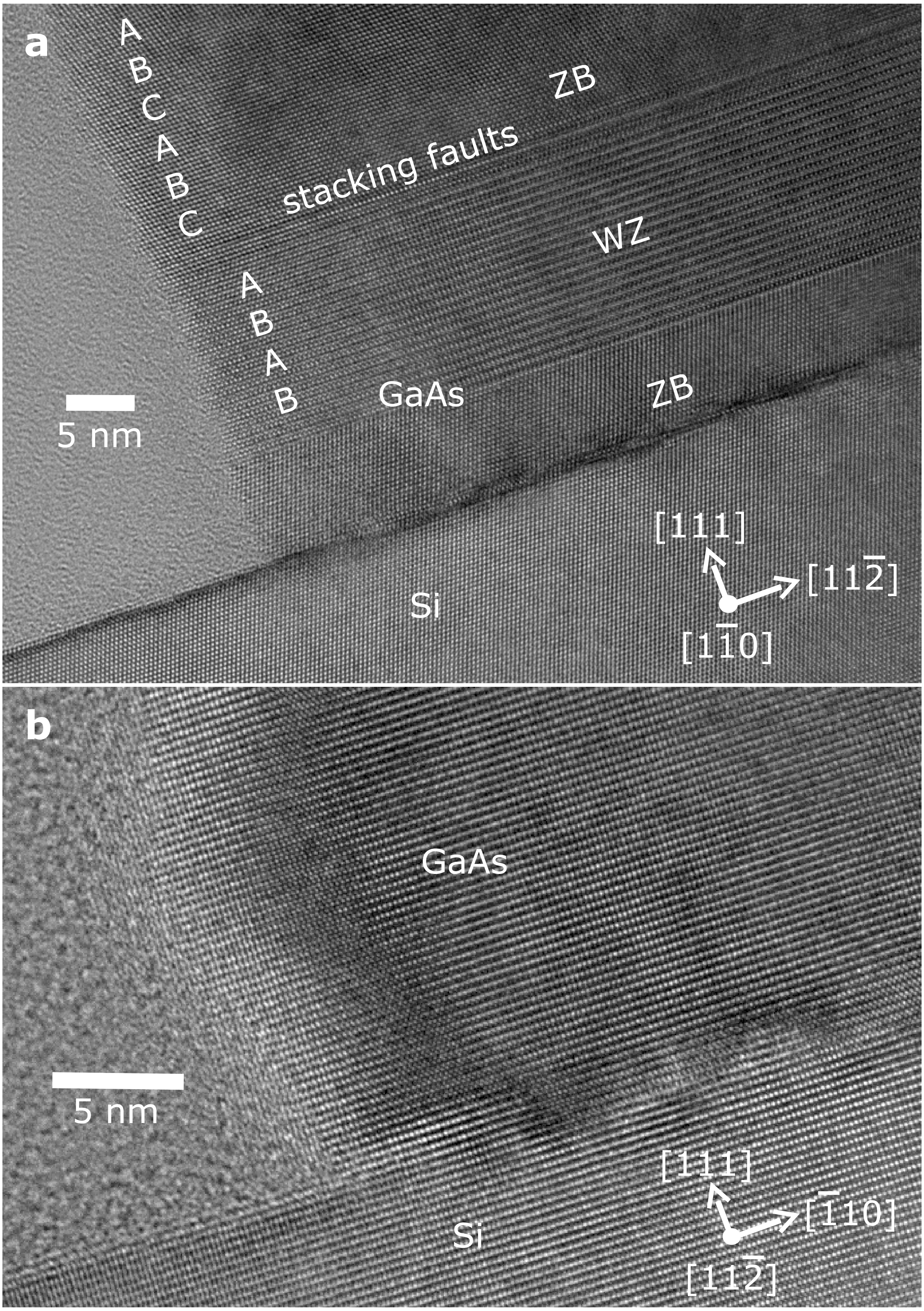

Figure 3.20.: **Bright-field HR-TEM images of GaAs-Si interface region.** Micrographs with the electron beam incidence (a) along the $\langle 1\bar{1}0 \rangle$ zone axis provides ZB-WZ contrast, and (b) along the $\langle 11\bar{2} \rangle$ zone axis indicates interface roughness. (Images taken by A. Trampert.)

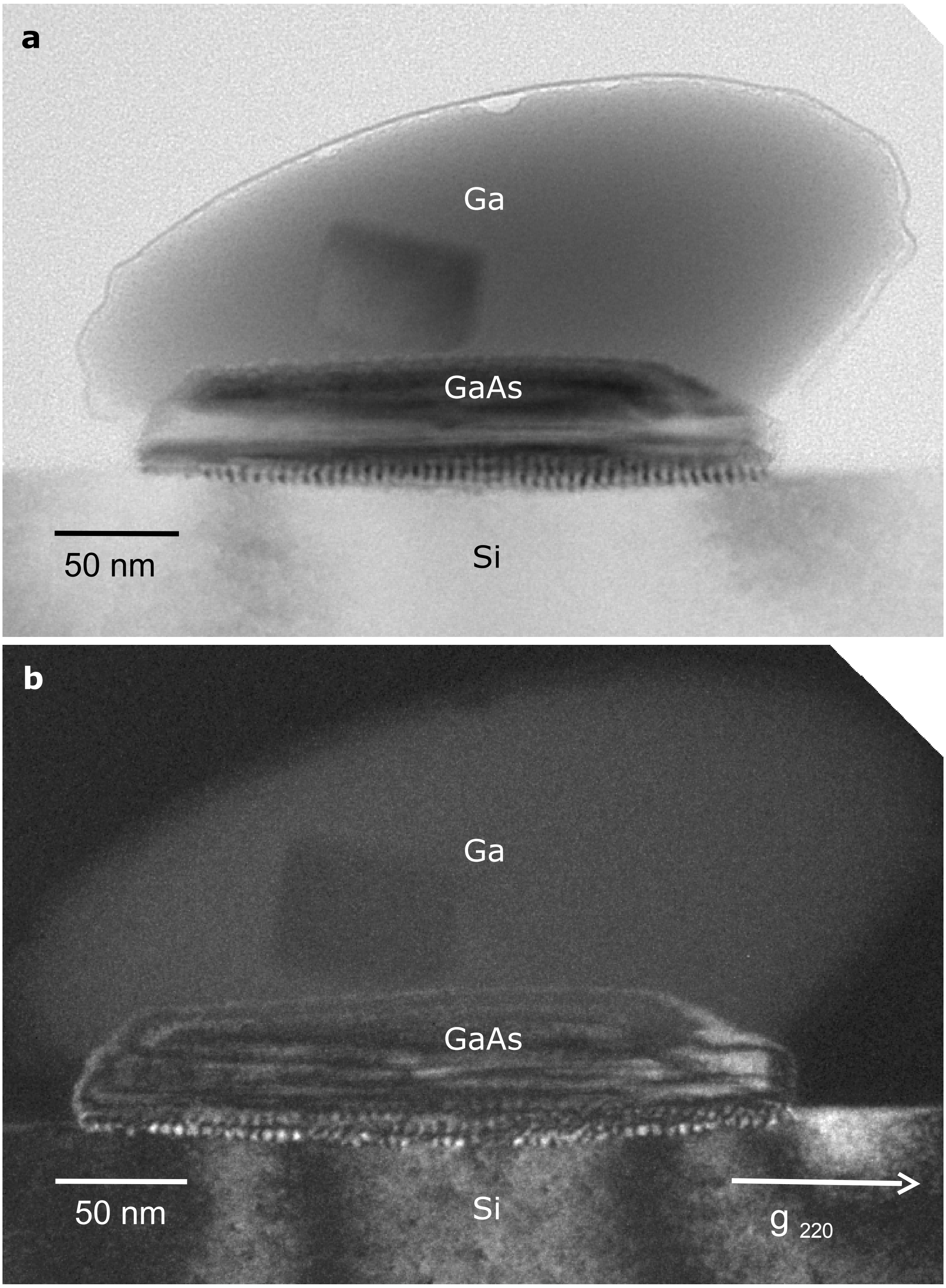

Figure 3.21.: **TEM micrograph of very short self-assisted GaAs nanowire.** The top Ga droplet is unusually large and was deformed during sample preparation. Bright-field image (a) shows overlapping lattices at the GaAs-Si interface, and weak-beam dark-field image (b) depicts a network of misfit dislocations. (Images taken by A. Trampert.)

3.2.4. Summary of Self-assisted Growth Experiments

Au-free growth of GaAs nanowires was achieved on Si(111) substrates that were covered with a thin layer of native SiO_x. Successful growth was first achieved in the 'Au' chamber and then transferred to the 'III-V' chamber of M6. Ga droplets form during the first instances of growth and were identified at the nanowire tips after growth completion. These observations demonstrate that self-assisted growth follows the VLS mechanism, with the Ga droplets functioning as assistant particles and material collectors. It was understood that the SiO_x functions as a mask, similar to selective area growth, which can be opened by liquid Ga droplets.

The nanowires grow epitaxially aligned with the Si(111) substrates in the [111] direction. The nanowire diameters were between 50 and 100 nm in good correspondence with the Ga droplet diameters. Between the nanowires, parasitic islands and sessile Ga droplets were found. Their volume fraction could be significantly reduced to 1/4 of the grown material when stoichiometric Ga and As supply and a low growth rate were used.

The crystal structure of the self-assisted nanowires was examined by RHEED, XRD and TEM. The nanowires were found to be predominantly ZB, include planar twin defects and a small fraction of WZ segments. A Synchrotron-XRD study with high spatial resolution showed that WZ signal arises from the base of the nanowires, close to the substrate interface. By HR-TEM, either twin planes or WZ stacking was found close to but not right at the interface. A roughening of the GaAs-Si interface as a result of interface reactions was found at the base of large-diameter nanowires.

3.3. Comparison of Au- and Self-assisted Growth Results

GaAs nanowires were successfully grown by the Au-assisted as well as the self-assisted VLS mechanism. The morphology of both nanowire types is generally similar: they grow in the [111] direction and have large aspect ratios, with typical diameters between 20 and 100 nm and lengths exceeding several μm. Although the GaAs nanowires were grown on Si(111) substrates, which involves 4% lattice mismatch, they were found to be free of strain by XRD measurements. This result was independent of the droplet material and is in accordance with the Principle of St. Venant (Sect. 2.2.1).

The amount of parasitic growth is substantial in the Au-assisted case, such that it completely covers the base between the nanowires. We will see in Chapter 4 that parasitic growth for Au-assisted GaAs nanowires on Si(111) is a result of the interface energies of the Au droplets on Si and on GaAs. This necessarily leads to the formation of a planar GaAs layer, which is very defective as known for planar GaAs on Si. In contrast, when Ga droplets were used, we were able to reduce parasitic growth to 1/4 of the total.

Under all growth conditions studied, the predominant crystal structure was WZ for the Au-assisted and ZB for the self-assisted case. Different surface energies of the Au and the Ga droplets might cause this behaviour and will be analysed in detail in Chapter 5.

Finally, some assistant material can remain at the substrate surface in both cases. Au clusters as well as sessile Ga droplets and interface roughening were observed. Therefore, incorporation of each assistant material into the substrate must be considered. While Ga is an intrinsic component of GaAs and a relatively harmless shallow acceptor in Si, Au atoms acts as deep traps in Si and as deep non-radiative recombination centres when incorporated into GaAs. The incorporation of the assistant material Au into the nanowires is studied in Chapter 6.

4. Nucleation of GaAs Nanowires

The nucleation of GaAs nanowires was studied in detail for both growth mechanisms. The focus was set on the morphological developments on the surface, which is important for nanowire shape, their positioning and separation.

While only little experimental data is published about the early stages of VLS nanowire growth, more information can be found in theoretical works that focus on the understanding of the VLS growth dynamics in detail. Glas et al. presented a TEM image of a very short GaAs nanowire on GaAs(111)B, which depicts a columnar nanowire with WZ structure on top of a pyramidal base with ZB structure.[67] The crystal structure change was explained by increase in droplet supersaturation that favours WZ (see Chapter 5 for details). Similar tapered bases have also been found for VLS-grown Si nanowires and were explained by an increase of the droplet contact angle during the initial growth, which leads to a diameter decrease and thus the formation of a nanowire on a wide base.[108] Recently, Schwarz and Tersoff have modelled the dynamical evolution of the nanowire shape basing on surface and interface energy minimization.[109,110] Their model predicts that different conditions can lead to straight vertical nanowires, or lateral growth of a *trace*, where the droplet crawls along the surface. An external perturbation can cause the nanowire to kink into a different direction.

First, the nucleation of Au-assisted GaAs nanowires on GaAs(111)B as well as on Si(111) is presented in Section 4.1. Then, the case for self-assisted nanowires grown on Si(111) follows in Section 4.2. Finally, the nucleation by both methods is compared in Section 4.3.

4.1. Au-assisted Nanowire Nucleation

The nucleation of GaAs nanowires grown by the Au-assisted VLS mechanism had not been analysed in detail before our work. Here we present a comparative study of the nucleation on GaAs(111)B as well as on Si(111) substrates.[111] It shows that the nucleation phase is very different on the two substrates, while eventually nanowires with very similar morphology grow. In the following section, a more detailed understanding of the observed delayed nucleation on Si(111) will be presented.[112]

4.1.1. Nucleation Series on GaAs(111)B and Si(111)

For a high level of nanowire growth control, it is important to understand the effects imposed by the substrate on nanowire shape and crystal structure. These substrate effects are strongest during nucleation. Judging by the knowledge of planar growth, strong differences between homoepitaxial and heteroepitaxial growth can be expected. For example, the crystal quality of planar GaAs layers on Si substrates still has not reached the level achieved by homoepitaxial GaAs, despite decades of intense research.[26] For nanowires, in contrast, the effect of the substrate is expected to be much smaller, since residual strain, which accumulates in heteroepitaxial planar layers, can laterally relax in nanowires at the free sidewalls (see Sec. 2.2.1).

Experimental

Samples of GaAs nanowires were grown on GaAs(111)B and Si(111) substrates in the 'Au-chamber' of M6. Homoepitaxial GaAs nanowire nucleation was studied on quartered two-inch, semi-insulating GaAs(111)B substrates. Substrate and Au droplet preparation were as described in Section 3.1.1. For nanowire growth, the substrate temperature was set to 500°C and a V/III flux ratio J_{As}/J_{Ga} =2 was used. The Ga flux was set to match a planar GaAs(111)B growth rate of 0.11 nm/s. The substrates were not rotated during growth, in order to permit the detailed RHEED analysis. The process was identical in all but growth time to that described in the last chapter (see also Figure 3.3).

Heteroepitaxial nucleation was studied on quartered two-inch, n-type, Si(111) $\pm 0.5°$ substrates. The Si substrate surface had been prepared by Ga-polishing (Sec. A.2). Further processing steps and the GaAs growth parameters were identical to the homoepitaxial case. These conditions were also identical in all but growth time to those applied for the exemplary sample shown in the last chapter (see also Figure 3.6).

Morphology

For ex-situ analysis of the surface morphology by SEM, series of growth experiments with different GaAs growth durations were prepared under otherwise identical conditions on both substrates. SEM images recorded under 45° sample inclination are depicted in Fig. 4.1. They show that the nucleation of nanowires on both substrates leads to an initially very different surface morphology, but eventually, rather similar nanowires grow.

On GaAs(111)B, after 5 s (Fig. 4.1a), 3-D structures are visible that exhibit an aspect ratio of about one. These are actually triangular pyramids, ca. 20 nm in diameter, and have a Au droplet on top. After 60 s (b), there are fully formed nanowires with vertical sidewalls which rest on much larger basal pyramids, whose diameter typically exceeds 200 nm. After 150 s (c), the nanowires as well as the basal pyramids have increased in height. The alignment of a nanowire and its corresponding basal pyramid is not concentric, but offset to one side, which is caused by growth without substrate rotation. After 1800 s (d), the basal pyramids have coalesced to a continuous rough layer and the nanowires reach an average length of (1.7 ± 0.3) μm.

On Si(111), after 5 s (Fig. 4.1e), horizontal traces with ca. 10 nm diameter and smaller structures are visible. We emphasize that the traces are pronouncedly elongated in the horizontal direction and thus exhibit a completely different shape than the structures found on GaAs(111)B. After 60 s (f), the horizontal length of the traces has increased, many elongated 3-D islands of irregular shape have appeared, the smaller structures are not visible, and very few vertical nanowires can be observed. After 150 s (g), the islands have coalesced to a connected network and there is a small number of vertical nanowires. After 1800 s (h), a higher number of vertical nanowires is present and the 3-D islands have completely covered the Si substrate.

The formation of traces was also reported for the Au-assisted nucleation of InAs nanowires on GaAs substrates by MOVPE.[113,114] Furthermore, on SEM images of InAs/GaP axial nanowire heterostructures in the supporting information of Dick et al., traces can clearly be seen on the substrate.[115]

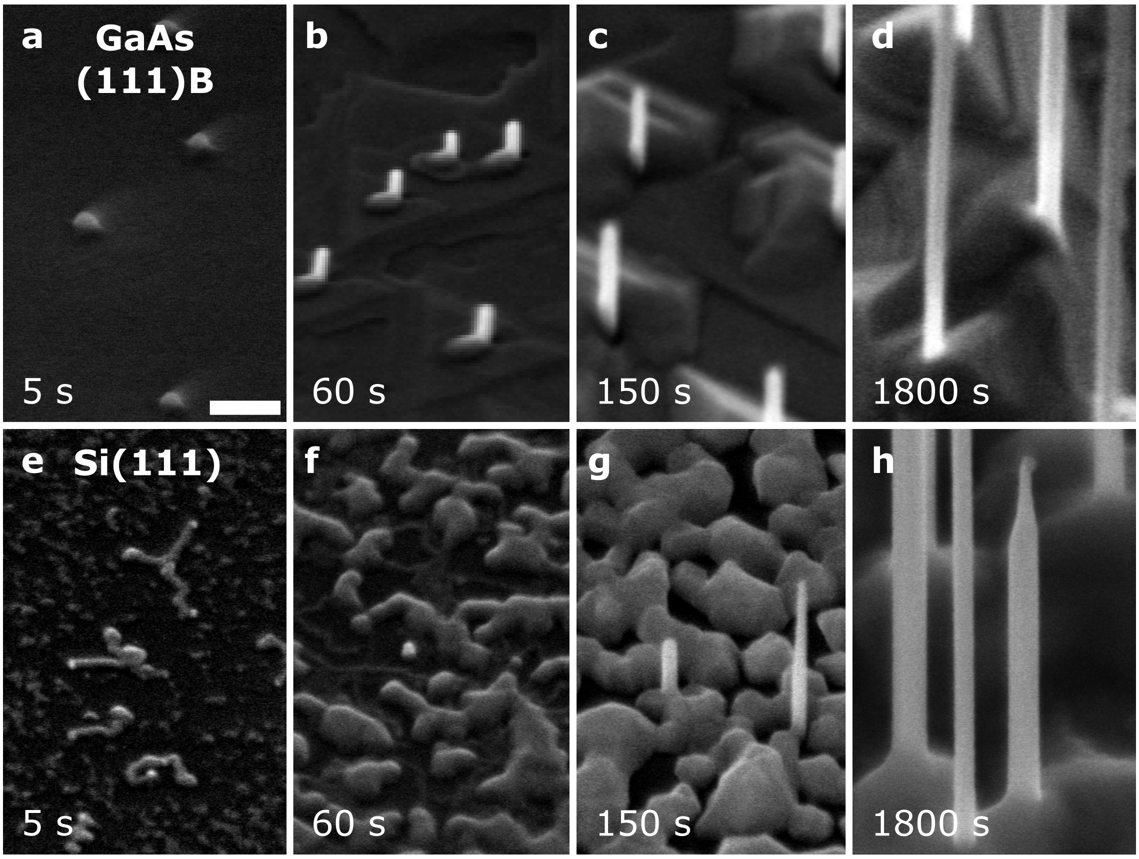

Figure 4.1.: **SEM images of GaAs(111)B and Si(111) substrates after Au-assisted GaAs growth for 5, 60, 150, and 1800 s,** (a-d) on GaAs(111)B, and (e-h) on Si(111). All images were recorded under 45° sample inclination and are shown with identical magnification as indicated by the 100 nm scale bar in (a).

For a quantitative study, further SEM images were recorded and analysed using ImageJ. The lengths l and diameters d of at least 30 nanowires were measured for each sample, except for the 60 s and 150 s samples on Si for which at least 8 nanowires were measured. The number density σ of vertical nanowires was determined using top-view images taken at three different positions on the sample and in two magnifications each. The average results are presented as plots versus growth time in Fig. 4.2. Error bars represent the standard deviation and linear approximations were obtained by least square fits. For the nucleation series on Si(111), the fraction of substrate area b covered by any shape of GaAs was determined from top-view micrographs in addition.

On GaAs(111)B substrates, there is no perfect linear fit for the nanowire lengths l. During the first 300 s of growth, an average axial growth rate of (0.7 ± 0.1) nm/s was determined as indicated in the plot, but the sample with 1800 s growth time yields (1 ± 0.2) nm/s instead. This may be related to a small number of nanowires having dropped out after some growth time and then the same amount of material would be shared by fewer nanowires. The nanowire diameters d are initially (22 ± 8) nm and the radial growth rate corresponds to 2 pm/s. The nanowire number densities σ are essentially constant at (12 ± 2) μm^{-2}. A slightly decreasing trend for longer growth times is observed but lies within the margin of variation between several images. Nevertheless, this might indicate

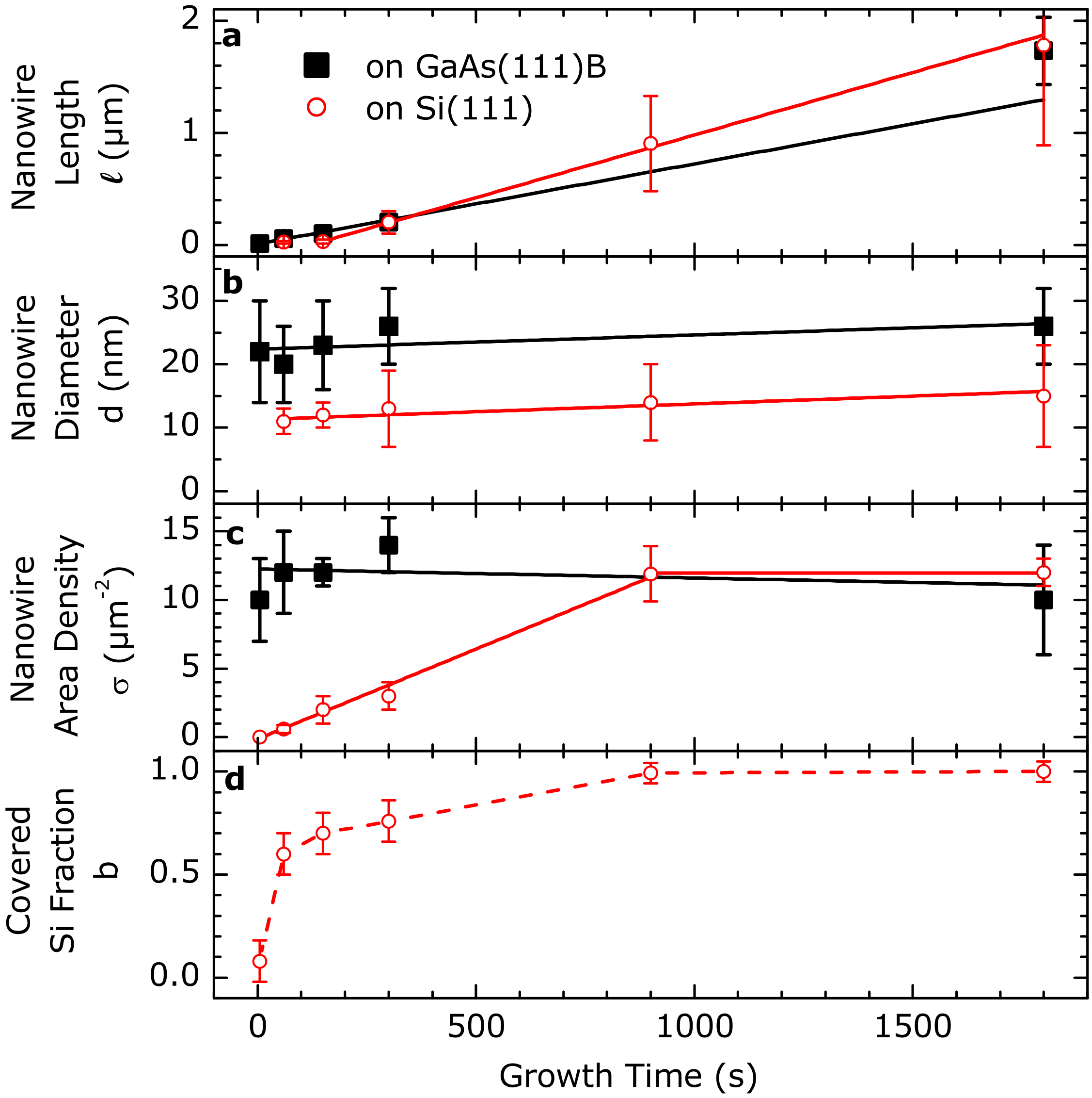

Figure 4.2.: **Morphology analysis of Au-assisted GaAs nanowires for samples grown on GaAs(111)B and Si(111)** (a) Average nanowire length l, (b) diameter d, and (c) number density σ, as well as (d) covered Si surface fraction b as a function of growth time were determined by analysis of SEM images. Linear fits to the data are shown as solid lines. Broken lines serve as guide to the eye.

the dropping out of a small number of nanowires for an unknown reason.

On Si(111) substrates, the nanowire number density σ is zero after 5 s of growth and increases within 900 s to the same value as on GaAs(111)B. For the nanowire lengths l on Si(111), a good linear fit is obtained for the four samples with the longest growth times and an average axial growth rate of (1.1 ± 0.3) nm/s is determined, which is in good agreement with the value on GaAs(111)B after longer growth times. However, the variation in the nanowire lengths on Si(111) is rather large. Thus, it cannot be established from these data whether a temporal change in the axial growth rate of individual wires has happened on Si(111) or not. Furthermore, the intercept with the zero length axis at

(120 ± 50) s is another indication for the delayed formation of nanowires. The nanowire diameters d after 1800 s of growth on Si(111) are (15 ± 8) nm and the radial growth rates on both substrates are very similar. The covered fraction b of Si(111) initially increases while GaAs traces, islands and nanowires form on the substrate. At some time between 300 and 900 s all these structures coalesce, the Si surface is completely covered by GaAs, and growth is effectively homoepitaxial.

The total coverage of the Si by GaAs explains the morphological similarities after longer growth times. It also explains why the axial as well as the radial growth rates of the nanowires are similar on both substrates. However, the nanowire diameter remains different on both substrates even after long growth times, because it is directly dependent on the size of the Au droplets, which is determined by self-organization phenomena on the as-prepared substrate surface. From this point of view, it appears to be coincidental that the final nanowire number density is the same on both substrates. We speculate that the use of colloidal Au particles with defined size would result in the same NW diameters on both GaAs and Si substrates (after the Si is buried by GaAs).

Crystal Structure

RHEED gives in-situ information about the crystal structure present during growth at and near the surface. The patterns were recorded during growth on both substrates with the incident electron beam along the $[1\bar{1}0]$ azimuthal direction and a selection of images is presented in Fig. 4.3. Initially, vertical streaks indicate the presence of atomically flat substrate surfaces, while the gradual appearance of spotty patterns shows the increasing dominance of 3-D structures.

On GaAs(111)B, initially GaAs in the cubic zinc-blende (ZB) structure can be identified, but by 60 s growth time, GaAs in the hexagonal wurtzite (WZ) structure dominates (Figs. 4.3b-e). On Si(111), initially the reflection patterns of ZB and its rotational twin, then additionally WZ spots, and finally only WZ spots are observed (Figs. 4.3g-j). Thus, in contrast to the nucleation on GaAs, on Si the rotational twin of the ZB structure forms and the transition to the WZ structure is delayed.

Discussion

The nucleation of Au-assisted GaAs nanowires is very different on the two substrates, but subsequent growth leads to rather similar nanowires once the nucleation stage is over. In the following, the distinct features of the nucleation on each substrate are explained and then the common morphology of longer nanowire growth is discussed.

On GaAs(111)B, in the very beginning GaAs grows under the Au droplets in the ZB crystal structure and forms triangular pyramids, cf. Figs. 4.3b and 4.1a. Such pyramids have been observed before[67] and their formation was explained by a reduction of the droplet contact angle at the beginning of growth.[108] When vertical nanowires appear, the crystal structure changes to WZ, cf. Figs. 4.3c and 4.1b. From then on, nanowire growth continues in the WZ structure. It is important to note here that on GaAs the material grows instantly in the vertical direction, as is expected for the VLS mechanism. As a result, the number density of nanowires on GaAs(111)B is constant from the beginning.

In contrast, on Si(111), horizontal traces instead of vertically growing structures are observed during the early stage of Au-assisted GaAs growth. During further GaAs growth, additional islands appear. By RHEED, traces and islands were found to have the ZB crystal structure and include rotational twins. In the following, a gradually increasing

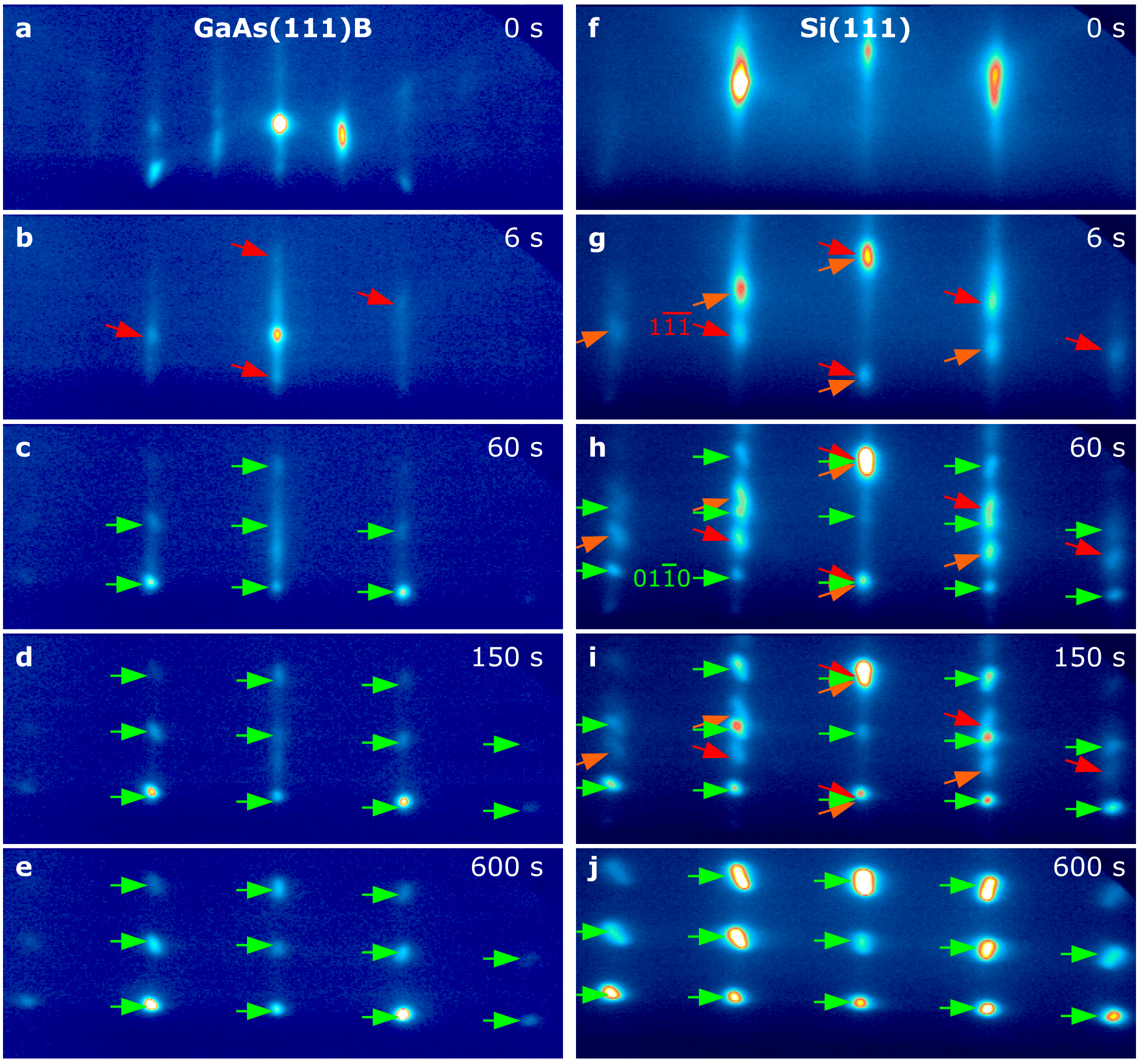

Figure 4.3.: **RHEED images in ⟨1$\bar{1}$0⟩ azimuth of GaAs(111)B and Si(111) substrates decorated with Au droplets (0 s), as well as of both substrates after Au-assisted GaAs growth for 6, 60, 150, and 600 s.** The reflections of ZB GaAs (↘), of its rotational twin (↗), and of WZ GaAs (→) are indicated. Two reflections, which were chosen for temporal intensity analysis, are labelled in g and h.

number of vertical nanowires appears. On Si as well as on GaAs, long vertical nanowires have the WZ crystal structure, cf. Figs. 4.3j, 4.1h, and 3.3.

The nucleation behaviour for the Au-assisted VLS growth of GaAs homoepitaxially on GaAs(111)B and heteroepitaxially on Si(111) is very different, although after long growth times similar nanowires develop on both substrates. Thus, the substrate has a direct influence on nanowire growth only during the initial nucleation stage. This phenomenon appears to be caused by the gradual covering of Si by GaAs structures such as traces and islands, whose eventual coalescence completely covers the Si(111) substrate. A study of the detailed process leading to delayed nanowire growth is presented in the following section.

4.1.2. Delayed Nanowire Growth on Si(111)

Here, a more detailed study of the nucleation of Au-assisted GaAs nanowires on Si(111) substrates is presented.[112] It is focused on uncovering the mechanism for the delayed nanowire formation on Si(111). The nucleation study presented in the last section is augmented by a temporal analysis of RHEED patterns and detailed HR-TEM microscopy of the three types of GaAs structures found on the surface: traces, islands and nanowires. The apparent connection between trace growth on Si and nanowire growth on GaAs is then explained by different interface energies of the Au droplets on these two materials and the evolution of the VLS growth process from horizontal trace to vertical nanowire growth is explained.

RHEED Intensity Development

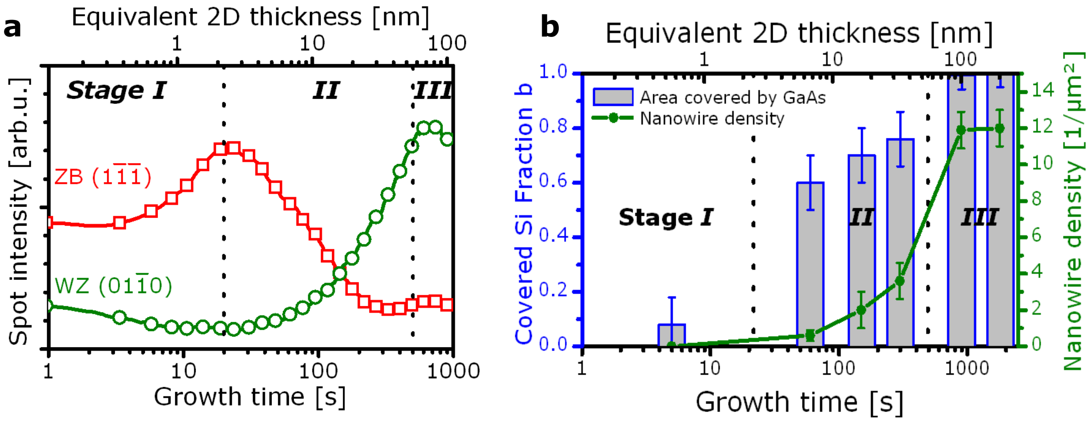

Figure 4.4.: **RHEED progression and SEM analysis.** (a) RHEED intensity progression of the chosen reflections evidencing a gradual change from nucleation in the zincblende to growth in the wurtzite crystal structure. (b) Plot of the percentage of the Si surface area covered by GaAs and the number density of nanowires versus growth time. Three resulting nucleation stages are indicated.

By comparison of RHEED and SEM, it was found in the last section that the vertical nanowires grow in the wurtzite crystal structure, whereas the earlier manifestations of GaAs, i.e. traces and islands, grow as zincblende GaAs. This difference can be used to acquire more quantitative information about the delayed appearance of nanowires. To this end, RHEED patterns were recorded every 200 ms during a full growth run for 900 s without rotation and the intensities of the zincblende and the wurtzite RHEED patterns was monitored over time. One reflection for each crystal structure was chosen for temporal intensity analysis: the wurtzite $01\bar{1}0$ and zincblende $1\bar{1}\bar{1}$, cf. Fig. 4.3g, h. Figure 4.4a shows the intensity progression of the two chosen reflections.

Prior to growth, the Si(111) reflection pattern without superstructure is observed, in agreement with the Si(111):As (1×1) surface expected to form in an As-containing MBE growth chamber.[116] The corresponding crystal truncation rods tail off into the regions of the two GaAs reflections chosen for analysis (see Fig. 4.3f). Thus, at the very beginning of growth, the progression shows non-zero intensities for both reflections. As growth begins, the Si crystal truncation rods gradually disappear, which leads to a marginal intensity decrease at the wurtzite position. Meanwhile, the zincblende intensity strongly increases, indicating 3-D growth of traces and islands. The zincblende intensity is at a maximum after 20 s. From then on, the zincblende intensity decreases and the wurtzite intensity increases, indicating the beginning of nanowire growth. However, it takes circa 500 s for the wurtzite intensity to reach this maximum. Simultaneously, the zincblende intensity vanishes. Since more zincblende GaAs exists in the basal layer below the nanowires, this indicates that the RHEED beam can no longer reach the base of the nanowires and probes their upper regions only.

In order to compare the temporal development of the crystal structure to that of the sample morphology, the results for the nanowire area density σ and the covered Si fraction b, which were obtained from the analysis of SEM micrographs (Fig. 4.2), are presented here again in Figure 4.4b.

The temporal development of the nanowire density closely resembles that of the wurtzite intensity. This demonstrates that the nanowires have the WZ crystal structure, as was already deduced earlier from the RHEED patterns. Conversely, a qualitative connection can be made between the zincblende intensity and the existence of uncovered Si areas.

According to the development of the RHEED intensities, the growth process can be divided into three stages: During the initial zincblende dominated period ('stage I'), from growth start until 20 s, only traces and islands form. During the transition period ('stage II'), from 20 s until 500 s, wurtzite nanowires gradually appear in increasing number. During the wurtzite saturated period ('stage III'), from 500 s until the end of growth, the wurtzite nanowires dominate and no more zincblende GaAs is detected by RHEED. The stages I, II, and III coincide with a sample morphology dominated by none, intermediate, and saturated nanowire density as well as low, intermediate, and full GaAs covering, respectively.

Microstructure of Nanowires, Islands and Traces

In the following, the observed morphology of the different manifestations of GaAs as well as their crystal structure are presented in detail. To this end, HR-TEM micrographs are shown, which were recorded at different regions on one same sample grown on Si(111) for 150 s ($d = 17$ nm) on which traces, islands and nanowires coexist. These micrographs and local 2-D Fourier transforms are shown in Figs. 4.5-4.7.

In an overview TEM micrograph (4.5a), a typical trace is displayed in its entirety. The total length is 70 nm. A high-resolution magnification of its frontal region is shown in (4.5b). The crystallized Au in front of the trace is identified by the lattice spacing of 2.4 Å determined from the encircled reflections, which corresponds well to the lattice parameter of face centred cubic Au(111) (2.36 Å).[69] The Au droplet exhibits one interface each to the Si substrate and to the GaAs trace. Moiré fringes indicate superposition of the respective lattice with that of Au. Close to the centre of the Fourier pattern, four additional spots can be identified of which one pair arises from the Moiré fringes of each interface.

The GaAs trace itself has a height comparable to that of the Au. The GaAs displays several twin planes which change the stacking sequence from the zincblende crystal structure (ABCAB) to its twin (BACBA) and back. In the Fourier pattern, the stacking sequence which corresponds to that of the Si substrate is indicated by full lines and its twin by dotted lines. Both have similar intensity. The low number of atomic layers in the GaAs trace compromises the quality of the Fourier pattern.

The Si substrate shows alloying with Au. However, since the interface with the GaAs trace is straight it appears that the alloy formation has taken place on a time scale longer

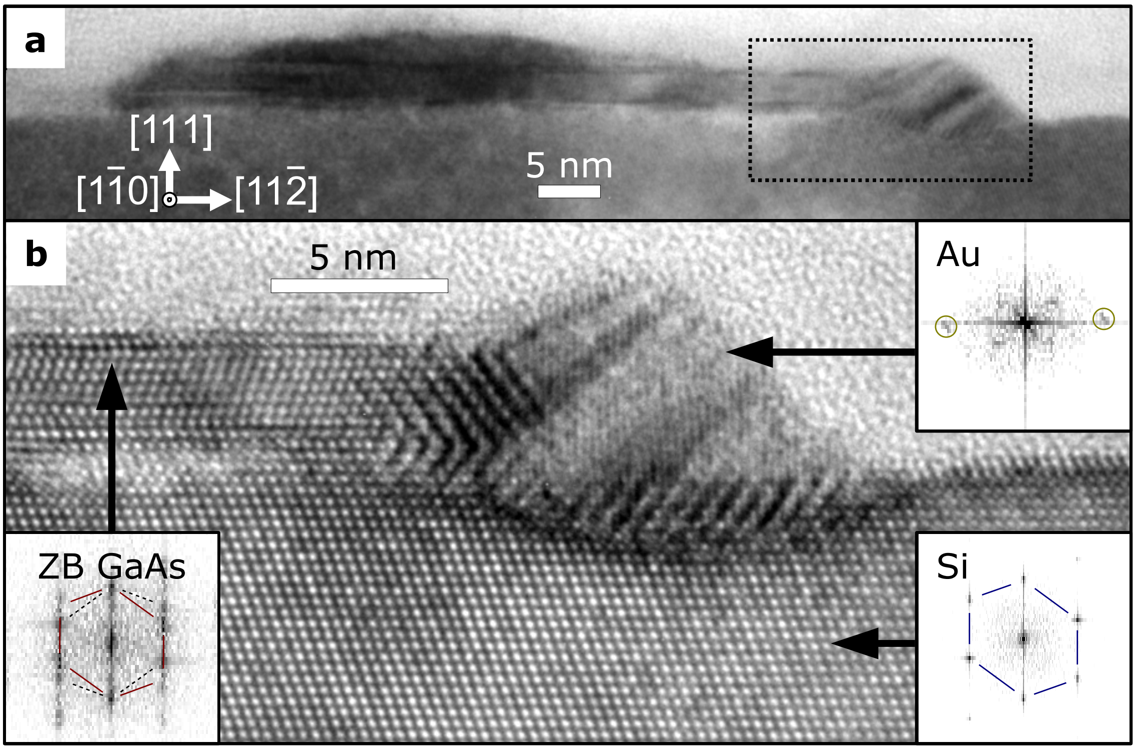

Figure 4.5.: **Au-assisted GaAs Trace on Si(111).** (a) TEM micrograph of GaAs trace with frontal Au droplet; (b) high-resolution micrograph of the front of the same trace showing the zincblende crystal structure with twins and the crystallized Au droplet. Insets show 2-D Fourier transforms of front (Au), tail (ZB GaAs) and substrate (Si) regions for their crystal structure identification. (Images taken by A. Trampert)

than the horizontal movement of the Au. The face centred cubic crystal structure of Si is identified by the Fourier pattern.

Figure 4.6 shows a HR-TEM micrograph of a typical island, that apparently grew without a Au droplet. The GaAs grew in the twinned zincblende structure with stacking faults and nanotwins. For this particular island, the zincblende stacking sequence corresponding to that of the Si substrate has a higher occurrence. However, the twin sequence prevailed for other islands. This indicates that on average none of the two zincblende sequences is favoured during growth. The density of planar defects is larger close to the Si substrate. Dislocations can be found at the interface between Si substrate and GaAs island, leading to plastic strain relaxation.

Figure 4.7 presents a HR-TEM micrograph of a typical nanowire. All analysed nanowires indeed display one Au droplet located at their tip and show the wurtzite crystal structure. Between the wurtzite GaAs nanowire and the Si substrate there is a base of zincblende GaAs. This base structurally closely resembles traces and islands in that there are many stacking faults. The Au droplet diameter matches the nanowire diameter, typically between 5 and 15 nm. This particular nanowire is 10 nm long, as measured over the wurtzite segment, and the zincblende base below is 22 nm high.

The HR-TEM investigation confirms the earlier assignments in crystal structure of wurtzite to nanowires and zincblende to traces. Furthermore, islands and the basal GaAs

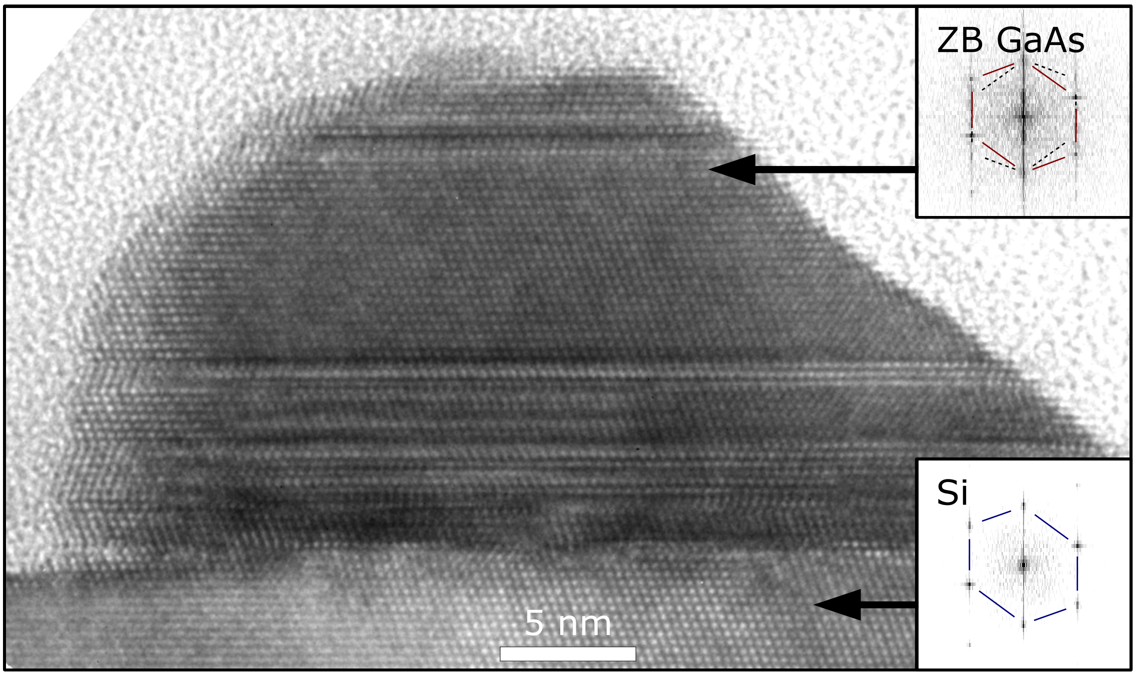

Figure 4.6.: **GaAs island on Si(111).** HR-TEM micrograph of typical 3-D GaAs island, structurally zincblende with twins. The insets show 2-D Fourier-transformations of selected regions for their crystal structure identification. (Image taken by A. Trampert)

also adopt the twinned zincblende structure. Additionally it is verified, that both traces and nanowires form by VLS growth from Au droplets.

Temperature series

In order to obtain further insight into the nucleation mechanisms a series of samples was grown for 150 s at different substrate temperatures. Figure 4.8a shows 45° incidence SEM images of the samples grown at $T_S = 350, 450, 550,$ and 600°C.

At 350°C the substrate was almost completely covered by GaAs that had already coalesced to a rough layer. Nanowires were present in between and no traces were seen. On the sample grown at 450°C there were fewer nanowires and some traces. GaAs coalescence and coverage of Si were less complete. At 550°C even more traces and free Si surface but less area covered by GaAs was present. Nanowires were few and short. The sample grown at 600°C showed the smallest covered surface fraction of the study. There were neither nanowires nor traces.

As before, normal incidence SEM images of these samples were analysed quantitatively and the results are shown in Fig. 4.8b. With increasing temperature the area fraction of Si covered by GaAs b exhibits an essentially decreasing trend. This reproduces the Au-free case,[117] in which a lower T_S effectively suppresses the kinetics of island formation by reduced Ga diffusion, and GaAs tends to grow as a closed layer. With increasing T_S from 350 to 525°C, the nanowire density decreases approximately in parallel with b. This means that the nanowire density is lower when the total GaAs coverage is lower, similar to the growth time series discussed earlier, which provides further ev-

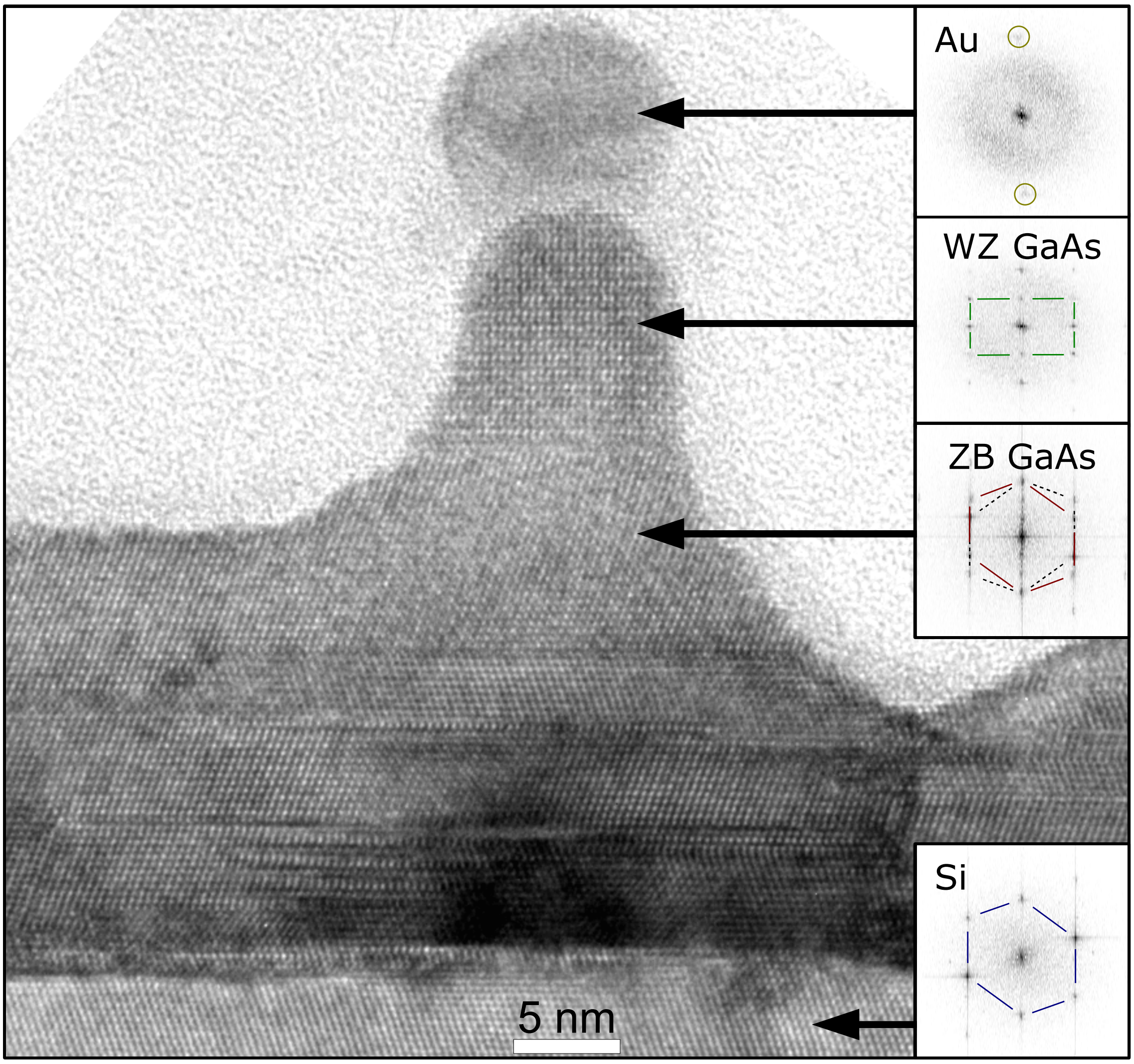

Figure 4.7.: **Au-assisted GaAs nanowire on Si(111).** HR-TEM micrograph of wurtzite GaAs nanowire with Au droplet at the tip and a zincblende GaAs base layer. The insets show 2-D Fourier-transformations of selected regions for their crystal structure identification. (Image taken by A. Trampert)

idence that nanowires form in connection with GaAs-covered areas. In the range from 500 to 550°C an increasing number of traces could be identified while nanowires were increasingly scarce. Possibly, trace growth is the origin of the rising slope of *b* in this temperature range. On the sample grown at 600°C neither nanowires nor traces are visible which indicates that growth by the VLS mechanism did not take place. This compares well with homoepitaxial GaAs nanowire growth on GaAs(111)B, where nanowire growth stops above 620°C.[48]

These observations show that the transition time of VLS growth from pure trace formation (Stage I) to pure nanowire formation (Stage III) depends on growth temperature and increases with temperature. For all temperatures below 600°C nanowires grew on GaAs, while traces grew on Si.

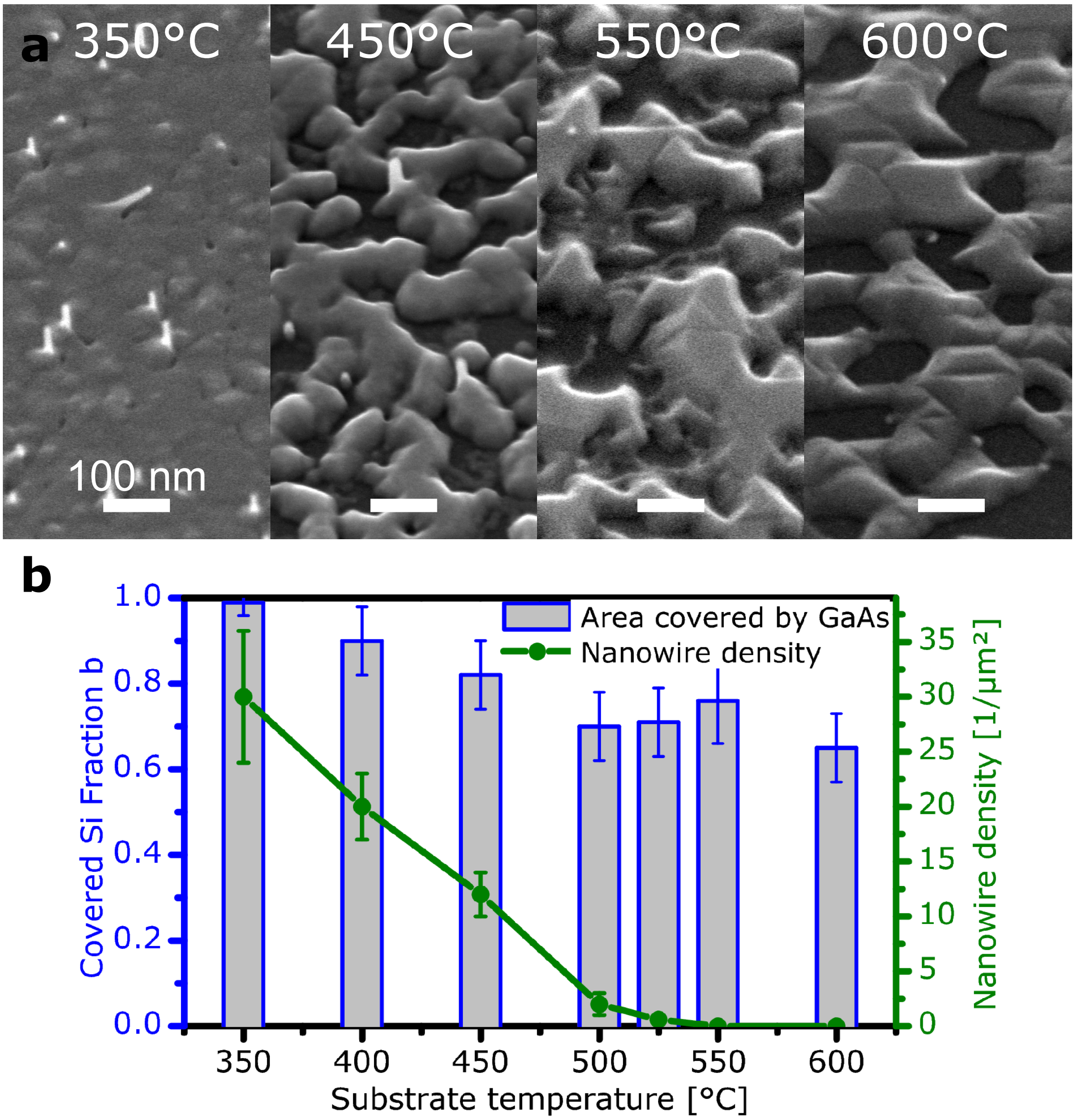

Figure 4.8.: (a) SEM images in 45° incidence of samples grown for 150 s at various substrate temperatures: at 350°C the Si substrate was covered by GaAs and many nanowires grew; at 450°C GaAs had formed islands, traces on remaining Si and nanowires on the GaAs islands; at 550°C island growth was confined to a smaller total area, many traces grew, and nanowires did not form; and at 600°C only islands grew. (b) Plot of the temperature dependence of the area covered by GaAs and the nanowire density. Both show an essentially parallel trend with temperature.

Interface Energies

The nucleation data show that nanowires develop gradually after a delay, which appears to be connected with the initial formation of traces. Since both, traces and nanowires, grow from Au droplets, one can expect that traces evolve to nanowires by some mechanism. What determines the evolution of the GaAs growth in stages from traces to nanowires? Both trace fronts and nanowires grow from Au droplets by the VLS mechanism, while in parallel direct epitaxial attachment first leads to the growth of trace ends to islands and possibly Volmer-Weber island nuclei, then adds to the coalescence of all GaAs structures and finally governs the growth of the basal layer between the nanowires. As a result, initially traces grow on Si and later nanowires grow on GaAs. For an understanding of the VLS growth evolution, the influence of the liquid-solid interface must be clarified.

In a nanowire, the liquid droplet exclusively adjoins GaAs and further growth adds material to this interface (Fig. 2.1). This is different in a trace (4.9a). Here, the droplet adjoins GaAs as well as Si and while further growth of GaAs from the droplet adds material homoepitaxially at the GaAs interface, the experimental data suggest that it is favourable for the droplet to keep the Si interface area constant by lateral motion. Thus, from the initial prevalence of traces, a smaller interface energy of Au/Si can be concluded as compared to Au/GaAs, i.e.

$$\gamma_{LS}^{\mathrm{Au/Si}} < \gamma_{LS}^{\mathrm{Au/GaAs}}. \tag{4.1}$$

In order to verify this, the energies of the two competing liquid-solid interfaces are estimated. In the present system, various experimental as well as theoretical studies allow the calculation of the interface energies by Young's equation

$$\gamma_{SV} = \gamma_{LV} \cos(\phi) + \gamma_{LS}, \tag{4.2}$$

where ϕ is the contact angle measured inside the droplet and γ_{SV}, γ_{LV} and γ_{LS} are the solid-vapour, liquid-vapour and liquid-solid interface energies, respectively.

To be precise, the liquid Au droplet accumulates Ga during growth and the resultant alloy has been shown to contain up to 50% Ga (stoichiometric AuGa) in an analysis of GaAs nanowires on the homoepitaxial substrate.[47] A simple estimation of γ_{LS} can be made using the experimental values[118] for γ_{LV} (Au) $= 1.14$ J/m^2, γ_{LV} (Ga) $= 0.72$ J/m^2, and interpolating to a Ga content of 50%.

The surface energy of Si(111) has been determined by cleavage experiments[119] to be $\gamma_{SV} = 1.23$ J/m^2, which is considered as an upper limit, since theoretical calculations demonstrate that the Si(111) surface energy is substantially lowered by the As-termination that arises in the As-rich growth conditions used.[120,121] The contact angle of liquid Au on Si(111) is $\phi = 43°$, which has been experimentally determined[122] and also corresponds to the angle visible by TEM (Fig. 4.5b). This yields an estimate of $\gamma_{LS}^{\mathrm{AuGa/Si}} \leq 0.55$ J/m^2 for stoichiometric AuGa and an even lower value ≤ 0.40 J/m^2 for pure Au.

For the GaAs interface energy, we consider the calculated[123] lowest energy surface under As-rich conditions, which is (111)B reconstructed with As trimers and has $\gamma_{SV} = 0.69$ J/m^2. The contact angle of liquid Au on GaAs nanowires as measured after growth was reported[67] to lie between 90° and 125°. There are difficulties associated with the determination of contact angles at nanowires due to the curvature of the underlying GaAs

(Fig. 4.7). Thus, the interface energy of the liquid droplet on GaAs(111)B is estimated to be $\gamma_{LS}^{\mathrm{AuGa/GaAs}} \geq 0.69\ \mathrm{J/m^2}$ and the same value for pure Au in accordance with Glas et al.[67]

From these estimations, we conclude that the interface energy of liquid droplets is indeed lower on Si(111) than on GaAs(111)B, which supports the trace formation mechanism described above.

Evolution Model

The initial prevalence of traces has been explained by the lower droplet interface energy on the exposed Si (stage I, Fig. 4.9a). Consideration of the increasing GaAs coverage elucidates the origin of the further two observed nucleation stages.

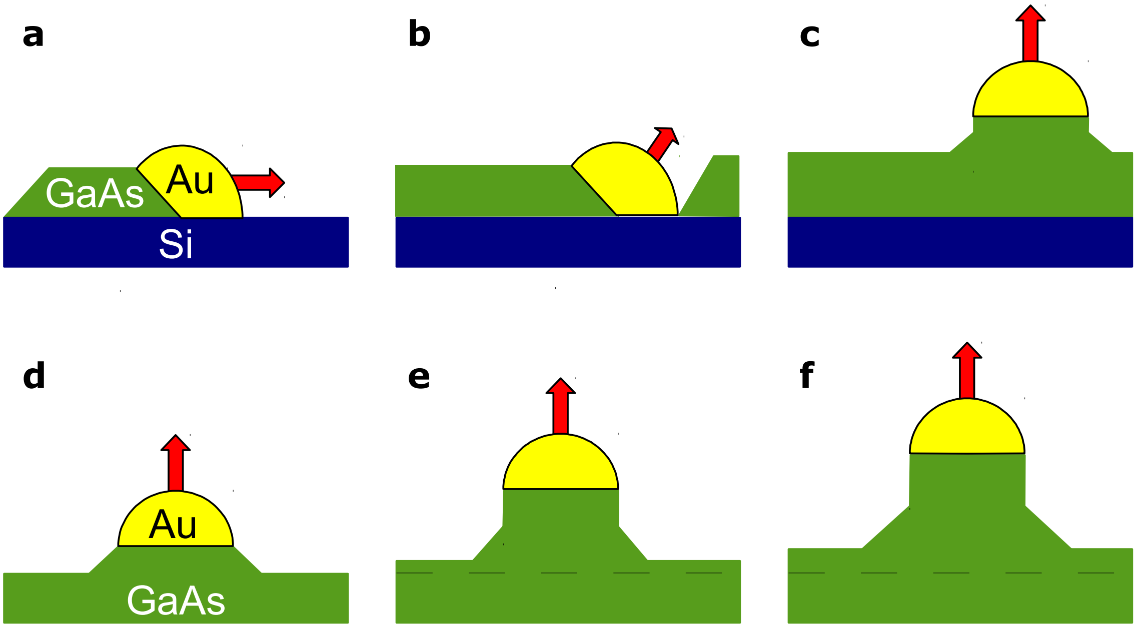

Figure 4.9.: **Schematic model of trace to nanowire evolution on Si and direct nanowire growth on GaAs.** Schematic of (a) trace growth, (b) transition from trace to nanowire growth, and (c) nanowire growth on Si, as well as (d) early, (e) intermediate, (f) final growth of vertical nanowires on GaAs. The resulting growth directions are indicated by arrows. The original height of the GaAs substrate is indicated by dashed lines.

In the process of VLS trace and VS island growth, GaAs gradually covers the Si substrate. Eventually, no more free Si surface is available in the neighbourhood of a particular Au droplet so that it cannot continue trace growth (Fig. 4.9b). This triggers the turnover from horizontal trace to vertical nanowire growth, since the driving force for lateral motion has vanished. The last Si remaining directly under the droplet is covered either by further lateral growth of the GaAs trace front or by GaAs nucleating at the Si interface. In both cases, the droplet is pushed upwards in the process.

From this moment on, the liquid-solid interface of the droplet is completely made up of Au/GaAs. This interface is again the location of GaAs precipitation but there is no more energy gain from lateral motion. Instead, the nanowire is pushed vertically upwards by its own precipitate (Fig. 4.9c). As soon as the now horizontal Au/GaAs interface has risen above the neighbouring GaAs structures, vertical sidewalls can be formed and a vertical nanowire can grow. Then, growth continues as on homoepitaxial GaAs substrates.

Due to the random positions of the Au droplets not all switch from trace to nanowire growth simultaneously. Stage II thus consists of the transition period that starts when the first droplet switched and ends when the last one did, i.e., until the Si is completely covered by GaAs. From then on, nucleation is finished and nanowires grow identical to the homoepitaxial case on GaAs substrates.

In homoepitaxial VLS growth, the nanowires grow instantly in the vertical direction. Additional parasitic planar growth has generally been found experimentally.[104] This case is schematically presented in Figure 4.9d-f and depicts representations of (d) the initial growth of a pyramid with tilted sidewalls, (e) the following development of vertical sidewalls, as well as (f) the continuing growth of vertical nanowire and basal pyramid by axial VLS as well as radial VS growth.

Discussion

Our study of Au-assisted VLS nucleation of GaAs nanowires on Si substrates shows that vertical nanowires grow effectively only on GaAs. On the initially exposed Si surface, horizontal traces form instead and delay vertical nanowire growth until the Si substrate is completely covered. This behaviour is effectively caused by a lower liquid-solid interface energy of the Au droplets on Si than on GaAs. In other words, the degree of wetting of Au droplets is higher on Si than on GaAs. Therefore, direct nanowire nucleation without delay can be expected for the opposite case of Au-assisted Si nanowires on GaAs substrates.

Due to the scarcity in nanowire nucleation studies, our findings can at present only be compared with the Au-assisted VLS growth of axial heterostructures of GaAs on Si *within* nanowires using MOVPE as published by Dick et al.[115] Straight heterostructures of GaAs on Si nanowires were observed, while Si segments on GaAs nanowires grew in kinked directions. This observation was interpreted as being caused by wetting of the Si nanowire base segment by the GaAs nanowire top-segment, without taking the Au droplets and their interface energies into account. When this is done, a lesser wetting of Au droplets on Si than on GaAs must be concluded, which is the exact opposite of our own result.

Thus, it seems that the wetting situation can depend on additional parameters such as a) the composition of the liquid droplet, b) presence and quality of ambient vapours or surfactants that change the surface and interface energies, and c) surface roughness that may prevent lateral movements of the Au droplets. Indeed, Dick et al. themselves expect that the wetting behaviour may change, if the interface energies are similar, which is in agreement with our estimations.[115]

4.1.3. Summary of Au-assisted Nucleation

The very early stages GaAs nanowires growth on GaAs(111)B by the Au-assisted VLS mechanism showed that nanowires form directly the vertical $[\bar{1}\bar{1}\bar{1}]$B direction. The number of nanowires stayed constant over the whole growth time. Additional pyramidal bases have been found at the bottom end of the nanowires.

In the Au-assisted VLS growth of GaAs on Si(111), nanowires started to grow only after the first ≈ 20 s (7 ML) and their number increased until ≈ 500 s. This nucleation delay was explained by the formation of horizontal traces, which arise since the liquid

Au droplets have a lower interface energy on Si than on GaAs. Further growth is then dominated by GaAs islands, which grow from trace ends or possibly from Volmer-Weber nuclei. Finally, vertical nanowires and an additional base layer grow. The latter is formed by coalescence of all earlier GaAs structures. In brief, the Au-induced nanowires grew only on a layer of GaAs.

The evolution model presented above explains the observed delay in GaAs nanowire formation on Si during Au-assisted nucleation. The sequence of nucleation stages is triggered by the initial formation of traces due to the lower interface energy of Au on Si than on GaAs. It must be stressed here that trace growth implicates two main disadvantages: loss of position control and unavoidable growth of a basal GaAs layer bridging individual nanowires.

4.2. Self-assisted Nanowire Nucleation

It became apparent already in the last chapter (Section 3.2), that the self-assisted growth of GaAs nanowires on Si(111) does not necessitate an intermediate GaAs layer, but instead a layer of SiO_x which functions as a mask for selective growth. From the dependence of the nanowire density on growth conditions, it was concluded that the SiO_x mask can be opened by liquid Ga droplets. The self-assisted nanowires are well separated even after long growth times. Even better, the remaining undesired co-growth of islands between the nanowires can be further reduced using a low deposition rate. These findings indicate already that the self-assisted nucleation is more direct than the one under Au-assistance. In order to further illuminate the self-assisted nucleation of GaAs nanowires on oxide-covered Si(111), several samples were grown for short durations.

First, an example of short self-assisted GaAs nanowires is presented, which grew under comparably large Ga droplets such that their morphology could be studied in high detail by SEM. However, the Ga droplets and so the GaAs nanowires typically had smaller diameters for most other samples. Therefore, the detailed analysis of a series of samples, which were grown under standard conditions for different durations, is presented subsequently.

4.2.1. Short Nanowires with Large Ga Droplets

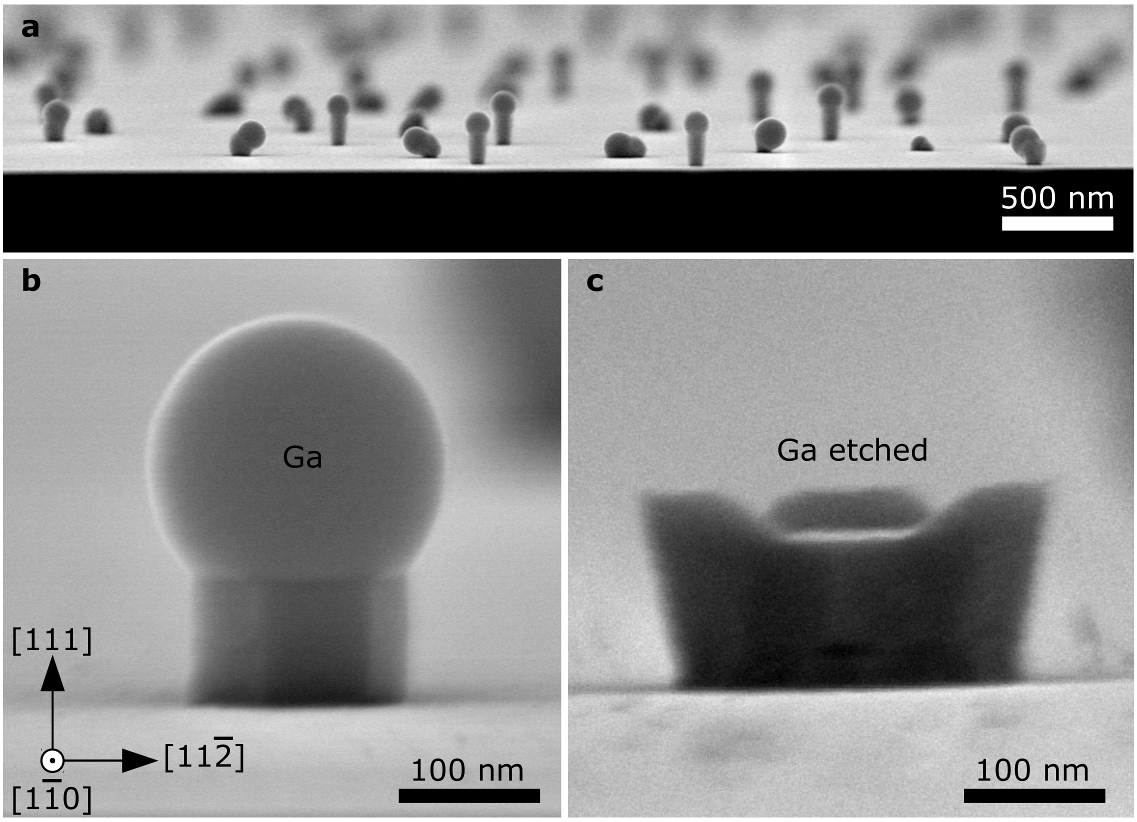

Figure 4.10.: **SEM micrographs of short self-assisted GaAs nanowires** in side-view showing (a) several vertical and kinked nanowires, as well as (b) single nanowire as grown, and (c) after selective Ga etching in HCl.

A series of samples of GaAs nanowires was grown on SiO_x/Si(111) under optimized growth conditions for reduced parasitic growth ($T = 580°\mathrm{C}$, $J_{Ga} = J_{As} = 0.6\ \mathrm{s}^{-1}\mathrm{nm}^{-2}$, see Sect. 3.2.1.) and for short growth times. On the employed substrates, larger Ga droplets (> 100 nm) formed than usual (< 50 nm), which made these samples ideal objects for the study of individual nanowires. Studies of these samples by Synchrotron XRD were performed by our collaborating group at Siegen University and led to single nanowire resolution and two research articles.[107,124]

The employed substrates, n-type, arsenic-doped 2″ Si(111) wafers with 0.002-0.01 Ωcm resistivity, corresponding to $n \sim 10^{18}\ \mathrm{cm}^{-3}$, from Silchem, showed larger Ga droplets and thicker nanowires. As a result, the nanowire growth rates were smaller. In addition, the Ga droplet sizes were inhomogeneously distributed on the substrates. We believe that some particular substrate quality has a strong effect the formation of native SiO_x. As possible candidates, surface roughness or doping level are suspected. Indeed, the thickness of native silicon oxide has been found to increase with the dopant concentration.[100]

SEM images of a sample grown for 5 min are presented in Figure 4.10. A side view (a) depicts GaAs nanowires grown vertically as well as some nanowires with kinks. All present structures are connected with a Ga droplet and thus appear to have formed by the VLS growth mode. For a few of the kinked nanowires, the Ga droplet has remained in contact with the substrate surface, which is reminiscent to the formation of traces found for Au-assisted VLS growth. However, the Ga droplets for other kinked nanowires are not in contact with the substrate surface. No droplet-free growth was found on the SiO_x.

A close-up of a single nanowire is shown in Figure 4.10b, where the spherical droplet shape is visible very well and three extended side facets can be seen. From the orientation of the substrate flat, the $\{1\bar{1}0\}$ orientation of the three facets was concluded. A similar nanowire is presented in (c) after the sample had been treated by HCl (32%, 30 min), a selective gallium etchant. The top Ga droplet has been removed by the procedure and the bare GaAs nanowire is visible. Prolongations of three second-next-neighbour facets have appeared and indicate that GaAs nucleation under the droplet has begun at the edge, i.e. at the so called triple-phase-line, TPL. These prolongations may have formed after the end of nanowire growth under reduced As conditions. The orientation of side facets and the site of beginning nucleation will be analysed in detail in Chapter 5.

These images show that initially all GaAs growth takes place in the VLS growth mode and there is no VS growth on the SiO_x mask. Nanowires grow either straight in the vertical [111] direction or have kinks. In the latter case, the Ga droplets do not necessarily maintain contact with the substrate, in contrast to the traces found for Au-assisted nanowire growth.

4.2.2. Nucleation Series

Nucleation experiments were also performed on the standard Si(111) substrates (n-type, phosphorous-doped 2″ Si(111) wafers from SiMat) covered with SiO_x, prepared identically to those presented in the last section. A series of samples was grown for different durations in order to study the morphology and structure during the different stages of nucleation. The growth conditions were as described above, viz. the growth temperature was 580 °C, the V/III atomic flux ratio was $J_{As}/J_{Ga} = 1$ and the individual fluxes were set to $J_{Ga} = J_{As} = 0.6\ \mathrm{s}^{-1}\mathrm{nm}^{-2}$, matching a planar growth rate of 0.028 nm/s (100 nm/h). In order not to consume any Ga droplets after the end of growth, the Ga and As shutters were closed synchronously for all samples but one.

Morphology and Crystal Structure

During GaAs growth, the crystal structure at the surface was monitored by RHEED, which indicated the epitaxial alignment of the growing GaAs to the Si substrate. After growth, the surface morphology was characterized by SEM and showed that vertical GaAs nanowires are present on all samples. Figure 4.11 presents the SEM images and the corresponding RHEED patterns of the samples after (a) 10 s, (b) 100 s, (c) 1000 s, and (d) 1800 s of self-assisted GaAs growth.

- After 10 s (4.11a), the total GaAs deposition is equivalent to a 2-D layer thickness of $z_d = 0.3$ nm. Several isolated manifestations of GaAs are visible. The spotty RHEED pattern indicates that these manifestations have a 3-D character. The transmission patterns of GaAs in the ZB crystal structure and its rotational twin are overlaid by remaining faint crystal truncation rods of the Si substrate.
- After 100 s (4.11b), $z_d = 2.8$ nm, larger GaAs structures are visible in the SEM micrographs. Some of them show a more distinctly vertical shape than others. These more vertical structures are identified as vertical nanowire nuclei, whereas the more horizontal structures are tentatively termed 'islands'. The majority of structures on the substrate are vertical nanowires. In RHEED, the transmission patterns of ZB GaAs and its twin are observed.
- After 1000 s (4.11c), $z_d = 28$ nm, the morphology of the nanowires as well as the islands is clearly visible. On average, the nanowires are around 250 nm long and have a diameter of 40 nm. Their top end is rounded, but does not show the bulging typical for Ga droplets, since, in this sample, the Ga droplets have been consumed after growth during a prolonged time (7 min) in As atmosphere at growth temperature, before the As shutter was closed and the substrate temperature was ramped down. The 3-D islands appear to grow along preferential inclined directions. The intensity of both ZB diffraction patterns has increased further. Additional reflections are faintly visible, whose origin could not be fully clarified.
- After 1800 s (4.11d), $z_d = 50$ nm, the nanowires have grown in length and exhibit Ga droplets, since for this sample the As supply was again stopped synchronously with the Ga supply. The islands have increased in size, some have coalesced with other islands and oblique nanowires. The obtained RHEED patterns had comparably low brightness, due to beam obstruction by a sample holder clamp, and indicate the ZB crystal structure with twins, as before.

Growth Directions

Further SEM micrographs of the sample with 1800 s growth time are presented in Figure 4.12. In side view (a), nanowires with top droplets can be seen, which have homogeneous lengths. In addition, some shorter nanowires without top droplet, but with sessile Ga droplets near their base are found. Almost all nanowires are oriented in the vertical [111] direction. Additional GaAs islands, sessile Ga droplets as well as uncovered parts of SiO_x/Si surface are visible. Most islands have grown along non-vertical $\langle 111 \rangle$ growth directions.

In the top view image (b), vertical [111]-oriented nanowires are completely hidden behind their top Ga droplets. For some oblique nanowires, oriented in non-vertical $\langle 111 \rangle$

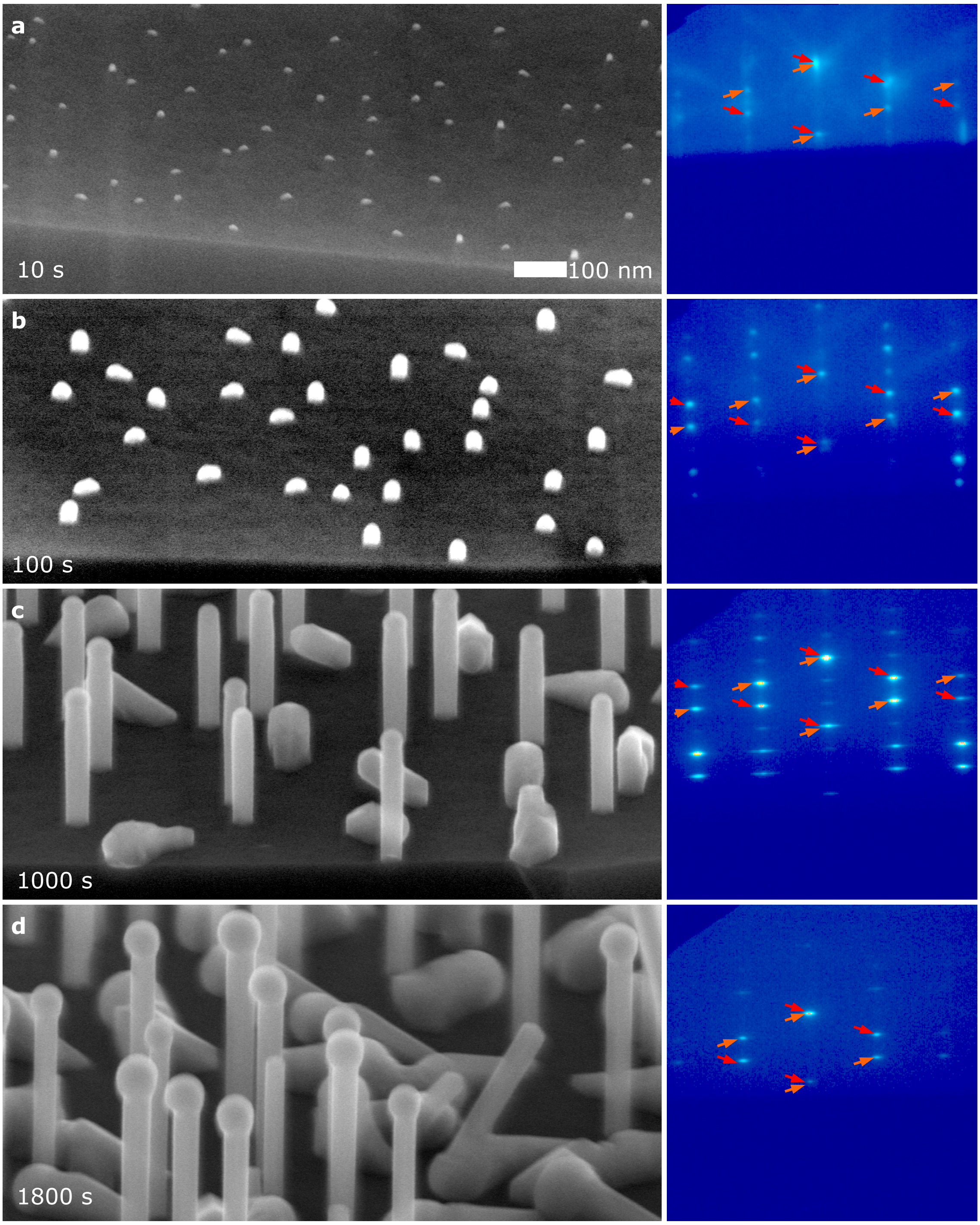

Figure 4.11.: **Self-assisted GaAs nucleation on Si/SiO$_x$.** Morphological (SEM, 45° incidence) and structural data (RHEED, $\langle 1\bar{1}0\rangle$ azimuth) after growth for (a) 10 s, (b) 100 s, (c) 1000 s, and (d) 1800 s. The reflections of ZB GaAs (↘), of its rotational twin (↗), and of unidentified origin (yellow triangles) are indicated.

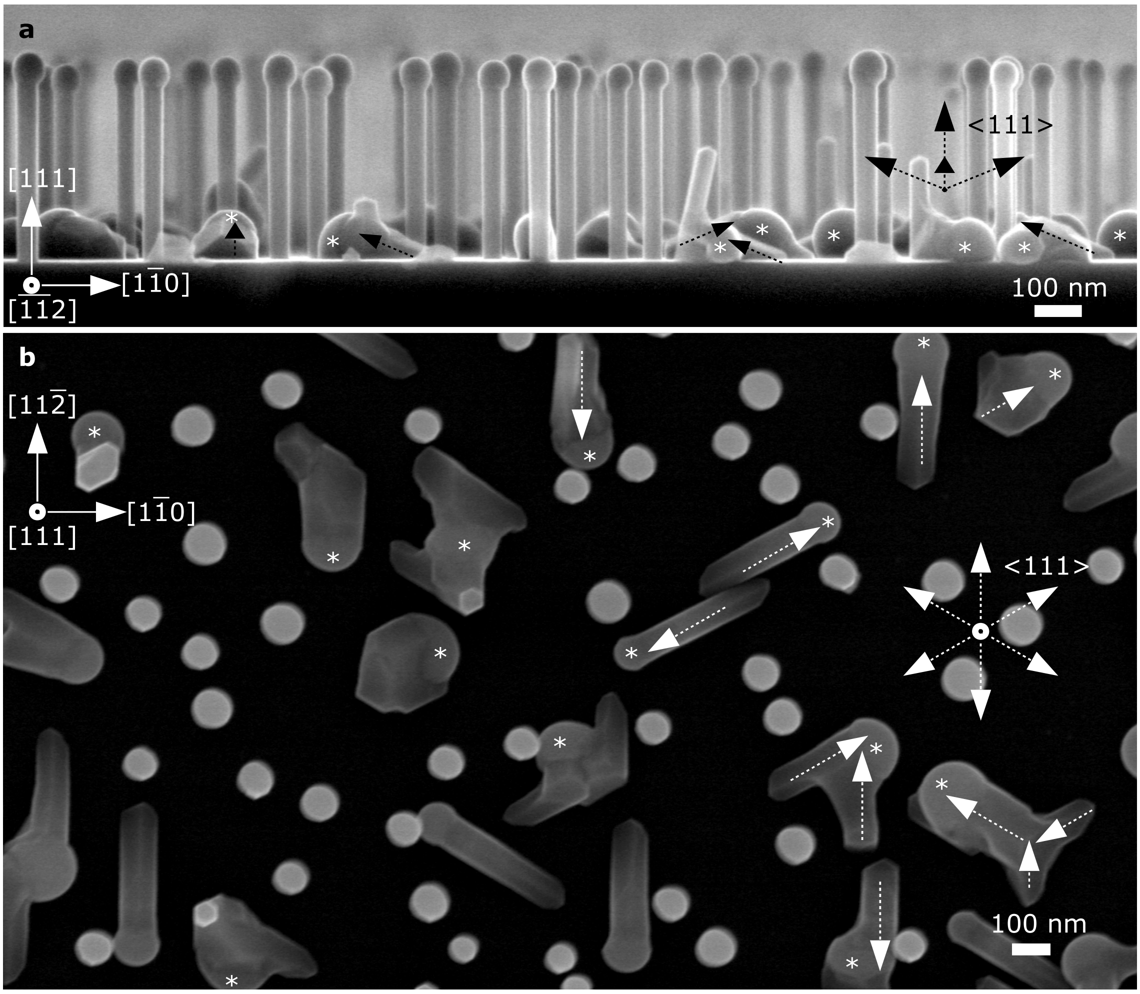

Figure 4.12.: **Morphology of Ga droplets and GaAs growth directions.** SEM micrographs of self-assisted GaAs nanowires after 1800 s of growth, in (a) top and (b) side view. Nanowires and other GaAs manifestations (faceted shapes) are all in contact with Ga droplets (round shapes). Ga droplets reside either at the nanowire tips or at the substrate surface (indicated by stars). Projections of $\langle 111 \rangle$ into the image planes are indicated (broken arrows) and correspond to the major growth axes of all GaAs structures on the surface.

directions, both the droplet and the nanowire itself can be seen. In this view it is also apparent, that islands and oblique nanowires are very similar. The major axes of all islands are also oriented along non-vertical $\langle 111 \rangle$ directions, and each island is connected to an associated Ga droplet. The more complex island shapes appear to originate simply from the coalescence of two or more oblique nanowires. As a result of such coalescence, the common Ga droplet has a larger diameter and may maintain or re-establish contact to the substrate surface, as indicated by the larger droplet diameters at the substrate than on the nanowire tips.

All manifestations of GaAs appear to originate from self-assisted VLS growth of GaAs nanowires. The only original distinction between the growth of vertical nanowires and that of islands appears to be the initial growth direction: the former grow along the vertical [111] and the latter in other $\langle 111 \rangle$ directions. For almost all structures, there is epitaxial alignment with the Si substrate through the thin oxide layer, most likely mediated by pinholes. The crystal structure of all GaAs structures as determined by RHEED is ZB with twin planes, in accordance with the earlier RHEED and TEM results (Sect. 3.2.1). This is in contrast to the nanowires grown with Au, which grew in the WZ structure.

SEM Analysis

A careful analysis of the nanowire morphology was made for all samples of the nucleation series and its results are presented in Figure 4.13. For the determination of the nanowire length l and diameter d, side view SEM micrographs were used. Measurements of 6-20 nanowires were averaged and the standard deviation was determined. Top view micrographs were analysed for the determination of the nanowire number density σ and the covered Si fraction b.

The results for the average nanowire lengths are presented in Figure 4.13a. There is an excellent linear fit, which indicates an axial growth rate of 0.22 ± 0.01 nm/s. This value is in strong excess of the planar growth rate equivalent to the supply flux of 0.028 nm/s. Substantial surface diffusion of Ga and also of As can thus be concluded, since the supply was stoichiometric $J_{Ga} = J_{As}$.

The average nanowire diameters d show a monotonically increasing trend, which indicates radial growth. Some inverse tapering was observed for the 1800 s sample: these nanowires had a roughly 10% larger diameter at the top just below the Ga droplet than at the bottom close to the substrate. The dependence of the diameters d on growth time $t \geq 100$ s can be described by a linear fit, from which a radial growth rate of (9 ± 3) nm/1000 s results. There is a superlinear behaviour at the start. Possibly, radial growth can also explain the observed inverse tapering, under the provision that the nanowires stand close enough for substantial shadowing effects to occur. This would result in more material arriving at the nanowire top than at its bottom end. Another possibility is that the Ga droplet has increased in size during growth, since the diameter of the nanowires follows that of the droplets. In contrast to the Au droplets, whose size increase during growth is limited by the maximum solubility of Ga in Au, the Ga droplet size is not limited in this way. Colombo et al. also found a constant rate of diameter increase for significantly longer growth times.[97]

The nanowire area density σ was determined by analysis of top view SEM micrographs, such as Fig. 4.12b, from which nanowires and traces could be distinguished. Within the first 100 s, the number of nanowires increases and then stays basically constant. The error values were estimated by analysing images recorded at different posi-

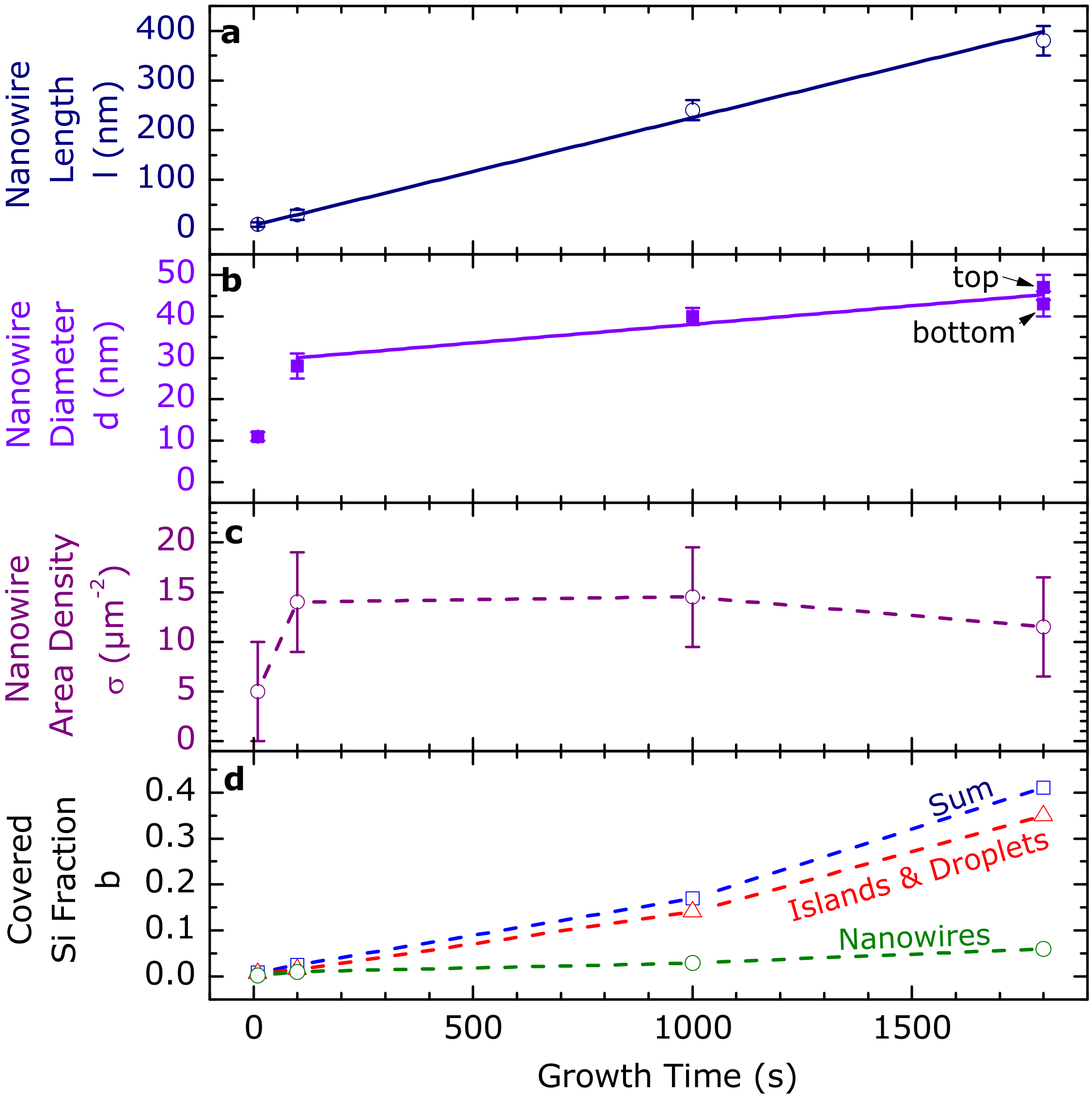

Figure 4.13.: **Morphology Analysis of Nucleation Series Samples.** Measurements of (a) length l, (b) diameter d, (c) density of self-assisted GaAs nanowires grown for 10, 100, 1000, and 1800 s on SiO_x/Si(111), as well as (d) covered Si fraction b. While solid lines represent fits to the data, broken lines serve as guides to the eye. Error bars represent the standard deviation in (a,b) and substrate inhomogeneity in (c).

tions of one sample. Differences in the nanowire densities are expected to be caused by inhomogeneity of the SiO_x quality (composition and thickness).

The total covered SiO_x/Si surface fraction b increases with growth time. After 1800 s, b has reached 41%, mainly due to the parasitic traces, while at the same time, nanowires cover only 5% of the surface. Furthermore, there is no dependence of σ on b. This is in strong contrast to the Au-assisted case, for which nanowires form only after the Si is completely covered.

Interface Energies

It has become clear that the self-assisted growth of GaAs nanowires on $SiO_x/Si(111)$ does not necessitate an intermediate GaAs layer. Instead, vertical nanowires grow isolated on the SiO_x-covered Si substrate. Nevertheless, an epitaxial relationship between GaAs nanowires and Si substrate has invariably been found by RHEED. Fontcuberta et al. presented a HRTEM image of a 20 nm diameter pinhole in their 5 nm-thick sputtered SiO_x that provided the epitaxial contact. They argued that the pinholes were opened by the reaction of SiO_x with Ga and As. Our data demonstrates that the native SiO_x can even be removed completely by the reaction with Ga (see Fig. 3.20).

Following the considerations of Section 4.1.2, the Ga droplets are expected to have a minimal interface energy when on GaAs, while their interface energy on Si is expected to be larger. The equivalent case for SiO_x is calculated in the following.

$$\begin{aligned} \gamma_{LS}^{Ga/GaAs} &< \gamma_{LS}^{Ga/Si} \\ \gamma_{LS}^{Ga/GaAs} &< \gamma_{LS}^{Ga/SiO_2} \end{aligned} \tag{4.3}$$

As before, the liquid-solid interface energies γ_{LS} are estimated using Young's equation (4.2) and literature data: $\gamma_{LV}^{Ga} = 0.67$ J/m^2,[125] $\gamma_{SV}^{GaAs} = 0.69$ J/m^2,[123] $\gamma_{SV}^{Si} = 1.23$ J/m^2,[119] $\gamma_{SV}^{SiO_2} = 0.33$ J/m^2,[126] $\phi_{Ga,GaAs} = 44°$,[127] $\phi_{Ga,Si} = 39°$,[128] and $\phi_{Ga,SiO_2} = 119°$.[126] Resulting interface energies of $\gamma_{LS}^{Ga/GaAs} = 0.21$ J/m^2, $\gamma_{LS}^{Ga/Si} = 0.71$ J/m^2, and $\gamma_{LS}^{Ga/SiO_2} = 0.65$ J/m^2 are thereby calculated, which must be considered as rough estimates, since (i) any orientation dependence was neglected and (ii) the unclear quality of the native SiO_x could be a source of significant error. Nevertheless, the results fulfil the expected relations. Therefore, the observed behaviour of direct vertical nanowire growth can be explained by a better wetting of Ga droplets on GaAs than on Si. These results are also in agreement with the observation of a preferred adhesion of Ga droplets to GaAs structures, as apparent from Fig. 4.12.

In terms of liquid-solid interface energies, the VLS growth of GaAs nanowires on SiO_x/Si using Ga droplets represents the opposite case to the growth of GaAs traces on Si(111) using Au droplets.

The question why some nanowires grow in oblique directions cannot be answered by a preferred wetting of Ga droplets on the SiO_x/Si substrate. Instead, we speculate that during the growth of oblique nanowires, the Ga droplet grows in lateral size faster than does the GaAs nanowire below it, which leads to a breaking of vertical symmetry and the creation of an oblique Ga/GaAs interface. Schwarz and Tersoff have pointed out that nanowires can kink when their growth is perturbed.[110]

4.2.3. Summary of Self-assisted Nucleation

The central result of this nucleation study is that the self-assisted VLS mechanism leads to direct growth of GaAs nanowires on SiO_x/Si substrates. The nucleation is direct in the sense that nanowire growth begins without any prior lateral droplet movement, as was the case for the Au-assisted nucleation on Si(111).

Virtually all VLS-grown GaAs structures were found to be epitaxially aligned to the Si substrate. While most nanowires grow in the vertical [111] direction, a minor fraction is aligned in oblique $\langle 111 \rangle$ directions and eventually forms islands with complex shapes upon coalescence.

For all samples, each individual GaAs structure is connected to a Ga droplet, which indicates that in all cases nucleation happened by the VLS mechanism. No liquid-free nucleation by the VS mode was observed directly on the SiO_x mask, which indicates excellent selectivity.

By an estimation of the liquid-solid interface energies of Ga droplets on GaAs, Si and SiO_x, the former was found to be minimal. This explains why the Ga droplets are not mobile and nanowire growth directly starts in the vertical direction.

4.3. Comparison of Au- and Self-assisted Nucleation

The nucleation studies using Au and Ga droplets show that the self-assisted mechanism leads to the direct formation of vertical nanowires on SiO_x/Si(111). In contrast, the Au-assisted nucleation on Si(111) is indirect, viz. vertical GaAs nanowires form only after other GaAs structures have coalesced to a planar layer on which the nanowires grow. This behaviour is a result of the interface energies between the involved substances. Au droplets wet Si better than GaAs, while Ga droplets wet GaAs better than Si (or SiO_x).

The different relations between the liquid-solid interface energies explain why on Si, self-assisted nucleation is more straight-forward than the one under Au-assistance. Au-assisted nanowires on Si are necessarily connected with other basal GaAs and position control is lost. In this view, the self-assisted mechanism produces the more promising results. However, the effect of the SiO_x quality on the Ga droplet diameters and densities has not yet been fully understood and needs further study. With such knowledge, it might be possible to tailor the SiO_x to achieve a desired number density and diameter of GaAs nanowires in a self-organized fashion. Furthermore, exact nanowire position control can be achieved when the SiO_x is patterned. First results for patterned growth of GaAs nanowires by the self-assisted mechanism have recently been presented, but full mastery must still be accomplished.[129,63]

5. Side Facet Formation During VLS Growth

The crystal structure is of paramount importance for semiconductor materials and their device applications. Virtually all semiconductor properties depend on the crystal structure, foremost the electronic band structure, but also mechanical and optical properties. Perhaps surprisingly, a semiconductor in nanowire shape does not necessarily adopt the same crystal structure as in the bulk, since energy contributions from the surfaces are no longer negligible. GaAs nanowires in the WZ phase provide an excellent example, since in the bulk form GaAs always adopts the ZB phase. When the nanowire crystal structures can be tailored by growth conditions, an additional degree of freedom for the material engineer is gained. To this end, a thorough understanding of the way the crystal structures form is necessary.

For nanowires with their large surface-to-volume ratio, the surface can become the most important part of the device. Surface effects need to be controlled and can even be employed for sensing applications.[130] Central to the semiconductor surface is the formation of electronic surface states, which can have several effects: an increased recombination of charge carriers, Fermi level pinning, internal electric fields, and the formation of accumulation or depletion layers.[131] Since the quality and quantity of surface states depends on the surface orientation, it is imperative to understand which nanowire side facets are present. Other important surface effects are the increase in ionisation energy of donors and acceptors caused by dielectric confinement, which leads to a reduced doping efficiency,[132,133] as well as the selection rules in Raman spectroscopy, which also depend on the surface orientation.[134]

Furthermore, it has been shown by Frank Glas et al., who adapted classical nucleation theory to nanowire growth, that the side facets can directly influence the nanowire crystal structure.[67] Furthermore, Johansson et al. demonstrated that Au-assisted III-V nanowires with ZB crystal structure are prone to a special kind of nano-faceting, which leads to the introduction of planar stacking faults.[135] Nano-faceting means the decomposition of an atomic plane with high surface energy into many smaller (nanometre-sized) facets of other orientations. By making stacking fault formation necessary, the side facets can have a strong influence on the crystal structure and crystalline quality of the nanowires. Therefore this chapter presents a study of the side facets of self- and Au-assisted GaAs nanowires by experimental as well as theoretical means. The theoretical results are the outcome of a fruitful cooperation with L. F. Feiner from TU Eindhoven.

At the beginning of this chapter, the experimental data by ourselves as well as from the literature is surveyed (Sect. 5.1). The surprising result is that the two droplet materials lead to mutually different side facet orientations. The observed side facets are classified according to atomic stacking sequence in order to point out common characteristics. The adaptation of classical nucleation theory to nanowire growth is reviewed (Sect. 5.2), which describes the dependence of the nanowire crystal structure on the surface energies of the possible side facets and serves as a basis for the following analysis. In the following, the required parameters are critically discussed (Sect. 5.3). Section 5.4 presents first a full calculation of the relative probabilities of critical nuclei with several different side facets using a specific set of input parameters. The result of Glas et al. that ZB (WZ) nuclei are favoured at low (high) supersaturation is reproduced. In the following, each crystal structure is considered separately and the dependence on two uncertain input parameters is studied. Facet stability for WZ, ZB and each droplet material are discussed in detail.

5.1. Experimental Observations of Side Facets

The nanowire side facet orientation can be fully determined only by carefully analysing HR-TEM images of one sample under different angles or, alternatively, by Synchrotron-XRD reciprocal space maps of nanowires. However, basic information about the projection of the facet normal to the substrate can be obtained more simply by SEM, provided the epitaxial relation to the substrate and the crystal structure of the nanowires are known. During MBE growth, both informations can readily be obtained by RHEED. There is abundant data showing that ZB as well as WZ nanowires can be grown by both droplet materials under adjusted growth conditions.[136,66]

5.1.1. Self-assisted GaAs Nanowires

Our MBE-grown self-assisted GaAs nanowires have a hexagonal cross section and $\{1\bar{1}0\}$ side facets, as was repeatedly observed by SEM, c.f. Fig. 5.1a,b. The orientations were determined in relation to the substrate cleavage edge after epitaxial alignment of grown GaAs nanowire and Si substrate had been confirmed by RHEED. Similarly prepared very thick wires (average diameter 600 nm) were analysed by Biermanns et al. using synchrotron XRD and clearly show crystal truncation rods arising from hexagonal $\{1\bar{1}0\}$ side facets.[137]

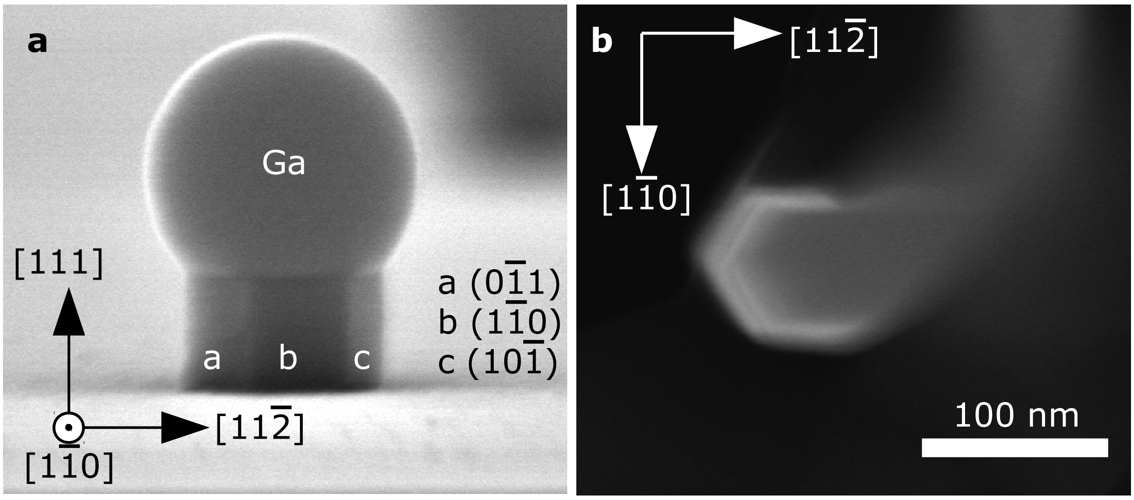

Figure 5.1.: **SEM micrographs of self-assisted GaAs nanowires for the identification of side facets.** Nanowires with different lengths are shown in (a) and (b) in side and top view, respectively. In (b), the focus is set to the base of the nanowire such that the hexagonal symmetry and four $\{1\bar{1}0\}$ oriented side facets can be seen.

A number of literature reports exist, which reveal side facets of self-assisted GaAs nanowires. All show the same result: Fontcuberta et al. found $\{1\bar{1}0\}$ sidewalls by HR-TEM and SEM analysis of the GaAs nanowires grown by MBE in their group.[138,139] Already in early 2007, the Fukui group reported $\{1\bar{1}0\}$ vertical sidewall facets for their GaAs nanowires fabricated using Au-free selective area MOVPE.[51] Cirlin et al. recently studied the facet orientation of MBE-grown self-assisted GaAs nanowires by SEM and reported $\{11\bar{2}\}$ sidewalls, but apparently they used the wrong cleavage plane orientation as reference.[140] When corrected (Si(111) readily cleaves along oblique {111} planes), their result turns into $\{1\bar{1}0\}$ sidewalls. It may be noted that all available sidewall facet data are for ZB nanowires, which we take as an indication for the comparable scarcity of WZ nanowires by the self-assisted VLS mechanism. Apparently, facets of self-assisted WZ nanowires have not yet been reported.

5.1.2. Au-assisted GaAs Nanowires

Our own Au-assisted nanowires on Si have very thin diameters ($\sim$10 nm) such that the facet shape is below SEM resolution and the resulting fragility makes preparation of nanowire cross sections for HR-TEM very involved. Instead we rely on the wealth of literature data about the side facets of Au-assisted GaAs nanowires.

A recent review of the MOVPE-grown Au-assisted nanowire activities in the Samuelson group by Dick et al. includes an overview of their side facet studies by SEM and HR-TEM and reports $\{10\bar{1}0\}$ facets for WZ segments, and $\{11\bar{2}\}$ extended facets (macro-facets) for twin-free ZB segments, as well as $\{111\}$A &$\{\bar{1}\bar{1}\bar{1}\}$B nano-facets for highly twinned ZB nanowires.[66] The existence of segments with $\{111\}$A and $\{\bar{1}\bar{1}\bar{1}\}$B nano-facets geometrically necessitates twin boundaries at their interface.[135,141] Wacaser et al. studied MOVPE growth of Au-assisted GaAs nanowires depending on the substrate orientation and found heavily twinned nanowires with $\{111\}$A &$\{\bar{1}\bar{1}\bar{1}\}$B nano-facets on GaAs(111)B, but twin-free $\{11\bar{2}\}$ facets on GaAs(111)A.[72] Mariager et al. analysed MBE-grown Au-assisted GaAs nanowires with both ZB and WZ segments by XRD and identified ZB segments with $\{111\}$A &$\{\bar{1}\bar{1}\bar{1}\}$B nano-facets, as well as $\{10\bar{1}0\}$ facets for WZ segments.[142,143] A detailed HR-TEM study of Au-assisted nanowires with axial GaAs-GaP heterostructures grown by MOVPE was performed by Verheijen et al. and showed that the GaAs segments have extended $\{11\bar{2}\}$ facets or composed $\{111\}$ and $\{001\}$ nano-facets.[144]

An additional aspect is that of lateral overgrowth. In general, the facets developed by VLS axial growth and VS radial overgrowth can be different, as has been demonstrated by the following authors. Using SEM, Plante et al. reported $\{10\bar{1}0\}$ facets for MBE-grown Au-assisted WZ nanowires after short growth times, but noted a change to $\{11\bar{2}0\}$ facets for longer growth times, after the nanowire had grown in the radial direction substantially.[95] Sköld et al. analysed MOVPE-grown GaAs nanowires surrounded by GaAs shells by SEM and HR-STEM and found that the GaAs cores show $\{11\bar{2}\}$ facets but $\{1\bar{1}0\}$ facets form when GaAs shells are grown at higher temperatures.[145,146] For GaAs nanowires growth using Au droplets with a bimodal diameter distribution as well as for growth on GaAs(311), Shtrikman et al. report pure ZB crystal structure, unusual $\langle 100\rangle$ and $\langle 1\bar{1}0\rangle$ growth directions and $\{1\bar{1}0\}$ and $\{001\}$ side facets. Strong tapering towards the nanowire tip indicates significant lateral growth.[73]

When lateral overgrowth is neglected, the nanowires produced by the Au-assisted VLS mechanism generally develop either extended ZB $\{11\bar{2}\}$ facets, or nano-faceted ZB $\{111\}$A &$\{\bar{1}\bar{1}\bar{1}\}$B segments separated by twin boundaries, or extended WZ $\{10\bar{1}0\}$ facets. ZB $\{1\bar{1}0\}$ facets are reported for Au-assisted nanowires only after lateral overgrowth.

5.1.3. Classification of Observed Side Facets

Here, a classification scheme of III-V nanowire side facets is presented. The atomic planes perpendicular to the growth directions, i.e. [111] and [0001], have hexagonal symmetry. Therefore, a hexagonal shape of the nanowire cross section generally leads to high coordination and a low interface energy. Two shapes are most probable: *(110)-type* facets delimit nanowire cross sections with sides parallel to the {110} cleavage planes of III-V compounds. In contrast, *(112)-type* facets delimit cross sections that are rotated by 30°.

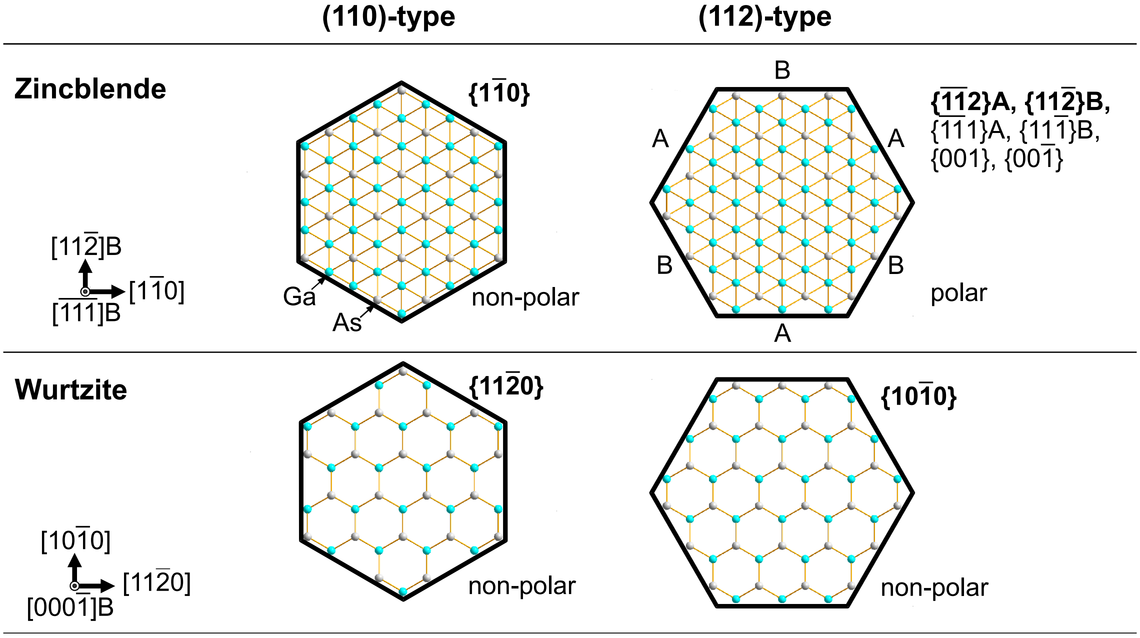

Figure 5.2.: **Classification of Observed Nanowire Side Facets.** Cross sections through nanowires in top view, revealing the orientations of observed side facets in relation to the bulk-truncated crystal structure. Extended facets parallel to the $[\bar{1}\bar{1}\bar{1}]$B growth axis are indicated by bold type. For zincblende nanowires, decomposition of overall $\{11\bar{2}\}$ oriented sidewalls into various tilted nanofacets regularly occurs.

Figure 5.2 depicts all observed nanowire facet orientations, grouped according to crystal structure and facet type, including the bulk truncated atomic structure. It is very noteworthy that all sidewall facets reported for the Au-assisted nanowires fall into the (112)-type. All ZB facets of this type are polar, i.e. planes parallel to the surface consist of either Ga or As. This is customarily indicated by the suffixes A (Ga) and B (As).[*] Around the perimeter of a nanowire segment with hexagonal cross section and polar facets, A and B surfaces alternate. In contrast, the generally reported $\{1\bar{1}0\}$ ZB facets for the self-assisted nanowires are non-polar. For WZ facets, the conceivable facet orientations, i.e. $\{11\bar{2}0\}$ (a-plane) as well as $\{10\bar{1}0\}$ (m-plane), are likewise non-polar and do not tend to nano-faceting. GaAs nanowires with the WZ structure were repeatedly observed

---

[*] A and B suffixes are not used for $\{001\}$ and $\{00\bar{1}\}$ surfaces, which constitute a special case. Both have identical surface energies, since reconstruction can transform one into the other. Nevertheless, their orientations are different. With respect to the nanowire growth axis, $\{001\}$ facets are tilted inwards, while $\{00\bar{1}\}$ facets are titled outwards.

to have $\{10\bar{1}0\}$ facets when the Au-assisted VLS growth had been used (without lateral overgrowth), while no reports are currently known for self-assisted nanowire growth.

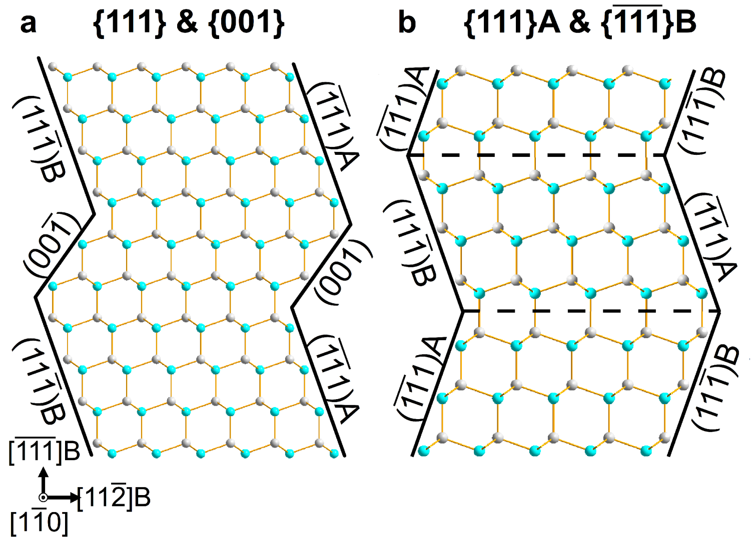

Figure 5.3.: **Zincblende (112)-type composed facets.** Bulk-truncated atomic structure of nanowires in side view. **a** Composition from segments with $\{111\}$A, $\{\bar{1}\bar{1}\bar{1}\}$B, $\{001\}$ and $\{00\bar{1}\}$ facets. **b** Alternative composition from segments with only $\{111\}$A and $\{\bar{1}\bar{1}\bar{1}\}$B facets, which requires repeated formation of twin planes (dashed lines).

Considering the atomic structure of the nanowires, four of the observed facets lead to extended vertical side facets, namely the ZB $\{1\bar{1}0\}$ and $\{11\bar{2}\}$ as well as both WZ orientations. Of these four, the ZB $\{11\bar{2}\}$ surface has the highest surface energy ($1.04\,\mathrm{J/m^2}$)[147], while those of the other three vertical facets are approximately $0.3\,\mathrm{J/m^2}$ smaller (see Table 5.1). As a result, a decomposition of the $\{11\bar{2}\}$ facet has to be considered.[148] Figure 5.3 shows the bulk-truncated atomic structure of two composed (112)-type facets that were reported for Au-assisted GaAs nanowires.

When nanowire segments with {111} and {100} facets are stacked (Fig. 5.3a), the lateral surface is composed of nano-facets. On average the ratio of both segment lengths must equal 2 : 1, in order to maintain the overall $\{11\bar{2}\}$ sidewall orientation. A regular $\{11\bar{2}\}$ extended facet is composed if the sequence is exactly 2 monolayers of GaAs with {111} followed by exactly 1 monolayer with {100} facets.[149]

In contrast, a nano-faceted $\{111\}$A & $\{\bar{1}\bar{1}\bar{1}\}$B surface arises (Fig. 5.3b), when on top of an outwards tilted $\{\bar{1}\bar{1}\bar{1}\}$B an inwards tilted $\{111\}$A facet is formed instead of a $\{001\}$ facet. Then, the nanowire obtains the shape of stacked octahedra.[135] This stacking sequence is necessarily associated with the formation of a twin plane at the boundary of the $\{111\}$A & $\{\bar{1}\bar{1}\bar{1}\}$B segments. It has been demonstrated that although the repeated stacking fault formation is energetically costly, the energy gained at the surface can (kinetically) stabilize this nanowire shape.[135,74] When the facet orientation is exchanged after each monolayer, the WZ crystal structure results.

Discussion

The observed sidewall facets depend on the droplet material used for VLS growth. Self-assisted nanowires readily grow in the ZB structure (but often contain twins). Their side facets are non-polar $\{1\bar{1}0\}$ surfaces, such that the nanowire shape is that of a prism with the cross section of a regular hexagon. The facet orientation of self-assisted nanowires with WZ crystal structure has not been reported.

In contrast, Au-assisted nanowires often adopt the WZ crystal structure and then show vertical $\{10\bar{1}0\}$ side facets. When Au-assisted nanowires grow in the ZB crystal structure, $\{11\bar{2}\}$ as well as nano-faceted $\{111\}\&\{100\}$, and $\{111\}$A & $\{\bar{1}\bar{1}\bar{1}\}$B side facets were observed, which are all polar. The $\{111\}$A & $\{\bar{1}\bar{1}\bar{1}\}$B configuration necessitates regular introduction of twin plane stacking faults. All of the facets for Au-assisted nanowires lead to hexagonal nanowire cross sections, with the sides rotated by 30° with respect to the $\{1\bar{1}0\}$ planes.

5.2. Model of Side Facet Stability

Why do self-assisted and Au-assisted ZB nanowires develop different sidewall facets? Which effect do the Ga and the Au droplets have? A theoretical understanding of the effects of the droplet material is sought. We use the monolayer nucleation model for the VLS mechanism originated by Glas et al.[67]

5.2.1. Review of VLS Nucleation Models

The Glas-model assumes that the atomic arrangement of a newly formed monolayer under the droplet is guided not by the minimum energy of the full layer, but instead by the minimum energy of a nucleus with critical size.[67] Once a critical nucleus has formed, it is assumed to spread over the whole nanowire cross section. The Glas model represents 2-D nucleation theory under chemical potential control[150] applied to nanowires. This approach was used to explain why III-V nanowires often adopt the WZ crystal structure.[67] A comparison of the stability of WZ and ZB nuclei, which form at the triple phase line with different side facets, led to the prediction that nanowires with WZ phase should be expected for high droplet supersaturation, which was verified for Au-assisted nanowires. In that work, only three (112)-type facets were compared. Dubrovskii, Glas et al. built on this model in order to predict a crystal structure change from ZB to WZ with increasing supersaturation $\Delta\mu$.[151]

Algra et al. expanded the model further and calculated the period of regular twinning observed in Au-assisted, $\{111\}$A & $\{\bar{1}\bar{1}\bar{1}\}$B nano-faceted InP nanowires with remarkable accuracy.[74] Joyce et al. for the first time considered all possible side facets and used their model to predict changes of the side facets with the droplet-nanowire contact angle β for Au-assisted InAs nanowires, but predictions were made only for facets within one type of facet.[152] Cirlin et al. already studied the difference between the Au and Ga droplets, but they did not predict sidewall facets.[140] Their result is that nucleation can happen at the triple phase line for Au-assisted nanowires, which gives rise to WZ under large $\Delta\mu$, but nucleation always happens at the centre of the nanowires for self-assisted growth, which gives always ZB. This result appears to be somewhat too rigid, particularly in the light of accounts of self-assisted WZ nanowires.[136] Krogstrup et al. recently added the nucleus position in a more natural way to the probability calculation of ZB and WZ and could thereby explain the experimentally observed shift from WZ to ZB with increasing chemical potential for self-assisted GaAs nanowires.[153]

A calculation of facet probabilities for Au- and self-assisted nanowires had not previously been done, and will be presented here. First, classical nucleation theory adapted to nanowires is reviewed, second, the crucial input parameters are presented, and third, the model predictions are discussed.

5.2.2. Classical Nucleation Theory Adopted to VLS Nanowire Growth

In MBE or MOVPE, the thermodynamically correct energy to minimize is the Gibbs free energy G, since temperature T, and pressure p are controlled (fixed), while entropy and volume are exchanged with the environment.[22] The VLS nucleation model, pioneered by Glas et al., considers a nucleus forming a new GaAs monolayer on the top of the nanowire just below the liquid droplet, as illustrated in Fig. 5.4.

The change in Gibbs free energy ΔG caused by the creation of the nucleus has three contributions: First, the process is driven by the energy yielded in the reaction of Ga and As in the liquid droplet to GaAs in the solid nucleus, which is described by the difference $\Delta\mu$ in the chemical potentials of supersaturated droplet and solid nucleus. Second, new lateral sidewall facets are formed that cost an effective interface energy Γ. Third, a stacking fault energy γ_F must be paid if the stacking sequence is WZ (ABAB) instead of ZB (ABCABC), since WZ GaAs is only metastable (see Sec. 2.3). These contributions make up the three terms of ΔG:

$$\Delta G = -Ah\Delta\mu + Ph\Gamma + A\gamma_{SN}, \tag{5.1}$$

where A is the nucleus base area, h is the nucleus height, P the nucleus perimeter, and γ_{SN} is the solid nanowire-nucleus interface energy, which equals γ_F for WZ and vanishes for ZB stacking. The effective lateral interface energy Γ depends on the position of the nucleus and on its sidewall facets.

Regarding the position of the nucleus with respect to the droplet there are two possibilities. Nuclei forming in the centre of the nanowire are completely surrounded by the liquid droplet and thus the lateral liquid-solid interface energy γ^0_{LS} is the only contribution to the effective interface energy

$$\Gamma^C = \gamma^0_{LS}, \tag{5.2}$$

where the index 0 indicates that identical solid-liquid facets are considered to form under the droplet irrespective of the solid-vapour side facet orientation (Fig. 5.4a).

In contrast, nuclei can form in direct contact with a side facet, i.e. at the triple phase line (TPL), where vapour, liquid and solid meet. Figure 5.4 schematically illustrates the geometry of a nucleus a the TPL. For these nuclei, there is an additional contribution $\Delta\Gamma_i$, which depends on the orientation of the side facet (indexed by i). It arises from the exchange of solid-liquid with solid-vapour interface around a portion x of the nucleus perimeter P. An expression for Γ_i^{TPL} can be derived considering that the work associated with the upward-shift of the triple phase line equals $W = \gamma_{SV} - \gamma_{LS} - \gamma_{LV}\cos\delta$,[†] where δ is the angle between facet and droplet, and $\cos\delta = \cos(\beta - \theta - \pi/2) = \sin(\beta - \theta)$.[74] In

---

[†] In the static case $W = 0$, and this turns into the derivation of Young's angle ϕ.

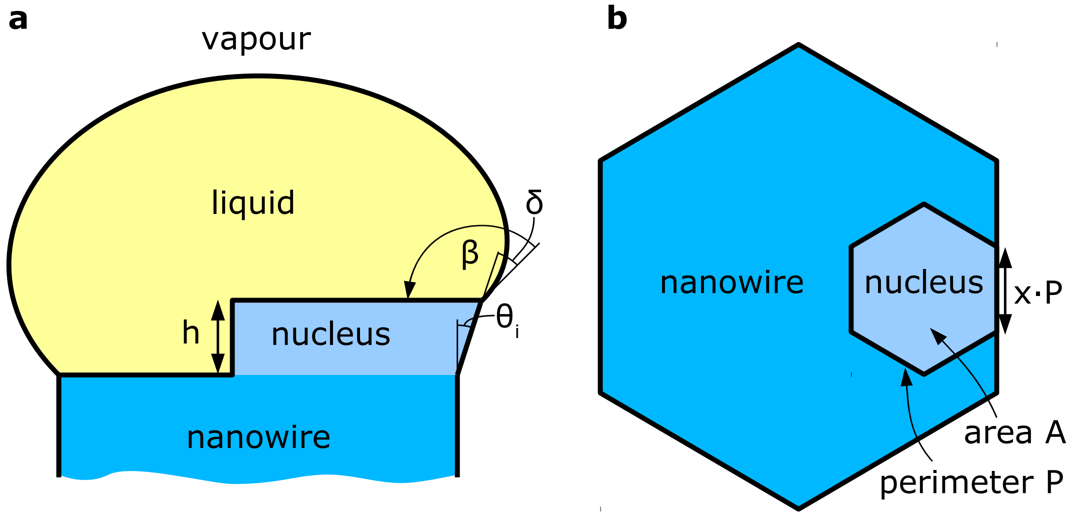

Figure 5.4.: **Geometry of VLS nucleation at the triple phase line.** Schematic illustration showing a hexagonal nucleus of height h as considered in the model (a) from the side, (b) from the top. The nanowire-liquid contact angle β, the facet tilt angle θ_i and the angle δ between facet and droplet are labelled as well as the perimeter fraction in contact with the triple phase line x.

the present case, we arrive at

$$\Gamma_i^{TPL} = \gamma_{LS}^0 + x\left(\frac{\gamma_{SV_i} - \gamma_{LV}\sin(\beta-\theta_i)}{\cos\theta_i} - \gamma_{LS}^0\right). \tag{5.3}$$

Here, the index i indicates parameters which depend on the side facet orientation. In particular θ_i denotes the tilt angle of the facet at the triple phase line, and β is the contact angle of the droplet with the top facet of the nanowire. Since the surface force balance for a droplet on a nanowire is different from the situation on a flat surface, β is generally different from Young's angle ϕ, i.e. the contact angle of the unconstrained droplet. Nucleation at the TPL generally dominates provided $\Gamma_i^{TPL} < \Gamma^C$, which means that energy is gained by the upwards-shift of the TPL.

5.2.3. Side Facet Probability

In order to single out those terms which depend on the orientation of the side facet at the TPL, the above formula is rewritten as

$$\begin{aligned}\Gamma_i^{TPL} &= (1-x)\gamma_{LS}^0 + x\left(\frac{\gamma_{SV_i}}{\cos\theta_i} + \gamma_{LV}\cos\beta\tan\theta_i - \gamma_{LV}\sin\beta\right)\\ &= (1-x)\gamma_{LS}^0 + x\left(\delta\Gamma_i - \gamma_{LV}\sin\beta\right),\end{aligned} \tag{5.4}$$

and the facet-depending terms are contained in

$$\delta\Gamma_i = \frac{\gamma_{SV_i}}{\cos\theta_i} + \gamma_{LV}\cos\beta\tan\theta_i. \tag{5.5}$$

Generally, the lower the lateral facet surface energy $\delta\Gamma_i$ of a nucleus, the more likely is its formation. Remarkably, γ_{LS}^0 does not affect $\delta\Gamma_i$ of (nuclei with) different side facets. However, since γ_{LV} and β depend on the droplet material, different facets can be expected for Ga and Au droplets.

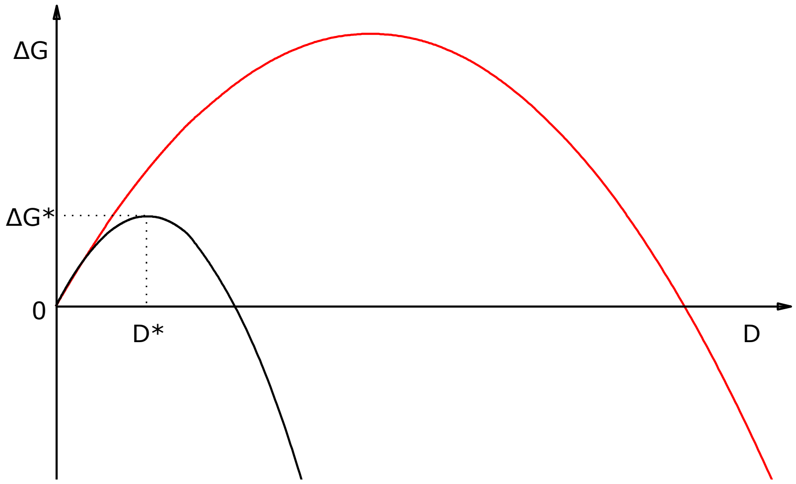

Figure 5.5.: **Gibbs free energy of nuclei versus radius.** Schematic plots of the formation energy ΔG of two nuclei with different side facets are presented. The energy barrier for formation of one nucleus is significantly lower. At its maximum, both the critical nucleus size r^* and the critical Gibbs free energy ΔG^* can be extracted.

When Γ_i is known for a nucleus with side facet i, $\Delta G_i(r)$ can be determined using (5.1) for a range of nucleus radii r, as illustrated in Fig. 5.5. Then, the critical Gibbs energy ΔG_i^* can be determined, which represents the energy barrier for the formation of this nucleus,

$$\Delta G_i^* = \Delta G_i|_{\frac{d\Delta G_i}{dr}=0}. \tag{5.6}$$

For the actual calculation of ΔG_i^*, this shape must be specified, and it should comply with the hexagonal crystal symmetry. Here we consider nuclei shaped as regular hexagons, which leads to $A = 3\sqrt{3}/2\, r^2$, $P = 6\, r$, $x = 1/6$ and thus

$$\Delta G_i^* = 3\sqrt{3}\frac{h\Gamma_i^2}{\Delta\mu - \gamma_{SN}/h}. \tag{5.7}$$

The probability of nucleus formation depends strongly on ΔG^*. In order to compare nuclei with different facets (indexed by i), Γ_i and ΔG_i^* are calculated using the surface energy $\gamma_{SV,i}$ and tilt angle θ_i of the particular facet. The normalized probability P_i of facet i is given by[135,152]

$$P_i = \exp\left(-\frac{\Delta G_i^*}{kT}\right) / \sum_j \exp\left(-\frac{\Delta G_j^*}{kT}\right). \tag{5.8}$$

In this way, the formation probability P_i of nuclei with each sidewall facet i and each crystal structure can be calculated. When comparing nuclei with identical crystal structure but different side facets, a high nucleus formation probability P_i is thus directly related to a low ΔG_i and by virtue of (5.7) and (5.3) also to a low Γ_i and $\delta\Gamma_i$.

5.3. Physical Parameters

For a quantitative analysis, the values of the involved physical parameters need to be known. For the complicated VLS system at hand, this is a formidable task. Here, we present the result of a thorough literature analysis of measurements and, where available, ab-initio calculations of the input parameters for our facet model. The parameters which do not involve the liquid phase and thus should be independent of the droplet material are discussed first. The values used in the calculations will be presented in Table 5.1. The quantities that obviously depend on the droplet material, viz. liquid-vapour γ_{LV} and liquid-solid γ_{LS} interface energies, Young's angle ϕ, and the nanowire contact angle β, will be presented in Table 5.2. Below, the parameters are discussed.

5.3.1. GaAs Solid-Vapour Interface Energies

The solid-vapour interface energy γ_{SV} can be determined experimentally by measuring the force necessary to move a crack in reversible fashion, but this method works only for cleavage planes, namely GaAs{110} and Si{111}, yielding $\gamma_{SV,GaAs\{110\}} = 0.86 \pm 0.15\,\mathrm{J/m^2}$ and $\gamma_{SV,Si\{111\}} = 1.14 \pm 0.14\,\mathrm{J/m^2}$.[154,119]

	Zincblende					Wurtzite	
	$\{1\bar{1}0\}$	$\{111\}$A	$\{\bar{1}\bar{1}\bar{1}\}$B	$\{001\}$	$\{00\bar{1}\}$	$\{10\bar{1}0\}$	$\{11\bar{2}0\}$
tilt angle θ	0°	-19.5°	19.5°	-35.3°	35.3°	0°	0°
$\gamma_{SV}^{(\mathrm{Ga})}\left(\frac{\mathrm{J}}{\mathrm{m}^2}\right)$	0.83	0.87	1.11	1.04	1.04	0.69	0.73
$\gamma_{SV}^{(\mathrm{As})}\left(\frac{\mathrm{J}}{\mathrm{m}^2}\right)$	0.83	0.87	0.90	0.93	0.93	0.69	0.73

Table 5.1.: **Surfaces energies of reconstructed GaAs surfaces.** Values are given for Ga-rich and As-rich vapour, in accordance with As chemical potentials of -0.64 (Ga-rich) and $-0.2\ \mathrm{meV/Å^2}$ (As-rich). The tilt angles θ_i of the surface plane with the [111] growth direction are also given, negative angles denote a tilt toward the inside of the nanowire. The γ_{SV} values are taken from compatible DFT calculations: Ref. 123 for ZB and Ref. 147 for WZ. Superscripts indicate references, see main text.

Alternatively, calculations using density functional theory (DFT) can give results for non-cleavage planes, can take into account a variety of ambient conditions as well as reconstructions, and can give more accurate results. Moll et al. calculated γ_{SV} for various ZB GaAs surfaces and their reconstructions as a function of the As chemical potential μ_{As}, which depends on the ambient As pressure p_{As} as $\mu_{As} = kT\ln(p_{As}/p_0)$, where p_0 denotes the pressure of As vapour in equilibrium with its solid.[123] The quality of the results is demonstrated by the fact that it reproduces the sequence of $\beta2(4\times2)$, $\beta2(2\times4)$ and $c(4\times4)$ reconstructions of GaAs(001) with increasing μ_{As} as observed by RHEED during MBE layer growth at 550°C.[155]

Boundaries on μ_{As} exist: at low μ_{As}, Ga droplets form at the surface, created from the disintegration of GaAs, while at very high μ_{As}, solid As crystals start to form, but this limit is out of reach for conventional MBE growth.[22] Hereafter, Ga-rich and As-rich growth conditions are considered, which correspond to a μ_{As} close to the lower and higher boundary, respectively. Approximately Ga-rich conditions are in accordance with the growth conditions for our Au- and self-assisted nanowires grown at low V/III flux ratios. Ga-rich conditions are obviously necessary to maintain the presence of the liquid Ga droplet during self-assisted nanowire growth. However, considerably more As-rich conditions cannot be excluded for Au-assisted GaAs nanowire growth experiments performed by other groups particularly using MOVPE.

In any case, the energy of the non-polar surfaces depends only weakly on μ_{As}.[123] Only polar GaAs surfaces, which contain unequal numbers of Ga and As atoms, can significantly be stabilized by reconstruction involving addition or removal of As or Ga, such that their surface energy will change with μ_{As}. This means that the following surfaces are considered to be stable: as-cleaved (relaxed but unreconstructed) GaAs(110), $\beta 2(4 \times 2)$ GaAs(100), relaxed GaAs(111)A with Ga vacancy, and relaxed GaAs($\bar{1}\bar{1}\bar{1}$)B with Ga adatom under Ga-rich conditions ($\mu_{As} \simeq -0.64$ meV/Å^2) and as-cleaved GaAs(110), $\beta 2(2 \times 4)$ GaAs(100), GaAs(111)A with (2×2) Ga vacancy, and relaxed GaAs($\bar{1}\bar{1}\bar{1}$)B with As trimers under As-rich conditions ($\mu_{As} = -0.2$ meV/Å^2).[123] The respective γ_{SV} are shown in Table 5.1.

Additionally, Rosini et al. have recently performed similar DFT calculations for WZ GaAs and used Moll's $\gamma_{SV,\{110\}}$ value as a reference point.[147] Although they did not consider a dependence on μ_{As}, reconstructions are not expected for the two non-polar WZ surfaces $\{1\bar{1}00\}$ and $\{11\bar{2}0\}$. Note that $\{11\bar{2}\}$ sidewalls are composed of monolayers with $\{111\}$&$\{100\}$ side facets. Thus, a complete set of compatible, DFT-calculated $\gamma_{SV,i}$ is available for GaAs, as presented in Table 5.1, which also shows the tilt angle of each facet with the vertical.

5.3.2. Interface Energies and Contact Angles for Ga Droplets

Although Ga-As liquid alloys are responsible for self-assisted VLS nanowire growth, the solubility of As in liquid Ga is very low.[22] Using the interface energies and contact angles of pure Ga droplets is therefore considered to be appropriate.

	Au-assisted		Self-assisted
	Au	$Au_{1-x}Ga_x$	Ga
γ_{LV} (J/m^2)	1.22[156]	≃ 1.5[157]	0.67[125]
γ_{LS} (J/m^2)		≃ 1[67]	0.39[127,158]
Young's angle ϕ		≃ 90°[67]	44°[127,158]
observed angle β		90°–140°[67,140]	90°–140°

Table 5.2.: **Mechanism-dependent parameters used in the calculations**: liquid-solid interface energy γ_{LS}, droplet-on-planar contact angle ϕ (Young's angle), and droplet-on-nanowire contact angle β (observed angle) for Au, $Au_{1-x}Ga_x$, and Ga liquid droplets. Superscripts indicate references, see main text.

The liquid surface energy γ_{LV}^{Ga} equals the surface tension and is relatively easy to determine experimentally.[118,159] From the shape of a droplet on well known silica surfaces the surface tension of Ga droplets in vacuum at 550°C, $\gamma_{LV}^{Ga} = 0.67$ J/m^2 was extracted.[125]

The liquid-solid interface energy γ_{LS} is the most difficult one to determine experimentally. It can however be calculated using Young's equation $\gamma_{SV} = \gamma_{LV}\cos(\phi) + \gamma_{LS}$, provided the other interface energies and Young's angle are known. Young's angle ϕ, which is the contact angle for a liquid droplet on a solid plane, has been measured for Ga on GaAs(111)A at two different temperatures and interpolation to 550°C results in

$\phi^{Ga}_{\{111\}A} = 44 \pm 2°$.[127] Other authors who did not take care to avoid surface oxidation erroneously measured much larger Young's angles, as described by Chatillon.[158] Using Young's equation, the value $\gamma^{Ga}_{LS} = 0.39$ J/m^2 results, which is also used for all other surface orientations, for which no experimental data exist.

The droplet-on-nanowire contact angle β is generally different from the droplet-on-planar contact angle, since the geometry differs from the planar case in that the solid-vapour interface is now vertical. Macroscopically and in thermal equilibrium, the general situation is described by

$$\gamma_{LV} \cos\beta^* = \gamma_{SV} \cos\alpha - \gamma_{LS}, \tag{5.9}$$

where α is the angle between the horizontal and the solid-vapour interface. For nanowires, this equation was analysed by Schmidt et al,[108] who also included the TPL line tension τ in their discussion. Since no experimental values for τ are available, it is neglected here and we note that calculation is only approximate. For non-tapered nanowires, $\alpha = \pi/2$ and we get an estimate for the contact angle

$$\cos\beta^* = -\frac{\gamma_{LS}}{\gamma_{LV}}, \tag{5.10}$$

which leads to $\beta^* = 125°$ for Ga droplets on GaAs nanowires.

Experimentally, β can be measured after growth provided the droplets are not consumed. We observe values between 90° and 140° for our self-assisted nanowires (e.g. Figs. 3.19 and 4.10). Similar angles are visible for the Ga droplets on self-assisted nanowires grown by other groups.[17,99]

5.3.3. Interface Energies and Contact Angles for Au Droplets

For Au-assisted nanowires, the droplets strictly consist of Au-Ga-As alloys. Again, the As content is very low,[60] but the Ga content is substantial. Thus, the Au-Ga-As droplet can be approximated as an $\mathrm{Au}_{1-x}\mathrm{Ga}_x$ alloy and atomic Ga fractions x up to 0.3-0.5 have been found after growth.[65] The surface energy $\gamma^{\text{Au-Ga}}_{LV}$ has commonly been determined by interpolation of γ^{Au}_{LV} and γ^{Ga}_{LV}.[67,140] By the oscillating drop method, the surface tension of liquid Au was measured both at ground and in space.[156] An extrapolation to extreme undercooling conditions at 550°C yields a value of 1.22 J/m^2.

However, Algra et al. proposed to use a higher value for $\gamma^{\text{Au-Ga}}_{LV}$ since the density of Au alloyed with Ga increases, suggesting intercalation of Ga atoms at interstitial sites into the Au matrix.[157] As a result, the density of bonds at the surface of the droplet increases. Thus, $\gamma^{\text{Au-Ga}}_{LV}$ is expected to take a value between γ^{Au}_{LV} and $\gamma^{\text{Au}}_{LV} + \gamma^{\text{Ga}}_{LV} \simeq 1.9$ J/m^2. In the following complete calculation, the estimate $\gamma^{\text{Au-Ga}}_{LV} \simeq 1.5$ J/m^2 is used. In the stability diagrams, a range between 1.2 and 1.5 J/m^2 is considered.

The liquid-solid interface energy $\gamma^{\text{Au-Ga}}_{LS}$ can again be determined using Young's angle. Glas et al. measured ϕ of Au droplets on planar GaAs(111)B just before nanowire growth and mention that it was "close to $\pi/2$".[67] This implies that $\gamma^{\text{Au-Ga}}_{LS} \simeq \gamma^{\text{Ga(111)B}}_{SV} = 1.11$ J/m^2, which is substantially higher than for pure Ga. In the following we will use a conservative estimate of $\gamma^{\text{Au-Ga}}_{LS} \simeq 1$ J/m^2, and again this will be used for all crystal orientations.

Typical contact angles of Au-Ga droplets on top of our nanowires were $90° \leq \beta \leq 140°$ as found by HR-TEM after growth (e.g. Figs. 3.8 and 4.7). Droplet contact angles $90° \leq \beta \leq 125°$ have been reported by other groups,[67,140] and it was explicitly stated that "the contact angles should be even larger during the growth when the droplets contain more Ga and some As".[140] Equation (5.10) and the above estimates for γ_{LV} and γ_{LS} result in $\beta^* = 130°$ for Au-Ga droplets on GaAs nanowires, but this value is associated with substantial uncertainty.

5.4. Predictions of the Model

Here, using the physical parameters discussed in the preceding section, the theoretical VLS growth model presented in Sec. 5.2 will be applied to predict the facet stability for self- and Au-assisted VLS-grown GaAs nanowires. Since the facets are different for ZB and WZ, the crystal structure is discussed at first.

5.4.1. Complete Calculation

The parameter values discussed above were applied to calculate the relative facet probabilities P_i using equations (5.1)-(5.8). Separate calculations were performed for ZB nuclei with $\{1\bar{1}0\}$ and (112)-type facets ($\{111\}$A, $\{\bar{1}\bar{1}\bar{1}\}$B, $\{001\}$, $\{00\bar{1}\}$) as well as the two WZ configurations ($\{10\bar{1}0\}$, $\{11\bar{2}0\}$). This approach is used to predict which crystal structures and which side facets lead to the lowest energy nuclei and should therefore prevail during VLS nanowire growth.

Figure 5.6.a presents an exemplary calculation for self-assisted GaAs nanowires of the critical Gibbs free energy ΔG_i^* (in units of kT at 550°C) for the different side facets i, as a function of the droplet supersaturation $\Delta\mu$, i.e. the difference in chemical potential between Ga as well as As in the droplet and precipitated GaAs in the solid nucleus. Thus, $\Delta\mu$ is a different quantity than the chemical potential of As μ_{As} at a solid surface subject to As_4 and Ga vapours, which was used to determine the various γ_{SV}'s in Sect. 5.3.1 above. Although the two quantities $\Delta\mu$ and μ_{As} are probably related, this relation is not trivial and depends on the kinetics of the VLS mechanism in an hitherto unknown way.

An intermediate value of $\beta = 125°$ and the set of γ_{SV_i} under Ga-rich conditions were used in the calculation. In Fig. 5.6.b, the corresponding normalized facet probabilities P_i are presented. These calculations demonstrate that the crystal structure depends on the supersaturation $\Delta\mu$, which can directly be varied by changing the growth conditions. It has been shown that $\Delta\mu$ increases with an increased As content in the Ga droplets.[153] At growth start, when no As is in the droplets, $\Delta\mu$ is expected to be close to zero and rises towards a steady-state value during continuous nanowire growth. When, after growth has ended, the As is allowed to leave the droplet, $\Delta\mu$ can decrease again. Similarly for Au-Ga droplets, $\Delta\mu$ increases with rising As and also with rising Ga content but decreases with rising temperatures.[60]

The change from ZB to WZ above a critical value $\Delta\mu_c$ is a general feature of the monolayer nucleation model.[67] Below this value, ZB nuclei with $\{1\bar{1}0\}$ facets have the lowest critical Gibbs free energy and thus the highest formation probability. For larger supersaturation, WZ nuclei with $\{10\bar{1}0\}$ facets are predicted to be most stable. At the beginning of growth, when the supersaturation increases from close to zero to some steady-state value, a crystal structure change from ZB to WZ is thus predicted. This result does not fully agree with the sequence of crystal structures observed during self-assisted growth, which is ZB-WZ-ZB (Fig. 3.20). The second switch (from WZ to ZB) has been explained by Krogstrup et al., who use an extension of the model and consider the critical radii of

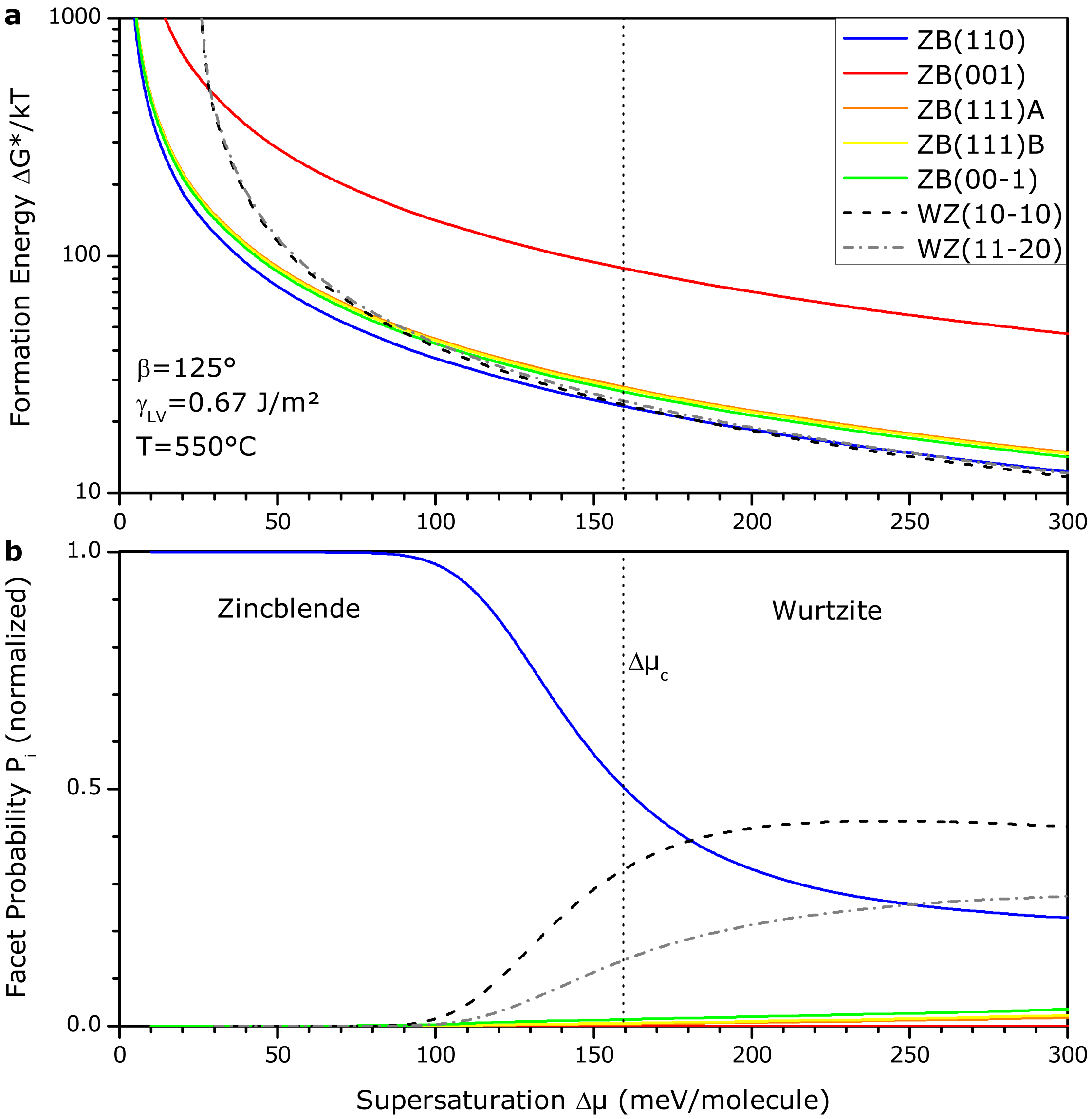

Figure 5.6.: **Exemplary calculation of critical Gibbs free energies and formation probabilities of GaAs nuclei with different TPL side facets.** ZB Nuclei with $\{1\bar{1}0\}$ facets have lowest ΔG^* and are most probable below a critical value $\Delta\mu_c$ (vertical dotted line), while WZ $\{10\bar{1}0\}$ and $\{11\bar{2}0\}$ side facets dominate above.

the nuclei.[153] However, this extension is left out of the present analysis because it is not important for the analysis of facets.

Unfortunately, it was found during repeated calculations, that the stable facets strongly depend on not accurately known parameters, in particular the contact angle β. Therefore, instead of calculating numerous ΔG^* and P_i plots, a more analytical understanding is sought. In the following we consider two cases: WZ facets (high $\Delta\mu$) and ZB facets (low $\Delta\mu$).

5.4.2. Wurtzite Facets

The formation of WZ nuclei arises from their lower γ_{SV} than for ZB nuclei. For sufficiently large $\Delta\mu$, the energetic cost associated with WZ stacking is thus outweighed by the gain in lateral surface energy. In the following, the probability P_i of nuclei with different side facets are compared. Assuming that the different nuclei have similar shapes, we do not need the whole calculation of all P_i, since the nucleus with the highest P_i will also have the lowest $\delta\Gamma_i$. Therefore, a comparison of the facet-depending lateral energy $\delta\Gamma_i$ suffices (see Equation 5.5).

For WZ, the two possible side facets $\{10\bar{1}0\}$ and $\{11\bar{2}0\}$ have $\theta_i = 0$ and Equation (5.5) simplifies to $\delta\Gamma_i = \gamma_{SV_i}$. Therefore, $\{10\bar{1}0\}$ WZ facets, which have the lower γ_{SV_i}, are predicted to have the highest probability of formation independent of the droplet material and β.

This result corresponds well to the observation of $\{10\bar{1}0\}$ facets for Au-assisted WZ GaAs nanowires. At the moment, this cannot be compared with self-assisted growth experiments, since to our knowledge there exist no reports about the WZ side facets of self-assisted GaAs nanowires.

5.4.3. Zincblende Facets for Self-Assisted Nanowires

In the following, we focus on the side facets of ZB nuclei. We consider self-assisted nanowire growth at first. Since the formation of Ga droplets is vital for this mechanism, Ga-rich ambient conditions are expected to prevail.

As for the WZ facets, the most 'stable' (i.e. most readily formed) facet can be calculated by minimization of $\delta\Gamma_i$ using equation (5.5). No further simplification is possible for ZB facets, since $\{111\}$ and $\{001\}$ facets are tilted ($\theta_i \neq 0$). The facet with minimum $\delta\Gamma_i$ has been calculated as a function of β and γ_{LV} and is presented in Fig. 5.7. Calculations for a wide range of β between 60° and 150° are shown in order to safely encompass all contact angles conceivable to be present during nanowire growth. In addition, γ_{LV} has been allowed to range from 0.5 to 2 $\mathrm{J/m^2}$ to enable a later comparison between Ga and Au-Ga droplets.

Regions of stability for three of the five considered facets are found, while nuclei with $\{001\}$ and $\{\bar{1}\bar{1}\bar{1}\}$B side facets are not stable at all under the considered set of γ_{SV} and β. The liquid-vapour energy for liquid Ga-As droplets is expected to be close to that of pure liquid Ga of $\gamma_{LV}(Ga) = 0.67\ \mathrm{J/m^2}$ with a possible small deviation caused by the incorporation of a low fraction of As. The contact angle β during growth is not known very exactly, but can be estimated by measurements after growth. In Fig. 5.7 the most probable range of γ_{LV} and β are indicated.

As a result, the model predicts $\{1\bar{1}0\}$ side facets for the whole range $70^\circ < \beta < 150^\circ$ for VLS growth under Ga droplets and Ga-rich conditions. This result establishes the generality of the earlier calculation (Figure 5.6, only for one specific γ_{LV} and β). This results also agrees with the experimental observations. It can be understood by consideration of the low surface energy of liquid Ga droplets, which does not suffice to support the creation of tilted sidewalls.

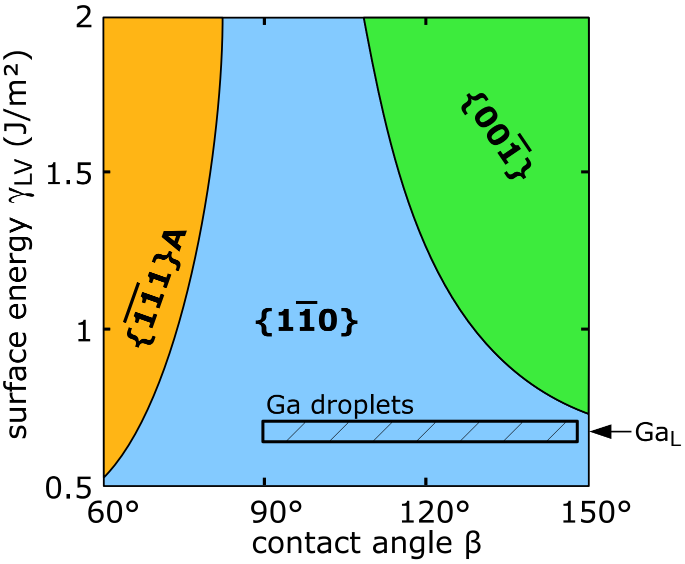

Figure 5.7.: **Facet stability for Ga-assisted VLS growth and Ga-rich conditions.** Results are obtained by minimisation of (5.5). Since the values for the droplet contact angle β and the surface energy of the liquid Ga droplet γ_{LV} during growth are not known accurately, the calculation is presented for a large range of the two physical parameters. The most probable range for Ga droplets during growth is indicated by a hatched rectangle. The value of γ_{LV} for pure liquid Ga is indicated.

5.4.4. Zincblende Facets for Au-Assisted Nanowires

For Au-assisted growth, it is not a priori clear if As-rich or Ga-rich conditions were present during growth and which reconstructions should thus be considered. Here, we analyse each case separately using the two different sets of γ_{SV} as given in Table 5.1.

As-rich Conditions

Figure 5.8 depicts the stability diagram of the side facets under As-rich growth conditions. The higher As content in the ambient vapour allows for a stabilization by As-enriched reconstructions, particularly of the polar $\{\bar{1}\bar{1}\bar{1}\}$B surface.

For the Au-Ga droplets, a range of contact angles from 90° to 140° as found after growth is considered. Their γ_{LV} is expected to lie between 1.2 and 1.5 $\mathrm{J/m^2}$ (see Sec. 5.3.3). In the major part of this range, inclined $\{\bar{1}\bar{1}\bar{1}\}$B and $\{00\bar{1}\}$ nuclei are now stable, in accordance with the experimental observations. A change from these (112)-type facets to $\{1\bar{1}0\}$ facets would require a change in the nanowire cross section associated with the formation of an energetically unfavourable intermediate section.

However, the formation of non-vertical facets leads to changes in β during growth, corresponding to horizontal movements in the stability diagrams. This can explain the repeated formation of segments with alternating facets in the following way. During growth of inclined side facets, the nanowire cross section approaches a triangular shape, since outwards-tilted B-facets shrink and inwards-tilted A-facets widen, as schematically shown in Figure 5.9a. This leads to a skewed droplet shape and a change of the droplet nanowire contact angle β, which decreases on B- and increases on A-facets (Fig. 5.9b).

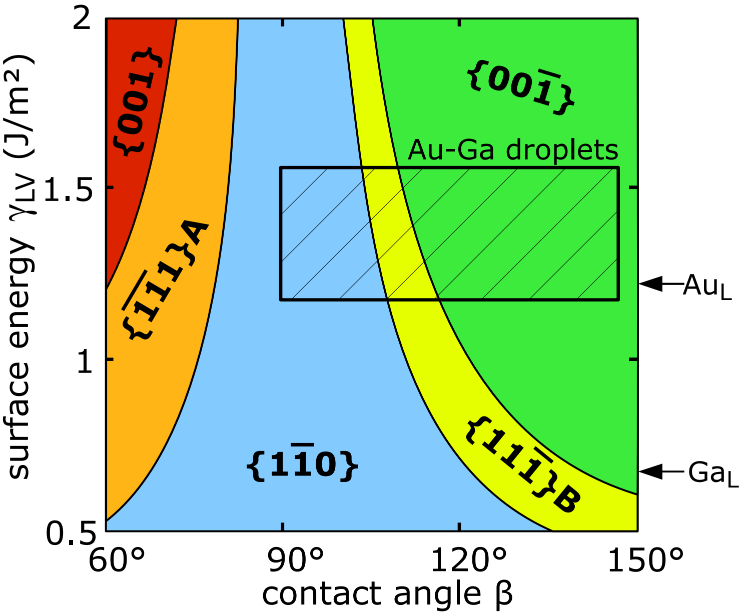

Figure 5.8.: **Facet stability for Au-assisted VLS growth under As-rich conditions.** Results are obtained by minimisation of (5.5). The most probable range for Au-Ga droplets during growth is indicated by a hatched rectangle. The values of γ_{LV} for pure liquid Ga and pure liquid Au are indicated.

Nevertheless, during growth of several monolayers the average contact angle can be stabilized by the following two processes:

- Caused by the growth of a number of GaAs monolayers with $\{\bar{1}\bar{1}\bar{1}\}$B facets, β_A at the opposite (or a neighbouring) A facet has sufficiently increased, that eventually a nucleus with $\{001\}$ facets forms (Fig. 5.9c). In this way, Algra et al. modelled vertical $\{11\bar{2}\}$ facet growth by repeated formation of $\{\bar{1}\bar{1}\bar{1}\}$B nuclei on B facets and $\{001\}$ nuclei on neighbouring A facets (with 2:1 probability).[149]
- Alternatively, after continuous nucleation of several monolayers with $\{\bar{1}\bar{1}\bar{1}\}$B side facets, β_B has decreased sufficiently that nucleation with outwards inclined $\{\bar{1}\bar{1}\bar{1}\}$B side facets at the neighbouring A side wall is more probable, even though this necessitates formation of a twin plane (Fig. 5.9d). Again, Algra et al. were able to explain the formation of composed $\{111\}$A &$\{\bar{1}\bar{1}\bar{1}\}$B facets in this way.[74]

As a result, β can be *dynamically stabilized* in cases when $\{\bar{1}\bar{1}\bar{1}\}$B nuclei are favoured, i.e. for $103° < \beta < 111°$ at γ_{LV} =1.5 J/m^{-2} (Fig. 5.8). It is expected, that whenever β is larger, $\{00\bar{1}\}$ facets are formed and β is reduced thereby until $\{\bar{1}\bar{1}\bar{1}\}$B facets are most favourable.

Thus, for Au-Ga droplets and As-rich conditions, formation of polar and composed $\{111\}$A &$\{\bar{1}\bar{1}\bar{1}\}$B or $\{111\}$ &$\{001\}$ facets is predicted, which is in agreement with experimental observations for Au-assisted GaAs nanowires.

Ga-rich growth conditions

While the model for Au droplets under strongly As-rich conditions agrees well with experimental observations, we also study what happens under more Ga-rich growth condi-

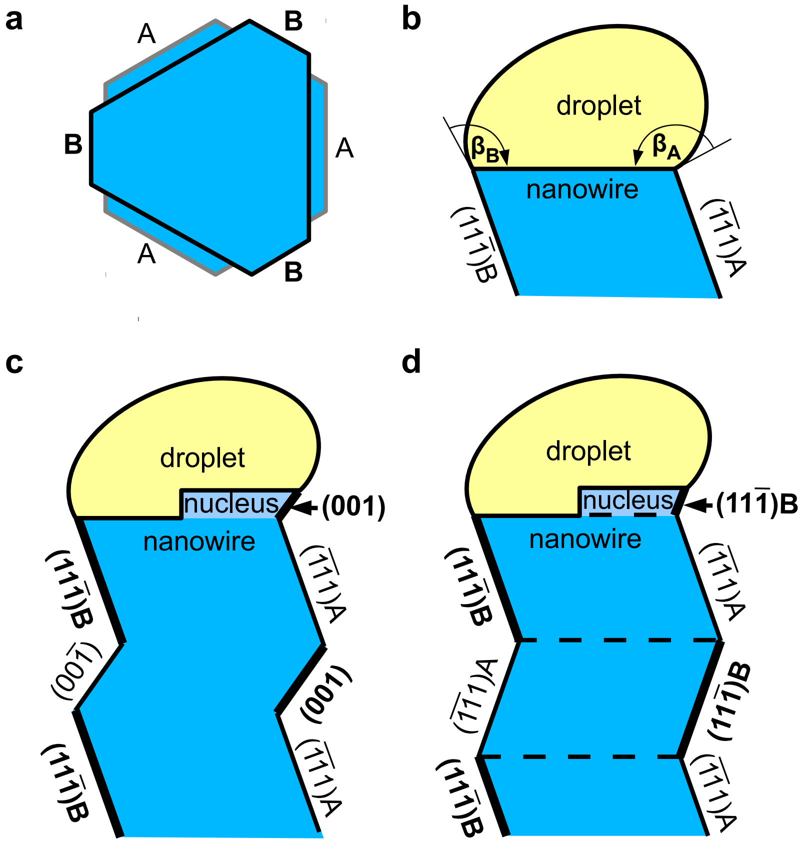

Figure 5.9.: **Formation of composed facets caused by contact angle changes.** (a) Nanowire cross sections approach triangular shape during growth of inclined side facets. (b) Resulting skewed droplet shape with reduced (enlarged) contact angles at B (A) facets. (c) Nucleation initiated at alternating positions (bold lines) by formation of outwards-tilted segments with $\{\bar{1}\bar{1}\bar{1}\}$B or $\{001\}$ facets. (d) Continuous nucleation of segments initiated by $\{\bar{1}\bar{1}\bar{1}\}$B facets, but at alternating locations and requiring regular formation of twin planes (dashed lines).

tions, since our Au-assisted growth experiments were performed with a flux ratio J_{As}/J_{Ga} close to stoichiometry.

Completely Reconstructed GaAs Figure 5.10a presents the facet stability diagram under Ga-rich conditions for Au-assisted VLS growth. The facet stability regions are equivalent to those presented before for self-assisted growth (Fig. 5.7), but considerably larger γ_{LV} and β^* prevail for the Au-Ga droplets considered here. This leads to the prediction of outwards tilted polar $\{100\}_B$ facets or $\{1\bar{1}0\}$ extended facets. The general observation of $\{111\}$A &$\{\bar{1}\bar{1}\bar{1}\}$B and $\{11\bar{2}\}$ side facets can not be explained by this set of parameters.

Partially Reconstructed GaAs So far, we focused on the dependence of facet stability on the two inaccurately known parametes γ_{LV} and β. In the following, changes in γ_{SV}

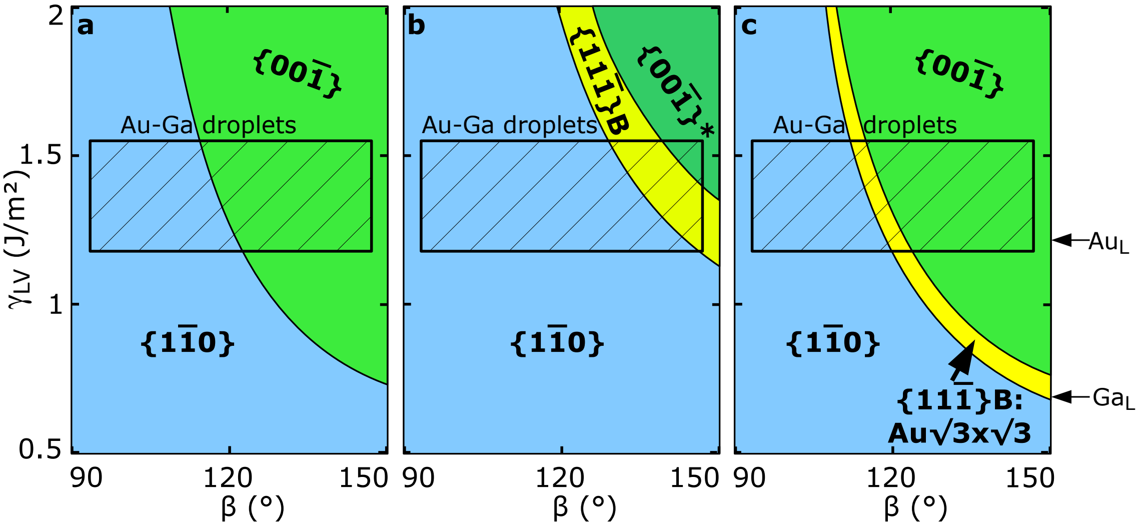

Figure 5.10.: **Facet stability for Au-assisted VLS growth under Ga-rich conditions.** Results are obtained by minimisation of (5.5). The most probable range for Au-Ga droplets during growth is indicated by a hatched rectangle. (a) Calculation for completely reconstructed GaAs. (b) Calculation for partially unreconstructed GaAs(100). (c) Calculation for GaAs(111) with extrinsic $(\sqrt{3}\times\sqrt{3})R30^\circ$ Au reconstruction.

are also considered. The employed set of γ_{SV} values are based on complete reconstruction of all GaAs surfaces. When nanowires have (nano-) facets which span over several monolayers (as observed for $\{111\}$A &$\{\bar{1}\bar{1}\bar{1}\}$B facets), there is expected to be enough space for the considered reconstructions to occur. To be precise, the lateral surface of the topmost monolayer itself may not be completely reconstructed, but its presence should allow a better reconstruction of the lateral surface below it, provided that both parts have identical orientation. Of the considered reconstructions, i.e. (111)A (2x2) Ga vacancy, (111)B (2x2) Ga adatom, and (001) $\beta2$(4x2), the latter has the largest unit cell.[‡] Furthermore, $\{001\}$ facets must consist of only one monolayer, when they are components of $\{11\bar{2}\}$ facets.[149] Then, there surely is insufficient space for the (4x2) reconstruction considered so far and an energetically less favourable surface has to be expected. Figure 5.10b presents a calculation for which the (100) surface energy was increased to an arbitrary value $\gamma_{SV}^{(100)} = 1.3\ \mathrm{J/m^{-2}}$, while the γ_{SV} values for the other orientations remain as before.

An extended stability region of $\{\bar{1}\bar{1}\bar{1}\}$B facets results, which is in accordance with the experimental observation. Furthermore, the estimation of the average contact angle basing on β^* (130° at $\gamma_{LV} = 1.5\ \mathrm{J/m^2}$) also predicts $\{\bar{1}\bar{1}\bar{1}\}$B facets. This plot demonstrates the effect of reconstructions on facet stability. Detailed DFT calculations of surface reconstructions near the nuclei edge would be necessary to decide on the applicability of this consideration.

Extrinsically Reconstructed GaAs Finally, we consider the effects of reconstructions with foreign atoms, which can have a strong effect on the surface and interface energies, particularly γ_{SV}. It was already noted that crystal structure and side facets of nanowires

---

[‡] The lowest energy GaAs (110) surface is not reconstructed but only relaxed.

can change in the presence of foreign material, such as by the introduction of Zn originally intended for doping.[74,160]

Here, we consider the effect of a foreign material, which is always present during Au-assisted VLS growth: Au. In particular, stabilization of $\{\bar{1}\bar{1}\bar{1}\}$B sidewalls by a reconstruction with Au atoms should be considered, since it has been reported that Au particles transferred by colloids onto a GaAs(111)B surface wet the surface between the droplets upon annealing and a $(\sqrt{3} \times \sqrt{3})R30^\circ$ Au reconstruction of GaAs(111)B results.[161]

The GaAs(111)B surface energy has been estimated to be reduced by approximately 8 meV/Å^2 when compared to that terminated with Ga adatoms, i.e. $\gamma_{SV}(\{\bar{1}\bar{1}\bar{1}\}B) = 0.98\ \mathrm{J/m^2}$.[162] Unfortunately, similarly detailed data is not available for the interaction of Au with the other GaAs surfaces. While further stabilization of the non-polar as-cleaved (110) surfaces appears unlikely, the polar (100) surfaces can also be expected to reconstruct with Au.

Using the Au-reconstructed γ_{SV} for $\{\bar{1}\bar{1}\bar{1}\}$B and the intrinsically reconstructed γ_{SV} for all other surfaces, the facet stability diagram is calculated again and presented in Figure 5.10c. A region of stability for the Au-reconstructed $\{\bar{1}\bar{1}\bar{1}\}$B exists, although it is rather small. Nevertheless, it should be sufficient for the formation of $\{111\}$A &$\{\bar{1}\bar{1}\bar{1}\}$B and $\{11\bar{2}\}$ facets to occur. Thus, there is some indication that the experimental observation of polar facets for Au-assisted nanowire growth could also be explained by Ga-rich conditions and a GaAs(111)B $(\sqrt{3} \times \sqrt{3})R30^\circ$ reconstruction with Au.

From the study of the Au-assisted VLS under Ga-rich conditions it becomes clear that surface reconstructions have a decisive effect on facet stability. Unfortunately, we cannot experimentally determine which reconstructions are actualised for the nanowire facets during their growth. The calculations contradict composed $\{111\}$A &$\{\bar{1}\bar{1}\bar{1}\}$B facets when the complete set of Ga-rich reconstructions is considered, but predict them when partial and extrinsic reconstructions are considered. Furthermore, the surface energy is expected to depend on the size of the facet, in particular for composed (nano-)facets. In order to clarify the matter, a theoretical study of the possible intrinsic and extrinsic (Au-induced) reconstructions next to a facet edge would be of great help.

5.5. Summary

Motivated by the importance of the surface orientation for electronic transport and optical properties, radial heteroepitaxy, as well as crystalline quality, the side facets of GaAs nanowires have been analysed.

A separate analysis has been performed for the two different crystal structures of the GaAs nanowires. For WZ, two possible facet orientations are conceivable, i.e. a-plane $\{10\bar{1}0\}$ and m-plane $\{11\bar{2}0\}$. The $\{10\bar{1}0\}$ orientation is predicted to be most probable basing on its lower surface energy. This is in accordance with the experimental findings for Au-assisted VLS growth. For self-assisted VLS grown nanowires, the same WZ facet orientation is predicted, but no experimental data are available for comparison.

For nanowires with the ZB crystal structure, the situation is more involved, since decomposition into nano-facets has been observed. Experimental data for nanowires grown by the self- and the Au-assisted VLS mechanism show mutually different side facets. ZB GaAs nanowires grown by the self-assisted VLS mechanism under Ga droplets are always observed to have non-polar $\{1\bar{1}0\}$ side facets. For the necessary Ga-rich conditions, this surface has the lowest energy of all surface orientations of ZB GaAs. The well-accepted VLS monolayer nucleation model is employed for a detailed calculation of the nucleus formation probabilities depending on the lateral facet. It is demonstrated that the most probable facet can more simply be calculated by a minimization of the lateral surface energy associated with each facet. This alternative approach is employed to study the dependence on two parameters, which are only inaccurately known, i.e. the contact angle β and the liquid-vapour surface energy γ_{LV}. The calculations theoretically affirm that $\{1\bar{1}0\}$ side facets are the most stable for the probable range of β, whose exact value during growth is unknown. The result of the calculation can qualitatively be understood in terms of the rather low value of $\gamma_{LV}^{\mathrm{Ga}}$, which makes the energy gain by forming outwards tilted sidewalls small. Thus, the formation of vertical $\{1\bar{1}0\}$ side facets is energetically most favourable.

For Au-assisted GaAs nanowires with ZB crystal structure, vertical $\{11\bar{2}\}$ extended facets as well as tilted $\{111\}$ and $\{001\}$ nano-facets have experimentally been found. These inclined GaAs facets have higher surface energies than the $\{1\bar{1}0\}$, but the observations can be explained by a consideration of the nanowire droplet contact angle β and the large $\gamma_{LV}^{\mathrm{Au\text{-}Ga}}$. The energy gained by an upwards-shift of the liquid droplet during facet growth can overcompensate the higher energy cost for tilted facets provided β is sufficiently large. Our analytical formulation and quantification leads us to the finding that this overcompensation can indeed be effectuated during growth using Au droplets. For the detailed analysis, different ambient conditions have been considered.

Under As-rich growth conditions, nuclei with outwards-inclined $\{\bar{1}\bar{1}\bar{1}\}$B and $\{00\bar{1}\}$ facets are predicted. From these, the formation of nanowires with composed facets ($\{111\}$ and $\{001\}$ or $\{111\}$A & $\{\bar{1}\bar{1}\bar{1}\}$B) or extended $\{11\bar{2}\}$ facets can be explained. The facet changes between the segments are induced by changes in β caused by the growth of inclined facets. Under Ga-rich conditions, which may also be present during Au-assisted VLS growth, a first direct calculation cannot predict the observed $\{\bar{1}\bar{1}\bar{1}\}$B side facets. Taking additional uncertainties in the solid-vapour surface energies γ_{SV} into account, we propose two possibilities. Allowing for an incomplete reconstruction of the lateral surfaces during growth, we have calculated the effect of an increased surface energy for the $\{001\}$ facets, which have the largest reconstruction unit cell. Alternatively, the reconstruction of GaAs(111)B with Au, which has been reported to reduce the surface energy, is considered. Both possibilities result in the stability of $\{\bar{1}\bar{1}\bar{1}\}$B as well as $\{00\bar{1}\}$, in accordance with the experimental observations.

As a result, the orientation of side facets is affected by the choice of liquid droplet material. This is understood to originate from the comparably low γ_{LV} of liquid Ga droplets, such that the vertical $\{1\bar{1}0\}$ facets prevail, while γ_{LV} of Au-Ga droplets is sufficiently high to stabilize inclined facets.

6. Suitability for Optoelectronic Applications

The central difference between the two nanowire growth methods under study is the presence or absence of Au during the growth process. When incorporated, Au is a deep centre in many semiconductors including GaAs, which drastically reduces the carrier lifetime and thereby diminishes device performance.[163–165] Therefore, the incorporation of Au could have grave consequences for the application of nanowires grown by the Au-assisted VLS mechanism.

The minority carrier lifetime τ of Au-assisted nanowires has repeatedly been measured at cryogenic temperatures.[166,167] When the nanowires were capped with a shell of (Al,Ga)As, in order to reduce the large surface recombination of the free GaAs surface, τ was found to reach close to the maximum possible value represented by the radiative (free exciton) lifetime τ_r, which lies between 1 and 10 ns for GaAs at temperatures below 10 K.[168,169] However, at room-temperature, when even longer τ can be expected for GaAs/(Al,Ga)As heterostructures,[170] the only available report for GaAs/(Al,Ga)As core-shell nanowires (which were grown by the Au-assisted VLS mechanism) resulted in substantially shorter τ below 20 ps.[171] These short τ might indeed cause some concern, since for most applications the room-temperature performance is relevant, and it raises the question whether Au-assisted GaAs nanowires are suitable for optoelectronic devices at all. For self-assisted GaAs nanowires, no comparable data was previously available.

Here, the potential of GaAs nanowires grown by both methods for actual optoelectronic applications is examined.[172] In Section 6.1, the growth and morphology of GaAs-(Al,Ga)As core-shell nanowires is presented. The results of continuous-wave and time-resolved photoluminescence (PL) spectroscopy at room temperature are presented in Section 6.2. From these data, the minority carrier lifetimes τ are determined and the relation to the internal quantum efficiency η, the central figure-of-merit for optoelectronic devices, is pointed out. Finally, Section 6.3 presents additional measurements of the thermal activation energy of a recombination centre found in the Au-assisted nanowires, in order to facilitate its identification.

6.1. GaAs/(Al,Ga)As Core-Shell Nanowires

In order to disable the dominant non-radiative recombination at the free GaAs surface, the GaAs cores were surrounded with (Al,Ga)As shells. This is of particular importance for room-temperature luminescence, since, in general, non-radiative recombination processes are temperature-activated.

6.1.1. Growth

GaAs/(Al,Ga)As nanowires were fabricated in the Au-chamber of M6 using the Au- as well as the self-assisted growth methods described in Chapter 3 before. After the standard growth of the GaAs nanowire cores, the (Al,Ga)As shells were grown under an additional Al flux while the Ga and As_4 fluxes as well as the temperature remained constant. For each mechanism, three samples were fabricated, their PL spectra and transients were measured, and it was found that they behave comparably. For a detailed analysis, one sample grown by each growth mechanism was chosen and will be presented in the following. The Au-assisted nanowires were grown using $J_{As} = 5\ \mathrm{s}^{-1}\mathrm{nm}^{-2}$, $J_{As}/J_{Ga} = 2$ at substrate temperature $T_S = 500°\mathrm{C}$ on deoxidized Si(111) substrates covered with Au nanodroplets. The self-assisted nanowires were fabricated using $J_{As} = 5\ \mathrm{s}^{-1}\mathrm{nm}^{-2}$, $J_{As}/J_{Ga} = 1$ at $T_S = 580°\mathrm{C}$ on Si(111) with remaining native oxide. For both samples, a shell of nominally $Al_{0.1}Ga_{0.9}As$ was grown after 30 min of GaAs growth for another 30 min under an additional Al flux $J_{Al} = J_{Ga}/10$ without any change in T_S, J_{Ga} or J_{As}.

6.1.2. Morphology

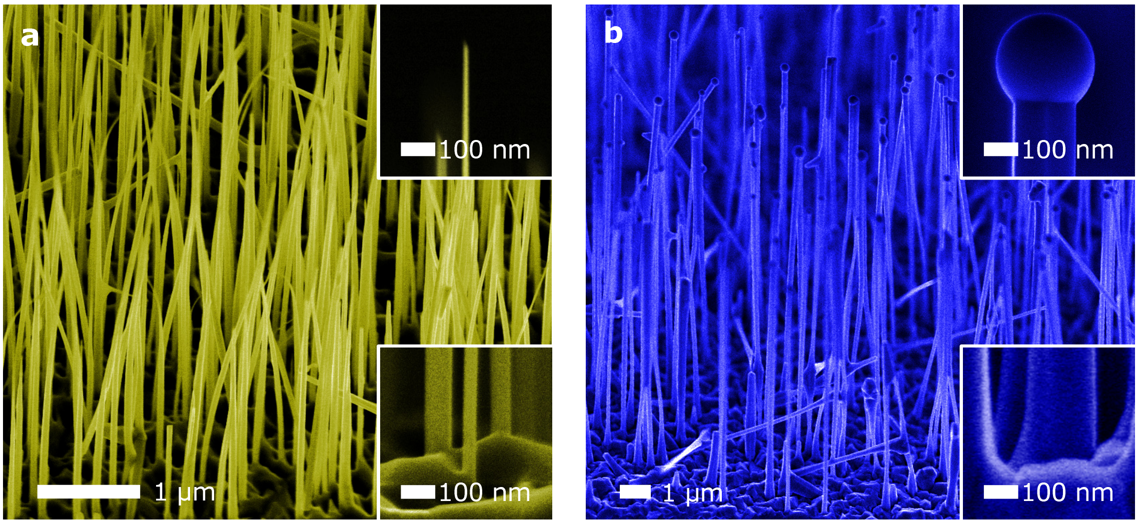

Figure 6.1.: **Morphology of Au- and self-assisted GaAs/(Al,Ga)As core-shell nanowires. a, b**, Scanning electron micrographs of (a) Au-assisted and (b) self-assisted GaAs/(Al,Ga)As core-shell nanowires on Si(111), insets show magnifications of the top and foot region.

Figure 6.1 shows SEM micrographs of one sample for each growth method. The Au-assisted nanowires are shorter and thinner but stand closer than the self-assisted ones.

As was observed before (see Fig. 3.6), the Au-assisted nanowires have a pencil shape, that arises from comparably small Au droplet diameters (around 10 nm, below the resolution of the micrograph) in conjunction with radial growth of the nanowires. Along the lower 3/4 of their lengths of $5 \pm 1\ \mu\mathrm{m}$, the Au-assisted wires have uniform diameters of 68 ± 12 nm, and above they are obviously tapered. Their average number density is $5\ \mu\mathrm{m}^{-2}$. The Au-assisted core diameters were determined to be 42 ± 7 nm by statistical analysis of SEM measurements.

In contrast, Ga droplets are clearly observable at the tip of the self-assisted nanowires, which show uniform diameters of 150 ± 25 nm along their entire lengths of $9 \pm 1\ \mu\mathrm{m}$. Their average number density is $1\ \mu\mathrm{m}^{-2}$. The diameters of the self-assisted GaAs cores were determined to be 106 ± 18 nm. Error values represent the standard deviation between different nanowires on the same sample.

6.2. Internal Quantum Efficiency

The internal quantum efficiency η is the central figure-of-merit expressing a material's potential for optoelectronic applications. For example, the value of η determines the threshold current density of injection laser diodes, the luminous efficacy of light-emitting diodes, and the power conversion efficiency of solar cells. Experimentally, η is proportional to the spectrally integrated intensity I of the spontaneous emission of the semiconductor,

$$\eta \propto I, \tag{6.1}$$

and is thus in principle accessible by recording its steady-state (continuous wave) PL spectrum. However, I is also affected by a multitude of other factors including the sample geometry and the coupling efficiencies of light into and out of the material. Since η may, in general, be written as

$$\eta = \tau / \tau_r, \tag{6.2}$$

with the minority carrier lifetime τ and the radiative lifetime τ_r (which is constant for a given doping level), it can be measured independently by time-resolved PL upon pulsed excitation. In contrast to the steady-state intensity I, τ is neither affected by volume nor by the coupling of light into and out of the structure. Thus, the relevant quantities are attainable by all-optical measurements. In this way, the data were obtained independent of any electrical contacts and any ambiguities inherent in electrical measurements are avoided.

6.2.1. Continuous-Wave Photoluminescence

Figure 6.2a shows the room-temperature micro-PL (μPL) spectra of the two representative samples measured side-by-side under identical conditions. The integrated PL intensity I of the self-assisted nanowires is larger than that of the Au-assisted nanowires by more than two orders of magnitude. The spectral positions of the bands at 1.429 eV, 1.446 eV and 1.522 eV correspond to radiative recombination in GaAs in the zincblende (ZB) phase for the self-assisted nanowires, as well as in GaAs and $\mathrm{Al}_x\mathrm{Ga}_{1-x}\mathrm{As}$ ($x = 0.06 \pm 0.01$) in the wurtzite (WZ) phase for the Au-assisted nanowires, respectively.[173,174] The fact that different polytypes are obtained by the Au- and self-assisted growth techniques is typical for nanowire growth under these conditions, see Sections 3.1.2 and 3.2.1.

The observation of PL emission from the $\mathrm{Al}_{0.06}\mathrm{Ga}_{0.94}\mathrm{As}$ barrier in the Au-assisted case is unusual. In contrast, no barrier emission is observed for typical planar GaAs/(Al,Ga)As double heterostructures (DHs), i.e. thick GaAs layers between (Al,Ga)As barriers. This can be understood by considering the minority carrier lifetime τ separately for layer (core) and barrier (shell) and neglecting differences of geometry and light coupling. While τ in the GaAs layer is typically of the order of nanoseconds for planar DHs (see Figure 6.3 below), in the barrier it is limited by the characteristic time for carrier diffusion into the layer (typically picoseconds). Thus, τ is several orders of magnitude larger in the layer than in the barrier, which by virtue of equations (6.1) and (6.2) leads to a proportionally larger PL emission in typical planar double heterostructures. As a result, layer emission outshines that of the barrier. For the Au-assisted nanowires, both core and shell show equally strong PL. Thus, τ is equally short for core and shell and similar to the carrier diffusion time. A minority carrier lifetime in the picosecond range is thus expected for the GaAs core grown using Au. In the following direct measurements of τ are presented.

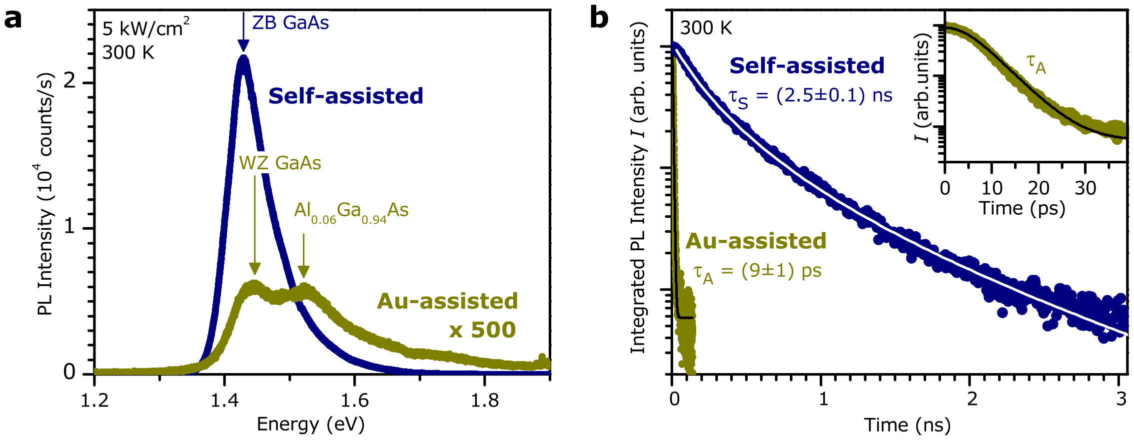

Figure 6.2.: **Photoluminescence spectra and transients of Au- and self-assisted GaAs/(Al,Ga)As core-shell nanowires.** **a**, μ-PL spectra of the Au-assisted and the self-assisted nanowires at room temperature. The spectra were recorded under identical excitation conditions. The integrated intensity for the self-assisted nanowires is larger than that for the Au-assisted ones by more than two orders of magnitude. Band-to-band transition energies of ZB and WZ GaAs as well as WZ Al$_x$Ga$_{1-x}$As with $x = 0.06$ are indicated. The spectra have been recorded by O. Brandt. **b**, μ-PL transients for the Au-assisted and the self-assisted nanowires at room temperature. The inset shows a the Au-assisted nanowire transient on an adjusted axis. Solid lines represent fits to the data. The obtained minority carrier lifetimes differ by more than two orders of magnitude. The transients have been recorded by T. Flissikowski.

6.2.2. Minority Carrier Lifetimes

Figure 6.2b displays PL transients of the two representative samples obtained by time-resolved PL spectroscopy at the energy of the band-to-band recombination of the respective polytype of GaAs. At room temperature, the recombination processes in GaAs are dominated by free-carrier recombination. PL decay kinetics characteristic for bimolecular recombination of free carriers are described by

$$I(t) \propto \{e^{-t/\tau}/[1+\alpha(1-e^{-t/\tau})]\}^2, \tag{6.3}$$

where α is the dimensionless effective injection level. The derivation is described in detail in the PhD thesis of Carsten Pfüller.[175] By least square fits to the transients, a carrier lifetime of $\tau_S = (2.5 \pm 0.1)$ ns and $\alpha = 5.2$ was extracted for the self-assisted nanowires, while $\tau_A = (9 \pm 1)$ ps results for the Au-assisted nanowires. The latter value is essentially identical to the one reported earlier for Au-assisted GaAs/(Al,Ga)As core-shell nanowires grown by metal-organic vapour phase epitaxy (MOVPE).[171] For the Au-assisted nanowires, the fit includes the convolution with the apparatus function and yielded $\alpha \approx 0$ indicating a single exponential decay.

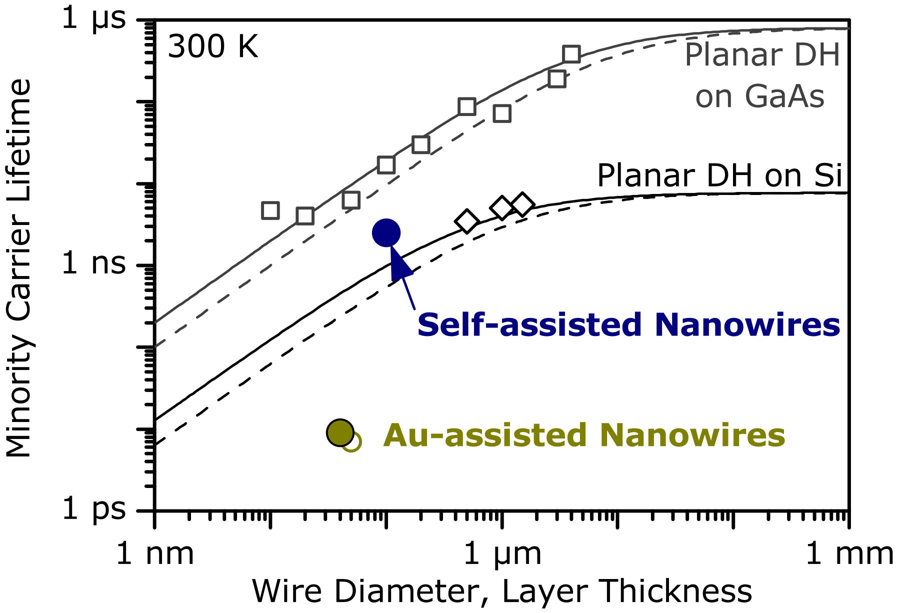

Figure 6.3.: **Comparison of GaAs/(Al,Ga)As core-shell nanowires and planar double heterostructures (DH).** Minority carrier lifetimes for core-shell nanowires on Si substrates (filled circles, this work), Au-assisted core-shell nanowires (open circle)[171], planar DH on GaAs substrates (squares)[170], and planar DH grown on step-graded Ge/(Ge,Si) buffer layers on Si substrates (diamonds)[176] are shown as a function of the GaAs dimension, i.e. the nanowire core diameter or the layer thickness without barriers. Fits (solid lines) for planar DH are shown as well as extrapolations (dashed lines) to core-shell nanowires with identical bulk and surface recombination parameters. While our self-assisted nanowires do not yet reach the quality of planar DH on GaAs, they are already better than the extrapolation for planar DH on Si. The optoelectronic material quality at room temperature of Au-assisted nanowires is considerably lower.

6.2.3. Comparison with Planar Double Heterostructures

In order to compare the lifetimes obtained here with those for planar heterostructures, we recall that the effect of interface recombination on τ is described by

$$1/\tau = 1/\tau_b + nS/d, \tag{6.4}$$

where τ_b is the bulk minority carrier lifetime, S is the interface recombination velocity, n equals 2 for planar geometry and 4 for nanowires with square or circular cross section, and d is the nanowire core diameter or layer thickness, respectively.[177,178] While the free GaAs surface is characterized by a large surface recombination velocity of $S = 3 \times 10^7$ cm/s,[179] much lower values can be obtained when the GaAs was covered with (Al,Ga)As. For state-of-the-art planar GaAs/(Al,Ga)As double heterostructures (DH) grown by MBE, $S = 250$ cm/s and $\tau_b = 0.8$ µs were reported.[170]

Figure 6.3 depicts the results of our measurements in the context of literature data for planar DHs representing the state of the art of planar growth by MBE. The lifetimes for homoepitaxially grown DHs on GaAs(001) as well as heteroepitaxially grown DHs on Si(001) using step-graded Ge/(Ge,Si) buffer layers are shown together with fits (solid lines) using the above equation, $n = 2$, and the values for S and τ_b that were extracted by the original authors.[170,176] Substitution with $n = 4$ yields extrapolations (dashed lines) for nanowires with identical interface and bulk quality. It follows that lifetimes between 0.2 and 10 ns should be expected for GaAs/(Al,Ga)As core-shell nanowires on Si with d between 40 and 100 nm.

6.2.4. Discussion

It is the central result of this study that only the self-assisted nanowires exhibit a minority carrier lifetime comparable to that expected for material of state-of-the-art quality. Moreover, the lifetime obtained for the self-assisted nanowires, τ_S, is larger by more than two orders of magnitude than the one measured for the Au-assisted nanowires, τ_A. This factor directly reflects the ratio of the internal quantum efficiencies η and also corresponds to the ratio of the PL intensities obtained in steady state. This drastic difference in minority carrier lifetime between nanowires synthesized using the Au-assisted and the self-assisted growth modes is observed for all analysed samples without exception.

Figure 6.3 reveals furthermore that non-radiative recombination at the interfaces influences the minority carrier lifetime even of state-of-the-art GaAs structure as long as $d < 10\ \mu$m. Evidently, an additional, highly efficient non-radiative recombination channel exists in the Au-assisted nanowires that drastically reduces the internal quantum efficiency of these structures. The obvious question is about the nature of this additional channel. Its effect is far too large to be explained by the 80°C lower growth temperature.[180] As a matter of fact, self-assisted nanowires grown at 540°C exhibit the same long lifetimes and the same high PL intensity as those grown at 580°C. A common growth temperature does not exist for the two growth modes used in this study: only very few Au-assisted nanowires nucleate at growth temperatures above 500°C (see Sect. 4.1.2), while no growth of self-assisted GaAs nanowires was achieved below 540°C.

The most straightforward and plausible explanation for our finding is that (i) Au is in fact incorporated into the nanowires during Au-assisted VLS growth *and* (ii) acts as non-radiative recombination centre. Concerning incorporation, Au is of course present in abundance at the growth front during Au-assisted growth. The solid solubility of Au in GaAs is 2.5×10^{16} cm^{-3} at 900°C.[181] This value may appear low, but a concentration of 10^{16} cm^{-3} still corresponds to one Au atom every 80 nm of length for a 40 nm diameter GaAs nanowire core. Given that the ambipolar diffusion length in GaAs is 0.69 μm,[182] all photoexcited carriers could indeed reach a Au centre. In Si wires, grown by the Au-assisted VLS mechanism, whose diameters of around 2 μm allowed SIMS analysis of the wires without disturbance by the Au droplets at the top, Au concentrations in the 10^{16} cm^{-3} range were detected in the wire core, which corresponds to the thermodynamic solid solubility level.[16] In the same study, Au concentrations exceeding 10^{19} cm^{-3} were found at the lateral nanowire surfaces. Au may produce deep-level, carrier recombination centres in Si, drastically reducing the minority carrier lifetime.

6.3. Activation Energy of Recombination Centre

Dramatic reductions in minority carrier lifetime (and thus η) are usually caused by electrically active defects. The influence of the surface, which can be regarded as a planar defect, has been discussed above. In the Au-assisted nanowires, an additional recombination centre was found, which might be located at the core-shell interface or in the core volume. By their ionization energy E_I, electrically active defects are traditionally grouped into two categories:

Hydrogenic (or shallow) impurities can be described by an electronic wave function that extends over many primitive unit cells. To describe them, the effective mass approximation can be used and then the motion of the impurity electron or hole is equivalent to that of the electron in the hydrogen atom.[183] As a result, shallow impurities have small ionization energies ($E_I \lesssim kT$ at room temperature) and control the number of charge carriers. $\mathrm{Si_{Ga}}$, $\mathrm{Ge_{Ga}}$, $\mathrm{S_{As}}$, and $\mathrm{Se_{As}}$ are examples of shallow donors in GaAs, while $\mathrm{Si_{As}}$, $\mathrm{Ge_{As}}$, $\mathrm{C_{As}}$, $\mathrm{Zn_{Ga}}$, and $\mathrm{Be_{Ga}}$ are shallow acceptors. In direct semiconductors, electronic transitions involving hydrogenic impurities are radiative, such that they can be identified by their characteristic emission energy in luminescence experiments.[173]

Deep centres have a strongly localized wave function and are typically accompanied by lattice relaxations. Both the impurity atom and the lattice atoms surrounding it can be involved in the relaxation. Thus, the effective mass approximation breaks down and a detailed understanding of deep centres is challenging both experimentalists and theoreticians.[183] Recombination involving a deep centre is often non-radiative, since energy can be dissipated by phonons. Commonly, deep centres have high ionization energies ($E_I \gg kT$) and their energy levels lie deep in the band gap. In contrast to hydrogenic impurities, the deep centre energy level (or deep level) depends on its electron occupancy. From the analysis of defect-assisted recombination, it becomes clear that the recombination rate increases the closer the defect level lies to mid gap.[184] As a result, deep centres can be efficient non-radiative recombination centres, which strongly reduce carrier lifetimes.

During Ga-assisted VLS growth of GaAs nanowires, only native defects can be created. The physics of native point defects and their solubilities in GaAs was comprehensively reviewed by Hurle.[185,186] Native defects can be shallow (e.g. $\mathrm{V_{As}}$) or deep (e.g. $\mathrm{As_{Ga}}$, the so-called EL2 defect[187]). The concentration of native defects can be well controlled during MBE growth, as attested by the long minority carrier lifetimes presented in Fig. 6.3.

Considering the behaviour of Au or a Au-related complex as a deep non-radiative recombination centre, we can examine its characteristic thermal activation energy E_A, which is related to the ionization energy E_I. However, care must be taken, since differences exist between the activation energy for thermal capture of a free electron (probed by PL), the thermal equilibrium depth (e.g. probed by Hall measurements), and the thermal activation depth corresponding to the energy needed to surmount the energetic barrier between the bound and the free state (e.g. determined by deep-level transient spectroscopy (DLTS) measurements).[188] Furthermore, activation and ionization energies of deep centres often depend on its charge state. This is demonstrated for Au impurities in Si, which form acceptor states at $E_C - 0.54$ eV and donor states at $E_V + 0.35$ eV in n-type and p-type silicon, respectively.[15]

A deep acceptor level with E_A of 405 meV was found by temperature dependent Hall measurements after the diffusion of Au into n-type GaAs and a shallow acceptor level with E_A of 50 meV also appeared.[164] The deep level at 400 meV was confirmed by DLTS,[165] while a level at 40 meV had been observed earlier by temperature-dependent photocon-

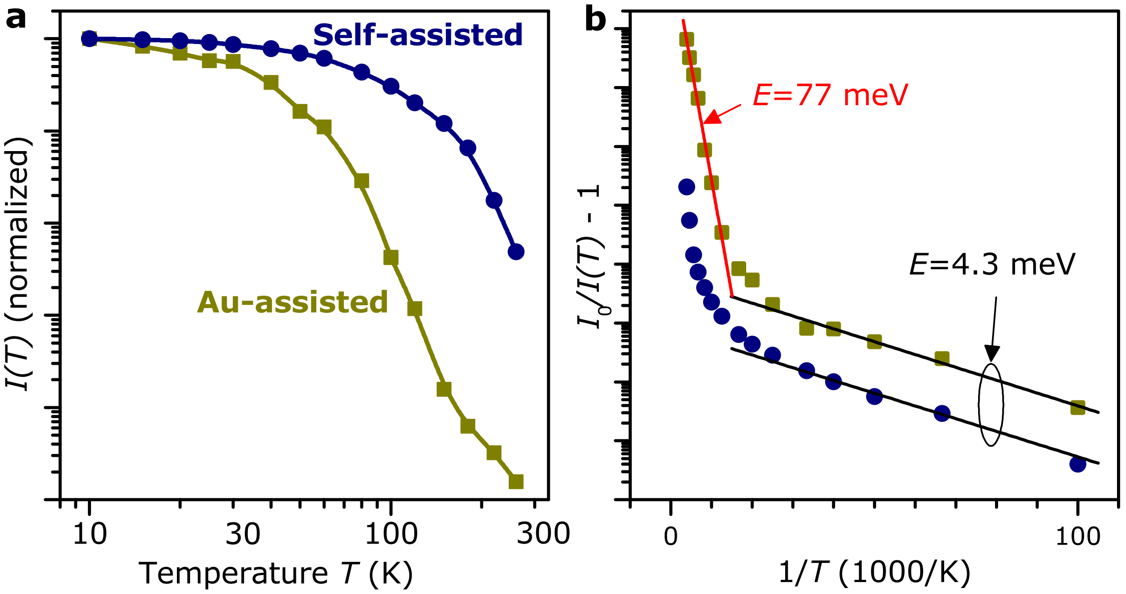

Figure 6.4.: **Thermal activation energies.** Temperature-dependence of the integrated PL intensities I of self-assisted and Au-assisted GaAs/(Al,Ga)As core-shell nanowires plotted in (a) double logarithmic representation, and (b) in a form suitable for the determination of activation energies. Linear fits to the low-temperature side in (b) yield activation energies of 4.3 meV, which correspond to the exciton binding energy in GaAs. A linear fit to the high-temperature side in (b) is possible only for the Au-assisted sample. The obtained energy of 77 meV is attributed to the thermal activation of carrier capture by a deep centre. The temperature-dependent PL measurements have been performed in cooperation with C. Pfüller.

ductivity.[189] Another study of temperature-dependent Hall coefficients showed an acceptor level at 90 meV but this could not be reproduced.[190,165]

Here, we probe the thermal activation energy of the capture of free carriers by a deep centre using temperature-dependent cwPL, for which we expect similar E_A as in the above reports.

6.3.1. Temperature-dependent PL

Figure 6.4a shows the temperature (T) dependence of the integrated PL intensities I_S and I_A for the self- and the Au-assisted nanowires, respectively. For low temperatures, both I_S and I_A saturate, indicating that η is basically unity at 10 K.

Even state-of-the-art planar heterostructures show non-radiative recombination at the interfaces (as can be seen in Fig. 6.3). Assuming that the interface recombination is independent of T, this leads to a variation of η with $1/\tau_r$ and thus approximately as $T^{-3/2}$,[191,177] which is close to what we observe for the self-assisted nanowires. For the Au-assisted nanowires, I_A falls off more rapidly with T, indicating a strongly temperature-activated non-radiative recombination channel. Close to room temperature, I_A is, as already reported above, more than two orders of magnitude smaller than I_S.

In Figure 6.4b, the data are presented such that the activation energy E_A can be determined from a linear slope similar to an Arrhenius plot, where I_0 is the PL intensity interpolated to 0 K. Using equations (6.1), (6.2) and $1/\tau = 1/\tau_r + 1/\tau_{nr}$, where τ_r and τ_{nr} are the radiative and non-radiative lifetime, respectively, one arrives at

$$I \propto 1/(1 + \tau_r/\tau_{nr}). \tag{6.5}$$

When only the non-radiative recombination is thermally activated, its rate depends on the temperature T as $1/\tau_{nr} = 1/\tau_{nr}^{\infty} \exp(-E_A/kT)$, where E_A is the activation energy, and $1/\tau_{nr}^{\infty}$ is the non-radiative recombination rate at very high T.[192] Thus,

$$I(T) = \frac{I_0}{1 + \tau_r/\tau_{nr}^{\infty} \exp(-E_A/kT)}, \tag{6.6}$$

where I_0 is the intensity extrapolated to 0 K. As a result, E_A can be determined from the linear slope in the plot of $\log(I_0/I(T) - 1)$ versus $1/T$.[192,193,175]

Towards lower T, both samples show the same behaviour with an E_A corresponding to the exciton binding energy in GaAs (4.2 meV). At higher T, however, only the Au-assisted nanowires exhibit an activated quenching with $E_A = (77 \pm 2)$ meV. A non-radiative deep recombination centre present only in the Au-assisted nanowires is thus identified.

6.3.2. Discussion

In accordance with the earlier observation of the low η in the Au-assisted nanowires, a deep centre was identified in these nanowires. This is further indication for impurity incorporation from the Au droplets during VLS growth. A thermal activation energy of 77 meV has been determined for the first time. No comparable data exist for the thermal PL activation in Au-doped GaAs.

The microscopic nature of the observed centre, i. e. whether it is due to substitutional Au, a Au-related complex or a Au-induced secondary centre, cannot be clarified in the present work. Such specifics on Au-related non-radiative recombination centres in GaAs are not presently available and are probably rather complex.[181,194,183] Furthermore, we cannot distinguish whether the centre is situated in the GaAs core or at the core-shell interface.

However, for all practical purposes, these details are quite inconsequential. Instead, it is most important that the detrimental centre is not present in the self-assisted nanowires, since we invariably observe a high internal quantum efficiency for nanowires grown by this technique. At the same time, all Au-assisted nanowires we have investigated, independent of the details of the growth conditions, suffer from very strong non-radiative recombination at room temperature.

6.4. Summary

Only the self-assisted nanowires exhibit a room-temperature minority carrier lifetime (and thus an internal quantum efficiency) comparable to the expectations for state-of-the-art material quality. The minority carrier lifetime for the Au-assisted nanowires is more than two orders of magnitude shorter than that, and this difference is directly reflected in the PL intensity of these structures. We interpret this drastic quenching as being due to the non-negligible incorporation of Au, an efficient non-radiative centre, into nanowires grown under the assistance of Au droplets. Thus, the use of Au-assisted GaAs nanowires for optoelectronic applications appears questionable, while their self-assisted counterparts do have promise.

7. Conclusion

Nanowires have gained wide attention during the last decade, because they allow the growth of strain-free semiconductor material with high crystalline quality essentially independent of the substrate.[5,6] In this way, the strong restriction to closely lattice matched systems that is imposed on traditional planar heteroepitaxy[18] can be lifted.

However, the physical properties of the resultant nanowires may depend on details of the growth process. In particular the common usage of Au during VLS nanowire growth causes concern in view of prospective application of the nanowires in electronics and optoelectronics, since Au is a deep recombination centre in many semiconductors, which can drastically reduce the minority carrier lifetime.[15] Alternatively, GaAs nanowires can be grown Au-free on substrates covered by thin SiO_x, which promotes the formation of Ga droplets that replace the Au.

In this thesis, the integration as nanowires of the prototypal compound semiconductor GaAs with the quintessential semiconductor substrate Si is studied in detail. The main aims were as follows:

- to grow GaAs nanowires on Si substrates using the Au- and the self-assisted VLS mechanism,
- to compare the physical properties of the nanowires, including morphology, crystal structure, and luminescence, as well as to analyse their nucleation behaviour, and
- to develop a theoretical understanding of the origin of specific properties that were found to differ between the nanowires growth by the two methods.

GaAs nanowires have been grown by the Au-assisted VLS mechanism on Si(111) and also on GaAs(111)B substrates, as well as by the self-assisted method on Si(111) substrates. In all cases, the nanowires are epitaxially well aligned in the [111] direction, i.e. perpendicular to the substrates, in agreement with earlier studies.[46] No residual strain can be found by HR-TEM at a distance d, similar to the nanowire diameter, away from the interface. This confirms the mechanical Principle of St. Venant, which concerns the strain release in any clamped rod.

All our Au-assisted VLS grown GaAs nanowires predominantly adopt the WZ crystal structure, with very short sections of ZB at the very bottom and sometimes also a the tip, in agreement with the monolayer nucleation model of Glas et al.[67] In contrast, the self-assisted nanowires are predominantly ZB and include several twin planes. Some samples show short WZ segments located in a region close to the nanowire ends, in agreement with similar observations reported by other authors.[63,153]

During the growth of Au-assisted nanowires, a highly defective planar basal layer forms, which traps a fraction of the Au in clusters at the interface. For self-assisted nanowires, parasitic growth can be reduced to 1/4 of the total incident supply, by adopting stoichiometric V/III supply flux ratio and low growth rates, but melt-back etching of the Si substrate has been observed at the basal interface.

The early stage of nanowire growth has been studied and reveals a strong dependence on the growth method. By the self-assisted VLS mechanism on Si(111) substrates, the majority of the GaAs grows immediately in the vertical [111] direction and forms well separated nanowires with very little parasitic growth in between. In contrast, the Au-assisted VLS mechanism on Si(111) substrates results in the crystallization of initially vertically elongated traces of GaAs, which gradually coalesce and cover the substrate surface, but eventually change growth direction into the vertical. This delayed vertical nanowire growth can be explained by the lower interface energy of the Au droplets on the free Si(111) substrate surface, when compared with that on the newly formed GaAs. This is corroborated by the observation that the Au-assisted nanowire nucleation on GaAs(111)B, on which the droplet-substrate and droplet-nanowire interface energies are identical, does not lead to trace growth and vertical nanowires form immediately.

Clearly, the initial growth of vertical traces by the Au-assisted method on Si is disadvantageous in view of technological applications, since it leads to the formation of a low-quality intermediate GaAs layer, thus sidestepping the advantage of the nanowire geometry. In terms of selectivity and reduced parasitic growth, the self-assisted growth of GaAs nanowires appears to be superior. However, a profound understanding of the influence of the oxide quality on the formation of Ga droplets and thus on nanowire growth remains to be achieved.

Caused by the large surface-to-volume ratio of nanowires, the side facets can have very significant influence on the performance of nanowires in future devices. The side facets of the Au-assisted and self-assisted GaAs nanowires grown by us have been analysed and compared with observations reported in the literature. The fascinating result is that the two methods lead to mutually different side facet orientations for GaAs nanowires with the ZB crystal structure. Current VLS nanowire growth theory, basing on the monolayer nucleation model by Glas,[67] has been applied in order to predict the dependence of the facet orientation on the droplet material.

A simple expression has been extracted, which describes the dependence of the lateral energy of nuclei on their side facet orientation. By a minimisation of this lateral energy, the nucleus with the smallest energy barrier and thus with the highest formation likelihood has been calculated. The lateral energy of the nucleus depends on the droplet material via the liquid-vapour surface energy and the nanowire contact angle, two parameters whose values during growth are not very accurately known, but which have been estimated. As a result, extended $\{1\bar{1}0\}$ facets are predicted to be most stable for self-assisted GaAs nanowire growth, while composed (112)-type facets consisting of $\{\bar{1}\bar{1}\bar{1}\}$B, $\{111\}$A, and $\{001\}$ nano-facets are predicted for different sets of plausible conditions for Au-assisted nanowire growth. Both theoretical predictions are in accordance with the experimental observations.

Finally, the possibly detrimental influence of Au used during nanowire synthesis is analysed by measurements of the minority carrier lifetime, which can readily be obtained on as-grown GaAs nanowire samples by time-resolved photoluminescence (PL) spectroscopy. For measurements of the minority carrier lifetime at room temperature, which is significantly more important for applications than at cryogenic temperatures, the GaAs nanowires have been capped with a shell of (Al,Ga)As in order to disable the large surface recombination of the free GaAs surface.

GaAs/(Al,Ga)As core-shell nanowires have been fabricated by the Au- and the self-assisted VLS mechanism with a nominal Al content of 10%. Their minority carrier lifetimes have been measured by time-resolved PL at room-temperature. While the self-assisted nanowires show lifetimes that reach the nanosecond range expected for high-quality GaAs/(Al,Ga)As material with these dimensions, the values for the Au-assisted nanowires lie in the low picosecond range, but nevertheless agree with other reported room-temperature lifetimes for Au-assisted GaAs/(Al,Ga)As core-shell nanowires, which were grown by MOVPE.[171] Since the effect is far too strong to be explained by the slightly different diameters and growth temperatures of the nanowires, an additional non-radiative recombination channel is concluded to be present in the Au-assisted nanowires.

Further measurements of the temperature-dependent PL intensity reveal that this additional channel in the Au-assisted nanowires is thermally activated, which is typical for non-radiative recombination at deep centres. We conclude that Au, which is a deep level in GaAs,[164,165] is indeed incorporated into the nanowire during growth and functions as a non-radiative recombination centre. The incorporated Au concentration is probably small since the solid solubility of Au in GaAs lies in the 10^{16} cm^{-3} range.[181] However, non-radiative recombination at deep centres is a highly efficient process. Thus, the suitability of Au-assisted nanowires for optoelectronic applications must be questioned, while the self-assisted wires show promise.

In conclusion, we find that GaAs nanowires grown by the self-assisted method have more appealing characteristics for device applications. They grow in standard MBE systems without the need for an additional Au cell. The nucleation of vertical nanowires is immediate and any parasitic growth between them can be reduced to a small fraction of the total GaAs volume. The stability of extended vertical $\{1\bar{1}0\}$ side facets completely avoids the formation of composed inclined side facets, whose growth can lead to twin plane defects. Most importantly, only the self-assisted nanowires have minority carrier lifetimes that can compete with planar double heterostructures.

In contrast, the Au-assisted GaAs nanowires are superior in minor aspects only. The easy growth of long nanowire segments with pure WZ crystal structure makes them suitable for a detailed analysis of the optical and electronic properties of WZ GaAs. The formation of (112)-type side facets, that are composed from $\{111\}$A &$\{\bar{1}\bar{1}\bar{1}\}$B segments separated by twin planes, can be used for the controlled growth of twin plane superlattices, which does not appear to be possible by self-assisted growth. Therefore, the Au-assisted mechanism might still be useful for more fundamental investigations. Nevertheless, the self-assisted mechanism appears to be vastly more advantageous for technological applications.

A. Appendix

A selection of experimental methods are presented here. The basics of molecular beam epitaxy, the technique most central to this work, are briefly discussed in Section 2.1.1. It is followed by a more detailed description of the calibration of substrate temperature and particularly beam flux measurements in Section A.1. Different methods for the preparation of an clean Si substrate surface are presented in Section A.2.

A.1. Calibration of MBE Machine

Central MBE parameters such as sample temperature and beam fluxes cannot simply be measured with good accuracy in a straight-forward fashion. Care has to be taken to ensure that measurements of these data can be compared between different growth runs and between different MBE machines.

Temperature Calibration

The calibration of substrate temperatures T_S during growth is a standard issue, since the standard thermocouples that measure T_S at the sample back side regularly deviate from the real temperature by more than 100°C. Thus, on the Si substrates, the substrate temperatures T_S were measured by pyrometers: Ircon Modline Plus in the Au chamber and Quasys ML-AAPX/090 in the V/III chamber. On GaAs substrates, which were used for comparative experiments and calibration layers, T_S was calibrated using the observation by RHEED of the oxide desorption at the exact temperature of $T_{des.} = 582°\text{C}$.[195] The error in the measurements of T_S is expected to be 10 K.

Source Calibration

Although the flux J of a molecular beam (number of particles per unit time and area) cannot directly be measured, a derived quantity can. The *beam equivalent pressure* (BEP) of the source element X, p_X, is the pressure measured by a (Bayard-Alpert) hot cathode ionization gauge when moved to the sample position. BEP readings are sufficient to reproduce the growth conditions within one MBE chamber over time. However, experimentally determined BEP values depend on the position of the ionization gauge, the condition of filament and collector, and the chamber geometry such that BEP readings from different MBE chambers cannot meaningfully be compared. For this purpose, a quantification of the actual fluxes is necessary. In principle, the following relation exists between the ratio of source fluxes J_V/J_{III} (flux ratio) and the ratio of measured BEPs p_V/p_{III} (BEP ratio)

$$\frac{J_V}{J_{III}} = \frac{p_V}{p_{III}} \frac{I_{III}}{I_V} \sqrt{\frac{T_V}{T_{III}} \frac{M_{III}}{M_V}}, \tag{A.1}$$

where p_V and p_{III} denote the ionisation gauge readings (BEPs), I_V and I_{III} are the ionisation cross sections, M_V and M_{III} the molecular weights of the beam species, and T_V

and T_{III} are the Kelvin temperatures of the species in the molecular beams, of V and III compound, respectively. The flux ratio J_V/J_{III} has the advantage that it is more conveniently related to growth stoichiometry than the BEP ratio. In practice, however, the parameters I_V and I_{III} are not known accurately enough to employ the above conversion. Fortunately, there exists an alternative. RHEED oscillations in the arsenic-rich and gallium-rich regimes can be used to accurately determine the actual incorporation rates of both gallium and arsenic. How this was done in practice is detailed in the following section.

Source Flux Calibration using RHEED Oscillations

The Ga and As fluxes can be calibrated using intensity oscillations of RHEED reflections caused by a periodic variation of the surface morphology during layer-by-layer growth.[196,197] The electron reflectivity and detected RHEED intensity are maximum when one single layer is completed and minimum when a half-complete layer leads to strong diffuse scattering. The oscillation period t_p corresponds to the growth duration for one single layer of GaAs, i.e. a complete layer of Ga and As atoms, here $d_{002} = a/2 \simeq 2.826$ Å in height. Therefore, the growth rate is $v = d_{002}/t_p$ and the incorporated flux of each element is $J = v/\Omega$, where $\Omega = a^3/4 \simeq 45.168$ Å^3 is the crystal volume of one Ga-As pair. Since the growth rate is limited by the smallest supply, the incorporated As flux can be determined under As-limited (Ga-rich) conditions and vice versa.

Of course, the thus determined incorporated fluxes are not generally identical to the supplied fluxes which were analysed in the preceding section. In particular for the arsenic supply, we would have to account for the dissociation of the incoming As_4 and its limited sticking coefficient, for which a maximum value of 0.5 has been reported.[198] However, it is the incorporated fluxes that we are most interested in when comparing growth conditions.

In order to observe RHEED oscillations in practise, an atomically flat surface with large terrace widths must be prepared first. We employed on-axis GaAs(001) substrates and grew a ~200 nm thick buffer layer in the following way.[199] At a substrate temperature $T_S = 580°\text{C}$, a high value of $p_{As} \approx 9 \times 10^{-6}$ mbar was set and the As shutter and valve were opened, while T_{Ga} was set to correspond to a low value of $p_{Ga} \approx 2 \times 10^{-7}$ mbar. Pulsed GaAs growth was started by opening the Ga shutter for a 20 s pulse and then closing it for a 60 s break until opening again. The high p_{As_4}/p_{Ga} ratio led to a As-rich (2×4) surface (readily identified by the 4× reflections on a Laue circle in the $[1\bar{1}0]$ azimuth). During the periods without new Ga arriving, the Ga atoms already present at the surface have a longer migration length and the chances to find the thermodynamically most stable arrangement without defects are enhanced.[200] Thus, pulsed growth leads to the formation of smooth (001) terraces even on originally rough surfaces. For typical as-delivered GaAs(001) substrates, 20 pulses sufficed. Afterwards, T_S was increased to 600°C and p_{As} was decreased until a 1× reconstruction in the $[1\bar{1}0]$ azimuth indicated (nearly) stoichiometry at the surface. In case that a 2× reconstruction or a even a decreasing RHEED pattern intensity indicated Ga-rich conditions, p_{As_4} was increased to return to stoichiometry. Under this new growth condition, a thick buffer layer of high quality GaAs was grown continuously for 30 min.

The substrate was thus ready for the study of RHEED oscillations. Initially, the desired p_{Ga} was set and the p_{As_4} was decreased in steps starting from a high value. After opening of the Ga shutter, layer-by-layer GaAs growth induced RHEED oscillations with decreasing amplitude. After about six oscillations, the Ga shutter was closed and the surface was annealed at 600°C for 5 min before the procedure was repeated for the next value of p_{As_4}.

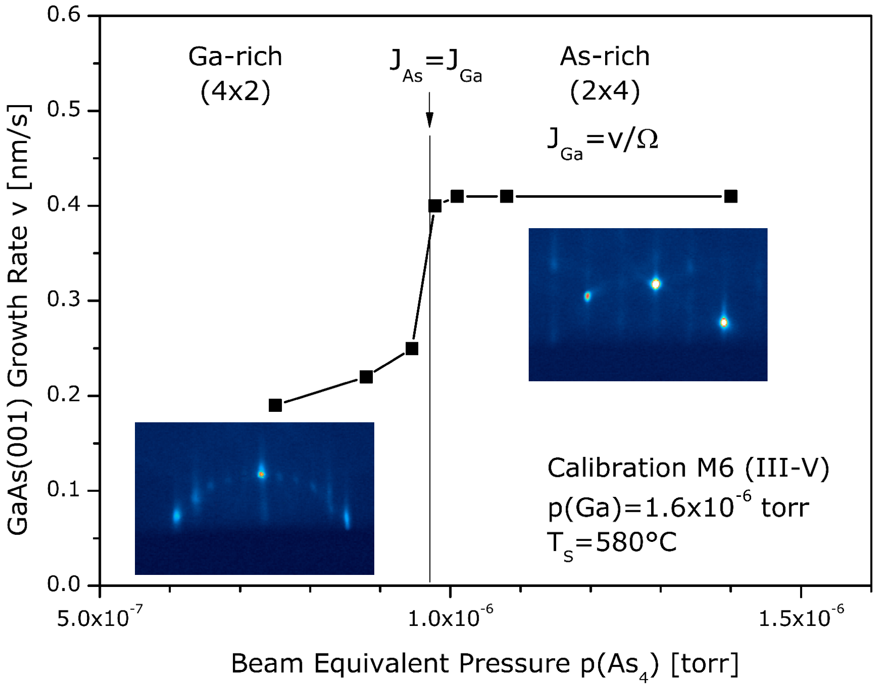

Figure A.1.: **Calibration of Group III and V fluxes** Dependency of growth rate v on p_{As_4}, as determined by RHEED oscillations on GaAs(001). In the As-rich regime, identified by the (2×4) reconstruction, v is limited by the constant Ga flux J_{Ga}, such that $v = J_{Ga}\,\Omega$. In the Ga-rich regime, the reconstruction changes to (4×2) and v depends on p_{As_4}. At the threshold marked by a vertical line, identical fluxes of both species are incorporated and $J_{As} = J_{Ga}$. Insets show RHEED patterns for both regimes obtained in the [110] azimuth.

Figure A.1 shows a plot of the planar growth rate v versus p_{As_4}. Under the As-rich growth conditions typical for GaAs layer growth, all arriving Ga atoms stick to the surface and are incorporated, such that the planar growth rate v is limited by the incident Ga flux which was constant. We thus find for example that the Ga supply with BEP $p_{Ga} = 1.6 \times 10^{-6}$ torr corresponds to an incorporated Ga flux of $J_{Ga} = v/\Omega \simeq 9.1\ \mathrm{s}^{-1}\mathrm{nm}^{-2}$. When p_{As_4} was reduced below a threshold value, the growth rate decreased. At this threshold, which also corresponds to the transition from As-rich (2×4) to Ga-rich (4×2) reconstruction,[155,201] the net incoming fluxes of both elements are just balanced and both sticking coefficients are maximal. Under this condition, just enough As atoms are available for every arriving Ga atom to find a reaction partner and $J_{As} = J_{Ga}$. In this way, it was found that the arsenic supply with BEP $p_{As_4} = 9.7 \times 10^{-7}$ torr corresponds to a net arriving atomic As flux $J_{As} = v/\Omega \simeq 9.1\ \mathrm{s}^{-1}\mathrm{nm}^{-2}$.

Wherever growth conditions are quoted throughout this work, the net incoming V/III flux ratio J_{As}/J_{Ga} is given. It is thereby implicitly assumed that the dissociation and sticking of Ga and As_4 do not depend on the surface orientation.

A.2. Silicon Surface Preparation

Substrate cleaning is a basic prerequisite for any epitaxial growth since surface contaminants generally create defects in the growing crystals. The preparation of a clean Si surface needed particular attention since a) Si buffer layer growth was not possible in our MBE, and b) very high temperatures are required for purely thermal desorption of oxides and carbides, which cannot be achieved in our MBE machine.

Temperatures around 1200°C have been employed to clean Si surfaces in UHV environment,[202,203] but they result in unintentional diffusion of impurities and dopants. Furthermore, crystal defects such as dislocations and stacking faults increase at this very high temperature. Several approaches have therefore been reported to prepare a clean Si surface below 900°C.[204]

Gallium Polishing

One cleaning strategy that is very simple to use in III-V MBE is the *Ga-Polishing* procedure, in which the Si substrate is subjected to an atomic Ga beam during or just before the heating to 800°C, thereby converting the stable silicon oxide to volatile gallium oxide.[92] It was shown that formation of silicon carbides can also be avoided by this procedure. The detailed Ga-polishing procedure used in our experiments is presented as follows.

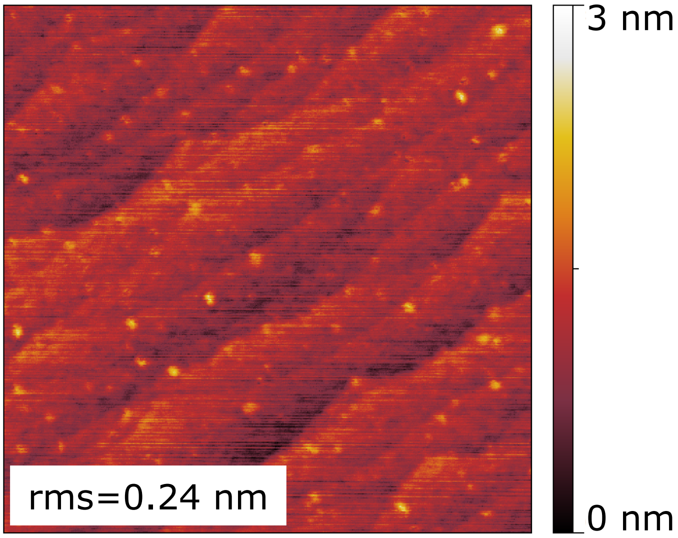

Figure A.2.: **Si(111) after cleaning by Ga-Polishing method** AFM micrograph (1µm × 1µm) shows Si(111) atomic terraces decorated with unintentional particles.

1 Degassing of the as-received Si(111) substrates at 300°C for 30 min in load lock

2 Deposition of ~ 3 nm of Ga at substrate temperature $T_S = 500°\mathrm{C}$ for 1 min

3 Heating to $T_S = 800°\mathrm{C}$ for 5-15 min, observation of an increase in the RHEED intensity

A typical AFM image of a Si(111) substrate cleaned by Ga-Polishing is depicted in Figure A.2. Terraces separated by (multi-)atomic steps have been formed but the surface is decorated with particles, which may be saw dust remaining from the sawing of the wafers.

Chemical Methods

Another group of techniques bases on chemical cleaning of the Si wafers prior to loading, in order to remove the damaged top Si layer including any contaminants and to form a thin protective oxide. According to the way in which this oxide is then removed, the chemical cleaning methods can generally be grouped into hydrophilic and hydrophobic.

The hydrophilic strategy consists in loading the substrates into the MBE with the protective oxide and removing it by a 800°C anneal using the reaction $Si + SiO_2 \rightarrow 2\,SiO$. The advantage of this strategy is that the protective oxide is inert against reactions with air and thus this process is rather robust. The main disadvantage of the hydrophilic method is that it has been associated with a significant contamination of the surface with boron dissolved from the glassware, which leads to unintentional p-type doping of the Si,[205] and an increased roughening of the surface.[206]

Alternatively, the protective oxide can be chemically removed prior to loading by short immersion in hydrofluoric acid (HF dip), thus creating a hydrophobic surface terminated by hydrogen, which is thermally desorbed in UHV at around 500°C. Thus, every hydrophilic cleaning recipe can be converted to a hydrophobic one by adding a final HF dip. The Si-H hydrogen termination is not stable in air but slowly reacts with ambient water vapour and oxygen to form Si-OH and native oxide. Therefore, the time between the HF dip and subsequent loading into UHV must be minimized.

Owing to the enormous technological importance of Si, there are numerous recipes for its chemical cleaning. Invented in the 1960s by Kern et al. at Radio Corporation of America, the RCA method consists of several chemical steps for removal of surface impurities and oxidation of the surface.[207] It has been improved by Ishizaka and Shiraki, who intentionally split the steps for removal of the damaged Si layer from those for the creation of the protective oxide, and thereby achieved increased surface purity.[204] However, their process is rather long as it involves 18 chemical steps.

Piranha Solution and Hydrofluoric Acid

In 1998, Miki et al. argued that the quality of Si wafers had sufficiently improved for the number of chemical Si cleaning steps to be maximally reduced.[206] They showed that a one-step treatment of as-received Si wafers in H_2SO_4:H_2O_2 solution (*"Piranha solution"*) and subsequent UHV anneal (hydrophilic strategy) led to identical results as did the Ishizaka-Shiraki method. The surface quality could be further improved by an additional HF dip (hydrophobic strategy), which reduced the boron contamination by an order of magnitude. The following steps were thus employed for the Si cleaning with H_2SO_4:H_2O_2 and HF, hereafter called *HF-Procedure*.

1 H_2SO_4 (98%):H_2O_2 (30%) 2:1 for 10 min

2 ultra pure H_2O rinse

3 HF(1%) dip, check for hydrophobic surface

4 transport substrate in ultra pure H_2O to MBE machine and load within 15 min

Since some substrates had been found to be decorated with unwanted particles (Fig. A.2), the steps 1-3 were repeated in order to remove more of the contaminated surface including the particles. The resultant Si surface morphology is presented in Figure A.3, which

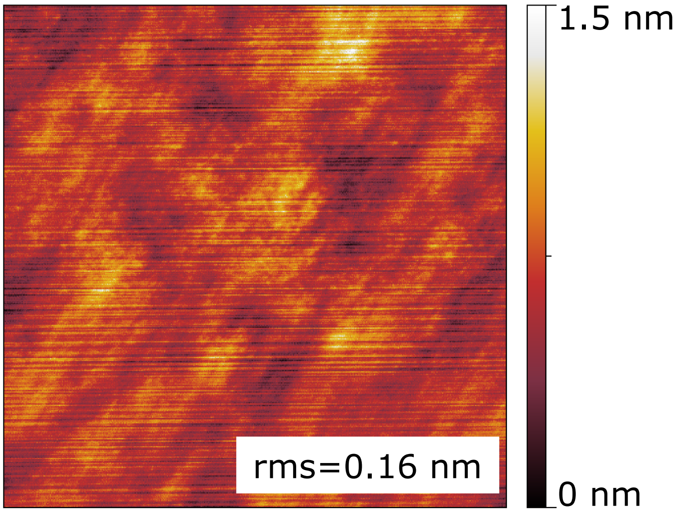

Figure A.3.: **Si(111) after cleaning by Piranha solution and Hydrofluoric Acid.** AFM micrograph (1 μm × 1 μm) shows that the surface is rough on the atomic scale.

shows that the surface has a very small root-mean-square (rms) roughness, but no atomic terraces can be identified.

Piranha Solution and Ammonium Fluoride

When atomically flat substrates are required, all chemical methods are faced with the problem that the oxidation of the Si substrate, that is necessary to remove the damaged top layer, creates a rough Si/SiO_2 interface.[93] Subsequent removal of the oxide by isotropic HF etching does not eliminate this roughness. In principle, heating to 800°C should recover atomic terraces, since then the Si atoms can rearrange over long distances. To explain the experimental finding that this is often not the case, it is natural to assume that residual contaminations efficiently block the Si diffusion. Residual boron contamination has been suggested to account for the observed rough surfaces prepared by the Ishizaka-Shiraki method and thermal annealing.[206] Arsenic might be similarly effective in preventing Si migration, since it is known to bind strongly to the Si surface and changes the Si(111) 7×7 reconstruction to a Si(111):As 1×1.[116] In our case, the formation of atomic terraces - and the 7×7 reconstruction - may thus be hampered by the residual As present in the growth chamber.

Fortunately, there exists an alternative route to achieving atomically flat Si(111) surfaces, namely by anisotropic etching with ammonium fluoride (NH_4F), which selectively etches all other orientations faster than (111).[102] Recently, the problem of NH_4F etching of creating triangular etch pits has been resolved by a simple two-step NH_4F treatment.[208]

The following *NH_4F-Procedure* was thus employed to produce atomically flat terraces on Si(111) wafers.

1 H_2SO_4 (98%):H_2O_2 (30%) 2:1 for 10 min

2 ultra pure H_2O rinse

3 NH_4F (40%) etch for 100 s

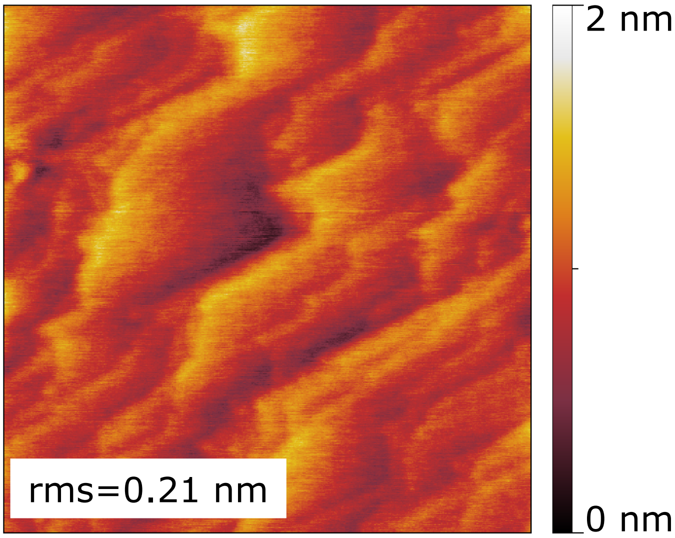

Figure A.4.: **Si(111) after cleaning by Piranha solution and Ammonium Fluoride.** AFM micrograph (1µm ×1µm) shows Si(111) atomic terraces decorated with unintentional particles.

4 NH_4F (40%) etch for 10 min in fresh solution

5 transport substrate in ultra pure H_2O to MBE machine and load within 15 min

Again, steps 1-3 were repeated to remove any remnant particles from the surface. Then, a particle-free, terraced surface morphology resulted as checked by AFM and presented in Figure A.4.

Bibliography

[1] J Bardeen and W H Brattain. The transistor; a semiconductor triode. *Physical Review*, 74:230, 1948.

[2] R E Hall, G E Fenner, J D Kingsley, T J Soltys, and R O Carlson. Coherent light emission from GaAs junctions. *Physical Review Letters*, 9:366, 1962.

[3] Z Alferov, V M Andreev, M B Kagan, I I Protasov, and V G Trofim. Solar-energy converters based on p-n Al(x)Ga(1-x)As-GaAs heterojunctions. *Soviet Physics - Semiconductors*, 4:2047, 1971.

[4] T Mimura, S Hiyamizu, T Fuji, and K Nanbu. A new field-effect transistor with selectively doped GaAs/n-AlxGa(1-x)As heterojunctions. *Japanese Journal of Applied Physics*, 19:L225, 1980.

[5] M G Lagally and R H Blick. A 'bed of nails' on silicon. *Nature*, 432:450, 2004.

[6] T Martensson, C P T Svensson, B A Wacaser, M W Larsson, W Seifert, K Deppert, A Gustafsson, L R Wallenberg, and L Samuelson. Epitaxial III-V nanowires on silicon. *Nano Letters*, 4(10):1987–1990, 2004.

[7] Frank Glas. Critical dimensions for the plastic relaxation of strained axial heterostructures in free-standing nanowires. *Physical Review B*, 74(12):121302(R), 2006.

[8] E Ertekin, P A Greaney, D C Chrzan, and T D Sands. Equilibrium limits of coherency in strained nanowire heterostructures. *Journal of Applied Physics*, 97:114325, 2005.

[9] S Harui, H Tamiya, T Akagi, H Miyake, K Hiramatsu, T Araki, and Y Nanishi. Transmission Electron Microscopy Characterization of Position-Controlled InN Nanocolumns. *Japanese Journal of Applied Physics*, 47:5330, 2008.

[10] F Patolsky, G Zheng, and C M Lieber. Nanowire sensors for medicine and the life sciences. *Nanomedicine*, 1:51, 2006.

[11] M D Kelzenberg, S W Boettcher, J A Petykiewicz, D B Turner-Evans, M C Putnam, E L Warren, J M Spurgeon, R M Briggs, N S Lewis, and H A Atwater. Enhanced absorption and carrier collection in Si wire arrays for photovoltaic applications. *Nature Materials*, 9:368, 2010.

[12] W Lu and C M Lieber. Nanoelectronics from the bottom up. *Nature Materials*, 6: 841, 2007.

[13] R S Wagner and W C Ellis. Vapor-Liquid-Solid mechanism of single crystal growth. *Applied Physics Letters*, 4:89, 1964.

[14] Maria E Messing, Karla Hillerich, Jonas Johansson, Knut Deppert, and Kimperly A Dick. The use of gold for fabrication of nanowire structures. *Gold Bulletin*, 42:172, 2009.

[15] W M Bullis. Properties of Gold in Silicon. *Solid-State Electronics*, 9:143–168, 1966.

[16] M C Putnam, M A Filler, B M Kayes, M D Kelzenberg, Y Giuan, N S Lewis, J M Eiler, and H A Atwater. Secondary Ion Mass Spectroscopy of Vapor-Liquid-Solid grown Au-catalyzed Si Wires. *Nano Letters*, 8:3109, 2008.

[17] A Fontcuberta i Morral, C Colombo, G Abstreiter, J Arbiol, and J R Morante. Nucleation mechanism of gallium-assisted molecular beam epitaxy growth of gallium arsenide nanowires. *Applied Physics Letters*, 92(6):063112, 2008.

[18] H Krömer. Quasi-electric fields and band offsets: teaching electrons new tricks. In *Nobel lecture, Stockholm*, 2000.

[19] E H C Parker, editor. *The technology and physics of molecular beam epitaxy*. Plenum Press, 1985.

[20] R F C Farrow. *Molecular beam epitaxy: applications to key materials*. Noyes Publications, Park Ridge, New Jersey, 1995.

[21] M A Herman and H Sitter. *Molecular beam epitaxy: fundamentals and current status*. Springer series in materials science. Springer Berlin, 1996.

[22] J Y Tsao. *Materials Fundamentals of Molecular Beam Epitaxy*. Academic Press, Boston, 1993.

[23] N N Ledentsov. *Growth Processes and Surface Phase Equilibria in Molecular Beam Epitaxy*. Springer Berlin, 1999.

[24] J A Venables, G D T Spiller, and M Hanbrücken. Nucleation and Growth of Thin Films. *Reports on Progress in Physics*, 47:399, 1984.

[25] S F Fang, K Adomi, S Iyer, H Morcoc, and H Zabel. Gallium arsenide and other compound semiconductors on silicon. *Journal of Applied Physics*, 68:R31, 1990.

[26] Y B Bolkhovityanov and O P Pchelyakov. GaAs epitaxy on Si substrates: modern status of research and engineering. *Physics - Uspekhi*, 51:437–456, 2008.

[27] Hiroyuki Usui, Hidehiro Yasuda, and Hirotaro Mori. Morphology and lattice coherency in GaAs nanocrystals grown on Si(100) surface. *Applied Physics Letters*, 89 (17):173127, 2006.

[28] V K Yang, M Groenert, C W Leitz, A J Pitera, M T Currie, and E A Fitzgerald. Crack formation in GaAs heteroepitaxial films on Si and SiGe virtual substrates. *Journal of Applied Physics*, 93:3859, 2003.

[29] H Krömer. Polar-on-Nonpolar Epitaxy. *Journal of Crystal Growth*, 81:193, 1987.

[30] Nozawa and Horikoshi. Effects of Annealing on the Structural Properties of GaAs on Si(100) Grown at a Low Temperature by Migration-Enhanced Epitaxy. *Japanese Journal of Applied Physics*, 29:L540, 1990.

[31] M Yamaguchi, M Tachikawa, Y Itoh, M Sugo, and S Kondo. Thermal annealing effects of defect reduction in GaAs on Si substrates. *Journal of Applied Physics*, 68: 4518, 1990.

[32] Wu-Yih Uen, Zhen-Yu Li, Yen-Chin Huang, Meng-Chu Chen, Tsun-Neng Yang, Shan-Ming Lan, Chih-Hung Wu, Hwe-Fen Hong, and Gou-Chung Chi. Heteroepitaxial growth of GaAs on Si by MOVPE using a-GaAs/a-Si double-buffer layers. *Journal of Crystal Growth*, 295(2):103 – 107, 2006.

[33] V. Schmidt, J. V. Wittemann, S. Senz, and U. Gösele. Silicon Nanowires: A Review on Aspects of their Growth and their Electrical Properties. *Advanced Materials*, 21: 2681, 2009.

[34] A E H Love. *A Treatise on the Mathematical Theory of Elasticity*. Dover, New York, 4th edition, 1944.

[35] S Timoshenko and J Goodier. *Theory of Elasticity, 2nd edition*. McGraw-Hill, New York, 1951.

[36] E P A M Bakkers, J A van Dam, S de Franceschi, L P Kouwenhoven, M Kaiser, M Verheijen, H Wondergem, and P van der Sluis. Epitaxial growth of InP nanowires on germanium. *Nature Materials*, 3:769, 2004.

[37] G E Cirlin, V G Dubrovskii, I P Soshnikov, N V Sibirev, Y B Samsonenko, A D Bouravleuv, J C Harmand, and F Glas. Critical diameters and temperature domains for MBE growth of III-V nanowires on lattice mismatched substrates. *Physica Status Solidi - Rapid Research Letters*, 3:112, 2009.

[38] K Tomioka, J Motohisa, S Hara, K Hiruma, and T Fukui. III-V Semiconductor Nanowires on Si: Selective Area MOVPE and Their Device Applications. In *MRS Spring Meeting, Symposium EE5.6*, 2011.

[39] Y Xia, P Yang, Y Sun, Y Wu, B Mayers, B Gates, Y Yin, F Kim, and H Yan. One-Dimensional Nanostructures: Synthesis, Characterization, and Applications. *Advanced Materials*, 15:353, 2003.

[40] K A Dick. A review of nanowire growth promoted by alloys and non-alloying elements with emphasis on Au-assisted III-V nanowires. *Progress in Crystal Growth and Characterization of Materials*, 54:138–173, 2008.

[41] Brent A Wacaser, Kimberly A Dick, Jonas Johansson, Magnus T Borgstrom, Knut Deppert, and Lars Samuelson. Preferential Interface Nucleation: An Expansion of the VLS growth mechanism for nanowires. *Advanced Materials*, 21(2):153–165, 2009.

[42] A I Persson, M W Larsson, S Stenström, B J Ohlsson, L Samuelson, and L R Wallenberg. Solid-phase diffusion mechanism for GaAs nanowire growth. *Nature Materials*, 3:677, 2004.

[43] T J Trentler, K M Hickman, S C Goel, A M Viano, P C Gibbons, and W E Buhro. Solution-Liquid-Solid Growth of Crystalline III-V Semiconductors: An Analogy to Vapor-Liquid-Solid Growth. *Science*, 270:1791, 1995.

[44] JD Holmes, KP Johnston, RC Doty, and BA Korgel. Control of thickness and orientation of solution-grown silicon nanowires. *Science*, 287:1471, 2000.

[45] A T Heitsch, D D Fanfair, H Y Tuan, and B A Korgel. Solution-Liquid-Solid (SLS) Growth of Silicon Nanowires. *Journal of the American Chemical Society*, 130:5436, 2008.

[46] K Hiruma, M Yazawa, T Katsuyama, K Ogawa, K Haraguchi, M Koguchi, and H Kakibayashi. Growth and optical properties of nanometer-scale GaAs and InAs whiskers. *Journal of Applied Physics*, 77:447, 1995.

[47] J. C. Harmand, G. Patriarche, N. Pere-Laperne, M-N. Merat-Combes, L. Travers, and F. Glas. Analysis of vapor-liquid-solid mechanism in Au-assisted GaAs nanowire growth. *Applied Physics Letters*, 87:203101, 2005.

[48] J. C. Harmand, M. Tchernycheva, G. Patriarche, L. Travers, F. Glas, and G. Cirlin. GaAs nanowires formed by Au-assisted molecular beam epitaxy: Effect of growth temperature. *Journal of Crystal Growth*, 301:853, 2007.

[49] M Ohtsuka and A Suzuki. Simulation of epitaxial growth over patterned substrates. *Journal of Crystal Growth*, 95:55, 1989.

[50] J Motohisa, J Noborisaka, J Takeda, M Inari, and T Fukui. Catalyst-free selective-area MOVPE of semiconductor nanowires on (111)B oriented substrates. *Journal of Crystal Growth*, 272:180, 2004.

[51] K Ikejiri, J Noborisaka, S Hara, J Motohisa, and T Fukui. Mechanism of catalyst-free growth of GaAs nanowires by selective area MOVPE. *Journal of Crystal Growth*, 298:616, 2007.

[52] K Tomioka, J Motohisa, S Hara, K Hiruma, and T Fukui. GaAs/AlGaAs Core Multishell Nanowire-Based Light-Emitting Diodes on Si. *Nano Letters*, 10:1639, 2010.

[53] R B Finkelman, R R Larson, and E J Dwornik. Naturally occurring vapour-liquid-solid (VLS) whisker growth of Germanium Sulfide. *Journal of Crystal Growth*, 22: 159, 1974.

[54] J L Carter. VLS (Vapor-Liquid-Solid): Newly discovered growth mechanism on the Lunar surface? *Science*, 181:841, 1973.

[55] Kimberly A Dick. *Epitaxial Growth and Design of Nanowires and Complex Nanostructures*. PhD thesis, Lund University, 2007.

[56] R S Wagner. *Whisker Technology*. Wiley-Interscience, New York, 1970.

[57] E I Givargizov. Fundamental Aspects of VLS Growth. *Journal of Crystal Growth*, 31: 20–30, 1975.

[58] Hugh Baker, editor. *ASM Handbook, vol. 3, Alloy Phase Diagrams*. ASM International. Handbook Committee., 1992.

[59] C T Tsai and R S Williams. Solid Phase Equilibria in the Au-Ga-As, Au-Ga-Sb, Au-In-As, and Au-In-Sb ternaries. *Journal of Materials Research*, 1:352, 1986.

[60] F. Glas, J. C. Harmand, and G. Patriarche. Nucleation Antibunching in Catalyst-Assisted Nanowire Growth. *Physical Review Letters*, 104:135501, 2010.

[61] Bernhard Mandl, Julian Stangl, Thomas Martensson, Anders Mikkelsen, Jessica Eriksson, Lisa S. Karlsson, Gunther Bauer, Lars Samuelson, and Werner Seifert. Au-free epitaxial growth of InAs nanowires. *Nano Letters*, 6(8):1817–1821, 2006.

[62] B Mandl, J Stangl, E Hilner, A A Zakharov, K Hillerich, A W Dey, L Samuelson, G Bauer, K Deppert, and A Mikkelsen. Growth Mechanism of Self-catalyzed Group III-V Nanowires. *Nano Letters*, 10:4443, 2010.

[63] S Plissard, K A Dick, G Larrieu, S Godey, A Addad, X Wallart, and P Caroff. Gold-free growth of GaAs nanowires on silicon: arrays and polytypism. *Nanotechnology*, 21:385602, 2010.

[64] M Koguchi, H Kakibajashi, M Yazawa, K Hiruma, and T Katsuyama. Crystal Structure Change of GaAs and InAs Whiskers from Zinc-Blende to Wurtzite Type. *Japanese Journal of Applied Physics*, 31:2061, 1992.

[65] M Tchernycheva, J C Harmand, G Patriarche, L Travers, and G E Cirlin. Temperature conditions for GaAs nanowire formation by Au-assisted molecular beam epitaxy. *Nanotechnology*, 17:4025, 2006.

[66] K A Dick, P Caroff, J Bolinsson, M E Messing, J Johansson, K Deppert, L R Wallenberg, and L Samuelson. Control of III-V nanowire crystal structure by growth parameter tuning. *Semiconductor Science and Technology*, 25:024009, 2010.

[67] F. Glas, J. C. Harmand, and G. Patriarche. Why does Wurtzite form in Nanowires of III-V Zinc Blende Semiconductors? *Physical Review Letters*, 99:146101, 2007.

[68] M. I. McMahon and R. J. Nelmes. Observation of a Wurtzite Form of Gallium Arsenide. *Physical Review Letters*, 95:215505, 2005.

[69] W Martinssen and H Warlimont, editors. *Springer Handbook of Condensed Matter and Materials Data*. Springer Berlin, 2005.

[70] I P Soshnikov, G E Cirlin, A A Tonkikh, Y B Samsonenko, V G Dubrovskii, V M Ustinov, O M Gorbenko, D Litvinov, and D Gerthsen. Atomic Structure of MBE-Grown GaAs Nanowhiskers. *Physics of the Solid State*, 47:2213, 2005.

[71] C Thelander, P Caroff, S Plissard, AW Dey, and KA Dick. Effects of crystal phase mixing on the electrical properties of InAs Nanowires. *Nano Letters*, 11:2424, 2011.

[72] B A Wacaser, K Deppert, L S Karlsson, and L Samuelson. Growth and Characterization of defect free GaAs nanowires. *Journal of Crystal Growth*, 287:504, 2006.

[73] H Shtrikman, R Popovitz-Biro, A Kretinin, and M Heiblum. Stacking-Faults-Free Zinc Blende GaAs Nanowires. *Nano Letters*, 9:215, 2009.

[74] R E Algra, M A Verheijen, M T Borgstrom, L-F Feiner, G Immink, W J P van Enckevort, E Vlieg, and E P A M Bakkers. Twinning superlattices in indium phosphide nanowires. *Nature*, 456:369–372, 2008.

[75] N Holonyak, C M Wolfe, and J S Moore. Vapor-Liquid-Solid Growth of Gallium Phosphide. *Applied Physics Letters*, 6:64–65, 1965.

[76] S Iida and Y Sugita. GaAs-Whisker Crystals containing Germanium Core. *Applied Physics Letters*, 8:77–78, 1966.

[77] AM Morales and CM Lieber. A Laser Ablation Method for the Synthesis of Crystalline Semiconductor Nanowires. *Science*, 279:208, 1998.

[78] X Duan and C M Lieber. General Synthesis of Compound Semiconductor Nanowires. *Advanced Materials*, 12:298, 2000.

[79] B J Ohlsson, M T Björk, M H Magnusson, K Deppert, L Samuelson, and L R Wallenberg. Size-, shape-, and position-controlled GaAs nano-whiskers. *Applied Physics Letters*, 79:3335, 2001.

[80] Z H Wu, X Y Mei, D Kim, M Blumin, and H E Ruda. Growth of Au-catalyzed ordered GaAs nanowire arrays by molecular beam epitaxy. *Applied Physics Letters*, 81:5177, 2002.

[81] Z H Wu, M Sun, X Y Mei, and H E Ruda. Growth and photoluminescence characteristics of AlGaAs nanowires. *Applied Physics Letters*, 85:657, 2004.

[82] V G Dubrovskii, G E Cirlin, I P Soshnikov, A A Tonkikh, N V Sibirev, Y B Samsonenko, and V M Ustinov. Diffusion-induced growth of GaAs nanowhiskers during molecular beam epitaxy: Theory and experiment. *Physical Review B*, 71:205325, 2005.

[83] M C Plante and R R LaPierre. Growth mechanisms of GaAs nanowires by gas source molecular beam epitaxy. *Journal of Crystal Growth*, 286:394, 2006.

[84] Soo-Ghang Ihn, Jong-In Song, Tae-Wook Kim, Dong-Seok Leem, Takhee Lee, Sang-Geul Lee, Eui Kwan Koh, and Kyung Song. Morphology- and orientation-controlled gallium arsenide nanowires on silicon substrates. *Nano Letters*, 7(1):39–44, 2007.

[85] I. P. Soshnikov, G. E. Cirlin, A. A. Tonkikh, V. N. Nevedomskii, Yu. B. Samsonenko, and V. M. Ustinov. Electron diffraction on GaAs nanowhiskers grown on Si(100) and Si(111) substrates by molecular-beam epitaxy. *Physics of the Solid State*, 49(8): 1440, 2007.

[86] S G Ihn, J I Song, Y H Kim, J Y Lee, and I H Ahn. Growth of GaAs Nanowires on Si Substrates Using Molecular Beam Epitaxy. *IEEE Transactions on Nanotechnology*, 6: 384, 2007.

[87] Y B Samsonenko, G E Cirlin, V A Egryorov, N K Polyakov, V P Ulin, and V G Dubrovskii. Specific Features of Formation of GaAs Nanowire Crystals during Molecular Beam Epitaxy on Different Silicon Substrates. *Semiconductors*, 42:1445, 2008.

[88] J. H. Paek, T. Nishiwaki, M. Yamaguchi, and N. Sawaki. MBE-VLS growth of GaAs nanowires on (111)Si substrate. *Physica Status Solidi (c)*, 5:2740–2742, 2008.

[89] A Y Cho. Morphology of epitaxial growth of GaAs by a Molecular Beam Method: The observation of surface structures. *Journal of Applied Physics*, 41:2780, 1970.

[90] P Chen, K C Rajkumar, and A Madhukar. Relation between reflection high-energy electron diffraction specular beam intensity and the surface atomic structure/surface morphology of GaAs(111)B. *Journal of Vacuum Science and Technology B*, 9:2312, 1991.

[91] D A Woolf, D I Westwood, and R H Williams. The homoepitaxial growth of GaAs(111)A and GaAs(111)B by molecular beam epitaxy: an investigation of the temperature-dependent surface reconstructions and bulk electrical conductivity transitions. *Semiconductor Science and Technology*, 8:1075, 1993.

[92] Steve Wright and Herbert Kroemer. Reduction of oxides on silicon by heating in a gallium molecular beam at 800 deg. C. *Applied Physics Letters*, 36:210, 1980.

[93] T Engel. The interaction of molecular and atomic oxygen with Si(100) and Si(111). *Surface Science Reports*, 18:91–144, 1993.

[94] L Geelhaar, C Chèze, B Jenichen, O Brandt, C Pfüller, S Münch, R Rothemund, S Reitzenstein, A Forchel, T Kehagias, P Komninou, G P Dimitrakopulos, T Karakostas, L Lari, P R Chalker, M H Gass, and H Riechert. Properties of GaN nanowires grown by molecular beam epitaxy. *IEEE Journal of Selected Topics in Quantum Electronics*, invited, submitted, 2011.

[95] M C Plante and R R LaPierre. Au-assisted growth of GaAs nanowires by gas source molecular beam epitaxy: Tapering, sidewall faceting and crystal structure. *Journal of Crystal Growth*, 310:356, 2008.

[96] M Mattila, T Hakkarainen, H Lipsanen, H Jiang, and E I Kauppinen. Catalyst-free growth of In(As)P nanowires on silicon. *Applied Physics Letters*, 89:063119, 2006.

[97] C. Colombo, D. Spirkoska, M. Frimmer, G. Abstreiter, and A. Fontcuberta i Morral Morral. Ga-assisted catalyst-free growth mechanism of GaAs nanowires by molecular beam epitaxy. *Physical Review B*, 77(15):155326, 2008. doi: 10.1103/PhysRevB.77.155326.

[98] Fauzia Jabeen, Vincenzo Grillo, Silvia Rubini, and Faustino Martelli. Self-catalyzed growth of GaAs nanowires on cleaved Si by molecular beam epitaxy. *Nanotechnology*, 19(27):275711, 2008. doi: 10.1088/0957-4484/19/27/275711.

[99] J. H. Paek, T. Nishiwaki, M. Yamaguchi, and N. Sawaki. Catalyst free MBE-VLS growth of GaAs nanowires on (111)Si substrate. *Physica Status Solidi (c)*, 6:1436–1440, 2009.

[100] A Wolkenberg. A Mechanism for the Effect of Doping on the Silicon Native Oxide Thickness. *Physica Status Solidi (a)*, 79:313, 1983.

[101] C Okada, H Kobayashi, I Takahashi, J Ryuta, and T Shingyouji. Growth of Native Oxide and Accumulation of Organic Matter on Bare Si Wafer in Air. *Japanese Journal of Applied Physics*, 32:L1031, 1993.

[102] M Hines. *Fundamental Aspects of Silicon Oxidation*, chapter Morphological Aspects of Silicon Oxidation in Aqueous Solutions, pages 13–34. Springer Berlin, 2001.

[103] Maria Hilse. Wachstum von GaAs-Nanodrähten mittels Molekularstrahlepitaxie. Master’s thesis, Humboldt-Universität Berlini, 2009.

[104] J C Harmand, F Glas, and G Patriarche. Growth kinetics of a single InP(1-x)As(x) nanowire. *Physical Review B*, 81:235436, 2010.

[105] M Heiss, E Riedlberger, D Spirkoska, M Bichler, G Abstreiter, and A Fontcuberta i Morral. Growth mechanisms and optical properties of GaAs based semiconductors microstructures by selective are epitaxy. *Journal of Crystal Growth*, 310:1049, 2008.

[106] A Dadgar, M Poschenrieder, J Bläsing, O Contreras, F Bertram, T Riemann, A Reiher, M Kunze, I Daumiller, A Krtschil, A Diez, A Kaluza, A Modlich, M Kamp, J Christen, FA Ponce, E Kohn, and A Krost. MOVPE growth of GaN on Si(111). *Journal of Crystal Growth*, 248:556, 2003.

[107] A Biermanns, S Breuer, A Davydok, L Geelhaar, and U Pietsch. Structural evolution of self-assisted GaAs nanowires on Si(111). *Physica Status Solidi - Rapid Research Letters*, 5:156, 2011.

[108] V Schmidt, S Senz, and U Gösele. The shape of epitaxially grown silicon nanowires and the influence of line tension. *Applied Physics A*, 80:445, 2005.

[109] KW Schwarz and J Tersoff. From Droplets to Nanowires: Dynamics of VLS Growth. *Physical Review Letters*, 102:206101, 2009.

[110] KW Schwarz and J Tersoff. Elementary Processes in Nanowire Growth. *Nano Letters*, 11:316, 2011.

[111] S Breuer, M Hilse, L Geelhaar, and H Riechert. Nucleation and Growth of Au-assisted GaAs Nanowires on GaAs(111)B and Si(111). *Journal of Crystal Growth*, Article in Press, 2011.

[112] S Breuer, M Hilse, A Trampert, L Geelhaar, and H Riechert. Vapor-Liquid-Solid Nucleation of GaAs on Si(111) - Growth evolution from traces to nanowires. *Physical Review B*, 82:75406, 2010.

[113] Xin Zhang, Jin Zou, Mohanchand Paladugu, Yanan Guo, Yong Wang, Yong Kim, Hannah J. Joyce, Qiang Gao, H. Hoe Tan, and Chennupati Jagadish. Evolution of Epitaxial InAs Nanowires on GaAs (111)B. *Small*, 5(3):366–369, 2009.

[114] J Bauer, U Pietsch, A Davydok, A Biermanns, V Gottschalch, and G Wagner. X-ray investigation of the interface structure of free-standing InAs nanowires grown on GaAs(111)B. *Applied Physics A*, 96:851–859, 2009.

[115] K A Dick, S Kodambaka, M C Reuter, K Deppert, L Samuelson, W Seifert, L R Wallenberg, and F M Ross. The Morphology of Axial and Branched Nanowire Heterostructures. *Nano Letters*, 7:1817–1822, 2007.

[116] R I G Uhrberg, R D Bringans, M A Olmstead, R Z Bachrach, and J E Northrup. Symmetric Arsenic Dimers on the Si(100) Surface. *Physical Review B*, 35:3945, 1987.

[117] D K Biegelsen, F A Ponce, A J Smith, and J C Tramontana. Initial stages of epitaxial growth of GaAs on (100) silicon. *Journal of Applied Physics*, 61:1856, 1987.

[118] A. Zangwill. *Physics at Surfaces*. Cambridge University Press, 1988.

[119] R J Jaccodine. Surface Energy of Germanium and Silicon. *Journal of the Electrochemical Society*, 110:524, 1963.

[120] R D Bringans, M A Olmstead, R I G Uhrberg, and R Z Bachrach. Interface formation of GaAs with Si(100), Si(111), and Ge(111): Core-level spectroscopy for monolayer coverages of GaAs, Ga, and As. *Physical Review B*, 36:9569, 1987.

[121] D K Biegelsen, R D Bringans, J E Northrup, M C Schabel, and L-E Swartz. Arsenic termination of the Si(110) surface. *Physical Review B*, 47(15):9589–9596, Apr 1993. doi: 10.1103/PhysRevB.47.9589.

[122] B. Ressel, K. C. Prince, S. Heun, and Y. Homma. Wetting of Si surfaces by Au-Si liquid alloys. *Journal of Applied Physics*, 93:3886, 2003.

[123] N. Moll, A. Kley, E. Pehlke, and M. Scheffler. GaAs equilibrium crystal shape from first principles. *Physical Review B*, 54:8844, 1996.

[124] A Biermanns, S Breuer, A Davydok, A Trampert, L Geelhaar, and U Pietsch. Strain release in Ga-assisted GaAs nanowires grown on Si(111). Manuscript in preparation.

[125] S C Hardy. The Surface Tension of Liquid Gallium. *Journal of Crystal Growth*, 71: 602, 1985.

[126] A K Kota, G Anand, S Ramakrishnan, L L Regel, and W R Wilcox. Influence of O, H, He, Ar and vacuum on the surface behavior of molten InSb, other semiconductors and metals on silica. *Journal of Crystal Growth*, 290:319, 2006.

[127] U König and W. Keck. Contact Angles Between III-V Melts and Several Substrates. *Journal of the Electrochemical Society*, 130:685, 1983.

[128] Sergio Bietti. *Nanostructured III-V epilayers on silicon substrate for optoelectronic applications*. PhD thesis, Milano-Bicocca University, 2011.

[129] B Bauer, A Rudolph, M Soda, A Fontcuberta i Morral, J Zweck, D Schuh, and E Reiger. Position controlled self-catalyzed growth of GaAs nanowires by molecular beam epitaxy. *Nanotechnology*, 21:435601, 2010.

[130] Y Cui, Q Wei, P Park, and CM Lieber. Nanowire nanosensors for highly sensitive and selective detection of biological and chemical species. *Science*, 293:1289, 2001.

[131] Hans Lüth. *Solid Surfaces, Interfaces and Thin Films, 4th edition*. Springer, Berlin, 2001.

[132] M Diarra, YM Niquet, C Delerue, and G Allan. Ionization energy of donor and acceptor impurities in semiconductor devices: Importance of dielectric confinement. *Physical Review B*, 75:45301, 2007.

[133] M T Björk, H Schmid, J Knoch, H Riel, and W Riess. Donor deactivation in silicon nanowires. *Nature Nanotechnology*, 4:103, 2009.

[134] I Zardo, S Conesa-Boj, F Peiro, JR Morante, J Arbiol, E Uccelli, G Abstreiter, and A Fontcuberta i Morral. Raman spectroscopy of wurtzite and zinc-blende GaAs nanowires: Polarization dependence, selection rules, and strain effects. *Physical Review B*, 80:245324, 2009.

[135] J. Johansson, L. S. Karsson, C. P. T. Svensson, T Martensson, B. A. Wacaser, K. Deppert, L. Samuelson, and W. Seifert. Structural properties of <111>B-oriented III-V nanowires. *Nature Materials*, 5:574, 2006.

[136] D Spirkoska, J Arbiol, A Gustafsson, S Conesa-Boj, F Glas, I Zardo, M Heigoldt, M H Gass, A L Bleloch, S Estrade, M Kaniber, J Rossler, F Peiro, J R Morante, G Abstreiter, L Samuelson, and A Fontcuberta i Morral. Structural and optical properties of high quality zinc-blende/wurtzite GaAs nanowire heterostructures. *Physical Review B*, 80:245325, 2009.

[137] A Biermanns, A Davydok, H Paetzelt, A Diaz, V Gottschalch, T H Metzger, and U Pietsch. Individual GaAs nanorods imaged by coherent X-ray diffraction. *Journal of Synchrotron Radiation*, 16:796, 2009.

[138] A Fontcuberta i Morral, D Spirkoska, J Arbiol, M Heigoldt, J R Morante, and G Abstreiter. Prismatic Quantum Heterostructures Synthesized on Molecular-Beam Epitaxy GaAs Nanowires. *Small*, 4:899, 2008.

[139] D Spirkoska, G Abstreiter, and A Fontcuberta i Morral. Size and environment dependence of surface phonon modes of gallium arsenide nanowires as measured by Raman spectroscopy. *Nanotechnology*, 19:435704, 2008.

[140] G E Cirlin, V G Dubrovskii, Y B Samsonenko, A D Bouravleuv, K Durose, Y Y Proskuryakov, B Mendes, L Bowen, M A Kaliteevski, R A Abram, and D Zeze. Self-catalyzed, pure zincblende GaAs nanowires grown on Si(111) by molecular beam epitaxy. *Physical Review B*, 82:035302, 2010.

[141] L S Karlsson, K A Dick, J B Wagner, J-O Malm, K Deppert, L Samuelson, and L R Wallenberg. Understanding the 3D Structure of GaAs<111>B nanowires. *Nanotechnology*, 18:485717, 2007.

[142] S O Mariager, C B Sorensen, M Aagesen, J Nygard, R Feidenhans'l, and P R Willmott. Facet structure of GaAs nanowires grown by molecular beam epitaxy. *Applied Physics Letters*, 91:083106, 2007.

[143] Simon O Mariager, Søren L Lauridsen, Claus B Sørensen, Asmus Dohn, Phillip R Willmott, Jesper Nygard, and Robert Feidenhans'l. Stages in molecular beam epitaxy growth of GaAs nanowires studied by x-ray diffraction. *Nanotechnology*, 21: 115603, 2010.

[144] M. A. Verheijen, R. E. Algra, M. T. Borgström, G. Immink, E. Sourty, W. J. P. van Enckevort, E. Vlieg, and E. P. A. M. Bakkers. Three-dimensional Morphology of GaP-GaAs Nanowires Revealed by Transmission Electron Tomography. *Nano Letters*, 7:3051, 2007.

[145] N. Sköld, J. B. Wagner, G. Karlsson, T. Hernán, W. Seifert, M.-E. Pistol, and L. Samuelson. Phase Segregation in AlInP Shells on GaAs Nanowires. *Nano Letters*, 6:2743, 2006.

[146] J B Wagner, N Sköld, L R Wallenberg, and L Samuelson. Growth and segregation of GaAs-(Al,In)P core-shell nanowires. *Journal of Crystal Growth*, 312:1755, 2010.

[147] M. Rosini and R. Magri. Surface Effects on the Atomic and Electronic Structure of Unpassivated GaAs Nanowires. *ACS Nano*, 4:6021, 2010.

[148] K Jacobi, L geelhaar, J Márquez, J Platen, and C Setzer. The morphology of high-index GaAs surfaces. *Applied Surface Science*, 166:173, 2000.

[149] R E Algra, M A Verheijen, L-F Feiner, G G W Immink, R Theissmann, W J P van Enckevort, E Vlieg, and E P A M Bakkers. Paired Twins and {11(2)over-bar} Morphology in GaP Nanowires. *Nano Letters*, 10(7):2349–2356, JUL 2010.

[150] Harald Ibach. *Physics of Surfaces and Interfaces*. Springer Berlin, 2006.

[151] V G Dubrovskii, N V Sibirev, J C Harmand, and F Glas. Growth kinetics and crystal structure of semiconductor nanowires. *Physical Review B*, 78:235301, 2008.

[152] H. J. Joyce, Jennifer Wong-Leung, Qiang Gao, H. Hoe Tan, and Chennupati Jagadish. Phase Perfection in Zinc Blende and Wurtzite III-V Nanowires Using Basic Growth Parameters. *Nano Letters*, 10:908, 2010.

[153] P Krogstrup, R Popovitz-Biro, E Johnson, M H Madsen, J Nygard, and H Shtrikman. Structural Phase Control in Self-catalyzed Growth of GaAs Nanowires on Silicon (111). *Nano Letters*, 10:4475, 2010.

[154] C Messmer and J C Bilello. The surface energy of Si, GaAs, and GaP. *Journal of Applied Physics*, 52:4623, 1981.

[155] L Däweritz and R Hey. Reconstruction and defect structure of vicinal GaAs(001) and AlxGa(1-x)As(001) surfaces during MBE growth. *Surface Science*, 236:15, 1990.

[156] Ivan Egry, Georg Lohoefer, and Gerd Jacobs. Surface Tension of Liquid Metals: Results from Measurements on Ground and in Space. *Physical Review Letters*, 75: 4043, 1995.

[157] R E Algra, M A Verheijen, L-F Feiner, G G W Immink, W J P van Enckevort, E Vlieg, and E P A M Bakkers. The role of surface energies and chemical potential during nanowire growth. *Nano Letters*, 11:1259, 2011.

[158] C Chatillon and D Chatain. Congruent vaporization of GaAs(s) and stability of Ga(l) droplets at the GaAs(s) surface. *Journal of Crystal Growth*, 151:91, 1995.

[159] S W Ip and J M Toguri. The equivalency of surface tension, surface energy and surface free energy. *Journal of Materials Science*, 29:688, 1994.

[160] J Wallentin, M Ek, L R Wallenberg, L Samuelson, K Deppert, and M T Borgstrom. Changes in Contact Angle of Seed Particle Correlated with Increased Zincblende Formation in Doped InP Nanowires. *Nano Letters*, 10:4807, 2010.

[161] E Hilner, A Mikkelsen, J Eriksson, J N Andersen, E Lundgren, A Zakharov, H Yi, and P Kratzer. Au wetting and nanoparticle stability on GaAs(111)B. *Applied Physics Letters*, 89:251912, 2006.

[162] Peter Kratzer. Private Communication.

[163] J W Chen and A G Milnes. Energy levels in Silicon. *Annual Review of Materials Science*, 10:15, 1980.

[164] P. Hiesinger. Hall-effect levels in Ag- and Au-doped p-type GaAs. *Physica Status Solidi (a)*, 33:K39, 1976.

[165] Z X Yan and A G Milnes. Deep Level Transient Spectroscopy of Silver and Gold Levels in LEC-grown Gallium-Arsenide. *Journal of the Electrochemical Society*, 129: 1353–1356, 1982.

[166] H J Joyce, Q Gao, H H Tan, C Jagadish, Y Kim, M A Fickenscher, S Perera, T B Hoang, L M Smith, H E Jackson, J M Yarrison-Rice, X Zhang, and J Zou. High Purity GaAs Nanowires Free of Planar Defects: Growth and Characterization. *Advanced Functional Materials*, 18:3794–3800, 2008.

[167] L M Smith, H E Jackson, J M Yarrison-Rice, and C Jagadish. Insights into single semiconductor nanowire heterostructures using time-resolved photoluminescence. *Semiconductor Science and Technology*, 25:024010, 2010.

[168] G W 't Hooft, W A J A van der Poel, L W Molenkamp, and C T Foxon. Giant oscillator strenght of free excitons in GaAs. *Physical Review B*, 35:8281, 1987.

[169] W J Rappel, L F Feiner, and M F H Schuurmans. Exciton-polariton picture of the free-esciton lifetime in GaAs. *Physical Review B*, 38:7874, 1988.

[170] D J Wolford, G D Gilliland, T F Kuech, J F Klem, H P Hjalmarson, J A Bradley, C F Tsang, and J Martinsen. Comparison of Transport, Recombination, and Interfacial Quality in Molecular-Beam Epitaxy and Organometallic Vapor-Phase Epitaxy GaAs/Al(x)Ga(1-x)As Structures. *Applied Physics Letters*, 64(11):1416–1418, 1994.

[171] P Parkinson, H J Joyce, Q. Gao, H. H. Tan, X Zhang, J Zou, C Jagadish, L M Herz, and M B Johnston. Carrier Lifetime and Mobility Enhancement in Nearly Defect-Free Core-Shell Nanowires measured using Time-resolved Teraherz Spectroscopy. *Nano Letters*, 9:3349, 2009.

[172] S Breuer, C Pfüller, T Flissikowski, O Brandt, H T Grahn, L Geelhaar, and H Riechert. Suitability of Au- and Self-assisted GaAs Nanowires for Optoelectronic Applications. *Nano Letters*, 11:1276, 2011.

[173] L Pavesi and M Guzzi. Photoluminescence of Al(x)Ga(1-x)As Alloys. *Journal of Applied Physics*, 75(10, Part 1):4779–4842, 1994.

[174] T B Hoang, A F Moses, H L Zhou, D L Dheeraj, B O Fimland, and H Weman. Observation of free exciton photoluminescence emission from single wurtzite GaAs nanowires. *Applied Physics Letters*, 94:133105, 2009.

[175] Carsten Pfüller. *Optical Properties of single semiconductor nanowires and nanowire ensembles*. PhD thesis, Humboldt Universität Berlin, 2011.

[176] R. M. Sieg, J A Carlin, JJ Boeckl, S A Ringel, M T Currie, S M Ting, T A Langdo, G Taraschi andE A Fitzgerald, and B M Keyes. High minority-carrier lifetimes in GaAs grown on low-defect-density Ge/GeSi/Si substrates. *Applied Physics Letters*, 73:3111, 1998.

[177] R K Ahrenkiel. *Semiconductors and Semimetals, Vol. 39*, chapter 2, page 39. Academic Press, 1993.

[178] J B Schlager, K A Bertness, P T Blanchard, L H Robins, A Roshko, and N A Sanford. Steady-state and time-resolved photoluminescence from relaxed and strained GaN nanowires grown by catalyst-free molecular-beam epitaxy. *Journal of Applied Physics*, 103:124309, 2008.

[179] A. Ehrhardt, W. Wettling, and A. Bett. Transient Photoluminescence Decay Study of Minority Carrier Lifetime in GaAs Heteroface Solar Cell Structures. *Applied Physics A*, 53:123–129, 1991.

[180] S R McAfee, W T Tsang, and D V Lang. The effect of substrate temperature on deep levels in n-AlGaAs grown by molecular beam epitaxy. *Journal of Applied Physics*, 52: 6165, 1981.

[181] A G Milnes. *Deep Impurities in Semiconductors*. Wiley-Interscience, 1973.

[182] H. A. Zarem, P.C. Sercel, J.A. Lebens, L.E.Eng, A. Yariv, and K.J. Vahala. Direct determination of the ambipolar diffusion length in GaAs-AlGaAs heterostructures by cathodoluminescence. *Applied Physics Letters*, 55:1647, 1989.

[183] Yu and Cardona. *Fundamentals of Semiconductors, 4th edition*. Springer Berlin, 2010.

[184] Sze. *Physics of Semiconductor Devices, 2nd edition*. Wiley, 1981.

[185] D T J Hurle. A comprehensive thermodynamic analysis of native point defect and dopand solubilities in gallium arsenide. *Journal of Applied Physics*, 85:6957, 1999.

[186] D T J Hurle. A thermodynamic analysis of native point defect and dopand solubilities in zinb-blende III-V semiconductors. *Journal of Applied Physics*, 107:121301, 2010.

[187] D J Chadi and K J Chang. Metastability of the Isolated Arsenic-Antisite Defect in GaAs. *Physical Review Letters*, 60:2187, 1988.

[188] D V Lang. *Deep centers in semiconductors*, chapter DX Centers in III-V Alloys (Chapter 7), Section 4.1 Ionization and Activation Energies, pages 518–523. Gordon and Breach Science Publishers, New York, 1986.

[189] M A Krivov, E V Malisova, and E N Mel'chenko. Investigation of the behavior of gold in gallium arsenide. *Soviet Physics - Semiconductors*, 4:693, 1970.

[190] F S Shishiyanu and B I Boltaks. *Soviet Physics - Solid State*, 8:1053, 1966.

[191] D J Wolford, G D Gilliland, T F Kuech, L M Smith, J Martinsen, R Venkatasubramanian, S K Ghandi, and H P Hjalmarson. Intrinsic recombination and interface characterisation in "surface-free" GaAs structures. *Journal of Vacuum Science and Technology B*, 9:2369, 1991.

[192] A Chiari, M Colocci, F Fermi, Y Li, R Querzoli, A Vinattieri, and W Zhuang. Temperature Dependence of the Photoluminescence in GaAs-GaAlAs Multiple Quantum Well Structures. *Physica Status Solidi (b)*, 147:421, 1988.

[193] L V Titova, T B Hoang, H E Jackson, L M Smith, J M Yarrison-Rice, Y Kim, H J Joyce, H H Tan, and C Jagadish. Temperature dependence of photoluminescence from single GaAs-AlGaAs nanowires. *Applied Physics Letters*, 89:173126, 2006.

[194] S T Pantelides, editor. *Deep centers in semiconductors: a state-of-the-art approach.* Gordon and Breach Science Publishers, New York, 2nd ed. edition, 1986.

[195] A J SpringThorpe, S J Ingrey, B Emmerstorfer, P Mandeville, and W T Moore. Measurement of GaAs surface oxide desorption temperature. *Applied Physics Letters*, 50:77, 1987.

[196] J H Neave, B A Joyce, P J Dobson, and N Norton. Dynamics of film growth on GaAs by MBE from Rheed observations. *Applied Physics A*, 31:1, 1983.

[197] B F Lewis, R Fernandez, A Madhukar, and F J Grunthaner. Arsenic-induced intensity oscillations in reflection high-energy electron diffraction measurements. *Journal of Vacuum Science and Technology B*, 4:560, 1986.

[198] C T Foxon. MBE growth of GaAs and III-V alloys. *Journal of Vacuum Science and Technology B*, 1:293, 1983.

[199] W Braun, B Jenichen, V M Kaganer, A G Shtukenberg, L Däweritz, and K H Ploog. Layer-by-layer growth of GaAs(001) studied by in situ synchrotron X-ray diffraction. *Surface Science*, 525:126, 2003.

[200] Yoshiji Horikoshi. Advanced epitaxial growth techniques: atomic layer epitaxy and migration-enhanced epitaxy. *Journal of Crystal Growth*, 201/202:150, 1999.

[201] Akihiro Ohtake. Surface reconstructions on GaAs(001). *Surface Science Reports*, 63: 295, 2008.

[202] G E Becker and J C Bean. Acceptor dopants in silicon molecular-beam epitaxy. *Journal of Applied Physics*, 48:3395, 1977.

[203] R C Henderson, W J Polito, and J Simpson. Observation of SiC with Si(111) 7x7 surface structure using high-energy electron diffraction. *Applied Physics Letters*, 16: 15, 1970.

[204] A Ishizaka and Y Shiraki. Low temperature surface cleaning of silicon and its application to silicon MBE. *Journal of the Electrochemical Society*, 133:666, 1986.

[205] A Casel, E Kasper, H Kibbel, and E Sasse. Boron contamination of in situ heated silicon surfaces. *Journal of Vacuum Science and Technology B*, 5:1650, 1987.

[206] K Miki, K Sakamoto, and T Sakamoto. Surface preparation of Si substrates for epitaxial growth. *Surface Science*, 406:312–327, 1998.

[207] W Kern and D A Puotinen. Cleaning solutions based on hydrogen peroxide for use in silicon semiconductor technology. *RCA Review*, 31:187–206, 1970.

[208] M Lublow, T Stempel, K Skorupska, A G Munoz, M Kanis, and H J Lewerenz. Morphological and chemical opimization of ex situ NH4F (40%) conditioned Si(111)-(1x1):H. *Applied Physics Letters*, 93:062112, 2008.

Acknowledgements

I have hesitated to write these acknowledgements for not knowing how to express what needs to be said and for the inevitability of forgetting someone. I have to apologize in advance then. You have not been forgotten, merely out of mind for a brief moment.

First I would like to thank Lutz Geelhaar who has been a wonderful guide throughout my work on this thesis and who has always had constructive and positive answers to all my questions, be they scientific or organisational. I am incredibly thankful for all the support that I have received over these years and for all the opportunities that I have been given.

I would also like to thank Henning Riechert, who took me on board of the Paul-Drude-Institut even before he had arrived and gave me the chance to dive deeply into this fascinating project. I am more than grateful for this big opportunity. His influence on the PDI has transformed it into a very lively place during my thesis years.

Towards the end of my PhD, I had the opportunity to collaborate with the distinguished visiting theoretician Lou-Fe Feiner from TU Eindhoven, who was an incredible source of insight and inspiration. It has been an honour to work with such a knowledgeable and curious scientist.

Oliver Brandt is acknowledged for always cheerfully finding time to share his deep insights into semiconductor growth and spectroscopy. I have always walked away from a conversation with more inspiration and clarity of understanding than I had before.

I would like to thank Achim Trampert for teaching me about Transmission Electron Microscopy and for taking all these wonderful images, without which many of our laboriously grown samples could not adequately be shown to the world.

Maria Hilse (née Wagler) is acknowledged not only for being such a good student, which made being her mentor very easy for me, but also for her extensive morphological analysis of the Au-assisted nucleation series.

Of course I have had the opportunity to work with very many talented scientists and technicians at the PDI without whom this thesis would not exist.

I would like the thank Claudia Herrmann, who has kept not only our MBE VI up and running and has taught me all about the technical aspects of MBE. Rudi Hey is acknowledged for several discussions through which I have learned a lot about the fundamentals of epitaxy. I also would like to acknowledge Manos Dimakis and Claudio Somaschini for several inspiring discussions about the epitaxy of virtually any nano-object.

Uwe Jahn is acknowledged for teaching me about Scanning Electron Microscopy and for many inspiring discussions. I would like to thank Anne-Kathrin Blum for regularly taking high quality SEM images. A large part of the SEM images in this thesis would not exist without her. I would also like to thank Jonas Lähnemann for the EDX measurements and long discussions.

I would like to thank Bernd Jenichen for teaching me about X-ray spectroscopy and for providing excellent spectra. Timur Flissikowski is acknowledged for making time-resolved photoluminescence measurements.

Then there are all those people at the institute who were not directly involved in the thesis but whose presence cheered me up in many different ways. I do not dare to begin dropping names because a very long but still incomplete list would follow.

I also would like to thank my family and friends who supplied me with wisdom and tireless support and much helped me make it through the harder times of this work.

Finally and most of all, I thank Steffi Quedenfeld-Breuer, my therapist, closest friend, ally and wife. I could not have done this without you.

Selbständigkeitserklärung

Ich erkläre, dass ich die vorliegende Arbeit selbständig und nur unter Verwendung der angegebenen Literatur und Hilfsmittel angefertigt habe.

Berlin, den 20.06.2011 Steffen Breuer